

NASA
CP
2085
pt.2
c.1

NASA Conference Publication 2085

Part II

LOAN COPY: RE
AFWL TECHNICAL
KIRTLAND AFB,

0099882



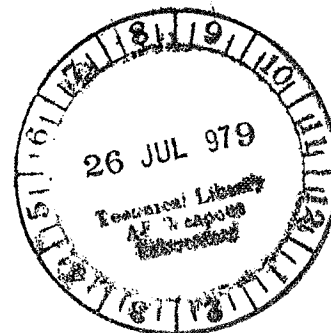
TECH LIBRARY KAFB, NM

Science and Technology of Low Speed and Motorless Flight

Proceedings of a symposium held at
NASA Langley Research Center
Hampton, Virginia
March 29-30, 1979

NASA

SSA





NASA Conference Publication 2085
Part II

Science and Technology of Low
Speed and Motorless Flight

Perry W. Hanson, *Compiler*
NASA Langley Research Center

Proceedings of a symposium cosponsored by
NASA Langley Research Center and the
Soaring Society of America, and held at
NASA Langley Research Center, Hampton, Virginia
March 29-30, 1979



National Aeronautics
and Space Administration

**Scientific and Technical
Information Office**

1979

Page intentionally left blank

PREFACE

This NASA conference publication contains the proceedings of the Third International Symposium on the Science and Technology of Low Speed and Motorless Flight held at the NASA Langley Research Center, Hampton, Virginia, March 29-30, 1979. The symposium was cosponsored by the Langley Research Center (LaRC) and the Soaring Society of America (SSA). Oran Nicks, Deputy Director of the Langley Research Center, and James Nash-Webber, Massachusetts Institute of Technology and past chairman of the SSA Technical Board, were general cochairmen. Perry Hanson, NASA LaRC, was the symposium organizer and technical program chairman. Hewitt Phillips, NASA LaRC (Retired); Joseph Gera, NASA LaRC; and Robert Lamson, Chairman of the SSA Technical Board, served as chairmen for the technical sessions.

The purpose of the Symposium was to provide a forum for the interchange of information on recent progress in the science and technologies associated with low speed and motorless flight. Twenty-eight papers were presented in the areas of low speed aerodynamics, new materials applications and structural concepts, advanced flight instrumentation, sailplane optimal flight techniques, and self-launching and ultralight glider technology. This NASA conference publication contains these presentations and a paper, which was not presented, on proposed definitions for various categories of sailplanes and gliders.

The use of trade names or manufacturer's names in this publication does not constitute an official endorsement of such products or manufacturers, either expressed or implied, by NASA. The included papers are largely as submitted. The physical quantities, whether in the International System of Units (SI) or U.S. Customary Units, are retained as submitted by the authors.

Page intentionally left blank

CONTENTS

PREFACE iii

PART I*

LOW-SPEED AERODYNAMICS

1. LOW-SPEED SINGLE-ELEMENT AIRFOIL SYNTHESIS 1
John H. McMasters and Michael L. Henderson

2. AN EXPLORATORY INVESTIGATION OF THE EFFECT OF A PLASTIC COATING
ON THE PROFILE DRAG OF A PRACTICAL-METAL-CONSTRUCTION SAILPLANE
AIRFOIL 33
Dan M. Somers

3. OPTIMUM TAIL PLANE DESIGN FOR SAILPLANES 65
Kay Mayland

4. THE EFFECT OF DISTURBANCES ON A WING 81
Richard Eppler

5. GENERATION AND BREAKDOWN OF AERODYNAMIC LIFT:
PHYSICAL MECHANISM 93
Wolfgang Liebe

6. INTRODUCTION TO THE ARCOPTER ARC WING AND THE BERTELSEN EFFECT
FOR POSITIVE PITCH STABILITY AND CONTROL 103
William D. Bertelsen

7. SOME NEW AIRFOILS 131
Richard Eppler

8. A COMPARISON OF THE AERODYNAMIC CHARACTERISTICS OF
EIGHT SAILWING AIRFOIL SECTIONS 155
Mark D. Maughmer

9. LENGTH AND BURSTING OF SEPARATION BUBBLES: A PHYSICAL
INTERPRETATION 177
John M. Russell

10. WING SHAPE OPTIMIZATION FOR MAXIMUM CROSS-COUNTRY SPEED,
WITH MATHEMATICAL PROGRAMMING 203
Gunter Helwig

*Papers 1 to 14 are presented under a separate cover.

ADVANCED INSTRUMENTATION

11. FURTHER DEVELOPMENTS IN SIMPLE TOTAL ENERGY SENSORS	219
Oran W. Nicks	
12. HOW ACCURATE IS NETTO	247
Stephen du Pont	
13. THE APPLICATION OF MICROPROCESSOR TECHNOLOGY TO IN-FLIGHT COMPUTATIONS	267
Patricia L. Sawyer and Dan M. Somers	

MOTORSOARERS

14. DESIGN OF PROPELLERS FOR MOTORSOARERS	285
E. Eugene Larrabee	

PART II

OPTIMAL FLIGHT TECHNIQUES

15. MINIMUM ALTITUDE-LOSS SOARING IN A SPECIFIED VERTICAL WIND DISTRIBUTION	305
Bion L. Pierson and Imao Chen	
16. A STUDY OF COURSE DEVIATIONS DURING CROSS-COUNTRY SOARING	319
Steven M. Sliwa and David J. Sliwa	
17. ON GLOBAL OPTIMAL SAILPLANE FLIGHT STRATEGY	355
G. Sander and F. X. Litt	
18. BALANCE TRAINING OF THE EQUILIBRIUM ORGAN AND ITS EFFECT ON FLIGHT STRATEGY	377
K. -D. Eikemeier, H. -D. Melzig, N. Reicke, and W. Schmidt	
19. A MONTE CARLO APPROACH TO COMPETITION STRATEGY	389
Michael P. Teter	

STRUCTURES AND MATERIALS

20. A GENERAL METHOD FOR THE LAYOUT OF AILERONS AND ELEVATORS OF GLIDERS AND MOTORPLANES	399
Manfred Hiller	
21. EXPERIMENTAL INVESTIGATION INTO THE FEASIBILITY OF AN "EXTRUDED" WING	419
Piero Morelli and Giulio Romeo	

22. TREATMENT OF THE CONTROL MECHANISMS OF LIGHT AIRPLANES IN THE FLUTTER CLEARANCE PROCESS	437
Elmar J. Breitbach	

23. ADVANCED COMPOSITES IN SAILPLANE STRUCTURES: APPLICATION AND MECHANICAL PROPERTIES	467
Dieter Muser	

ULTRALIGHT SAILPLANES AND HANG GLIDERS

24. THE ULTRALIGHT SAILPLANE	485
J. H. McMasters	

25. ANALYTICAL AND SCALE-MODEL RESEARCH AIMED AT IMPROVED HANG GLIDER DESIGN	505
Ilan Kroo and Li-Shing Chang	

26. IMPROVEMENT OF HANG GLIDER PERFORMANCE BY USE OF ULTRALIGHT ELASTIC WING	523
Jerzy Wolf	

27. EXPERIMENTAL STUDY OF THE FLIGHT ENVELOPE AND RESEARCH OF SAFETY REQUIREMENTS FOR HANG-GLIDERS	537
Claudius La Burthe	

28. WIND TUNNEL TESTS OF FOUR FLEXIBLE WING ULTRALIGHT GLIDERS	557
Robert A. Ormiston	

CONTEMPORARY SOARING NOMENCLATURE**	591
S. O. Jenko	

ATTENDEES	595
---------------------	-----

**Paper not presented at symposium.

MINIMUM ALTITUDE-LOSS SOARING IN A
SPECIFIED VERTICAL WIND DISTRIBUTION

Bion L. Pierson and Imao Chen
Iowa State University

SUMMARY

Minimum altitude-loss flight of a sailplane through a given vertical wind distribution is discussed. The problem is posed as an optimal control problem, and several numerical solutions are obtained for a sinusoidal wind distribution.

INTRODUCTION

The problem of determining the optimal sailplane trajectory through a prescribed vertical wind distribution for minimum altitude loss is formulated and solved as an optimal control problem. The flight is assumed to take place in a vertical plane over a fixed range, and the rotational or pitch dynamics of the sailplane are neglected. Sailplane lift coefficient serves as the control function in the nonlinear point-mass equations of motion.

For oscillatory vertical wind distributions, this problem belongs to the class of "optimal dolphin soaring" problems. In qualitative terms, these problems exhibit solutions for which the sailplane speed is decreased in upcurrents to prolong the altitude gain and increased in downcurrents to lessen the altitude loss (ref. 1). Earlier solutions to these problems have assumed either piecewise-static flight (equilibrium glide through segments of constant vertical wind--see, for example, reference 2) or quasi-static flight (kinematic equations of motion only--see, for example, references 3 through 6). Thus, the primary distinguishing feature of this paper is the use of the full nonlinear translational equations of motion and the corresponding use of a modern optimal control algorithm for numerical solutions. Additional research on the application of optimal control theory to dynamic sailplane performance problems may be found in references 7 through 9.

PROBLEM FORMULATION

A brief derivation of the equations of motion used here is provided in the Appendix. The basic assumptions are: flight in a vertical plane, uniform gravity acceleration g and atmospheric density ρ , a point-mass sailplane of constant mass m , and vertical wind of magnitude W . If the vertical wind distribution is further assumed to be independent of altitude ($W = W(x)$), then the right-hand sides of the equations of motion do not depend on altitude Y . The altitude equation (10A) can therefore be incorporated into the performance index (altitude loss)

$$\begin{aligned}
J = Y(0) - Y(t_f) &= \int_0^{t_f} (-\dot{Y}) dt \\
&= - \int_0^{t_f} (W + V \sin \gamma) dt
\end{aligned} \tag{1}$$

and need not be regarded as a differential constraint.

Furthermore, it will be convenient to regard the range X as the independent variable rather than the time t . Since the final range, $X(t_f) = X_f$, is to be specified, this change of variables will result in a fixed "end-time" optimal control problem which is inherently easier to solve than a variable "end-time" problem. The range equation (9A) can also be omitted from consideration as a differential constraint. It must be tacitly assumed, however, that the optimal trajectory will not include any kind of looping maneuver which would result in zero values for $V \cos \gamma$. Using (9A) then, the performance index (1) becomes

$$J = - \int_0^{X_f} \left[\frac{W + V \sin \gamma}{V \cos \gamma} \right] dX \tag{2}$$

and the remaining equations of motion, (11A) and (12A), become

$$\frac{dV}{dX} = - \left\{ \rho V^2 C_D S / (2m) + [(V \cos \gamma) (dW/dX) + g] \sin \gamma \right\} / (V \cos \gamma) \tag{3a}$$

$$\frac{d\gamma}{dX} = \left\{ \rho V C_L S / (2m) - [\cos \gamma (dW/dX) + g/V] \cos \gamma \right\} / (V \cos \gamma) \tag{3b}$$

respectively.

Finally, the nondimensional quantities

$$x = X/X_f, \quad v = V(gX_f)^{-1/2}, \quad w = W(gX_f)^{-1/2} \tag{4}$$

are introduced. The resulting optimal control problem may be stated as follows. Find that control function $u(x)$, $0 \leq x \leq 1$, which minimizes the augmented performance index

$$\begin{aligned}
J = - \int_0^1 \left[\frac{v \sin \gamma + w(x)}{v \cos \gamma} \right] dx &+ K_1^{-1} \int_0^1 [v/v_{\text{stall}} - 1]^{-1} dx \\
&+ K_2^{-1} \int_0^1 [1 - v/v_{\text{max}}]^{-1} dx
\end{aligned} \tag{5}$$

subject to the second-order dynamic system

$$\frac{dv}{dx} = - [\eta C_D(u) v^2 + (1 + \dot{w}) \sin \gamma] / (v \cos \gamma), \quad v(0) = v_0 \tag{6a}$$

$$\frac{d\gamma}{dx} = [\eta C_L(u) v^2 - (1 + \dot{w}) \cos \gamma] / (v^2 \cos \gamma), \quad \gamma(0) = \gamma_0 \quad (6b)$$

and subject to the terminal state constraints

$$\psi_1 = v(1)/v_0 - 1 = 0 \quad (7a)$$

$$\psi_2 = \gamma(1) - \gamma_0 = 0 \quad (7b)$$

$$\text{where } C_D(u) = a_1 + a_2 C_L + a_3 C_L^2 \quad (8)$$

$$C_L(u) = C_{L_{\max}} (2 \sin^2 u - 1) \quad (9)$$

$$\eta = \frac{1}{2} \rho (S/mg) g X_f \quad (10)$$

and where $w(x)$ is the prescribed wind distribution, $\dot{w} = (dw/dx)(dx/dt) = (dw/dx)v \cos \gamma$, and X_f is the fixed range. Minimum altitude-loss equilibrium glide (still air) values are adopted for the fixed and equal initial and terminal state values, v_0 and γ_0 . Several additional explanatory comments are required.

First, note that minimum (stall) and maximum (flutter) state inequality constraints on the airspeed are enforced using integral interior penalty functions (ref. 10) shown in terms two and three, respectively, of equation (5). Thus, a sequence of optimal control problems (5) - (10) must be solved for specified positive penalty constants K_1 and K_2 . The penalty constants are then increased between subproblems. The solution obtained from each subproblem is used as starting data for the subsequent subproblem. The sequence of subproblems is terminated when each penalty function value is sufficiently small.

Secondly, it may be observed that the lift coefficient is bounded via the transformation (9). That is, for any value of the control function $u(x)$, the control inequality constraints

$$- C_{L_{\max}} \leq C_L(u) \leq C_{L_{\max}} \quad (11)$$

are satisfied where $C_{L_{\max}}$ is a specified constant. Also, note that a quadratic drag polar (8) is used. More accurate drag polars may be used instead provided that an analytical relation is available between C_D and C_L . Finally, it should be observed that for a fixed wing loading, the nondimensional aerodynamic parameter η in equation (10) is proportional to the specified terminal range X_f .

This is the basic optimal control problem considered here. A variation of this problem will also be presented later.

NUMERICAL RESULTS

All computations have been performed on coupled IBM 360/65 and Ite1 AS/5 computers using a FORTRAN IV compiler and double precision arithmetic. The numerical integration of the required differential equations has been performed using a standard fourth-order Runge-Kutta method with 100 fixed uniform integration steps.

The numerical results have been obtained for the case of a sinusoidal wind distribution

$$w(x) = w_A \sin(2\pi x), \quad 0 \leq x \leq 1 \quad (12)$$

and the Nimbus II open-class sailplane using the gradient projection algorithm presented in reference 11. The sinusoidal wind distribution (12) is simply an idealized model of an oscillatory vertical wind which satisfies a "continuity" condition: the integral of $w(x)$ over the fixed range is zero. The values for the coefficients

$$a_1 = 0.009278, \quad a_2 = -0.009652, \quad a_3 = 0.022288 \quad (13)$$

of the quadratic drag polar (8) for the Nimbus II have been obtained from a least-squares fit of data taken from the manufacturer's velocity polar. For standard sea level conditions and a wing loading, mg/S , of $(32)(9.81) \text{ N/m}^2$, the aerodynamic parameter in equation (10) is given by $\eta = 0.01916 X_f$. Additional constant data chosen include: $C_L = 1.4$, $(gX_f)^{\frac{1}{2}} v_{\text{stall}} = 18 \text{ m/s}$ and $(gX_f)^{\frac{1}{2}} v_{\text{max}} = 70 \text{ m/s}$. Finally, in qualitative terms, the gradient projection method is a direct method in the sense that the control function $u(x)$ is changed during each iteration so as to produce both a decrease in the performance index value (eq. (5)) and full satisfaction of the terminal state constraints (eqs. (7)).

Specified Initial State

In this case, the initial and final state are to be held fixed and equal. In particular, the values

$$(gX_f)^{\frac{1}{2}} v_0 = 28.1676 \text{ m/s} \quad \text{and} \quad \gamma_0 = -0.019106 \text{ rad} \quad (14)$$

are to be used in equations (6) and (7) and correspond to the minimum altitude-loss equilibrium glide conditions for the Nimbus II in still air with a drag polar given by equations (8) and (13). The vertical wind amplitude is chosen as $(gX_f)^{\frac{1}{2}} w_A = 2 \text{ m/s}$, and a fixed range of 1000 meters is used.

The resulting optimal trajectory and the corresponding optimal lift coefficient distribution are presented in figures 1 and 2, respectively. The optimal flight can be divided into three successive segments: an initial climb, a maximum C_L arc, and a dive followed by a short pull-up. The initial climb is intuitively reasonable since the sailplane must gain as much altitude as

possible while in the initial upcurrent. The maximum C_L arc is a continuation of the first phase and lasts as long as the wind is strong enough to sustain it. The following dive is made to pass through the downcurrent as quickly as possible. The final pull-up is necessary to meet the terminal state constraints (7). The stall speed inequality constraint was active for this solution, but the maximum speed constraint was not.

The minimum altitude loss for this optimal trajectory is only 12.19 m. By comparison, the minimum altitude loss during an equilibrium glide in still air over the same 1000 m range is 19.11 m. This represents a 36% altitude-loss reduction.

Free but Equal Initial and Final States

Here, the initial and final speed and local flight path angle values are no longer specified, but the respective initial and final values are still required to be equal. The gradient projection algorithm, as described in reference 11, can accommodate the addition of the two control parameters $v(0)$ and $\gamma(0)$ representing variable initial states. However, the presence of these same two control parameters in the terminal state constraints necessitates a further modification to the projection operator equations.

Since the optimal trajectories are now being selected from a larger class, additional performance gains are expected. However, for a final range of 1000 m, the minimum altitude loss improves only 1.4%: from 12.19 m to 12.01 m. For comparison purposes, the optimal trajectory is also shown in figure 1. In this case, the optimal trajectory exhibits a higher altitude gain during the climb phase, a longer maximum C_L arc and a lesser altitude loss in the downcurrent when compared with the previous solution. The initial (and final) airspeed has increased approximately 1.2 m/s to 29.384 m/s.

Effects of Wind Amplitude

The initial and final states are again free but equal. For an increased wind amplitude of $(gX_f)^{1/2} w_A = 5$ m/s, a substantial improvement is obtained as may be noted from the optimal trajectory shown in figure 3. A net altitude gain of 5.158 m is now available over the 1000 m course. Clearly, for higher amplitudes of an oscillating vertical wind, more energy can be extracted from the wind to sustain cross-country flight.

Effects of Varying the Fixed Range

The wind amplitude is held fixed at 5 m/s, and free but equal initial and final states are again considered. Changes in the final range X_f affect only the constant aerodynamic parameter η and the characteristic length and time used in the nondimensionalization. Varying X_f is equivalent to varying the frequency of the sinusoidal wind distribution for sustained flights.

Upon reducing X_f from 1000 m to 500 m, a radically different optimal trajectory was obtained. The corresponding optimal trajectory and optimal C_L distribution are shown in figures 4 and 5, respectively, and will be referred to as a Type II solution. In this case, a dive-first climb-later flight pattern is observed. The average speed is much higher, and the net altitude gain is considerably higher than for the earlier Type I trajectory. The net altitude gain of 23.10 m exceeds that achieved on the previous Type I solution for double the range. For the Type II trajectories, the maximum speed inequality constraint is active rather than the stall speed constraint.

By employing the results of previous Type I solutions as starting data, it was possible to also obtain a Type I solution for $X_f = 500$ m. However, this Type I relative minimum solution yields a net altitude loss of 4.45 m. Thus, at least for relatively small X_f and large W_A , the Type II solution is decidedly superior to Type I solutions. As a matter of conjecture, the Type II solution may cease to exist for sufficiently large final ranges and/or for sufficiently small wind amplitudes. Two additional solutions were also obtained: a Type I solution for $X_f = 750$ m and a Type II solution for $X_f = 625$ m.

Effect of Wing Loading

If the nominal wing loading, mg/S, is increased by 15%, the aerodynamic parameter η becomes $0.01666 X_f$ (see equation (10)). Nothing else is changed. In this case, a Type I solution was obtained for $X_f = 1000$ m, $W_A = 5$ m/s and free but equal initial and final states. The resulting optimal trajectory provides a net altitude gain of 1.14 m which is nearly 4 m less than the comparable 5.16 m obtained earlier for the nominal wing loading. Both the optimal trajectories and the optimal lift coefficient histories for the two solutions are very similar.

The key results for the eight optimal solutions presented here are summarized in table I.

CONCLUSIONS AND DISCUSSION

The optimal control problem treated here is of at least moderate difficulty in view of the state variable inequality constraints present. Relatively few numerical solutions are currently available because of the considerable computational effort involved. However, several tentative conclusions emerge from the computational results obtained thus far.

- 1) For a sinusoidal vertical wind distribution, which serves as a simple model of a zero range-averaged oscillatory wind, substantial altitude savings are available when compared with optimal equilibrium glides in still air. The relative advantage increases for higher wind amplitudes.

- 2) Equal initial and final state vector elements can be treated as additional control parameters in the optimal control algorithm and therefore varied as part of the optimization process. The additional altitude gains obtained in this case are, however, rather small.
- 3) For relatively short ranges and high wind amplitude, it is possible to obtain optimal trajectories which exhibit an unexpected "dive first, climb later" maneuver sequence. Optimal trajectories of this second type involve higher speeds and better final altitude gains than the usual "dolphin" style optimal trajectory.
- 4) As expected, an increase in sailplane wing loading increases the minimum altitude loss when other conditions are held fixed.

The most surprising finding of this study is the apparent existence of two distinct types of extremal solutions at least for restricted ranges of the parameters involved. Clearly, the Type II trajectory deserves further research effort.

There is also a need to obtain results for other wind distributions and to make definitive comparisons with previous optimization studies which do not incorporate the full translational equations of motion. The related problem of minimum-time flight through a given vertical wind distribution for a specified altitude loss is of perhaps even greater interest. Research on this latter problem is currently underway.

REFERENCES

1. Reichmann, H., Cross-Country Soaring (English translation of Streckensegelflu, Thompson Publications, Santa Monica, California, 1978.
2. Meyer, R., "Dolphin-style gliding," Technical Soaring, Vol. 5, No. 1, 1-9, May 1978.
3. Arho, R., "Optimal dolphin soaring as a variational problem," Acta Polytechnica Scandinavica, Mechanical Engineering Series No. 68, 1972.
4. Irving, F. G., "Cloud-street flying," Technical Soaring, Vol. 3, No. 1, 1-8, Winter 1973.
5. Metzger, D. E. and Hedrick, J. K., "Optimal flight paths for soaring flight," Journal of Aircraft, Vol. 12, No. 11, 867-871, December 1975.
6. de Jong, J. L., "The 'optimal-range-velocity-polar', a new theoretical tool for the optimization of sailplane flight trajectories," Memorandum COSOR 77-28, Department of Mathematics, Eindhoven University of Technology, December 1977.
7. Pierson, B. L., "Maximum altitude sailplane winch-launch trajectories," Aeronautical Quarterly, Vol. 28, No. 2, 75-84, May 1977.
8. Pierson, B. L. and de Jong, J. L., "Cross-country sailplane flight as a dynamic optimization problem," International Journal for Numerical Methods in Engineering, Vol. 12, No. 11, 1743-1759, 1978.
9. Genalo, L. J. and Pierson, B. L., "A singular-arc approximation to a dynamic sailplane flight path optimization problem," Engineering Optimization, Vol. 3, No. 4, 175-182, 1978.
10. Lasdon, L. S., Waren, A. D., and Rice, R. K., "An interior penalty function method for inequality constrained optimal control problems," IEEE Transactions on Automatic Control, Vol. AC-12, No. 4, 388-395, August 1967
11. Pierson, B. L., "Panel flutter optimization by gradient projection," International Journal for Numerical Methods in Engineering, Vol. 9, No. 2, 271-296, 1975.

APPENDIX: DERIVATION OF THE EQUATIONS OF MOTION

The sailplane velocity vector, relative to the surrounding air, is given by (see figure 6)

$$\vec{V} = \dot{\vec{R}} - \vec{W} \quad (1A)$$

where \vec{R} is the inertial velocity vector for the sailplane, and $\vec{W}^T = [0, W(X,Y)]$ is the deterministic vertical wind distribution. The angle γ shown in figure 6 is the usual flight path angle for the case of no wind. In the inertial (X,Y)-coordinate frame, the translational equations of motion for unpowered flight in a uniform gravity field may be written as

$$m \ddot{\vec{R}} = \vec{L} + \vec{D} + \vec{G} = m(\dot{\vec{V}} + \dot{\vec{W}}) \quad (2A)$$

where \vec{L} and \vec{D} are the usual aerodynamic lift and drag forces, respectively, \vec{G} is the weight force, and m is the constant sailplane mass. Equation (2A) can be rearranged to yield

$$\begin{aligned} \dot{\vec{V}} &= (\vec{L} + \vec{D} + \vec{G})/m - \dot{\vec{W}} \\ &= \vec{L}/m + \vec{D}/m + [0, -g]^T + [0, -\dot{X}(\partial W/\partial X) - \dot{Y}(\partial W/\partial Y)]^T \end{aligned} \quad (3A)$$

where g is the constant gravity acceleration.

Primarily because of the definitions of lift and drag, it is desirable to rewrite equation (3A) with respect to a rotating (ξ, η) -coordinate frame defined by the unit vectors \hat{e}_ξ , directed toward \vec{V} , and \hat{e}_η , directed normal to \vec{V} along the lift vector. The inertial time derivative of \vec{V} , referred to this rotating frame, is then given by

$$\begin{aligned} \dot{\vec{V}} &= (d\vec{V}/dt)_{(\xi, \eta)} + \vec{\omega} \times \vec{V} \\ &= \dot{V} \hat{e}_\xi + (\dot{\gamma} \hat{e}_\zeta) \times (V \hat{e}_\xi) \\ &= \dot{V} \hat{e}_\xi + V \dot{\gamma} \hat{e}_\eta \end{aligned} \quad (4A)$$

where $\hat{e}_\zeta = \hat{e}_\xi \times \hat{e}_\eta$. Note that any vector in the plane, say \vec{A} , can be expressed in the rotating (ξ, η) -frame using the following rotation matrix.

$$\vec{A} = \begin{bmatrix} A_\xi \\ A_\eta \end{bmatrix} = \begin{bmatrix} \cos\gamma & \sin\gamma \\ -\sin\gamma & \cos\gamma \end{bmatrix} \begin{bmatrix} A_X \\ A_Y \end{bmatrix} \quad (5A)$$

Using equation (5A), one obtains

$$\vec{G}/m - \dot{\vec{W}} = -[\dot{X}(\partial W/\partial X) + \dot{Y}(\partial W/\partial Y) + g][\sin\gamma \hat{e}_\xi + \cos\gamma \hat{e}_\eta] \quad (6A)$$

The term, $g + \dot{\vec{W}} = g + \dot{X}(\partial W/\partial X) + \dot{Y}(\partial W/\partial Y)$, is often referred to as the apparent gravity acceleration.

Finally, using equations (4A) and (6A) and the usual expressions for lift and drag, equation (3A) can be written in scalar form as follows.

$$\dot{V} = - \rho V^2 C_D S / (2m) - [\dot{X}(\partial W / \partial X) + \dot{Y}(\partial W / \partial Y) + g] \sin \gamma \quad (7A)$$

$$V \dot{\gamma} = \rho V^2 C_L S / (2m) - [\dot{X}(\partial W / \partial X) + \dot{Y}(\partial W / \partial Y) + g] \cos \gamma \quad (8A)$$

From equation (1A) and the inverse of equation (5A), the kinematic equations may be written as

$$\dot{X} = V \cos \gamma \quad (9A)$$

$$\dot{Y} = W + V \sin \gamma \quad (10A)$$

Therefore, equations (7A) and (8A) become

$$\begin{aligned} \dot{V} = - \rho V^2 C_D S / (2m) - [(V \cos \gamma)(\partial W / \partial X) \\ + (W + V \sin \gamma)(\partial W / \partial Y) + g] \sin \gamma \end{aligned} \quad (11A)$$

$$\begin{aligned} \dot{\gamma} = \rho V C_L S / (2m) - [\cos \gamma (\partial W / \partial X) + (W / V + \sin \gamma)(\partial W / \partial Y) \\ + g / V] \cos \gamma \end{aligned} \quad (12A)$$

TABLE I. Summary of Optimal Solutions

TYPE	RANGE m	WIND AMPLITUDE m/s	$V(0) = V(1)$ m/s	$\gamma(0) = \gamma(1)$ rad.	ALTITUDE CHANGE m
I	1000	2	28.168 ^a	-0.0191 ^a	-12.187
I	1000	2	29.384	0.0511	-12.012
I	1000	5	31.899	-0.0528	5.158
II	500	5	55.011	-0.6286	23.098
II	625	5	53.253	-0.5285	11.283
I	750	5	31.518	-0.0089	-4.454
I	500	5	30.940	0.0039	-4.452
I	1000	5	33.346	0.0903	1.140 ^b

^a fixed boundary conditions

^b wing loading increased 15%

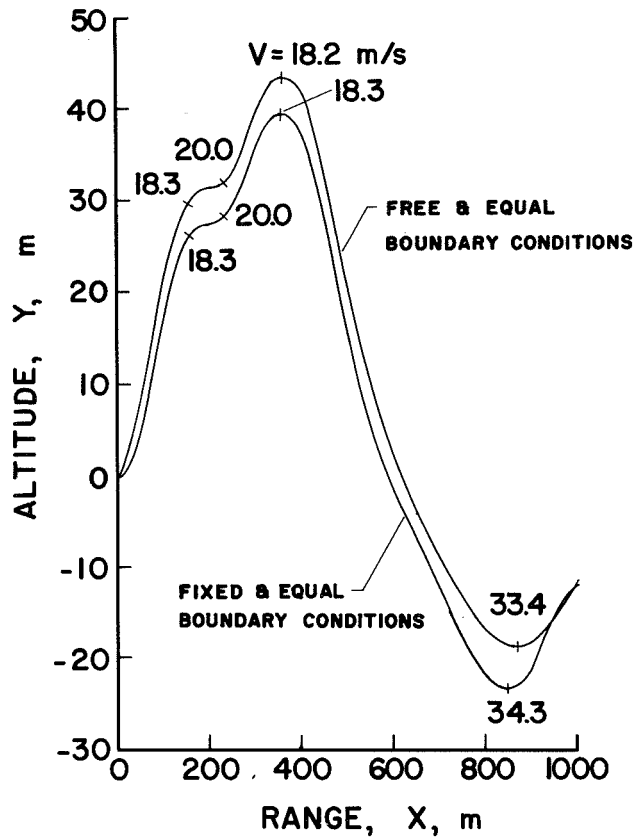


Figure 1.- Optimal trajectories of Type I: $W_A = 2$ m/s, $X_f = 1000$ m, $V_{stall} = 18$ m/s, $C_{L_{max}} = 1.4$.

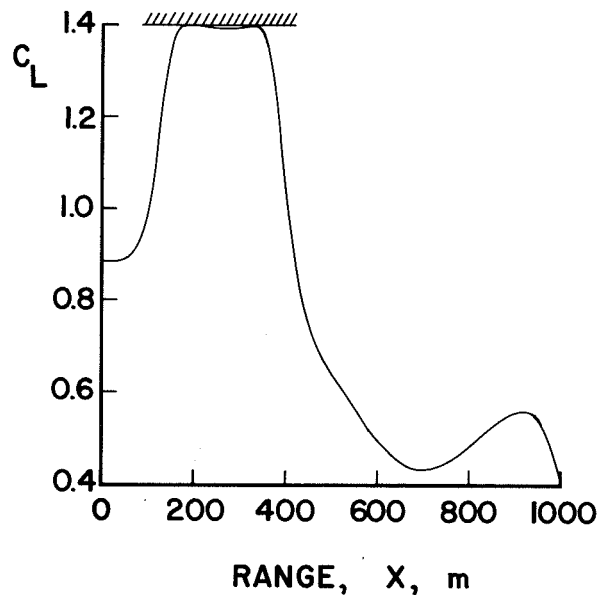


Figure 2.- Optimal lift coefficient distribution for fixed and equal boundary conditions: $W_A = 2$ m/s, $X_f = 1000$ m, $V_{stall} = 18$ m/s, $C_{L_{max}} = 1.4$.

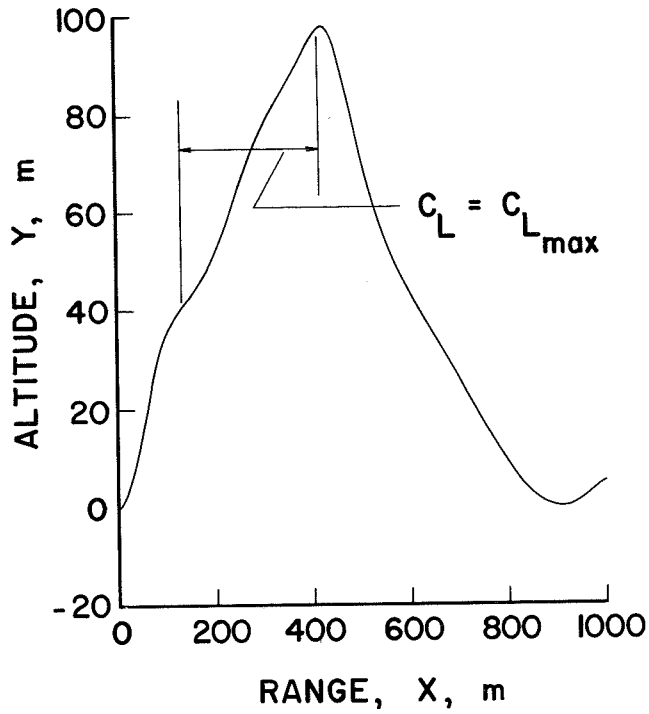


Figure 3.- Optimal Type I trajectory for high wind amplitude: $W_A = 5 \text{ m/s}$,
 $X_f = 1000 \text{ m}$, $V_{\text{stall}} = 18 \text{ m/s}$, $C_{L_{\text{max}}} = 1.4$.

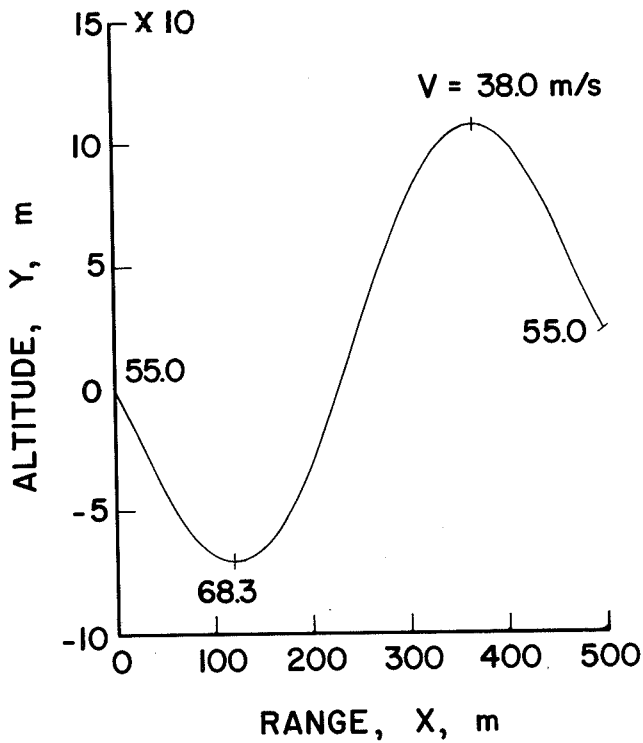


Figure 4.- Optimal Type II trajectory: $W_A = 5 \text{ m/s}$, $X_f = 500 \text{ m}$, $V_{\text{max}} = 70 \text{ m/s}$.

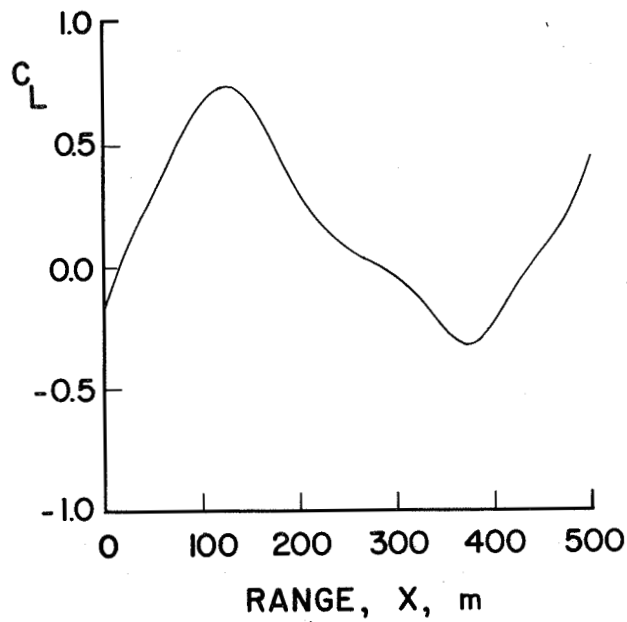


Figure 5.- Optimal lift coefficient distribution for Type II trajectory:
 $W_A = 5$ m/s, $X_f = 500$ m, $V_{\max} = 70$ m/s.

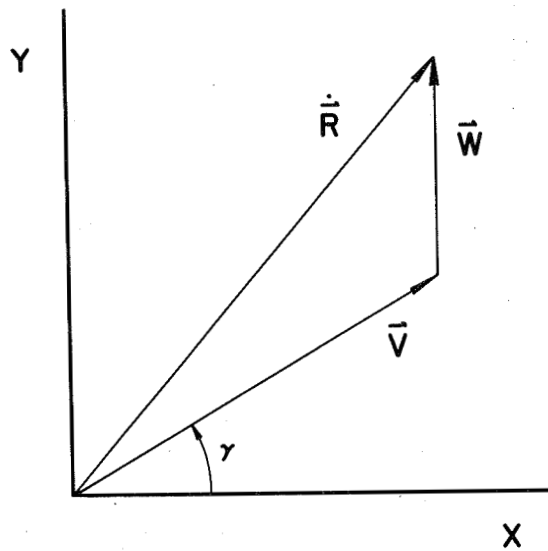


Figure 6.- Velocity vector diagram.

A STUDY OF COURSE DEVIATIONS DURING CROSS-COUNTRY SOARING

Steven M. Sliwa
Langley Research Center

David J. Sliwa
University of Illinois at Urbana-Champaign

ABSTRACT

Several models are developed for studying the impact of deviations from course during cross-country soaring flights. Analyses are performed at the micro-strategy and macro-strategy levels. Two types of lift sources are considered: concentrated thermals and thermal streets. The sensitivity of the optimum speed solutions to various model, piloting and performance parameters is evaluated. Guides are presented to provide the pilot with criterions for making in-flight decisions. In general, course deviations are warranted during weak lift conditions, but are less justifiable with moderate to strong lift conditions.

INTRODUCTION

There have been many attempts to develop optimum piloting strategies for the vertical plane of cross-country soaring (for example, references 1 through 5), which basically yield an optimal airspeed given the airmass characteristics, but little has been done with the horizontal plane. References 6 through 8 point out that substantial departures from the optimum speed-to-fly result in small degradations in achieved speed. In fact, the biggest contributing factors influencing average speed are maximizing the achieved rate-of-climb in lift and minimizing the atmospheric sink rate between regions of lift. So it seems that cross-country soaring performance is most influenced by the pilot's decisions made in the horizontal plane.

This paper will address itself to developing some models reflecting typical course deviation decisions a pilot is likely to be confronted with during a cross-country soaring flight. The accompanying analysis should provide guidelines for the pilot to rationally select flight paths which optimize the anticipated lift conditions. Two types of convective lift conditions are considered: soaring conditions where the regions of lift are small relative to the distance flown (circling required) and conditions where the regions of lift are of the order of the distance flown (thermal street flying). In addition, two categories of models are investigated. Micro-strategy models are used to analyze the choice of lift along a desired course line. Macro-strategy models are used for studying the influence of choosing a course line to a goal.

The analysis contained herein assumes parabolic performance polars with numerical examples computed for parameters typical of a modern standard class sailplane. The pilot is assumed to fly at the optimal airspeed for all course choices since perturbations are assumed to have a minor effect. Since final glides are not considered and potential energy is conserved, all models begin and end at the same altitude, cloudbase. Furthermore, all solutions neglect survivability, i.e., they assume the pilot will complete the task no matter which choices are made. Finally, all situations assume that the pilot is far from a ground referenced goal and that the lift is not ground referenced so the influence of wind can be neglected.

LIST OF SYMBOLS

A	Parasitic drag factor, $\frac{1}{2V_o^2(L/D)_{\max}}$
B	Induced drag factor, $\frac{V_o^2}{2(L/D)_{\max}}$
D	Distance on course to lift source goal for thermal street model
d	Distance on course to lift source goal for thermal models
d'	Projected distance of alternate lift source onto course line, Fig. 1
F ₁ , F ₂	Intermediate calculation variables
f	Intermediate calculation variable
h _{CL}	Altitude gained climbing in street lift
h _{CR}	Altitude lost cruising between streets
\dot{h}	Average rate-of-climb while circling in thermals
\dot{h}_s	Rate-of-climb averaged while cruising thermal street lift
K	Intermediate calculation constant, defined in Appendix C, Equation 3
K'	Intermediate calculation constant, defined in Appendix C, Equation 10
(L/D) _{max}	Equivalent to maximum glide ratio in still air
ℓ	Distance flown along street, Fig. 12
ℓ*	Distance to fly along street for optimum time

ℓ'	Distance to fly along street for time equal to not making course deviation
ℓ/D	Non-dimensionalized distance to fly along street, break-away point
m	Slope of tangent line
n	Length of second leg of course deviation, Fig. 12
R	Total distance of a cruise/climb street cycle
R_{CL}	Distance of climb phase of a street cycle
R_{CR}	Distance of cruise phase of a street cycle
Q_i	Value of defining polynomial for i th iteration
s	Total deviation distance of using a street parallel to course line, Fig. 9
s', s_1, s_2	Distance of individual legs of course deviation, Fig. 9
s/D	Deviation distance ratio of parallel street model, Fig. 9
T_D	Time to fly glide/climb thermal cycle on course
$T_{\ell n}$	Time to fly course deviation
V	Airspeed while cruising, knots
V^*	Optimum speed-to-fly between lift, knots
V_i^*	Guess of V^* during i -th iteration, knots
V_s^*	Sink rate flying at an airspeed of V^* , knots
V_{at}	Average vertical sinking velocity of atmosphere between lift, knots
V_{CL}	Airspeed while climbing in a street, knots
V_{CR}	Required airspeed to cruise in street lift and maintain constant altitude, knots
V_D, V_ℓ, V_n	Airspeed along legs D, ℓ, n respectively

V_G	Average ground speed after a complete glide/climb thermal cycle, knots
V_{GS}	Average ground speed after a complete glide/climb thermal street lift cycle, knots
V_{MIN}	Airspeed for minimum sink rate, knots
V_O	Speed at which $(L/D)_{max}$ occurs, knots
V_S	Sink rate flying at airspeed V , knots
V_{sn}	Sink rate flying at airspeed V_n , knots
W, X, Y, Z	Geometry labels for course deviation models
x	Total deviation distance, Fig. 1
x_1, x_2	Deviation distance legs, Fig. 1
x/d	Deviation distance ratio
y	Distance between parallel street and course line, Fig. 9
y/d	Spacing distance ratio
ζ	Ratio of average rate-of-climb on course to average rate-of-climb along course deviation
η	Ratio of average atmospheric sink rate between lift sources to average rate-of-climb in lift
σ	Ratio of average ground speed on course deviation in augmented lift to ground speed achieved on course with average lift conditions
ϕ	Angle between thermal street and course line
Ψ	Angle of thermal model course deviation

PRESENTATION OF RESULTS

Thermal Models

Micro-Strategy

The first case considered is depicted in figure 1. It represents a frequent decision confronting the pilot during cross-country soaring. The pilot,

after departing the thermal at X at cloudbase, must choose between staying on course along path XZ and achieving the average rate-of-climb for that time of day at thermal Z or deviating along XY to the thermal at Y, which looks as if it might yield a higher achieved rate-of-climb. Then the pilot returns to the course after deviating to Y by flying to thermal Z. Given the geometry, the question remains how much greater must be the rate-of-climb at thermal Y than the rate-of-climb at thermal Z to yield the same time for both the direct course and the extended route.

Figure 2 shows the result for a sailplane representative of the standard class. The required rate-of-climb in the thermal at Y is plotted against the non-dimensional deviation distance ratio for a variety of average lift conditions assuming the pilot flies the optimum airspeed, the calculation of which is shown in Appendix A. The curves in figure 2 can be treated as time boundaries. Points to the above and left of a curve indicate that a deviation would be faster than staying on course whereas points to the bottom and right represent conditions for which staying on course would be more profitable.

The importance of deviating for minor gains in lift when the conditions are weak is shown by examining the curve for 1 knot average rate-of-climb on course. A 25% course elongation requires a little over 2 knots rate-of-climb in the thermal at Y. If the expected rate-of-climb in Z were 4 knots (moderate lift conditions), a 25% course deviation ratio would need to have an achieved rate-of-climb better than 15 knots to result in the same time to the top of the thermal at Z. The implication is that when lift conditions are weak (1-2 knots average rate-of-climb), course deviations would be advantageous for modest gains in lift. However, for moderate to strong lift conditions (4 knots and above average rate-of-climb), sizeable gains in lift will permit only minor deviations from the course line.

This result is further emphasized in figure 3 where the deviation distance ratio is plotted against a non-dimensionalized lift ratio for a number of lift conditions. The weak conditions warrant substantial deviation distance ratios even in non-dimensional form while, in contrast, the stronger conditions begin to coincide upon a boundary requiring large lift ratios for any appreciable distance ratio.

The influence of sailplane performance upon the pilot's decisions is shown in figure 4. Rate-of-climb required at thermal Y is plotted as a function of deviation distance ratio for three classes of sailplanes. Sailplane A is the standard class aircraft considered previously; sailplane B represents a one-design sport class; and aircraft C represents a sailplane in the open class. It is readily apparent that sailplane performance has a minor effect on the pilot's willingness to deviate from course. However, there is a trend for sailplanes of lesser performance to be willing to make slightly greater course deviations.

The previous curves were developed with an assumed average atmospheric subsidence equal to 20 percent of the rate-of-climb (reference 9). As expected, slight course extensions with this model can be justified with reduced sink rate

(figure 5). However, the influence of sink rate on the pilot's decision to deviate from course, assuming that both flight paths undergo the same average sink rate, is negligible.

An important variable in the geometry shown in figure 1 is d'/d . It impacts the performance of the extended course by determining how much of the altitude to be regained will be done in the stronger thermal at Y. The generalized results for d'/d of .25, .5, and .75 are shown in figure 6 for average lift conditions of 2 knots and 6 knots. It is readily apparent from figure 6 that substantially larger course deviations can be justified with larger values of d'/d . The greater the distance between X and Y for a given deviation distance ratio, the greater the altitude which is gained in the stronger lift at Y, thereby increasing the achieved speed.

The net result of the foregoing analysis is that the deviation angle, Ψ , should be kept as small as possible. This is especially true for moderate to strong lift conditions. This result is in basic agreement with the macro-strategy model presented in reference 10 which is of similar format to the micro-strategy model considered here.

It should be noted that the preceding results can be directly applied to a more generalized model including multiple glide/circle cycles along the course line segments \overline{XZ} and \overline{XY} . This is true as long as the deviation flight path includes only one glide/circle cycle along \overline{YZ} . The reason multiple thermals do not affect the analysis is due to the simplification that net ground speed is a function of achieved rate-of-climb, so the time to reach cloudbase at the end of a segment will be the same no matter how many thermals are used.

The results of another micro-strategy analysis are shown in figure 7. Speed ratio, achieved ground speed with vertical air motion between thermals normalized by achieved ground speed with no vertical air motion between thermals, is plotted against sink ratio, which is the ratio of average vertical air motion between lift sources to achieved rate-of-climb in lift for a variety of lift conditions. Negative sink ratios are indicative of what pilots call "reduced sink," i.e., positive vertical air motion too weak to yield a positive rate-of-climb, but still result in a reduction of the rate at which altitude is lost. The curves in figure 7 are continued in the negative sink ratio direction until "zero sink" (the point at which the net altitude loss during cruising is zero) is achieved.

Speed ratios greater than 1 can be interpreted as deviation distance ratios. For example, a speed ratio of 1.1 implies that a pilot could deviate from his straight line course by 10% and still have the same achieved ground speed for a complete glide/circle cycle. If the pilot deviates from course any less, for the indicated lift and sink conditions, a net gain in cross-country speed will result. These results reiterate the necessity for minimizing sink rate by making minor deviations during inter-thermal cruise to optimize the achieved cross-country performance.

Macro-Strategy

Macro-strategies involve the choice of courses to a desired goal rather than the flight path selection to individual sources of lift. Macro-strategies are used to fly through regions of improved lift conditions. So once a macro-strategy is developed, an undetermined number of micro-strategies are used to fly the prescribed course.

The results of the thermal macro-strategy model are shown in non-dimensional form in figure 8. Speed ratio is plotted as a function of lift ratio for a variety of average lift conditions. As before, the non-dimensionalized speed ratio can be interpreted as the deviation distance ratio boundary required for equal time to reach the goal. It is immediately obvious, by comparing figures 3 and 8, that decisions on the macro-strategy level have a much greater impact upon the achieved cross-country soaring performance than decisions at the micro-strategy level. A lift ratio of 2.0 yields more than twice the speed ratio for all lift conditions for the macro-strategy case in comparison with the micro-strategy case. The importance of choosing courses that will pass through more favorable sectors is of greater importance for weak conditions as opposed to moderate or strong thermal conditions.

As before, although sailplane performance and sink between thermals will affect achieved groundspeed, they have little influence upon the pilot's decision of when to make course deviations.

Street Models

Many times the pilot will have occasion to utilize convective lift while cruising along course line. This condition where the regions of lift make up a substantial portion of the flight path is usually referred to as streeting. Making effective use of these large regions of lift usually involves speeding up in sink and slowing down in lift. There have been several analyses of this mode of flying, for example, references 2 through 5 and 11 through 14. In this paper, however, simplified and conservative control laws have been implemented for studying thermal street flying. For the most part, the pilot flies at the speed for minimum sink rate while in lift until cloud base is reached, at which time the pilot speeds up and flies so as to maintain altitude. The pilot cruises between lift as dictated by the equations of Appendix B. As it turns out, this procedure is not far from the optimum as demonstrated in reference 5.

Micro-Strategy

The first model to be considered is shown in figure 9. The pilot has reached cloud base at Point W and is trying to get to Point Z. He must decide if flying straight to Z or deviating to use the thermal street along XY will yield the fastest time to cloud base at Point Z. It is assumed that

the pilot is capable of achieving an average rate-of-climb along \overline{XY} equal to half the rate-of-climb obtainable from circling in thermals on course $\frac{\dot{h}_s}{h} = 0.5$.

Optimal inter-lift cruising speeds are obtained from Appendices A and B. The pilot uses the control law previously mentioned for cruising in the lift along \overline{XY} .

The results are shown in figures 10 and 11 for this model. Boundaries of deviation distance ratio, s/D , yielding the same time to cloudbase at Z are plotted against average lift conditions for a variety of street length ratios, s'/D , in figure 10. As anticipated, the geometry of the situation confronting the pilot has a much greater influence on his decision than rate-of-climb, sail-plane performance or inter-lift sink. Obviously, the greater the length of \overline{XY} (s'), the greater the distance the pilot should be willing to transverse to improve his cross-country soaring performance. Course deviations for weak conditions can be about 10% longer than for moderate to strong conditions.

A more convenient way for the pilot to picture how far of a course deviation is warranted is shown in figure 11. It is a plot of curves showing allowable spacing-distance ratio, y/D , against achieved rate-of-climb for street length ratios of 0.2 and 0.8. Spacing distance ratios of about 35% and 45% respectively are justified for weak conditions while spacing distance ratios of about 25% and 35% are allowed for moderate to strong thermal conditions.

The second micro-strategy thermal street model is shown in figure 12. The pilot has just reached cloudbase in a thermal at X and desires to reach cloudbase at the thermal at point Z . He must decide between flying directly on course or deviating to use the street along \overline{XY} and then flying to Z . It is assumed that the average vertical atmospheric velocity along \overline{XY} is equivalent to that which would yield half the rate-of-climb from thermalling at points X or Z . The pilot flies along \overline{XY} at the speed which yields no net altitude change and then flies along \overline{YZ} at the speed-to-fly indicated by the methods of Appendix A.

Prior to analyzing the model, it is necessary to determine the optimum method of flying the street and the sensitivity to variations from the optimal procedures. Figure 13 is a series of plots showing speed ratio, i.e., the speed obtained by deviating to fly the street at angle ϕ normalized by the speed obtained flying straight ahead in the classical circle/glide manner, as a function of breakaway distance ratio, l/D , for a variety of street angles. Speed ratios greater than one correspond to flight path extensions which would yield a faster time to cloudbase at Z than the straight-ahead choice. Figure 13 shows the following: 1) there are many ways to fly the thermal street so as to obtain a speed ratio greater than 1; 2) there exists, for thermal street angles less than about 60° , an optimal distance along the street to break away and begin flying toward Z to optimize speed ratio; 3) this optimum breakaway distance is highly sensitive to street angle and not very sensitive to rate-of-

climb; 4) the greatest speed ratios are obtained with small angles and weak lift conditions; and, 5) optimum speed ratio is highly sensitive to breakaway point for weak lift and small street angles.

The breakaway point which yields equal time to fly the street and the straight ahead glide/circle cycle and the breakaway point for the optimum time by flying the street is analytically derived in Appendix C. The locus of breakaway points for equal time (straight ahead versus deviating along the street), ℓ'/D , and optimum time, ℓ^*/D , is shown as a function of obtainable average rate-of-climb thermalling for a variety of street angles in figure 14. The optimum breakaway point from the street is not greatly affected by average rate-of-climb whereas the breakaway point for equal time can be extended along the street substantially during weaker conditions as compared with moderate to strong lift conditions. As expected, figure 15, which shows obtainable speed ratio for a variety of thermal street angles, indicates that the largest gains in speed ratio from flying the thermal street are possible with weak conditions and/or small thermal street angles.

The influence of street angle on breakaway points for optimum time and equal time is shown in figure 16. It is clear that deviating along a street is not beneficial for street angles of 60° or more. In addition, it can be observed that there is a very large margin between the locus of points equal time and optimum time, indicating that the pilot can choose a large number of breakaway points and still improve his performance. Even so, it would probably be beneficial for the pilot to study this plot and develop rules of thumb for deciding upon the optimum breakaway point given a geometry and lift condition. For example, neglect obtainable average rate-of-climb thermalling and just decide by reference to street angle-- 15° fly an ℓ/D of 90%; 30° fly an ℓ/D of 70%; 45° fly an ℓ/D of 50%; and 60° and greater fly straight ahead ignoring the street. The magnitude of the benefits to be obtained from deviating along streets as a function of street angle is demonstrated in figure 17.

Macro-Strategy

The equations for studying the effect of streeting are developed in Appendix B. The macro-strategy model to be considered is basically the same as considered previously except that some portion of the course deviation is under the influence of convective lift. As before, it is assumed that the average vertical air velocity encountered while cruising is equivalent to half the achieved rate-of-climb in thermals.

It is assumed that after a long enough stretch of cloud street flying that the net change in altitude is constrained to be zero. This is valid only at the macro-strategy level because the pilot might be willing, in the short term, to tolerate slow losses of altitude in order to make progress along the desired course. The required ratio of distance flown while climbing to total distance covered is plotted in figure 18 against achieved rate-of-climb in thermals for 3 sailplanes. The sport class sailplane requires considerably more of the flight path in lift than the other two classes studied. It should also be remembered that

this assumes static equilibrium flight and neglects the performance differences due to the dynamics of pulling up and pushing over, which should increase the differences between classes. Some of these dynamic effects have been studied previously, for example, reference 14.

The importance of deviating from course to be able to cruise while climbing is shown in figure 19. Speed ratio is shown as a function of rate-of-climb achievable by thermalling for three ratios of distance covered while climbing in thermal streets to total distance covered. Here it is assumed, that in order to have no net change in altitude after a long period of time, one of two approaches must be taken: 1) if there is more lift available than necessary to maintain altitude, the excess will be used to increase speed at cloudbase until no net change in altitude will occur; or, 2) if there is not enough lift available to maintain altitude, the pilot will circle to cloudbase at the end of the cruise at the average rate-of-climb expected in thermals at that time. The fourth curve is a locus of points obtained from figure 18 showing the achieved performance if the ratio of distance covered climbing to total distance covered were at the correct value to yield no net altitude change from climbing by cruising at the speed for minimum sink and cruising between lift at the appropriate speed-to-fly (Appendix B).

Several assumptions have been made during the development of the street flying analyses which need to be considered. The authors have studied the influence of sailplane performance and inter-thermal sink and found that, although the cross-country performance may be significantly affected, the pilot's decision in regards to non-dimensionalized course deviations is not altered. The assumption that the average vertical atmospheric velocity encountered while climbing is 50% that of the vertical air velocity obtainable in thermals at the time does influence various parts of the analysis. It is felt, however, that this does not have a major impact upon the trends demonstrated in this paper. Furthermore, neglecting winds in these analyses probably would affect the decisions a pilot would make during cross-country street flying. Thermal streets are usually fostered by gentle winds and the inclusion of this factor warrants further research. As exemplified in reference 15, the pilot would probably be willing to make further progress against the wind in streets than the optimum solutions for still air reported herein.

SUMMARY OF RESULTS

Several trends came out of the analysis of the thermal models in this paper. It is apparent that decisions to deviate from course are of much greater significance at the macro-strategy level than the micro-strategy level. A pilot can enhance his performance by choosing sectors of the sky to improve his achieved rate-of-climb. At both the micro- and macro-strategy levels it is clear that substantial deviations from course may be warranted for weak lift whereas when the thermal conditions are moderate or strong, only very minor course deviations can be justified. In all cases, cross-country soaring performance can be augmented by making course deviations with the

smallest possible deviation angles. This indicates that pilots should make course change decisions as soon as possible and be willing to ignore lift not near the course, which is especially true for moderate or strong lift.

A large improvement in average cross-country speed is attainable by cruising while climbing, such as in streeting conditions. In the street models considered, the percentage of the flight path in lift had a big influence upon the achieved performance and pilot's decision criteria. In the case of the parallel street micro-strategy model, streets with spacing distance ratios of 30% or less could be justified to increase the attained cross-country speed. Deviation distance ratios can be extended by about 10% for weak conditions as compared to moderate or strong lift conditions.

The study of streets at an angle to the course line results in some interesting observations. There exists an optimum point of breakaway from the street to minimize the time required to reach the top of the next thermal. This breakaway point is primarily a function of street angle. Although the optimum augmentation of speed is highly sensitive to breakaway point for weak conditions at small street angles, for most combinations of street geometry and lift conditions there exists a range of possible solutions which yields a faster time than the straight ahead glide/circle cycle. It can be shown that cloud streets at an angle greater than 60 degrees are not beneficial and should not be used to improve average ground speed.

CONCLUDING REMARKS

Several assumptions have been made which may affect the applicability of the results reported upon herein. A premise for all the cases studied was that survivability is ignored. Speed was considered as the performance function to be optimized whereas if the pilot was concerned about not being able to complete the flight, altitude conservation would be of prime importance.

A constraint for each exercise was that net altitude loss would be zero; hence, the results are not applicable to final glides. A possible focus of future research may be to study the impact of course deviations upon final glides. Also, it was arbitrarily assumed for the street models that average lift in a street was approximately 50% of the lift found in thermals at that time. This has an obvious impact upon the performance gains of deviating to use streets, but general trends of the analyses are still valid.

A significant limitation of the approach presented in this paper is the assumption implied by considering lift as solely air referenced. This negates the influence of winds for reaching ground referenced goals or lift sources. It is expected that decisions reached during the street analysis will be shifted into the wind. For example, the pilot will probably want to make more progress into the wind while in lift than otherwise indicated by the breakaway point solutions. Since thermal streets are usually formed in light to medium winds, the inclusion of winds in the foregoing analyses is currently being undertaken by the authors.

The models developed in this paper are simplified and general in nature. It is hoped that they or a linear superposition of more than one of them are representative of typical lift geometries a pilot may encounter during a cross-country soaring flight. The results presented in this paper are not meant to be cockpit aids for interpreting the most promising flight paths. Instead, they illustrate the desirability and indicate an approach, for analytically studying typical course selection decisions beforehand, enabling the pilot to more effectively evaluate the potential tradeoffs for arriving upon a more optimal solution while in flight.

APPENDIX A

OPTIMUM SPEED-TO-FLY CALCULATIONS FOR THERMAL MODELS

To facilitate the calculations required in this paper and in other investigations (reference 16), analytical expressions needed to be derived for the familiar inter-thermal speed-to-fly solution (reference 1). Although the defining equations are easily derived and have been presented in numerous publications (for example, references 3 and 5), a closed form analytical solution for calculating numerical results is not generally available in the literature and is given below. The graphical interpretation of the results which is widely used by pilots is shown in figure 20. The first case considered is where the sailplane performance is known and is assumed to be parabolic; the average rate-of-climb in the next thermal is known; the ratio of sink rate between thermals to rate-of-climb in them is known; and the optimum speed-to-fly between the thermals and the corresponding average ground speed is desired. The sailplane performance relation is:

$$V_s = AV^3 + \frac{B}{V} \quad (A1)$$

where

$$A = \frac{1}{2V_o^2 (L/D)_{\max}} \quad (A2)$$

$$B = \frac{V_o^2}{2(L/D)_{\max}} \quad (A3)$$

The defining equation can be found from figure 20 or by derivation to be

$$\frac{V_s + \dot{h} + V_{at}}{V} = \frac{d}{dV} V_s \quad (A4)$$

By applying the definition of sink ratio, η , and utilizing equations (A1), (A2), and (A3), equation (A4) becomes the following fourth degree polynomial:

$$V^4 - \frac{\dot{h}(1 + \eta)}{2A} V - \frac{B}{A} = 0 \quad (A5)$$

The root of interest was found to be calculated by the following relations:

$$v^* = \sqrt{\frac{f}{2}} + \sqrt{\frac{-f + \frac{(1+\eta)\dot{h}}{A\sqrt{v}}}{2}} \quad (\text{A6})$$

$$f = \sqrt[3]{F_1 + F_2} + \sqrt[3]{F_1 - F_2} \quad (\text{A7})$$

$$F_1 = \frac{(1+\eta)^2 \dot{h}^2}{8A^2} \quad (\text{A8})$$

$$F_2 = \sqrt[2]{\frac{[(1+\eta)\dot{h}]^4}{64A^4} + \frac{64B^3}{27A^3}} \quad (\text{A9})$$

The average ground speed for a complete glide/circle cycle is given by

$$V_G = \frac{v^* \dot{h}}{Av^{*3} + B/v^* + (1+\eta)\dot{h}} \quad (\text{A10})$$

The second case considered is where the sailplane performance is known in the form as before, the sink ratio can be assumed, the desired average ground speed is known, and the optimum speed-to-fly and the required rate-of-climb given the preceding are to be found. The defining equation can be easily attained from figure 20 by equating the slope of the tangent line,

$$m = \frac{v_s^*}{v^* - (1+\eta)V_G} \quad (\text{A11})$$

to the slope of the sailplane polar found by differentiating equation (A1)

$$\frac{d}{dv} v_s = 3Av^2 - \frac{B}{v^2} \quad (\text{A12})$$

The defining equation for the optimum solution becomes

$$v^{*5} - \frac{3}{2}(1+\eta)V_G v^{*4} - \frac{B}{A}v^* + \frac{B}{2A}(1+\eta)V_G = 0 \quad (\text{A13})$$

Use Newton's method for estimating roots. Let

$$Q_i = v_i^{*5} - \frac{3}{2}(1+\eta)V_G v_i^{*4} - \frac{B}{A}v_i^* + \frac{B}{2A}(1+\eta)V_G \quad (\text{A14})$$

$$\frac{d}{dV^*} Q_i = 5V_i^{*4} - 6(1 + \eta)V_G V_i^{*3} - \frac{B}{A} \quad (A15)$$

then,

$$V_{i+1}^* = V_i^* - \frac{Q_i}{\frac{d}{dV^*} Q_i} \quad (A16)$$

A good initial guess for V_i^* could arbitrarily be $V_0 + 5(1 + \eta)h$. A fair amount of accuracy can be obtained with just five iterations in this manner. The required rate-of-climb for an average ground speed of V_G is given by the following relation:

$$h = \frac{AV_G V^{*3} + BV_G/V^*}{V^* - (1 + \eta)V_G} \quad (A17)$$

APPENDIX B

OPTIMUM SPEED-TO-FLY CALCULATIONS FOR THERMAL STREETS

The defining relations and a geometric interpretation (figure 21) of the optimum speed-to-fly between lift, given the sailplane performance, the inter-lift sink ratio, the rate-of-climb and the speed at which the lift is transversed (V_{CL}), were presented in reference 5. The defining equation is

$$\frac{d}{dV} V_s = \frac{V_s + h_s + V_{at}}{V^* - V_{CL}} \quad (B1)$$

Assuming a parabolic polar, equations (A1), (A2), and (A3), the following fifth degree polynomial can be derived

$$V^{*5} - \frac{3}{2} V_{CL} V^{*4} - \frac{(1 + \eta)}{2A} h_s V^{*2} - \frac{B}{A} V^* + \frac{BV_{CL}}{2A} = 0 \quad (B2)$$

Newton's iterative method of estimating real roots was used to solve the fifth degree equation for the desired root.

Let

$$Q_i = V_i^5 - \frac{3}{2} V_{CL} V_i^{*4} - \frac{(1 + \eta)}{2A} h_s V_i^{*2} - \frac{B}{A} V_i^* + \frac{BV_{CL}}{2A} \quad (B3)$$

$$\frac{d}{dV^*} Q_i = 5V_i^{*4} - 6V_{CL} V_i^{*3} - \frac{(1 + \eta)}{A} h_s V_i^* - \frac{B}{A} \quad (B4)$$

then

$$V_{i+1}^* = V_i^* - \frac{Q_i}{\frac{d}{dV^*} Q_i} \quad (B5)$$

A good value for the initial guess of V_i^* might arbitrarily be the solution to the thermal model problem developed in Appendix A. A near optimum value for the climbing velocity, V_{CL} , would be the speed for minimum sink rate, V_{MIN} .

$$\frac{d}{dV} V_s \equiv 0 = 3AV^2 - \frac{B}{V^2} \quad (B6)$$

$$V_{\text{MIN}} = \sqrt[4]{\frac{B}{3A}} = V_o \sqrt[4]{1/3} \quad (\text{B7})$$

$$V_{\text{MIN}} = .7598 V_o \quad (\text{B8})$$

The average ground speed for a complete cycle, as pictured in figure 22, is calculated as follows:

$$V_{\text{GS}} = \frac{\dot{h}_s}{3AV^{*2} - \frac{B}{V^{*2}}} + V_{\text{MIN}} \quad (\text{B9})$$

These equations were derived assuming that the net altitude change after each cruise/climb cycle was zero. Referring to figure 22, a relation can be derived to yield the proportion of the flight path which must be under the influence of lift to result in no net altitude change after each cycle ($h_{\text{CR}}/h_{\text{CL}} = 1$).

Starting with

$$h_{\text{CR}} = \frac{R_{\text{CR}}}{V_{\text{CR}}} (V_s^{*2} + \eta \dot{h}_s) \quad (\text{B10})$$

$$h_{\text{CL}} = \frac{R_{\text{CL}}}{V_{\text{CL}}} \dot{h}_s \quad (\text{B11})$$

and

$$\frac{R_{\text{CL}}}{R} = \frac{\left(\frac{R_{\text{CL}}}{R_{\text{CR}}} \right)}{1 + \frac{R_{\text{CL}}}{R_{\text{CR}}}} \quad (\text{B12})$$

The following equation is derived

$$\frac{R_{\text{CL}}}{R_{\text{CR}}} = \frac{\left(\frac{h_{\text{CL}}}{h_{\text{CR}}} \right) \left(\frac{V_{\text{CL}}}{V^{*}} \right) \left(\frac{V_s^{*2}}{\dot{h}_s} + \eta \right)}{1 + \left(\frac{h_{\text{CL}}}{h_{\text{CR}}} \right) \left(\frac{V_{\text{CL}}}{V^{*}} \right) \left(\frac{V_s^{*2}}{\dot{h}_s} + \eta \right)} \quad (\text{B13})$$

A plot of R_{CL}/R as a function of \dot{h}_s for three sailplanes is shown in figure 18.

In the event that there is a larger proportion of the flight path under the influence of lift than required for no net altitude change, then the pilot needs to cruise at a velocity which gives a sink rate equal to the vertical air velocity to keep from climbing into the cloud. This airspeed can be calculated as follows:

$$V_{at} \equiv V_s = AV^3 + B/V \quad (B14)$$

$$V_{CR} = \frac{\sqrt{f}}{2} + \sqrt{\frac{-f + 2V_s}{2A\sqrt{f}}} \quad (B15)$$

$$f = \sqrt[3]{F_1 + F_2} + \sqrt[3]{F_1 - F_2} \quad (B16)$$

$$F_1 = \frac{V_s^2}{2A^2} \quad (B17)$$

$$F_2 = \sqrt{\frac{V_s^4}{4A^4} - \frac{64B^3}{27A^3}} \quad (B18)$$

APPENDIX C

CALCULATION OF BREAK-AWAY POINTS FROM
A CLOUD STREET AT AN ANGLE TO THE DESIRED COURSE

Using the geometry defined in figure 12, a relation can be defined to determine the appropriate breakaway points in terms of sailplane performance parameters and atmospheric lift conditions. The first case considered is finding the breakaway point, the distance to be flown along the street, ℓ , to yield the same time to the top of the thermal as Z as by flying directly from X to Z . The time to fly along the street, fly to Z and then climb to cloud-base at Z is given by:

$$T_{\ell n} = \frac{\ell}{V_{\ell}} + \frac{n}{V_n} + \frac{n}{V_n} \left(\frac{V_{sn}}{h} + \frac{\dot{h}\eta}{h} \right) \quad (C1)$$

$$T_{\ell n} = \frac{\ell}{V_{\ell}} + \frac{n}{V_n} \left(1 + \frac{V_{sn}}{\dot{h}} + \eta \right) \quad (C2)$$

if

$$K = 1 + \frac{V_{sn}}{\dot{h}} + \eta \quad (C3)$$

then

$$T_{\ell n} = \frac{\ell}{V_{\ell}} + \frac{n}{V_n} K \quad (C4)$$

Using the Law of Cosines

$$n^2 = D^2 + \ell^2 - 2D\ell \cos \phi \quad (C5)$$

Squaring equation (C4) yields

$$T_{\ell n}^2 - 2\frac{\ell}{V_{\ell}} T_{\ell n} + \frac{\ell^2}{V_{\ell}^2} = \frac{n^2}{V_n^2} K^2 \quad (C6)$$

Substituting equation (C5) into (C6) gives

$$T_{\ell n}^2 - 2\frac{\ell}{V_{\ell}} T_{\ell n} + \frac{\ell^2}{V_{\ell}^2} = \frac{K^2}{V_n^2} \left[D^2 + \ell^2 - 2D\ell \cos \phi \right] \quad (C7)$$

From the definition of completing either route in equal time and from the assumptions of Appendix A, V_n and V_D are equal since they are both calculated based on the thermal at Z, the following can be written:

$$T_{\ell n} \equiv T_D = \frac{D}{V_n} \left(1 + \frac{V_{sn}}{h} + \eta \right) = \frac{D}{V_n} K \quad (C8)$$

Substituting (C8) into (C7) results in

$$\ell^2 \left(\frac{V_n^2}{V_\ell^2} - K^2 \right) + \ell \left(2DK \right) \left(K \cos \phi - \frac{V_n}{V_\ell} \right) = 0 \quad (C9)$$

If we define the following constant,

$$K' = \frac{V_n}{V_\ell} \frac{1}{K} \quad (C10)$$

then equation (C9) can be solved for the roots as follows

$$\frac{\ell'_1}{D} = 0 \quad (C11)$$

$$\frac{\ell'_2}{D} = \frac{2 \left(\cos \phi - K' \right)}{1 - K'^2} \quad (C12)$$

The second case considered is the solution for the non-dimensionalized breakaway point, $\frac{\ell^*}{D}$, for minimum time to reach the top of the thermal at Z. Starting with equation (C4) and substituting the square root of equation (C5) into it, the following function is obtained:

$$T_{\ell n} = \frac{\ell}{V_\ell} + \frac{K}{V_n} \left(D^2 + \ell^2 - 2D\ell \cos \phi \right)^{\frac{1}{2}} \quad (C13)$$

The minimum time solution for $T_{\ell n}$ is found by differentiating with respect to ℓ and setting it to zero.

$$\frac{d}{d\ell} T_{ln} \equiv 0 = \frac{1}{V_\ell} + \frac{K}{V_n} \frac{\ell - D \cos \phi}{(D^2 + \ell^2 - 2D\ell \cos \phi)^{\frac{1}{2}}} \quad (C14)$$

Rearranging (C14) and substituting in equation (C10) gives the following quadratic equation:

$$\ell^2 (1 - K'^2) + \ell (2D \cos \phi) (K'^2 - 1) + D^2 (\cos^2 \phi - K'^2) = 0 \quad (C15)$$

The root of interest from equation (C15) is

$$\frac{\ell^*}{D} = \cos \phi - \sqrt{\frac{K'^2 (1 - \cos^2 \phi)}{(1 - K'^2)}} \quad (C16)$$

REFERENCES

1. McCready, Paul B.: "An Optimal Airspeed Selector," Soaring, May 1954.
2. Mozdiniewicz, W.: "Cloud Street Flying," Soaring, Vol. 35, No. 11, 1971 pp. 26-27.
3. Irving, F. G.: "Cloud Street Flying," NASA CR-2315, 1972, pp. 274-286.
4. Gedeon, Jozsef: "Dynamic Analysis of Dolphin-Style Thermal Cross-Country Flying," Technical Soaring, Vol. 3, No. 1, 1973.
5. Abzug, Malcolm J.: "A Speed Ring for Cloud Street Flying," Technical Soaring, Vol. 14, No. 1, 1976.
6. Irving, F. G.: "The Effect of Errors in Inter-Thermal Speed on the Average Cross-Country Speed," Technical Soaring, Vol. 3, No. 2, 1973.
7. Schuemann, Wil: "The Price You Pay for MacCready Speeds," Presented at the 1972 Symposium on Competitive Soaring, Soaring Symposia, Cumberland, Maryland, 1973.
8. Teter, Michael P.: "Competition Strategy and Tactics for Beginners," Soaring, August, 1975, pp. 26-28.
9. Johnson, Richard H.: "Cross-Country Soaring," American Soaring Handbook, Soaring Society of America, 1962, Chapter 6, pg. 8.
10. Alleman, Rudolf T.: "Notes on the Dilemma of Deviation from Course Line," Soaring, March, 1962, pp. 12-14.
11. Arho, Risto: "Optimal Dolphin Soaring as a Variation Problem," Technical Soaring, Vol. 3, No. 1, 1973.
12. Arho, Risto: "Some Notes on Soaring Flight Optimization Theory," Technical Soaring, Vol. 14, No. 2, 1974.
13. Metzger, Darryl E. and Hedrick, J. Karl: "Optimal Flight Paths for Soaring Flight," Proceedings of Second International Symposium on the Technology and Science of Low-Speed and Motorless Flight, Cambridge, Mass., 1974.
14. Gedeon, Jozsef: "The Influence of Sailplane Performance and Thermal Strength on Optimal Dolphin-Flight Transition Piloting Techniques," Presented at the XV OSTIV Congress, Rayskala, Finland, 1976.
15. Reichman, Helmut: Cross-Country Soaring: A Handbook for Performance and Competitive Soaring, Thompson Publications, Santa Monica, California, 1978.
16. Sliwa, Steven M.: "A Computer Simulation of Cross-Country Soaring," Soaring, January 1976.

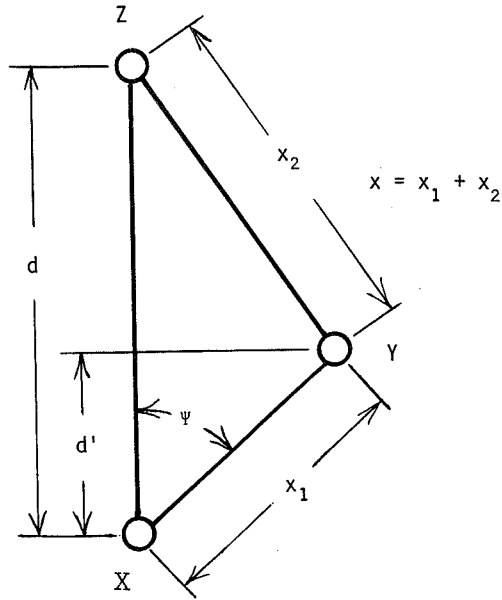


Figure 1. - Micro-strategy thermal model.

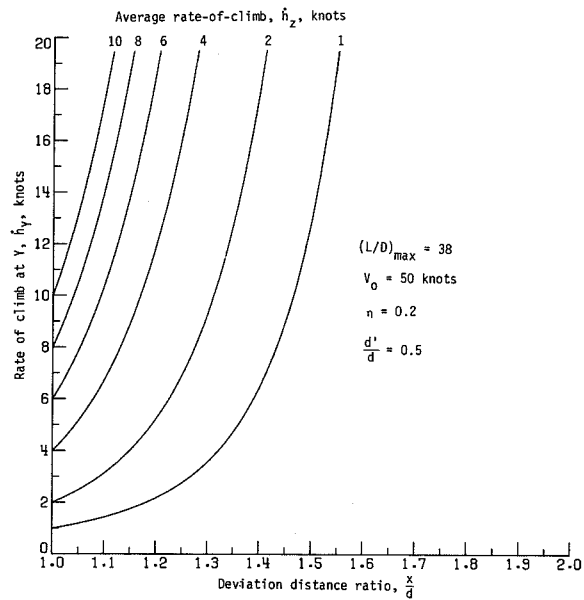


Figure 2. - Required rate-of-climb at Y as a function of deviation distance ratio for micro-strategy thermal model.

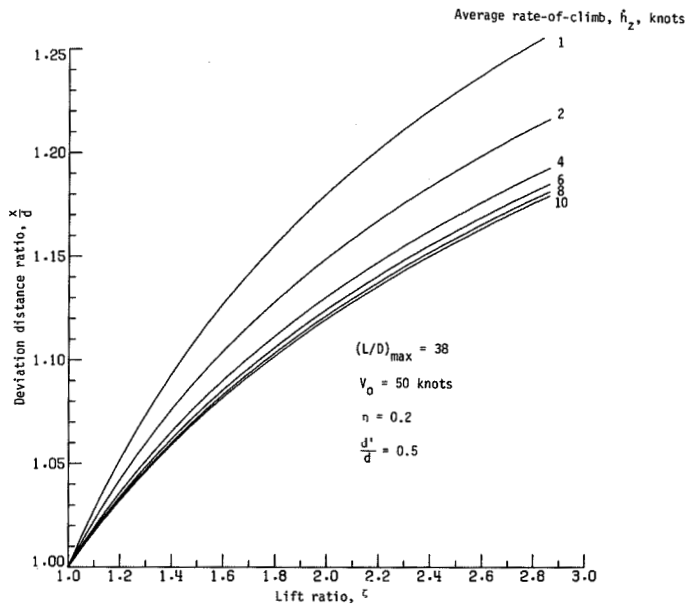


Figure 3. - Deviation distance ratio as a function of lift ratio for micro-strategy thermal model.

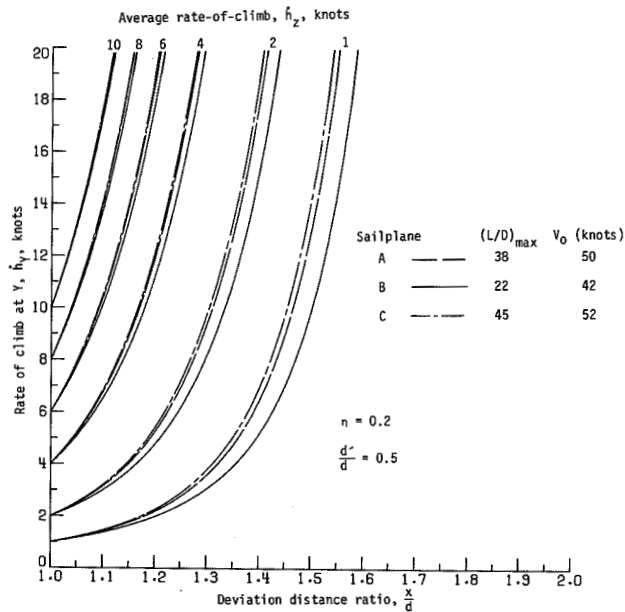


Figure 4. - Required rate-of-climb at Y versus deviation distance ratio illustrating impact of sailplane performance for micro-strategy thermal model.

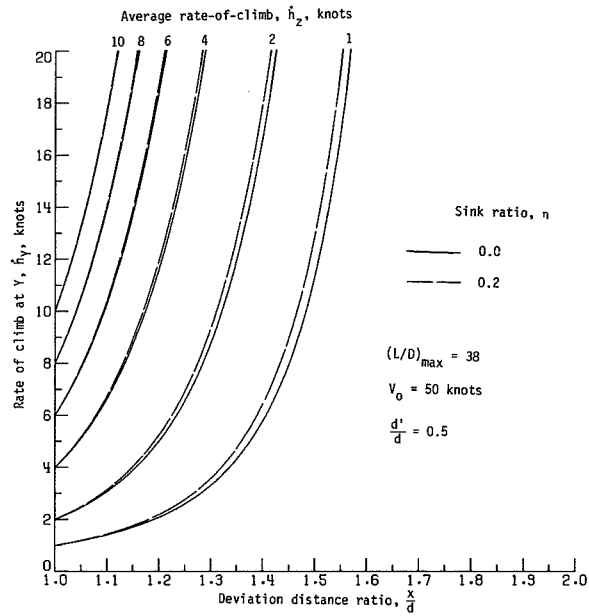


Figure 5. - Required rate-of-climb at Y versus deviation distance ratio illustrating impact of sink ratio for micro-strategy thermal model.

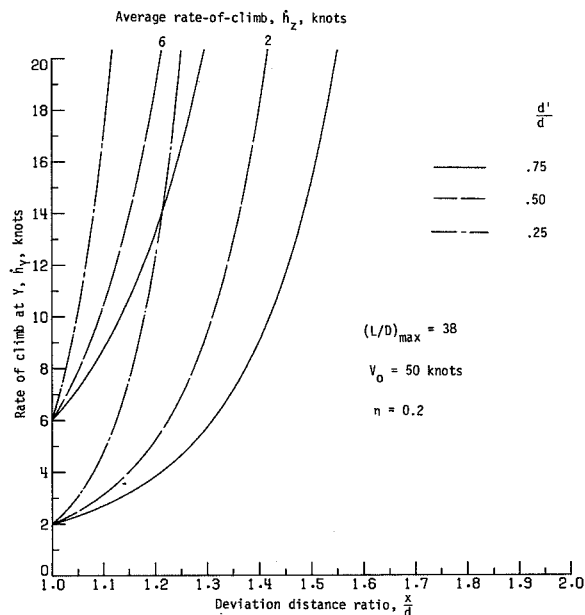


Figure 6. - Required rate-of-climb at Y versus deviation distance ratio illustrating impact of d'/d for micro-strategy thermal model.

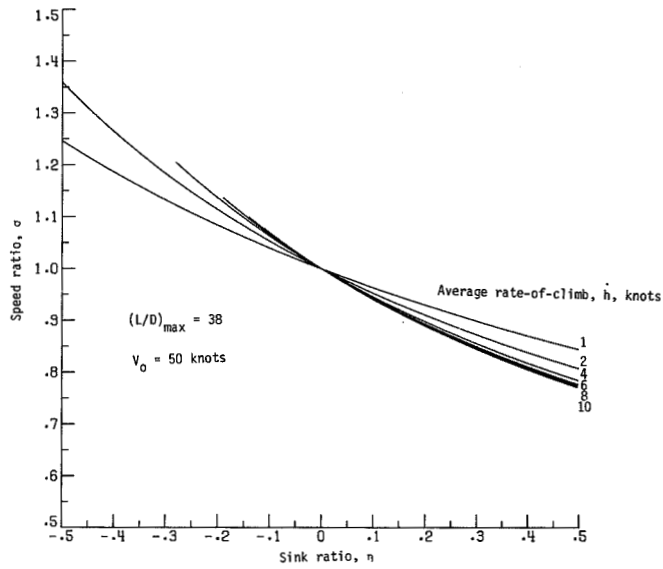


Figure 7. - Speed ratio versus sink ratio for micro-strategy thermal analysis.

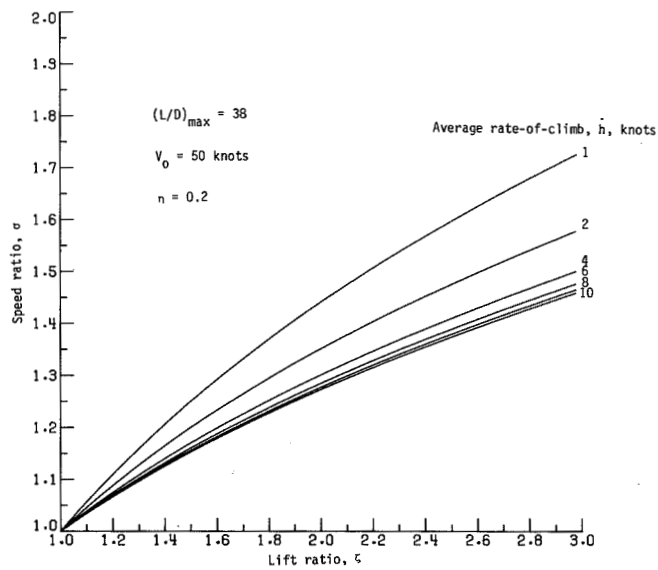


Figure 8. - Speed ratio versus lift ratio for macro-strategy thermal model.

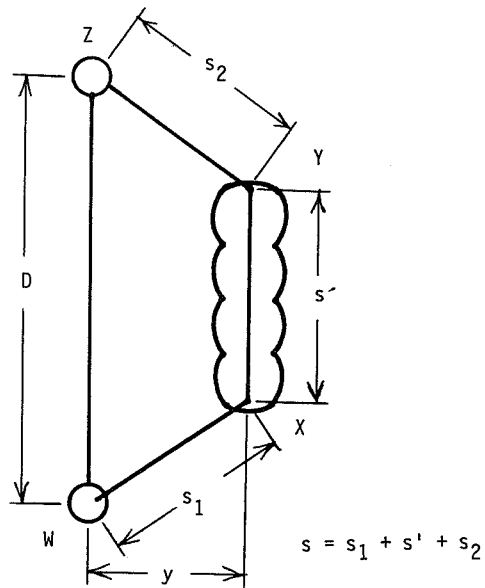


Figure 9. - Micro-strategy model with thermal street parallel to course line.

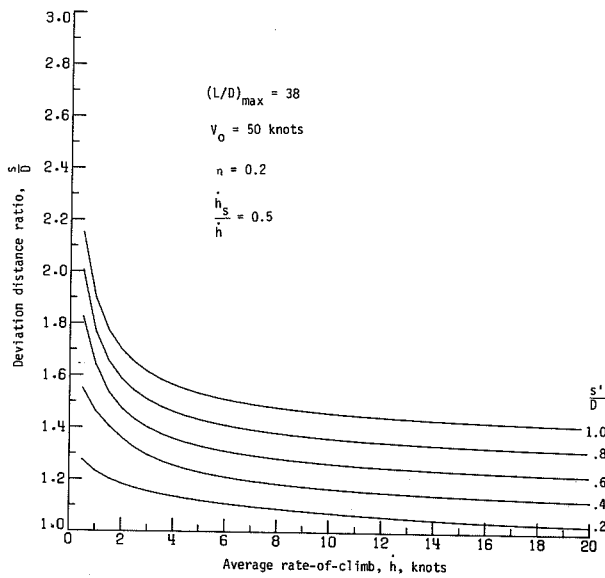


Figure 10. - Deviation distance ratio versus average rate-of-climb for parallel thermal street micro-strategy model.

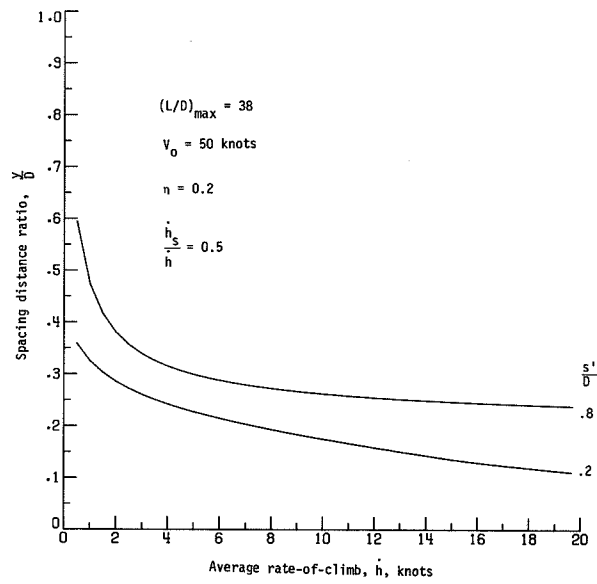


Figure 11. - Spacing distance ratio versus average rate-of-climb for parallel thermal street micro-strategy model.

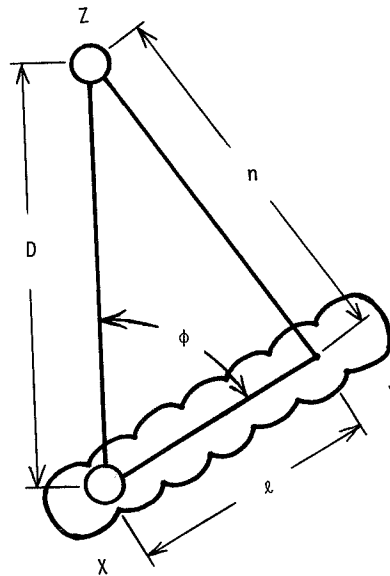
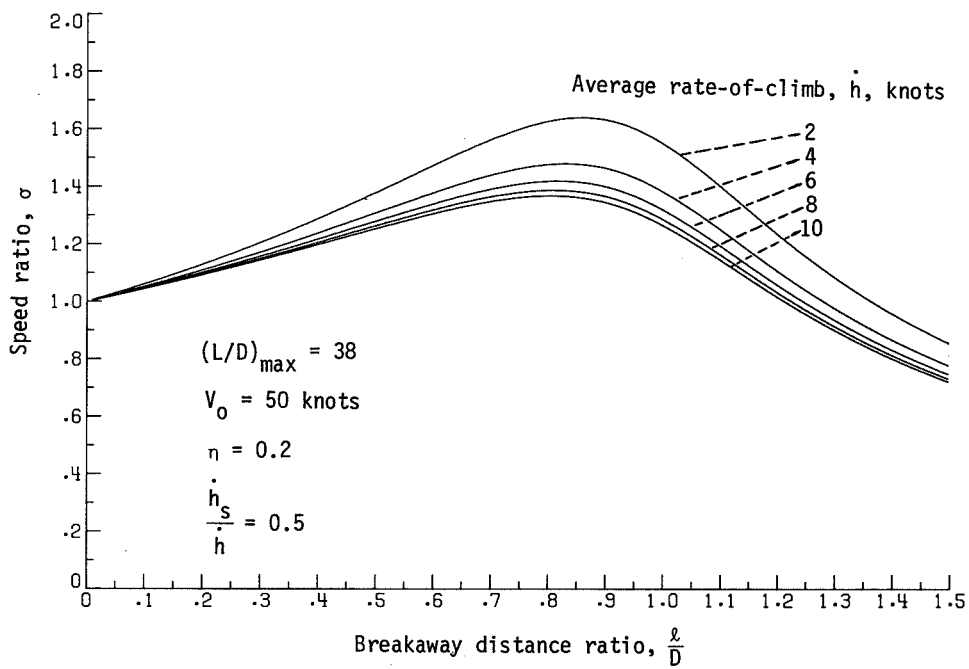
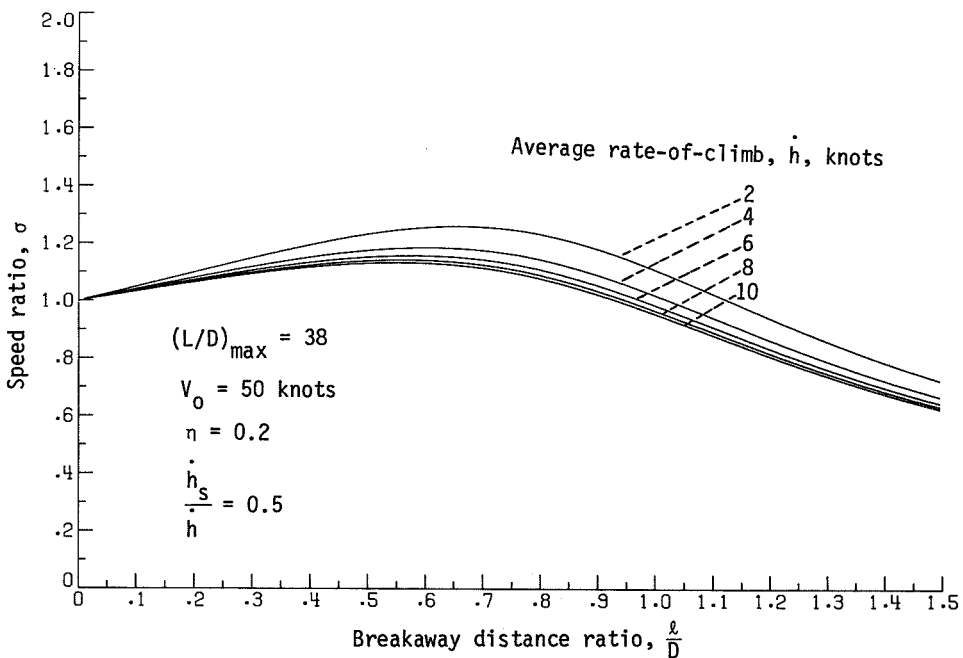


Figure 12. - Micro-strategy model with thermal street at an angle with course line.

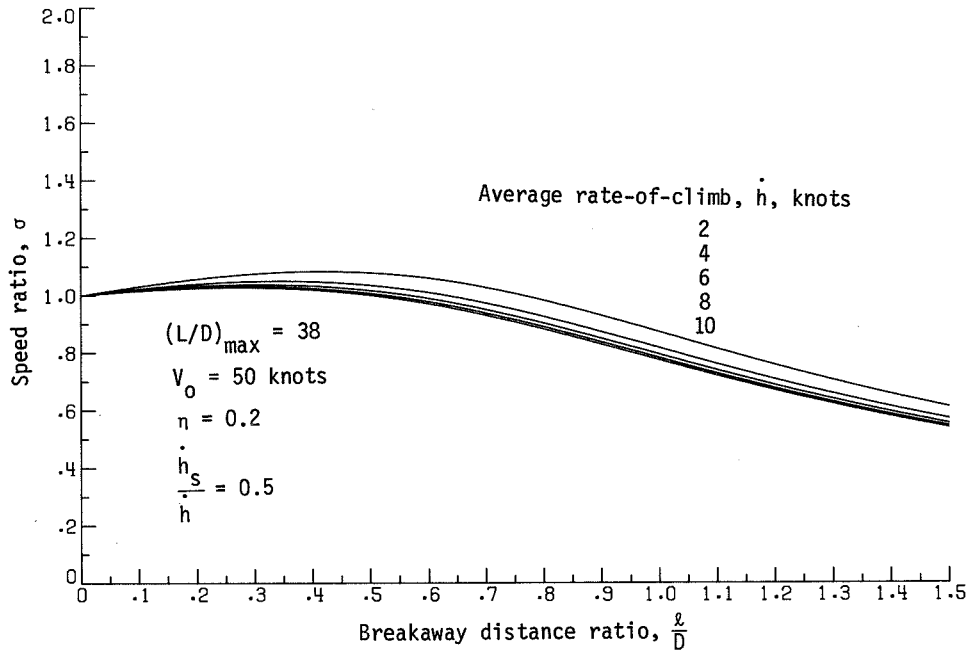


(a) $\phi = 15^\circ$

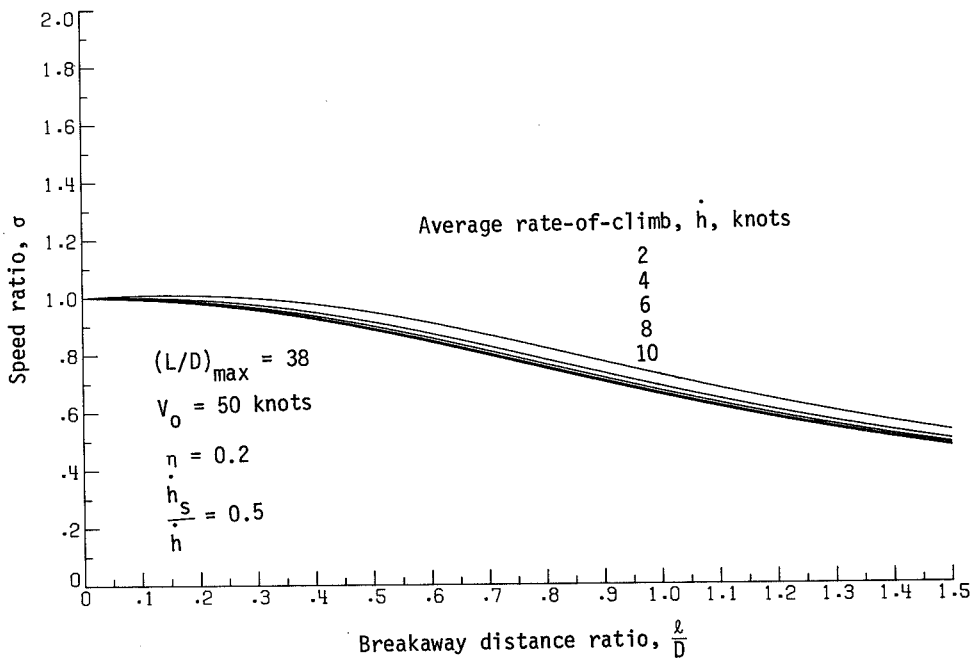


(b) $\phi = 30^\circ$

Figure 13. - Speed ratio versus breakaway distance ratio for a thermal street at an angle to course line.

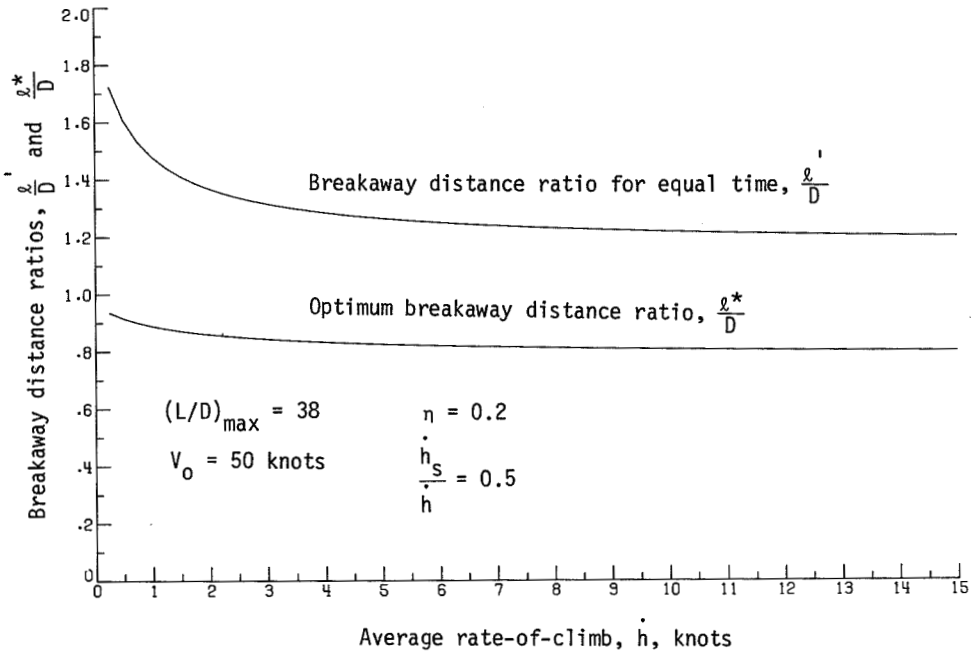


(c) $\phi = 45^\circ$

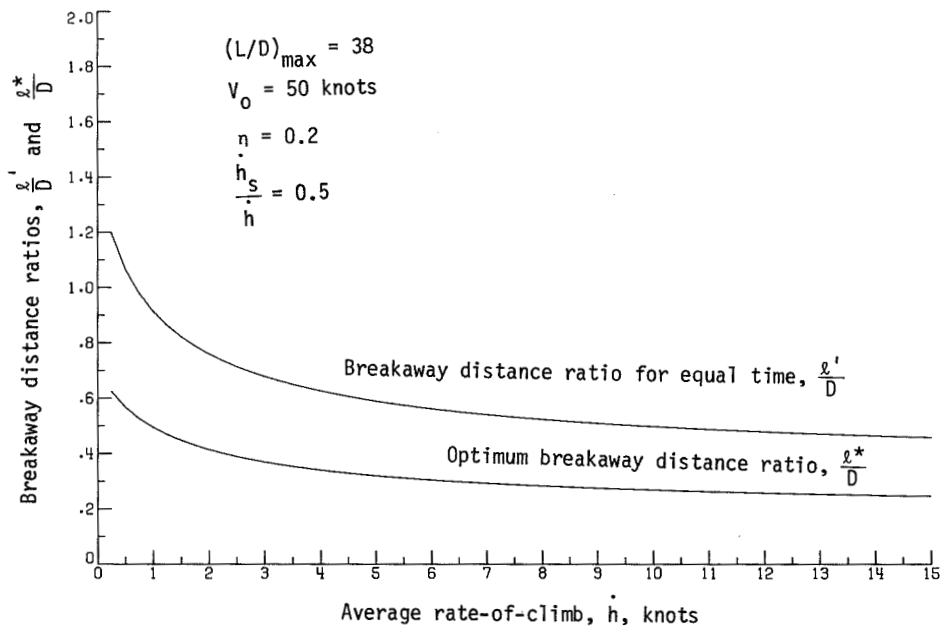


(d) $\phi = 60^\circ$

Figure 13. - Concluded.



(a) $\phi = 15^\circ$



(b) $\phi = 45^\circ$

Figure 14. - Breakaway distance ratios for equal time and optimum time versus average rate-of-climb for a thermal street at an angle to course line.

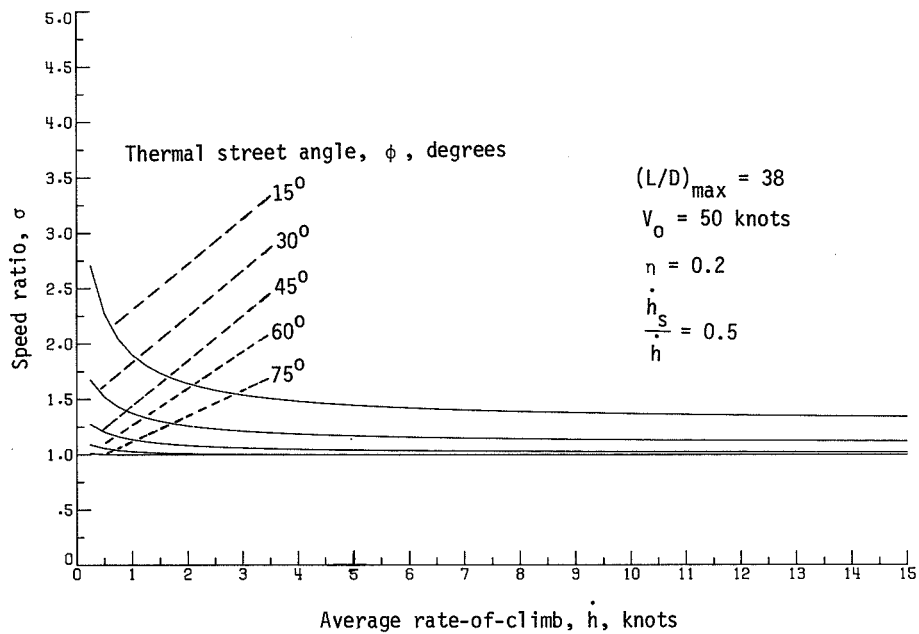


Figure 15. - Speed ratio versus rate-of-climb for a variety of street angles for a thermal street at an angle to course line.

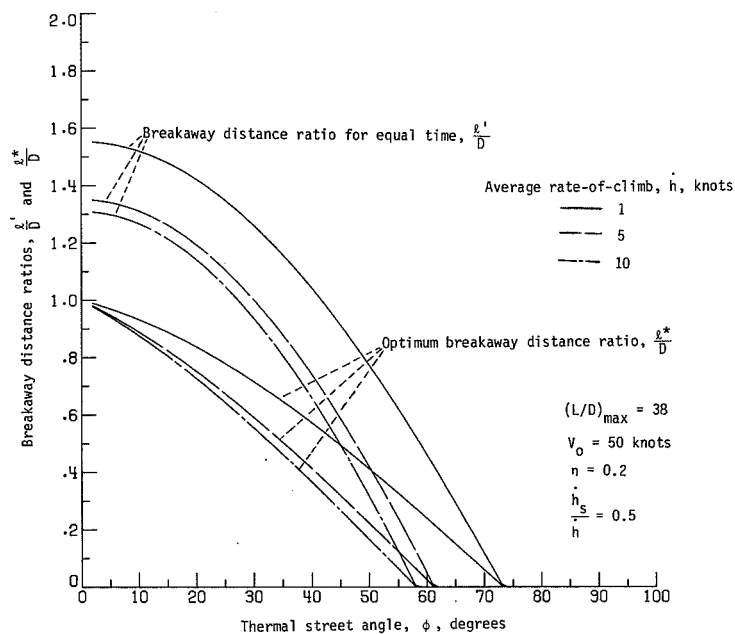


Figure 16. - Influence of thermal street angle upon breakaway distance ratio for a thermal street at an angle to course line.

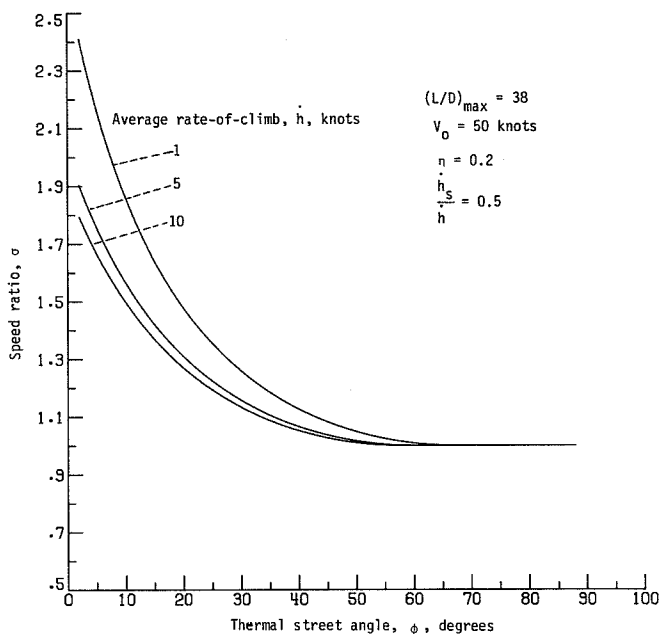


Figure 17. - Speed ratio versus thermal street angle for micro-strategy thermal street model.

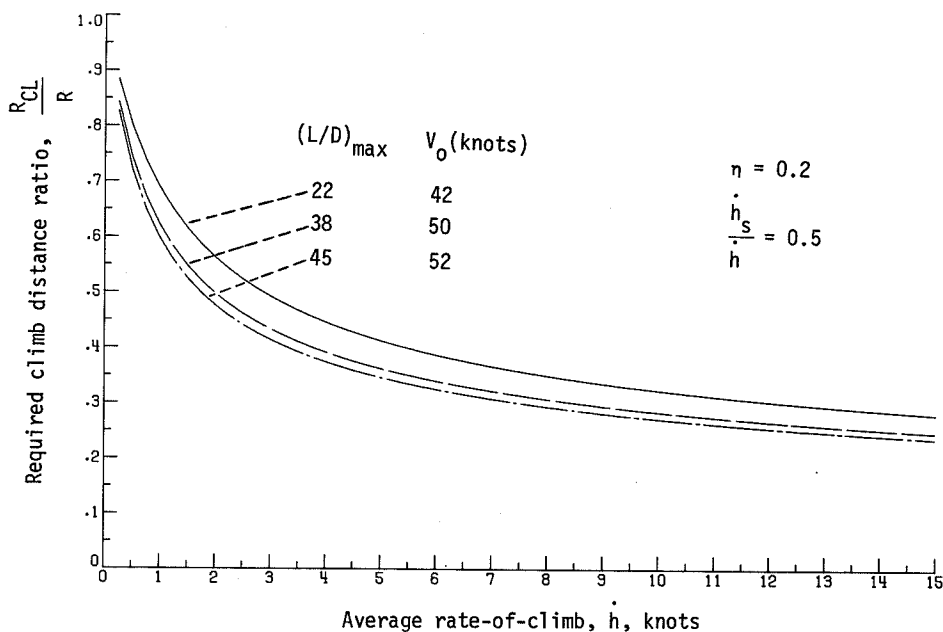


Figure 18. - Required climb distance ratio versus average rate-of-climb for thermal street macro-strategy analysis.

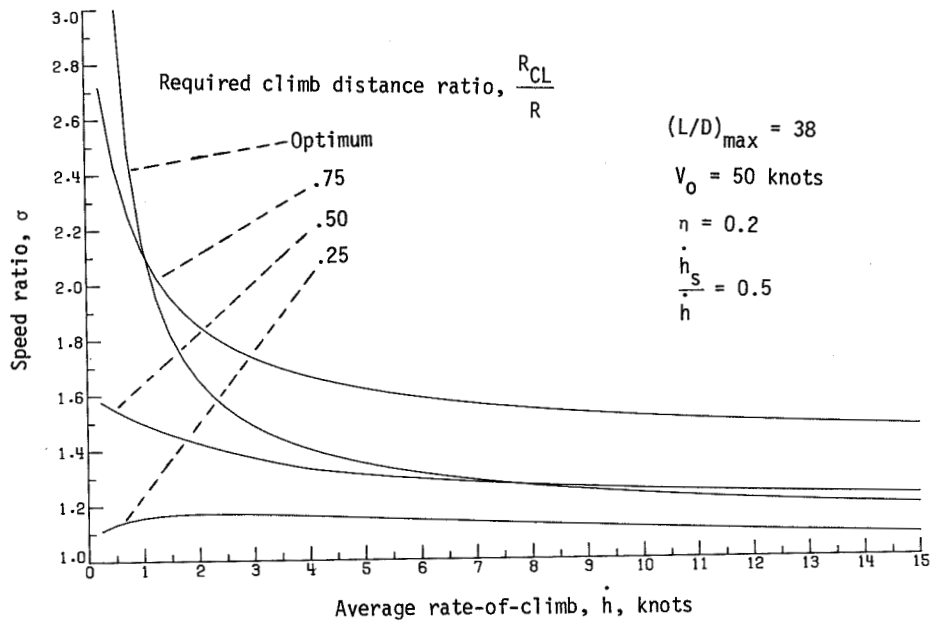


Figure 19. - Speed ratio versus average rate-of-climb for thermal street macro-strategy model.

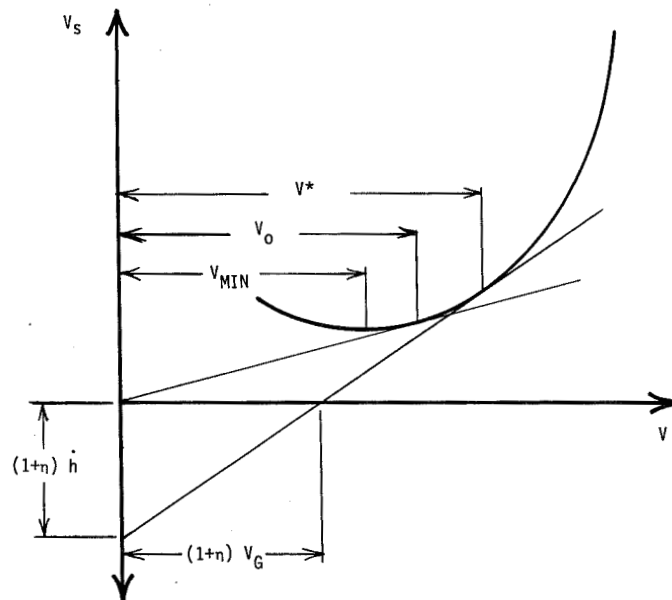


Figure 20. - Sailplane polar showing optimum speed-to-fly constructions for thermal soaring.

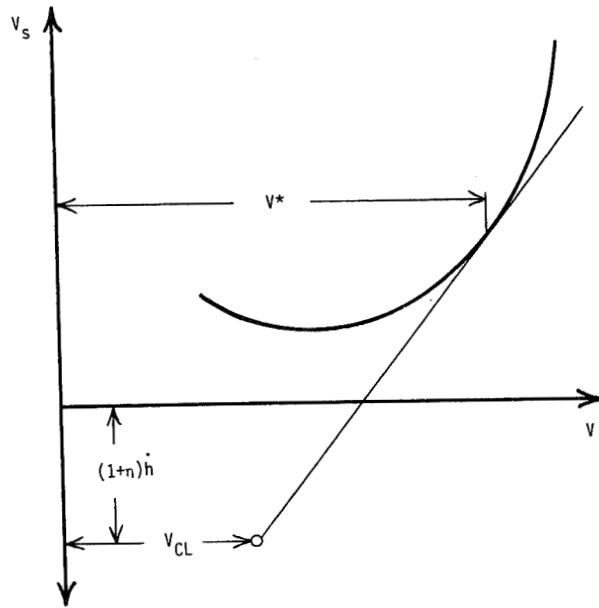


Figure 21. - Sailplane polar showing optimum speed-to-fly constructions for thermal street soaring.

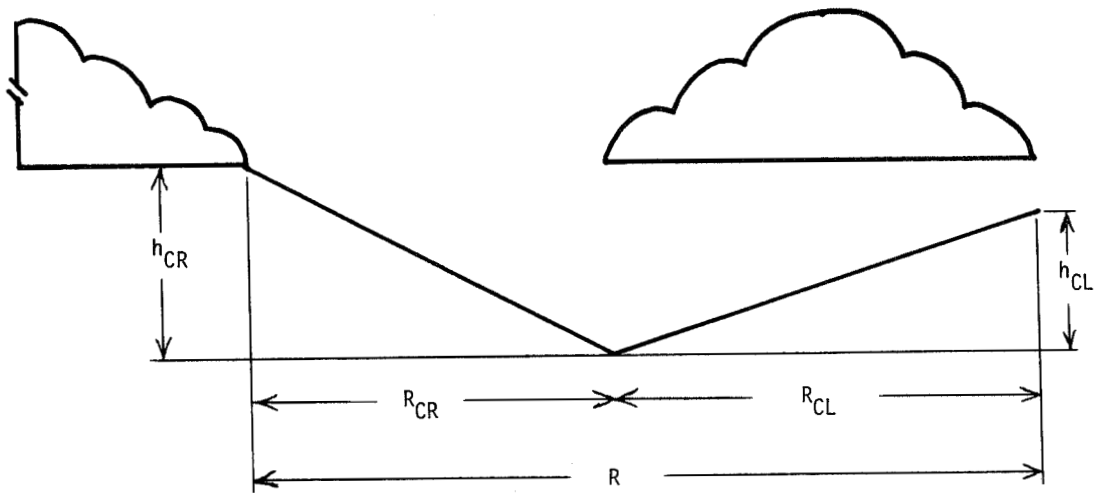


Figure 22. - Flight profile of a glide/climb cycle for thermal street soaring.

Page intentionally left blank

ON GLOBAL OPTIMAL SAILPLANE FLIGHT STRATEGY

G. Sander and F. X. Litt
University of Liège, Belgium

SUMMARY

The present paper concentrates on the derivation and interpretation of the necessary conditions that a sailplane cross-country flight has to satisfy to achieve the maximum global flight speed. Simple rules are obtained for two specific meteorological models. The first one uses concentrated lifts of various strengths and unequal distance. The second one takes into account finite, non-uniform space amplitudes for the lifts and allows, therefore, for dolphin-style flight. In both models, altitude constraints consisting of upper and lower limits are shown to be essential to model realistic problems. Numerical examples illustrate the difference with existing techniques based on local optimality conditions.

INTRODUCTION

The problems associated with the optimization of sailplane flight paths to achieve maximum cross-country speeds have recently received special attention in the literature. This has been stimulated by the modern competitive soaring which consists almost exclusively in racing and by the development of high performance sailplanes allowing for new, highly efficient flight techniques. Starting with the now classical MacCready [1] results, most of the investigations have been concerned essentially with local optimization problems, that is, finding the optimum flight strategy for various specific situations encountered in a short section of a flight [1 to 10].

In recent papers [2, 4, 5, 8] the optimum speeds to fly in a variety of atmospheric vertical velocity distributions have been determined from the basic assumption that the corresponding flight segments had to be crossed with zero net altitude loss. Conditions under which a transition from the circling mode of climb to the dolphin or essing modes has to be decided have been examined [4]. Although such results yield extremely valuable guidelines for selecting a flight strategy, they only optimize the speed over a limited portion of the total flight.

It is well known, however, in optimization theory that a succession of locally optimum solutions does not, in general, lead to a globally optimum result [11]. It is worth pointing out that a globally optimum flight strategy can only be determined if the assumption is made that the distribution of atmospheric velocities over the whole flight path is known in advance and is independent of time. Although this is never achieved in practice, it is felt that the derivation of global optimality conditions allows for a new insight into the sailplane flight technique by giving a posteriori the decisions that the pilot should have taken and the influence of factors that have

been up to now neglected in the analysis, such as the effect of the unequal distribution and strength of the lifts and the effect of minimum and maximum altitude limitations. Such altitude constraints reveal an essential ingredient in the formulation. Their necessity appears as follows. If they are absent and if the lifts are of unequal strength, the globally optimum solution turns out to be trivial and consists of a glide until the maximum lift existing along the path is reached and a climb to an altitude that allows completion of the task, the speed on both segments corresponding to the MacCready setting for that strongest lift [12].

The present paper provides simple rules for global optimality for two simple atmospheric models. These appear to be in agreement with the techniques intuitively used by good competition pilots.

PROBLEM FORMULATION

In both atmospheric models used in the following, the horizontal (wind) velocity of the air mass is assumed to be either zero or to be taken into account by an appropriate modification of the polar equation. The vertical velocity (lift) of the air mass c_i is defined by the so-called netto value. It is constant in the vertical direction between the altitude limits. The flight path is supposed to be constituted by a succession of segments of variable lengths in which the air mass exhibits vertical velocities c_i which are constant along a given segment but vary from one to the other. The altitude constraints consist in constant upper and lower limits denoted \bar{h} and \underline{h} . Note that variable altitude limits could be easily incorporated. For simplicity the lower altitude limit is taken as zero ($\underline{h} = 0$).

Concentrated Lift Model

In a first model, the lengths of the segments where a positive vertical velocity is encountered are supposed to be negligible, that is, the lifts are considered as concentrated. The air mass between the lifts is supposed to be stable. Climbing is therefore achieved only by circling at fixed locations corresponding to the lifts. If a lift is not used, its crossing is supposed not to affect the glide and the dynamical aspects of the transition from gliding to circling are not considered. The model is illustrated in figure 1 which is drawn in the vertical plane. The signs of the velocities are taken according to the positive sign of the axes.

The flight consists of a succession of climbs in the selected lifts followed by a glide at constant speed which possibly crosses discarded lifts. The pilot controls the selection of the lifts where he decides to gain altitude, the amount of altitude gained, and the speed to fly between the selected lifts. During the climbs the vertical speed of the sailplane is simply taken as the algebraic sum of the air mass vertical velocity and the minimum sinking speed of the glider. The increase of sinking speed due to variations in bank angle is not considered explicitly and should be incorporated in the polar definition.

The variations in altitudes are given by

$$h_{2i+1} - h_{2i} = \Delta h_i \quad i = 0, 1, \dots, n-1 \quad (1)$$

$$h_{2i+2} - h_{2i+1} = \frac{w(v_i)}{v_i} l_i$$

where the sinking speed $w(v_i)$ is given by the polar equation. The classical quadratic approximation has been used for numerical examples

$$w = A v^2 + B v + C \quad (2)$$

The time spent at each step consists of the sum of the time used in climbing and the transition time between lifts

$$t_{2i} = \frac{\Delta h_i}{c_i + w_m} \quad i = 0, 1, \dots, n-1 \quad (3)$$

$$t_{2i+1} = \frac{l_i}{v_i}$$

The achieved rate of climb is the sum of the air mass velocity c_i and the glider minimum sinking speed w_m . The constraints on the altitude and altitude gains are expressed by

$$\text{A control constraint} \quad \Delta h_i \geq 0 \quad (4)$$

$$\text{Initial and terminal constraints, say} \quad h_0 = 0 \quad h_{2n} = 0 \quad (5)$$

$$\text{Altitude constraints at each step} \quad h_{2i+1} \leq \bar{h}; \quad h_{2i} \geq 0 \quad (6)$$

$$i = 0, 1, \dots, n-1$$

The mathematical problem can be treated by the classical discrete optimal control theory [11] and consists of finding the sequence(s) $\Delta h_0, v_0, \Delta h_1, v_1, \dots, v_{n-1}$ which satisfy the relations (1), (4), (5), and (6) and minimizes the total flight time

$$T = \sum_{i=0}^{n-1} (t_{2i} + t_{2i+1}) \quad (7)$$

Distributed Lift Model

In this second model, the length of the segments is always finite and non-vanishing. Between lifts the air mass may present negative vertical velocities so that any desired air mass vertical balance can be achieved. The model is illustrated in figure 2. An important difference with the preceding model is brought by the possibility of crossing a lifting segment at a horizontal speed v_i less than the speed corresponding to the minimum sinking speed w_m . This is achieved by using the equivalent polar illustrated in figure 3 and already used in other similar works [4]. For horizontal speeds less than that corresponding to the minimum sinking speed, the sinking speed remains constant. This appears to be sufficiently accurate to simulate the transition from pure dolphin flight to essing or circling or a combination of equivalent manoeuvres achieved to cross a lifting area in the time required to gain a certain amount of altitude. Note that the same approximation is used as the basis for speed control in some modern instrumentation. In the numerical applications, the quadratic approximation (2) remains applicable at speeds higher than $v(w_m)$.

The variations in altitude are governed by

$$h_{i+1} - h_i = \frac{w(v_i) + c_i}{v_i} l_i \quad i = 0, 1, \dots, n-1 \quad (8)$$

If $v_i \leq v(w_m)$, then $w = w_m = \text{Constant}$ and thus the altitude gain is entirely controlled by the equivalent horizontal speed v_i . The altitude gain no longer appears as an explicit control variable. The time spent in each segment is given by

$$t_i = \frac{l_i}{v_i} = \frac{h_{i+1} - h_i}{w(v_i) + c_i} \quad (9)$$

while the altitude constraints read

$$\begin{array}{l} \text{At initial and terminal} \\ \text{points} \end{array} \quad h_0 = 0 \quad h_n = 0 \quad (10)$$

$$\begin{array}{l} \text{At each step} \end{array} \quad 0 \leq h_i \leq \bar{h} \quad i = 1, 2, \dots, n-1 \quad (11)$$

The mathematical problem consists of finding the sequence(s) v_0, v_1, \dots, v_{n-1} satisfying the relations (8), (10), and (11) and minimizing the total flight time

$$T = \sum_{i=0}^{n-1} t_i \quad (12)$$

NECESSARY OPTIMALITY CONDITIONS

The first-order necessary conditions for optimality can be deduced by the classical methods of discrete optimal control [11]. Such methods have been used in previous work [4, 6]. A detailed treatment can be found in [12, 13] for the two atmospheric models presented here, as well as for certain more complex situations. The conclusions are summarized as follows.

Concentrated Lift Model

The Hamiltonian turns out to be

$$H(h_{2i}, \Delta h_i, p_{2i+1}, p^0, 2i) = p^0 \frac{\Delta h_i}{c_i + w_m} + p_{2i+1} \Delta h_i \quad (13)$$

$$H(h_{2i+1}, v_i, p_{2i+2}, p^0, 2i+1) = p^0 \frac{\ell_i}{v_i} + p_{2i+2} \frac{w(v_i)}{v_i} \ell_i$$

It has to be maximized with respect to Δh_i or v_i for each i . The so-called adjoint variables p_i have to satisfy the relations

$$\begin{aligned} p^0 - p_1 &= 0 & p^0 &\leq 0 \\ p_{2i+1} - p_{2i+2} &= \lambda_{2i+1} & i &= 0, 1, \dots, n-1 \\ \lambda_{2i+1} (h_{2i+1} - \bar{h}) &= 0 & \lambda_{2i+2} &\leq 0 \\ p_{2i} - p_{2i+1} &= -\lambda_{2i} & i &= 1, 2, \dots, n-1 \\ \lambda_{2i} h_{2i} &= 0 & \lambda_{2i} &\leq 0 \end{aligned} \quad (14)$$

where the λ_i are Lagrange multipliers. From those conditions, it can be shown [12] that a reduced set of adjoint variables $\eta_0, \eta_1, \dots, \eta_{n-1}, \psi_0, \psi_1, \dots, \psi_{n-1}$ and of Lagrange multipliers $\mu_1, \mu_2, \dots, \mu_{n-1}$ can be derived which, in an optimal solution, have to satisfy the following conditions

$$\mu_{2i+1} (h_{2i+1} - \bar{h}) = 0 \quad \mu_{2i+1} \leq 0 \quad i = 0, 1, \dots, n-1 \quad (15)$$

$$\mu_{2i} h_{2i} = 0 \quad \mu_{2i} \leq 0 \quad i = 1, 2, \dots, n-1 \quad (16)$$

$$\Delta h_i \geq 0 \quad \eta_i \geq 0 \quad \eta_i \Delta h_i = 0 \quad i = 0, 1, \dots, n-1 \quad (17)$$

$$\eta_{i+1} = \eta_i + c_i - c_{i+1} + \mu_{2i+1} - \mu_{2i+2} \quad i = 0, 1, \dots, n-2 \quad (18)$$

$$v_i \frac{dw(v_i)}{dv_i} - w(v_i) + \psi_i = 0 \quad \psi_i > 0 \quad i = 0, 1, \dots, n-1 \quad (19)$$

$$\psi_{i+1} = \psi_i - \mu_{2i+2} + \mu_{2i+3} \quad i = 0, 1, \dots, n-2 \quad (20)$$

$$\psi_i = \eta_i + c_i + w_m + \mu_{2i+1} \quad i = 0, 1, \dots, n-1 \quad (21)$$

Distributed Lift Model

The optimal solution (h_i, v_i) must be such that the Hamiltonian

$$H(h_i, v_i, p_{i+1}, p^0, i) = p^0 \frac{\lambda_i}{v_i} + p_{i+1} \frac{w(v_i) + c_i}{v_i} \lambda_i \quad (22)$$

$$i = 0, 1, \dots, n-1$$

is maximized with respect to v_i for each i . The adjoint variables p_i have to satisfy the relations

$$\begin{aligned} p^0 - p_1 &= 0 & p^0 &\leq 0 \\ p_i - p_{i+1} &= -\lambda_i^{(1)} + \lambda_i^{(2)} & i &= 1, 2, \dots, n-1 \\ \lambda_i^{(1)} h_i &= 0 & \lambda_i^{(1)} &\leq 0 \\ \lambda_i^{(2)} (h_i - \bar{h}) &= 0 & \lambda_i^{(2)} &\leq 0 \end{aligned} \quad (23)$$

where $\lambda_i^{(1)}$ and $\lambda_i^{(2)}$ are Lagrange multipliers. Again a set of reduced variables and Lagrange multipliers

$$\left(\psi_0, \dots, \psi_{n-1}, \mu_1^{(1)}, \dots, \mu_{n-1}^{(1)}, \mu_1^{(2)}, \dots, \mu_{n-1}^{(2)} \right)$$

allows to present the optimality conditions in a more suitable form which turns out to be [13]

$$\begin{aligned} \mu_i^{(1)} h_i &= 0 & \mu_i^{(1)} &\leq 0 \\ \mu_i^{(2)} (h_i - \bar{h}) &= 0 & \mu_i^{(2)} &\leq 0 \end{aligned} \quad i = 1, 2, \dots, n-1 \quad (24)$$

$$v_i \frac{dw(v_i)}{dv_i} - w(v_i) - c_i + \psi_i = 0 \quad i = 0, 1, \dots, n-1 \quad (25)$$

$$\psi_i = \psi_{i-1} - \mu_i^{(1)} + \mu_i^{(2)} \quad i = 1, 2, \dots, n-1 \quad (26)$$

$$\psi_i > 0 \quad \psi_i \geq w_m + c_i \quad i = 0, 1, \dots, n-1 \quad (27)$$

PHYSICAL INTERPRETATION

The interpretation of the two sets of optimality conditions follows similar lines. A first conclusion is drawn from equation (19) or (25) which governs the speed to fly in a segment. Note that equation (25) reduces to equation (19) if the air mass vertical velocity c_i is zero, as assumed in the first model. From figure 3, the reduced adjoint variable ψ_i appears to correspond to a classical MacCready setting and indeed equation (25) appears in most other works on optimization [4, 5, 8]. In the following, the notation $MCS(c_i)$ denotes the setting corresponding to an air mass velocity c_i as defined by equation (25). The next interpretation concerns the Lagrange multipliers μ_i in equation (15), (16), or (24). These multipliers are zero in entering $\left(\mu_{2i}^{(1)} \text{ or } \mu_i^{(1)}\right)$ or leaving $\left(\mu_{2i+1}^{(2)} \text{ or } \mu_i^{(2)}\right)$ a segment if the LAL (lower altitude limit) or UAL (upper altitude limit) is not reached.

From equation (20) or (26) the important conclusion is drawn that the MCS cannot change from a segment to the next one unless either the UAL or the LAL has been reached, that is, if one of the Lagrange multipliers μ becomes negative. If, and only if, the UAL is reached, then the MCS may be reduced. Conversely, the MCS may be increased only if the LAL is touched. To proceed further with the interpretation requires distinguishing between the two models.

Concentrated Lift Model

The reduced adjoint variables η_i appears from equation (17) as indicators of whether the lifts c_i may be used ($\eta_i = 0$) to climb or not ($\eta_i > 0$). With these results in mind, it becomes easy to deduce from equations (18), (20), and (21) the logic for deriving iteratively the optimum solution.

Consider the beginning of the flight at a location where a lift A exists. Denote by B the first lift stronger than A along the flight path. The following iterative reasoning can be made. If B can be reached from the UAL in A with a $MCS(A)$, that is, a MCS corresponding to the lift A, then one has to climb in A just enough to reach B at LAL with a $MCS(A)$. If B cannot be reached with $MCS(A)$ even when climbing at UAL in A, then climb to UAL in A and look for the next best lift, denoted C, between A and B. Evidently $C < B$ and $C \leq A$. Try to reach B at LAL with a MCS inferior to $MCS(A)$ but superior to $MCS(C)$. If this is impossible because C cannot be reached, then restart the reasoning with A unchanged and B replaced by C; if this is impossible because B cannot be reached, then take a $MCS(C)$ to reach C and restart the reasoning with B unchanged and A replaced by C.

Consider now the case where a lift A is stronger than all remaining ones on the flight path. Denote by B the strongest of the remaining lifts. Unless in the special case where the task could be ended from A with a MCS(A) without climbing up to the UAL, one necessarily has to climb up to the UAL and take a MCS superior to the MCS(B) but equal or inferior to the MCS(A). If the task cannot be ended, reach B with a MCS(B) and climb in it up to the UAL. Repeat the reasoning in B for the next strongest lift. If B cannot be reached from A with MCS(B), look for the best lift between A and B, denoted C, and try if B can be reached at LAL with a MCS between MCS(B) and MCS(C). If necessary climb in C if the MCS is equal MCS(C). If it is impossible to reach C at LAL with a MCS(C) look for the best lift, say D, between A and C and repeat the reasoning. If there is no lift, try MCS(O). If it still does not work, the flight is evidently impossible.

A combination of the two reasonings proposed above for increasing or decreasing lifts allows the construction of the optimal solution. Note that it is not necessarily unique.

It is worth pointing out that the optimal solution leads always when going from a lift A to a lift B to use a MCS corresponding to the weaker of the two lifts. If $A > B$ the UAL has to be taken in A while B has to be reached at LAL if $A < B$. Similar conclusions have been obtained independently by a variationa approach in [14].

Distributed Lift Model

In this model, the decision to gain altitude in a lift is dictated by equation (27). If $\psi_i > w_m + c_i$ the speed v_i is larger than $v_i(w_m)$ and therefore is uniquely determined by equation (25). The lift has then to be crossed at the corresponding speed. This appears to be a pure dolphin mode. If, and only if, $\psi_i = w_m + c_i$ the decision of climbing may be taken as the speed v_i becomes equal to or smaller than the speed $v(w_m)$. Indeed, due to the form use for the equivalent polar, the speed v_i cannot be computed by equation (25). Its value is dictated by the need to gain a certain amount of altitude in that lift, given by

$$\Delta h_i = \psi_i t_i = (w_m + c_i) \frac{l_i}{v_i} \quad (28)$$

If the speed v_i is inferior to $v_i(w_m)$, Δh_i is larger than the value obtained in pure dolphin mode which implies that some sort of manoeuver like essing and/or circling is achieved while flying through the segment.

Except for the process of gaining altitude in a non-dolphin mode, the conclusions reached for the preceding model are still valid. From equation (26) the MCS may not be changed unless the altitude limits are reached. It may increase only if the LAL is touched and may decrease only when reaching the UAI. The process for constructing numerically an optimum solution is as follows.

Start by trying to use the MCS of the best existing lift, say A, for all the segments. If the LAL is not reached, increase the setting until either the task can be ended or the LAL is reached. At that point, the MCS may be increased.

If the MCS corresponding to the best lift allows reaching the LAL before the segment where it occurs, look for the strongest lift between the present point and A. Denote it by B. Then try to reach A at the LAL with a MCS(B). If this is not possible, climbing in B is allowed. If B cannot be reached with a MCS(B), look for the best lift between the present point and B and repeat the reasoning as necessary, keeping in mind the rules that allow climbing in a lift and those that allow changing the MCS.

NUMERICAL EXAMPLES

Concentrated Lift Model

As a simple example, a 300 km flight is schematized in figure 4. The lifts are equidistant (10 km) for simplicity although it is by no means implied in the preceding rules for optimality. The lift strengths are indicated in m/sec along the y-axis. They increase progressively during the flight, then decrease, but are in general unequal. The altitude limits are 0 and 1000 m. The sailplane polar is approximated by

$$w = -1.65 \cdot 10^{-3} v^2 + 61.6 \cdot 10^{-3} v - 1.026 \quad (\text{m/sec})$$

and corresponds to a dry open class ship. The optimal strategy for that lift distribution and altitude constraints is illustrated in figure 4. The MCS for each glide is indicated. It follows as a simple and systematic application of the rules for optimality established above. Note that the flight strategy consists in hitting systematically the altitude limits, except at 110 km and 170 km where the altitude just necessary for reaching the next best lift at LAL is gained. Note also that the MCS is not always equal to the strength of one of the two lifts defining the glide. Finally, note that this example justifies the practical rule of flying "low" when the lifts are improving and keeping "high" when they are deteriorating. The cruising speed for that flight is 81.01 km/h.

As a test for the sensitivity of the speed with respect to the MCS, the same problem has been solved with the additional constraints of keeping the same MCS which implies the same speed between any two selected lifts. The optimal MCS for that situation has been obtained in [13] in the form

$$\psi = \frac{L}{\sum \frac{l_i}{c_i + w_m}} \quad (29)$$

where L is the total length of the flight (300 km) and $c_i + w_m$ is the achieved rate of climb in each selected lift. Note that the selection of the lifts is highly dependent upon the altitude limits. In the present example $\psi = 1.23$ m/sec and the corresponding constant speed between the thermals is 133 km/h. The new constrained optimal speed becomes 79.51 km/h which differs by only 1.85% from the exact optimum. Although some restrictions have to be mentioned (see [13]) concerning the applicability of equation (29) in a general case, it indicates clearly that in an atmosphere corresponding to the present model, the MCS is much less important than the correct selection of the lifts. This is again well known for many competition pilots [15].

Distributed Lift Model

The flight polar has been approximated by

$$w(v) = -1.896 \cdot 10^{-3} v^2 + 77.8 \cdot 10^{-3} v - 1.27 \quad (\text{m/sec})$$

which corresponds also to a dry open class glider and to the model used in [4] and [5]. Three distributions of lifts have been selected and are presented in figures 5, 6, and 7 and denoted flights I, II, and III. These flights are all 200 km long and correspond to different weather conditions. In flight I the lifts are relatively concentrated except at two places and their strengths are rather different from each other. The length of the lifting zones represents 36% of the total which is rather critical for the transition from thermaling to dolphining [4]. The air mass balance is positive, that is, the average over the distance of the air mass (netto) vertical velocities yields 0.39 m/sec. In flight II the lifting zones represent 31% of the distance and their strengths are much more similar to each other. The lifting and sinking areas exactly balance each other; that is, not only the average vertical velocity is zero, but the air mass is organized in a succession of cells which are 20 to 40 km long where the exact air mass balance is also achieved. This allows for using the classical rules for local optimality [4] in crossing these cells and compares with the globally optimal solution. In flight III the lifts are weaker and their strengths still closer to each other. The lifting zone represents 49% of the total. The air mass balance yields 0.236 m/sec and the lifting zones are again organized in cells in which approximately the same air mass balance is maintained. For each of these atmospheric models three upper altitude limits have been considered $\bar{h} = 1000$ m, 1500 m, and 2000 m. The LAL has been kept at $h = 0$ which is evidently not necessarily the ground level.

The numerically obtained optimal solutions are illustrated in tables I, II, and III in digital form and in figures 8, 9, and 10 in graphical form. The satisfaction of the optimality conditions described above are easily verified. The lifts in which gaining altitude in circling or essing are indicated as well as the corresponding equivalent horizontal speed which is then smaller than the speed of minimum sink $v(w_m) = 20.52$ m/sec. In the other segments, crossed in dolphin mode, the optimum MCS is given. Note that $w_m = 0.47$ m/sec. The influence of the altitude limits is illustrated by the following table:

	$\Delta h = 1000 \text{ m}$	$\Delta h = 1500 \text{ m}$	$\Delta h = 2000 \text{ m}$	$\Delta h = \text{Unlimited}$
Flight I	$v = 94.5$	97.94	100.19	100.57
Flight II	$v = 73.76$	81.2	83.10	84.20
Flight III	$v = 85.87$	87.98	88.16	88.16

where Δh is the allowed altitude range and v is the optimum average speed in km/h. The application of various non-globally optimal flight strategies based on the use of existing rules for optimizing the speed in each individual meteorological cell [4, 5] resulted in average speed from 5 to 15% inferior depending on the allowed altitude limits and on the various conditions selected in applying these rules.

CONCLUSIONS

Simple rules for obtaining numerically the optimum flight strategy in two meteorological models have been obtained. Their applications reveal that the altitude limits imposed for the flight may have, as known from experience, a much more significant influence on the achieved speed than the selection of MCS. Additional investigation is required to determine the relation between the various possible weather profiles and the optimum flight strategies as well as altitude limits influence. The in flight recording of such atmospheric profiles over rather long distances would allow for studying systematically the optimum solution corresponding to a number of classical situations.

SYMBOLS

A, B, C	flight polar coefficients
c_i	air mass netto vertical velocity
h_i	altitude
\bar{h}	upper altitude limit
H	Hamiltonian
l_i	flight segment length
p_i	adjoint variable
t_i	elapsed time
T	total flight time
v_i	horizontal speed
w	sailplane sinking speed
w_m	minimum sinking speed
λ_i, η_i, μ_i	Lagrange multipliers
ψ_i	reduced adjoint variable = MCS
\bar{i}	index of a flight segment
UAL, LAL	upper (lower) altitude limits
MCS	MacCready setting

REFERENCES

1. MacCready, P.: Optimum Speed Selector. *Soaring*, Apr. 1954.
2. Reichmann, H.: Zum Problem der Fahrtoptimierung im Streckensegelflug. Diss. Univ. Karlsruhe, Int. Bericht no. 76/2.
3. Reichmann, H.: Strecken-Segelflug. Motor Buch Verlag, Stuttgart, 1976.
4. Metzger, D.; and Hedrick, J.: Optimum Flight Paths for Soaring Flights. *J. of Aircraft*, vol. 12, no. 11, Nov. 1975.
5. Arho, R.: Some Notes on Soaring Flight Optimization Theory. *Tech. Soaring*, vol. IV, no. 2, 1977.
6. Irving, F.: Cloud-Street Flying. *Tech. Soaring*, vol. III, no. 1, 1976.
7. Gedeon, J.: Dynamic Analysis of Dolphin Style Thermal Cross Country Flight. *Tech. Soaring*, vol. III, no. 1, 1976.
8. Arho, R.: Optimal Dolphin Soaring as a Variational Problem. *Tech. Soaring*, vol. III, no. 1, 1976.
9. Bohli, H.: Optimale Dolphinfluggeschwindigkeit auf Streckensegelflug. *Aero Revue*, no. 8, Aug. 1971.
10. Pirker, H.: Some Computer Calculations on Optimum Water-Bollest of Sailplanes. 15th OSTIV Congress, Räyskälä, Finland, 1976.
11. Cannon, M.; Cullum, C.; and Polak, E.: *Theory of Optimal Control and Mathematical Programming*. McGraw Hill, 1970.
12. Litt, F. X.; and Sander, G.: Optimal Strategy in a Given Space Distribution of Lifts With Minimum and Maximum Altitude Constraints. Report SART 78/03, Service de Régulation et Automatique, Univ. Liège, Belgium, June 1978. Also presented at XVI OSTIV Congress in Châteauroux, France.
13. Litt, F. X.; and Sander, G.: Global Optimization of Sailplane Flight Techniques. Report SART 79/02, Service de Régulation et Automatique, Univ. Liège, Belgium, Feb. 1979.
14. de Jong, J. L.: De optimale MacCready-ring instellingen by inachtnaam van verticale begrenzingen van de bruikbare thermiek hoogte. COSOR R-78-05, Tech. Hogeschool Eindhoven, Holland, April 1978.
15. Schuemann, W.: The Price You Pay for MacCready Speeds. Proc. Symp. on Competitive Soaring, 1972, U.S.A.

TABLE I.- OPTIMAL SOLUTION FOR FLIGHT I

Segment no.	$H_{\max} = 1000 \text{ m}$				$H_{\max} = 2000 \text{ m}$			
	MCS	h_{out}	v_i	Mode	MCS	h_{out}	v_i	Mode
1	0.53	425	0.6	C	0.53	425	0.6	C
2	0.53	0	30.8	D	0.53	0	30.8	D
3	1.03	481	1.0	C	1.03	481	1.0	C
4	1.03	0	34.8	D	1.03	0	34.8	D
5	2.03	732	2.7	C	2.03	732	2.7	C
6	2.03	288	41.7	D	2.03	288	41.7	D
7	2.03	213	38.4	D	2.03	213	38.4	D
8	2.03	233	34.8	D	2.03	233	34.8	D
9	2.03	0	44.7	D	2.03	0	44.7	D
10	3.03	164	34.8	D	3.03	164	34.8	D
11	3.03	1000	18.1	C	3.03	1781	9.3	C
12	1.57	646	47.8	D	3.03	1396	55.3	D
13	1.57	356	45.0	D	3.03	1069	52.8	D
14	1.57	249	35.0	D	3.03	826	44.7	D
15	1.57	350	31.0	D	3.03	749	41.7	D
16	1.57	712	21.0	D	3.03	913	34.8	D
17	1.57	53	42.0	D	3.03	121	50.3	D
18	1.57	0	35.1	D	3.03	0	44.7	D
19	4.61	268	42.2	D	4.03	370	38.4	D
20	4.61	1000	27.0	D	4.03	2000	12.3	C
21	1.38	428	43.8	D	2.69	1365	51.1	D
22	1.38	0	40.7	D	2.69	858	48.5	D
23	1.53	858	8.9	C	2.69	1056	32.1	D
24	1.53	437	38.4	D	2.69	506	45.7	D
25	1.53	0	41.7	D	2.69	0	48.5	D
Speed	94.54 km/h				100.19 km/h			

h_{out} = altitude at the end of the segment (meters)

Mode = D for dolphin

C for climbing with $v_i < v_i(w_m)$

MCS, v_i = m/sec

TABLE II.- OPTIMAL SOLUTION FOR FLIGHT II

Segment no.	$H_{\max} = 1000 \text{ m}$				$H_{\max} = 2000 \text{ m}$			
	MCS	h_{out}	v_i	Mode	MCS	h_{out}	v_i	Mode
1	0.53	447	2.9	C	0.53	447	2.9	C
2	0.53	284	30.8	D	0.53	284	30.8	D
3	0.53	541	20.5	D	0.53	541	20.5	D
4	0.53	0	38.4	D	0.53	0	38.4	D
5	1.03	617	8.3	C	1.03	617	8.3	C
6	1.03	0	38.4	D	1.03	0	38.4	D
7	2.03	1000	10.1	C	2.03	2000	5.0	C
8	1.03	443	41.7	D	2.03	1398	47.6	D
9	1.03	237	38.4	D	2.03	1165	44.7	D
10	1.03	181	30.8	D	2.03	1014	38.4	D
11	1.03	895	7.2	C	2.03	1149	30.8	D
12	1.03	278	38.4	D	2.03	450	44.7	D
13	1.03	0	41.7	D	2.03	149	47.6	D
14	2.03	1000	10.1	C	2.03	2000	5.5	C
15	0.53	729	38.4	D	1.53	1711	44.7	D
16	0.53	144	34.8	D	1.53	1055	41.7	D
17	0.53	890	10.6	C	1.53	1215	30.8	D
18	0.53	781	30.8	D	1.53	1074	38.4	D
19	0.53	0	34.8	D	1.53	200	41.7	D
20	1.53	1000	7.6	C	1.53	1092	8.6	C
21	0.78	0	36.7	D	1.53	0	41.7	D
Speed	73.76 km/h				83.10 km/h			

h_{out} = altitude at the end of the segment (meters)

Mode = D for dolphin

C for climbing with $v_i < v_i(w_m)$

MCS, v_i = m/sec

TABLE III.- OPTIMAL SOLUTION FOR FLIGHT III

Segment no.	$H_{\max} = 1000 \text{ m}$				$H_{\max} = 2000 \text{ m}$			
	MCS	h_{out}	v_i	Mode	MCS	h_{out}	v_i	Mode
1	0.53	364	3.6	C	0.53	364	3.6	C
2	0.53	200	30.8	D	0.53	200	30.8	D
3	0.53	586	20.6	D	0.53	586	20.6	D
4	0.53	0	34.8	D	0.53	0	34.8	D
5	1.03	999	20.6	D	1.03	999	20.6	D
6	1.03	594	47.6	D	1.03	594	47.6	D
7	1.03	37	41.7	D	1.03	37	41.7	D
8	1.03	968	16.6	C	1.03	968	16.6	C
9	1.03	411	41.7	D	1.03	411	41.7	D
10	1.03	0	38.4	D	1.03	0	38.4	D
11	1.53	1000	15.3	C	1.53	1737	8.8	C
12	0.56	608	35.0	D	1.53	1299	41.7	D
13	0.56	208	44.9	D	1.53	887	50.3	D
14	0.56	587	20.8	D	1.53	1046	30.8	D
15	0.56	0	35.0	D	1.53	390	41.7	D
16	1.03	673	15.3	C	1.53	759	26.2	D
17	1.03	617	30.8	D	1.53	656	34.8	D
18	1.03	0	38.4	D	1.53	0	41.7	D
Speed	85.87 km/h				88.16 km/h			

h_{out} = altitude at the end of the segment (meters)

Mode = D for dolphin

C for climbing with $v_i < v_i(w_m)$

MCS, v_i = m/sec

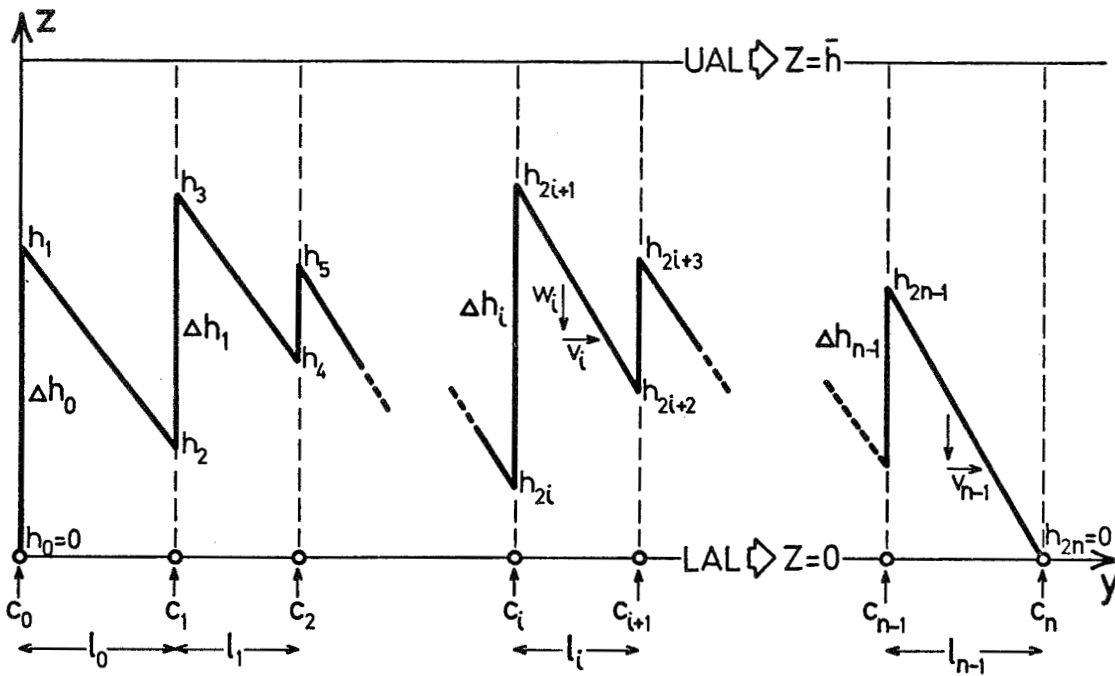


Figure 1.- Concentrated lift model.

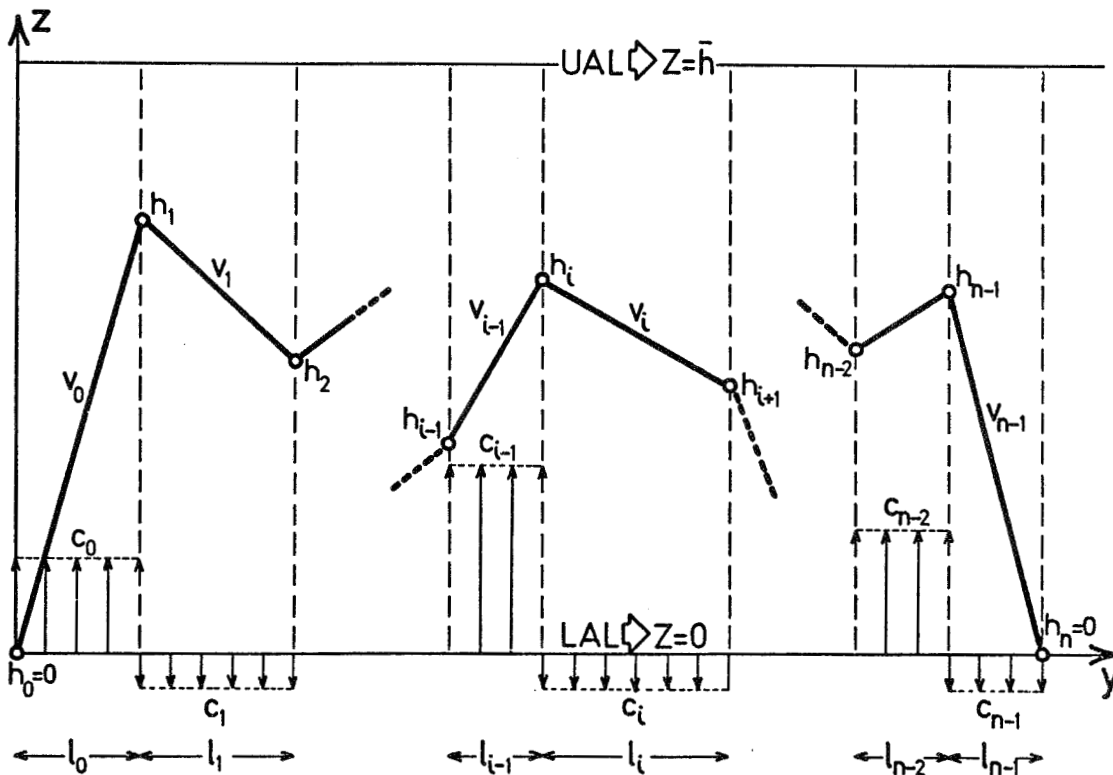


Figure 2.- Distributed lift model.

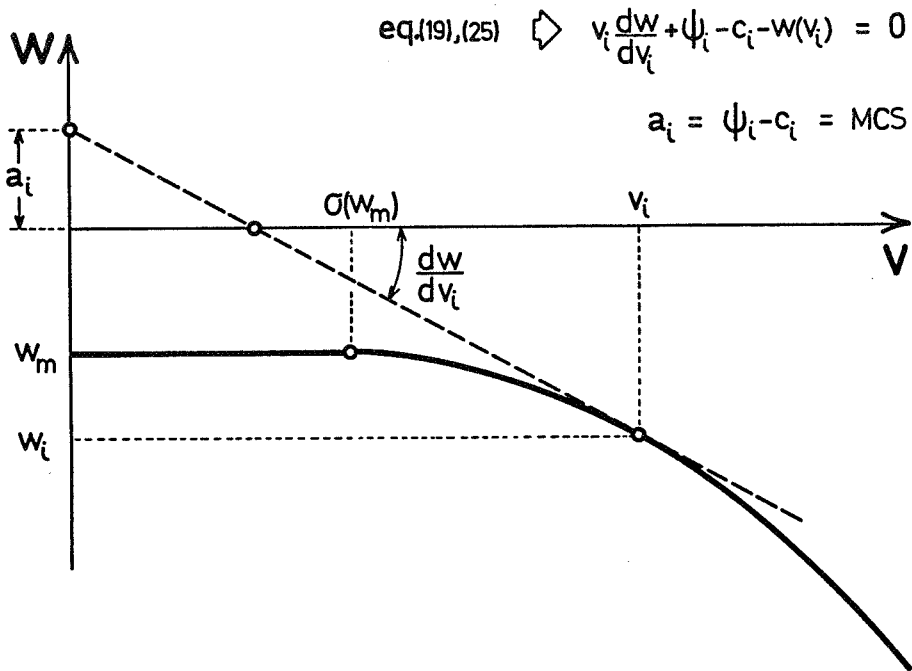


Figure 3.- The equivalent polar.

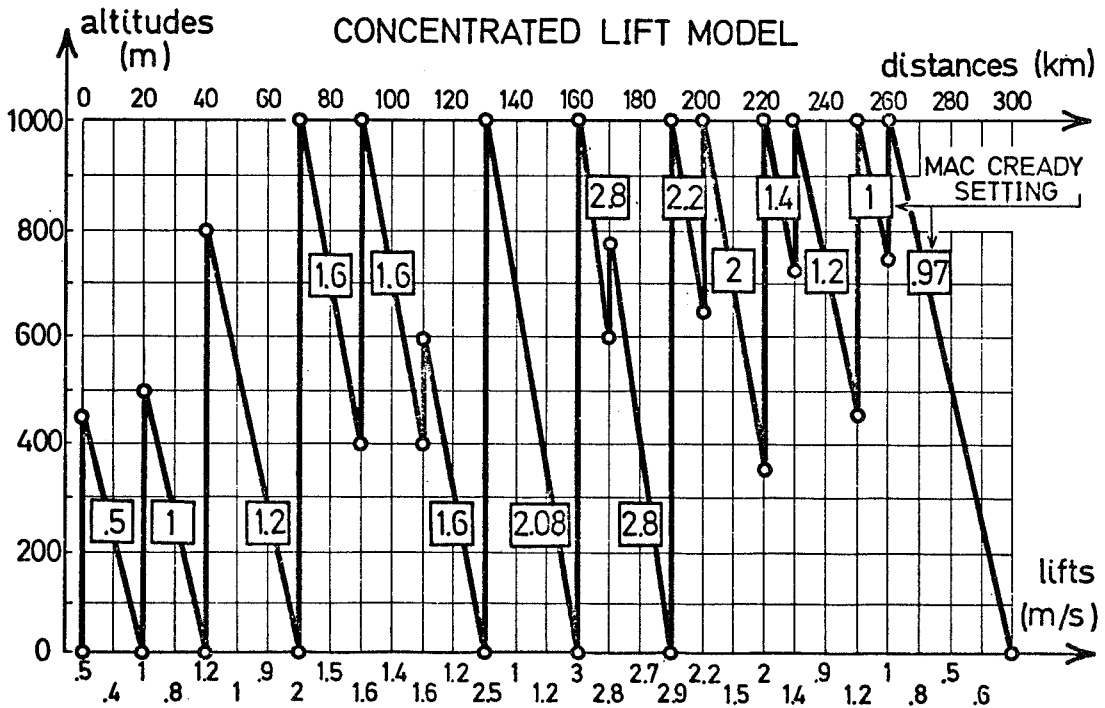
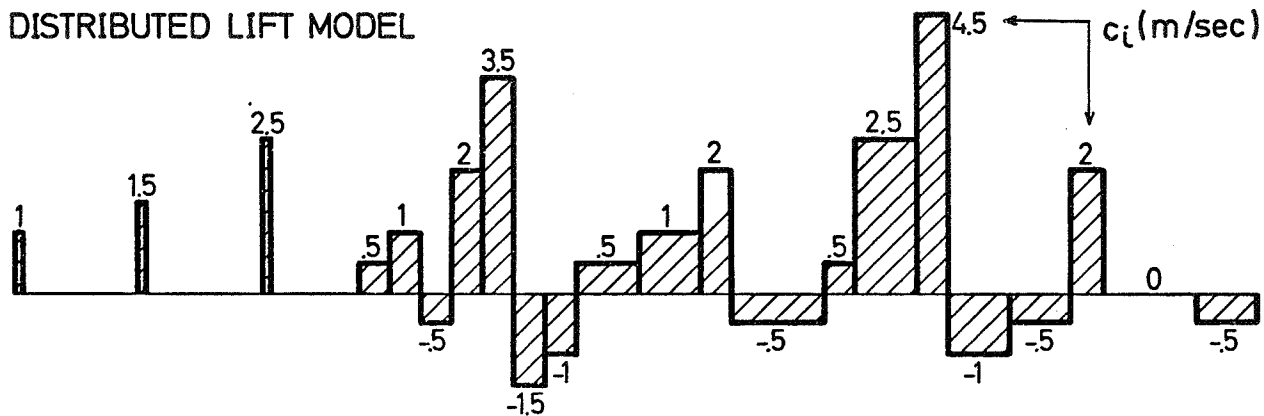


Figure 4.- Optimum flight strategy.

DISTRIBUTED LIFT MODEL



flight segment no.		1	2	3	4	5	6	7	8	9	10			
c_i	(m/sec)	1	0	1.5	0	2.5	0	5	1	-5	2			
l_i	(km)	.5	19.5	.5	19.5	1	14	5	5	5	5			
11	12	13	14	15	16	17	18	19	20	21	22	23	24	25
3.5	-1.5	-1	.5	1	2	-5	.5	2.5	4.5	-1	-5	2	0	-5
5	5	5	10	10	5	15	5	10	5	10	10	5	15	10

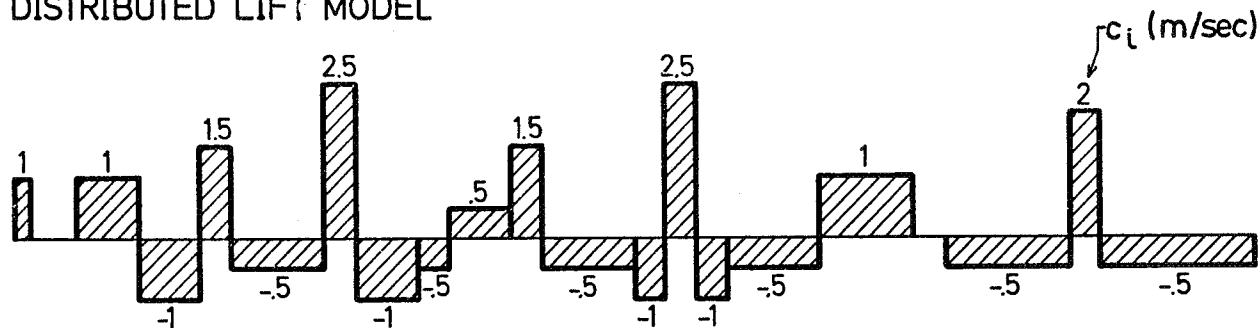
$$L = \sum l_i = 200 \text{ km}$$

$$\bar{c} = \frac{\sum c_i l_i}{L} = .39 \frac{\text{m}}{\text{sec}}$$

LIFTING ZONES = 36%

Figure 5.- Lift distribution for flight I.

DISTRIBUTED LIFT MODEL



flight segment no.		1	2	3	4	5	6	7	8	9	10
c_i	(m/sec)	1	0	1	-1	1.5	-5	2.5	1	-5	.5
l_i	(km)	2.5	7.5	10	10	5	15	5	10	5	10
11	12	13	14	15	16	17	18	19	20	21	
1.5	-5	-1	2.5	-1	-5	1	0	-5	2	-5	
5	15	5	5	5	15	15	5	20	5	25	

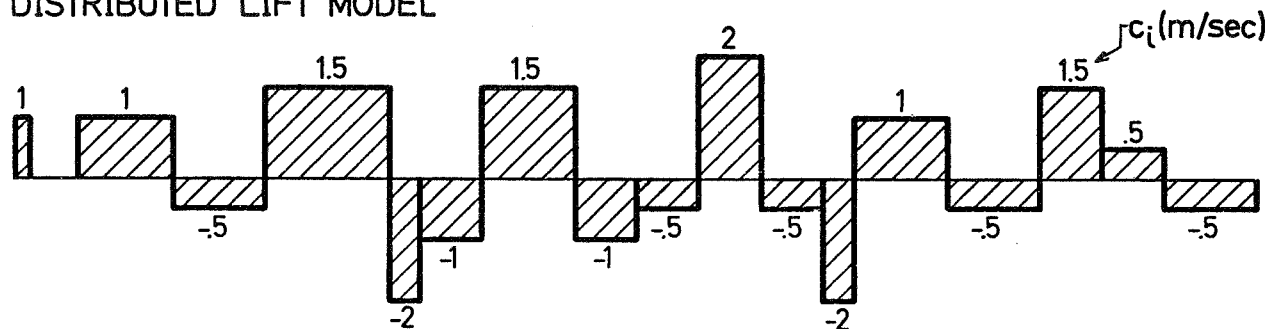
$$L = \sum l_i = 200 \text{ km}$$

$$\bar{c} = \frac{\sum c_i l_i}{L} = 0 \text{ m/sec}$$

LIFTING ZONES = 31%

Figure 6.- Lift distribution for flight II.

DISTRIBUTED LIFT MODEL



flight segment no.	1	2	3	4	5	6	7	8	9	10
c_i (m/sec)	1	0	1	-5	1.5	-2	-1	1.5	-1	-5
l_i (km)	2.5	7.5	15	15	20	5	10	15	10	10

	11	12	13	14	15	16	17	18
	2	-5	-2	1	-5	1.5	.5	-5
	10	10	5	15	15	10	10	15

$$L = \sum l_i = 200 \text{ km}$$

$$\bar{c} = \frac{\sum c_i l_i}{L} = .236 \frac{\text{m}}{\text{sec}}$$

LIFTING ZONES = 49%

Figure 7.- Lift distribution for flight III.

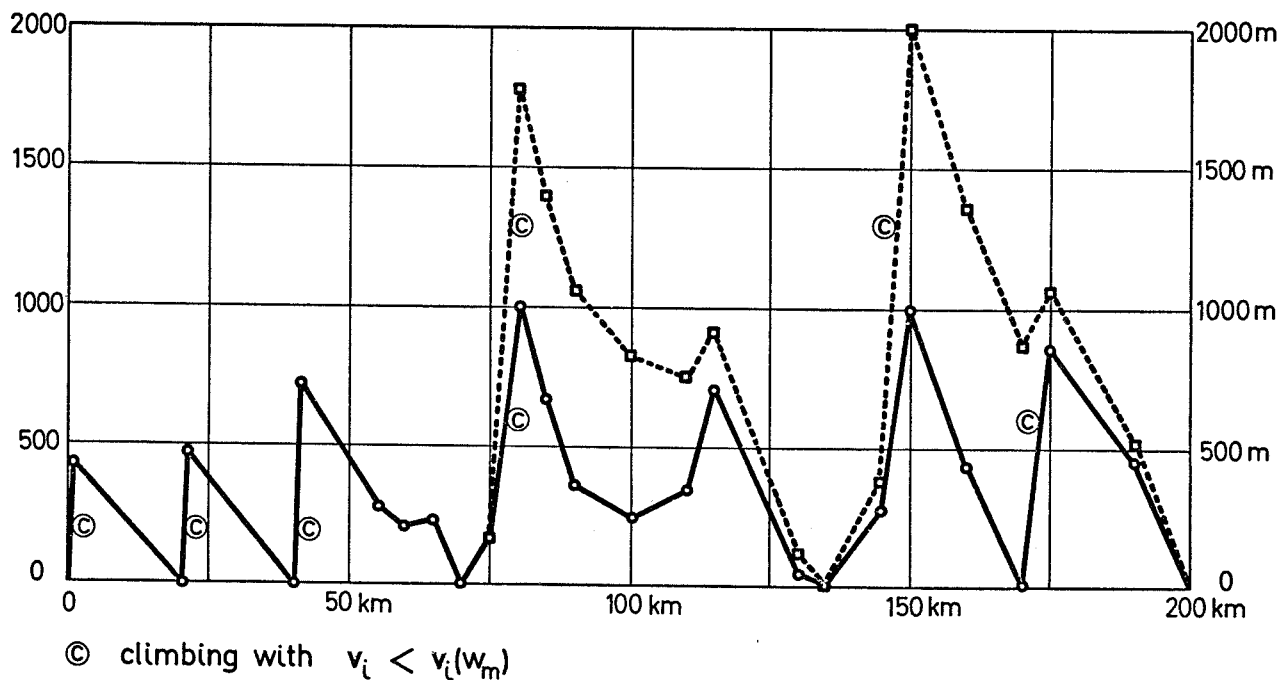


Figure 8.- Optimal solution for flight I.

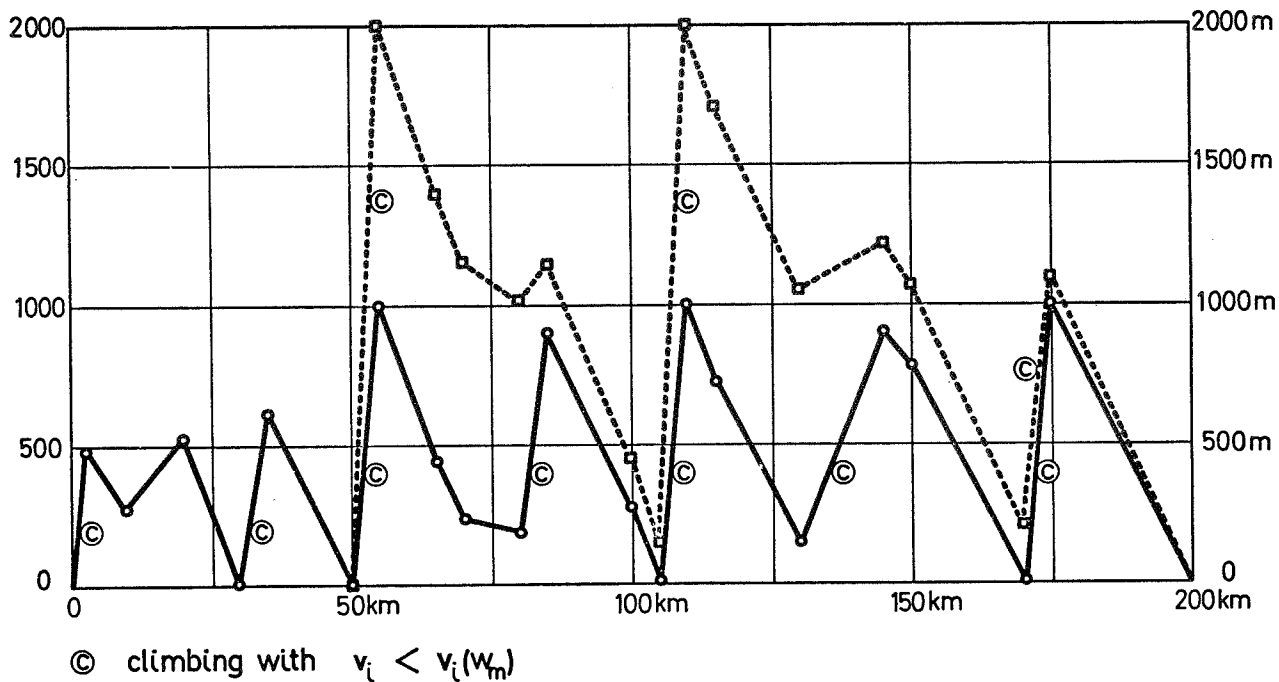


Figure 9.- Optimal solution for flight II.

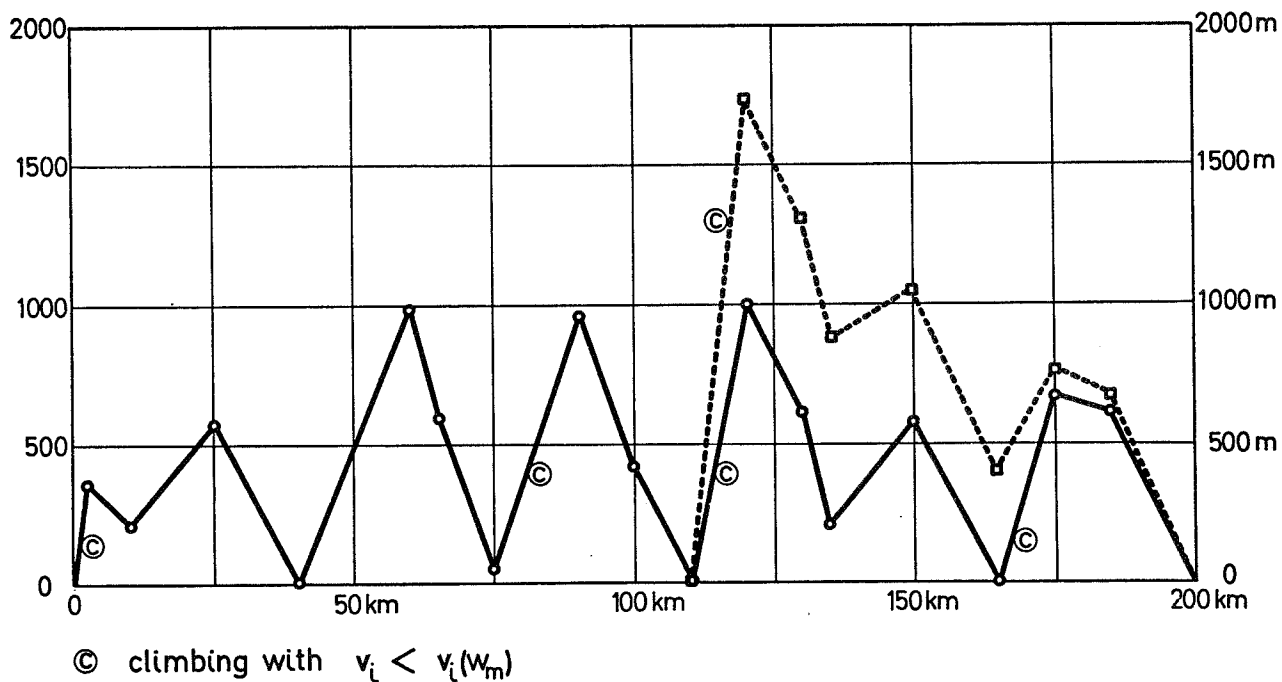


Figure 10.- Optimal solution for flight III.

Page intentionally left blank

BALANCE TRAINING OF THE EQUILIBRIUM ORGAN AND ITS
EFFECT ON FLIGHT STRATEGY

K. -D. Eikemeier^{*†§}, H. -D. Melzig^{*},
N. Reicke[†], W. Schmidt[†]

† Medizinische Hochschule Hannover

§ Akademische Fliegergruppe Hannover

* DFVLR, Institut für Flugmechanik, Braunschweig

INTRODUCTION

It is known that sailors, rope dancers, ballet dancers and astronauts have trained their sense of equilibrium.

The question is whether the glider pilot by his long-duration circling in thermals has also acquired a training of his equilibrium sense. More than the motor pilot with his long straight flights, the glider pilot's equilibrium sense is severely taxed by the simultaneously performed circling and steady observing of instruments and the aerial region.

To investigate this, an experimental program was conducted with the pendular platform of the Oto-Rhino-Laryngology Clinic, which was developed for the investigation of disturbances of the equilibrium.

EXPERIMENT 1

The test person was standing upright and free on the pendular platform which was oscillating in a sinusoidal pattern around the vertical axis with various angular accelerations from 17 to 520 degrees/sec².

The arms were crossed over the chest, the eyes blindfolded and the ears covered with noise protection capsules to eliminate the visual and acoustic spatial orientation (fig. 1).

The oscillation of the body, which deviates from the oscillation of the platform due to the stato-motoric counter regulation, was picked up by a potentiometer and recorded to an oscillograph, together with the signal from the oscillation of the platform.

The principle of measurement is based on the physiological and neuro-anatomical process. The nervus vestibularis from the equilibrium organ

cooperates with the nerves from eyes, cerebellum, tractus vestibulospinalis and reflection circuits from the muscle and ligament spindle, for instance from neck and legs (fig. 2).

RESULTS 1

The first experiment investigated short-term training. It lasted for 20 minutes with an angular acceleration of 415 degrees/sec². The amplitude of the body oscillation decreased in the beginning and increased again later on (fig. 3). Since the absolute height of the amplitude is different due to the different mass of inertia of the test persons, only the relative changes were correlated.

The enveloping curves of 10 glider pilots were compared by setting the minima to a base line (fig. 4).

The training's effect, which is the adaptation of the test person to the oscillating angular acceleration, can be seen from the envelope. It decreases steeply in the first minutes, flattens off later and arrives at its minimum after about 14 minutes. Thereafter it increases again steeply and the test person arrives at his fall-down threshold where he avoids falling by gripping hold with his hands.

The reason for the flattening is the overlapping of muscle and other fatigue over the training effect.

In the first minutes we see a linear decrease of the envelope which would reach a training maximum of 100% after $4,3 \pm 1$ minutes.

CONCLUSIONS 1

For the practice we can draw the following conclusions:

1. About $4,3 \pm 1$ minutes after entrance in a thermal in circling flight, the pilot has reached the maximum adaptation of his equilibrium sense to the changing accelerations.

For 10 minutes more we see an optimal disposition to changing accelerations. During this time he should be capable of utilizing the thermal best. Later fatigue effects are superimposing and it should be recommended that he flies straight for awhile to recover.

2. The glider student with 5 minute start and landing flights does not acquire reasonable training of his equilibrium to acceleration. To give him this training, the instructor of glider students should include thermal flights at an early stage.
3. We know from accident statistics that prior to outfield landings the pilot tries to work thermals by performing steep turns in low altitude. At that

time his equilibrium sense by the long-duration straight flight is disoriented when he suddenly enters curved flight conditions, and he needs about 4 minutes again to adapt to the changing accelerations.

After he has begun circling, the pilot imagines that the speed of his straight flight still exists and he begins to pull for optimum ascent speed. In reality by turbulent air and by changing lift the critical speed is already reached.

This phenomenon can be studied in an acceleration disorientation chamber in which the pilot is moving in a circular path while he is accelerated in different directions.

EXPERIMENT 2

In the second experiment the long-term training effect was investigated on 35 glider pilots. The test person was placed on a scale, standing once on the tips of the toes and once on the heels (fig. 5). Eyes and ears were covered again. The attempts to regulate the equilibrium caused a change in force on the scale which was recorded by means of force transducers on an oscillograph (fig. 6).

After this test the pilot was placed on the pendular platform for 24 minutes. The eyes had to be opened and closed according to a predetermined scheme (fig. 7). The angular acceleration was raised step by step with breaks of the oscillations between each change. After this oscillating test the pilot was placed on the scale again.

RESULTS 2

It can be seen that amplitude and frequency have decreased compared to the test before the training on the pendulum (fig. 8).

The effect of training correlates with the number of flight hours. All test persons (glider pilots and non-pilots) had a training effect of 20% (fig. 9). After 30 hours a steep increase begins which reaches 70% at 60 hours. Thereafter saturation begins which reaches 95% after 160 hours.

Including the flight experience by plotting the training effect against the total flight hours/years of flying changes the effect. Again the increase starts after 30 hours/year but is much steeper, reaching 80% after 60 hours/year (fig. 10). It can be deduced from these results that a glider pilot who does not fly more than 30 hours per year does not add any gain to his training. Before starting cross country flight at the beginning of the season it would be useful to build up training with 30 flight hours as soon as possible.

After 16 ± 4 years the pilot has arrived at his maximum training. In the investigated group the pilots began their instruction in flying with 19 ± 4 years of age. The effect of training decreases again after 35 ± 4 years of age (figs. 11 and 12). Similar results are known from other disciplines of sports.

CONCLUSIONS 2

The question to be answered after knowing these results was whether it is possible to train the glider pilot on the pendular platform prior to beginning a season. This would be advantageous for the improvement of safety for everybody and of success for the contestants.

Up to now we have only subjective reports from pilots, who felt a positive influence of such a training.

In the summary we can conclude from the second experiment that the effect of training is dependant upon

1. Age
2. Number of years flying
3. Flight hours

BIBLIOGRAPHY

- Cotton, F.S.: The center of gravity in man. Amer. Journ. of Physical Anthropology 18 (1934) 401-405.
- Eikemeier, K. -D.; Schmidt, W.; Reicke, N.: Thermikkreise müssen nicht zum Problem werden. Aerokurier, Oct. 1978.
- Jongkees, L.B.W.: Physiologie und Pathophysiologie des Vestibularorganes. Arch. klin. exp. Ohr-, Nas.- u. Kehlk.-Heilk. 194 (1969) 1 - 110.
- Lyndon B. Johnson Space Center: The Proceedings of the skylab life sciences symposium. Vol. 1 and 2, JSC-09275, NASA TM X-58154, Nov. 1974.
- Osterhammel, P.; Terkildsen, K.; Zilstorff, K.: Vestibular habituation in ballet dancers. Acta oto laryng. 65 (1968), 527 - 532.
- Reicke, N.: Der Pendel-Plattform-Test. Eine neue Untersuchungsmethode bei Gleichgewichtsgestörten. Fortschr. Med. 8 93 (1975) 361 - 364.
- Reicke, N.: The Pendular-Platform Test (P.P.T.). Adv. Oto-Rhino-Laryng., vol. 22, pp. 143-151.
- Rohen, J.W.: Funktionelle Anatomie des Nervensystems. 2. Auflage. Schattauer Verlag Stuttgart-New York (1975).

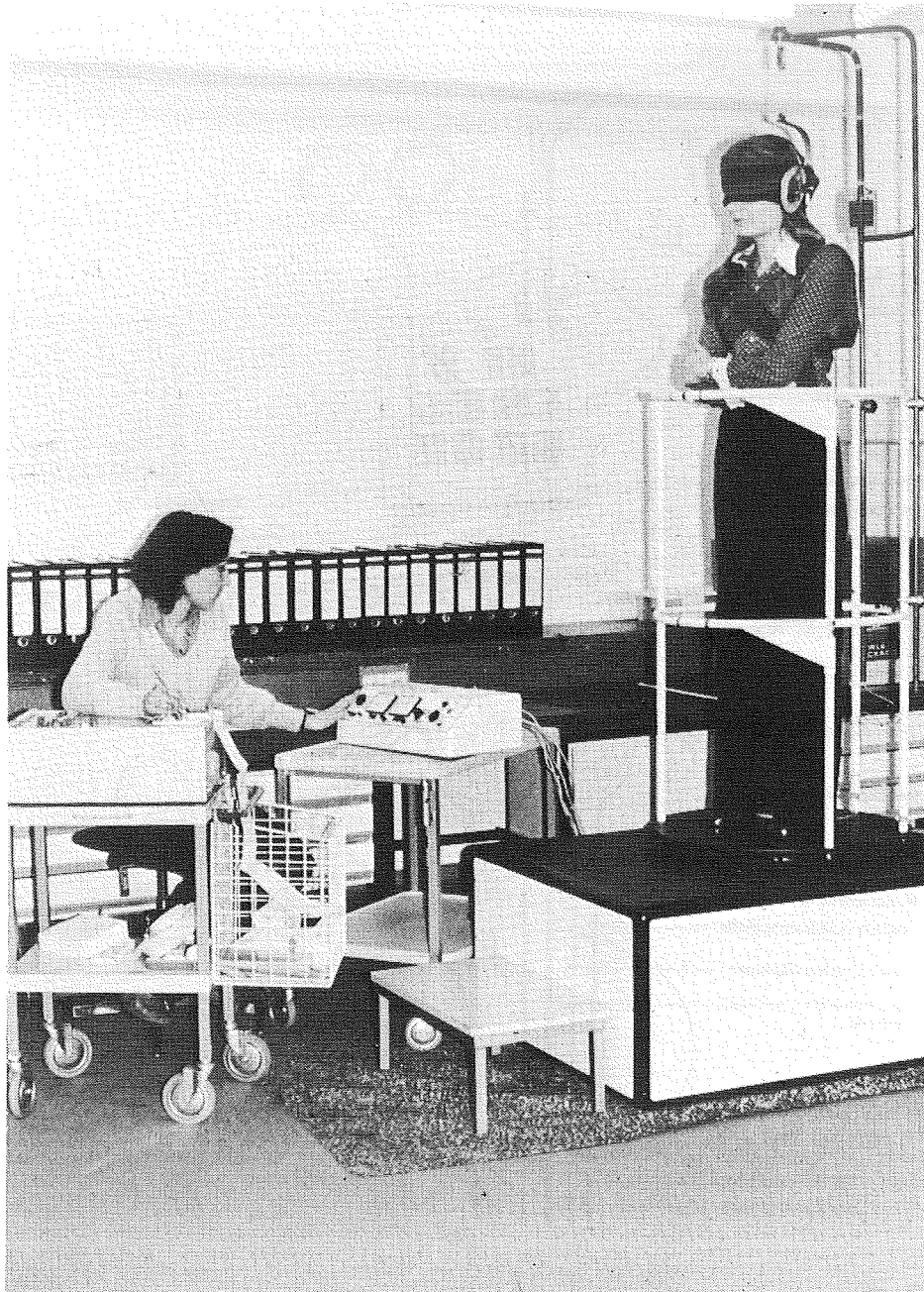


Figure 1.- Pendular platform. The test person is oscillated around the vertical axis with angular accelerations between 17 and 520 deg/sec. Ears and eyes are covered.

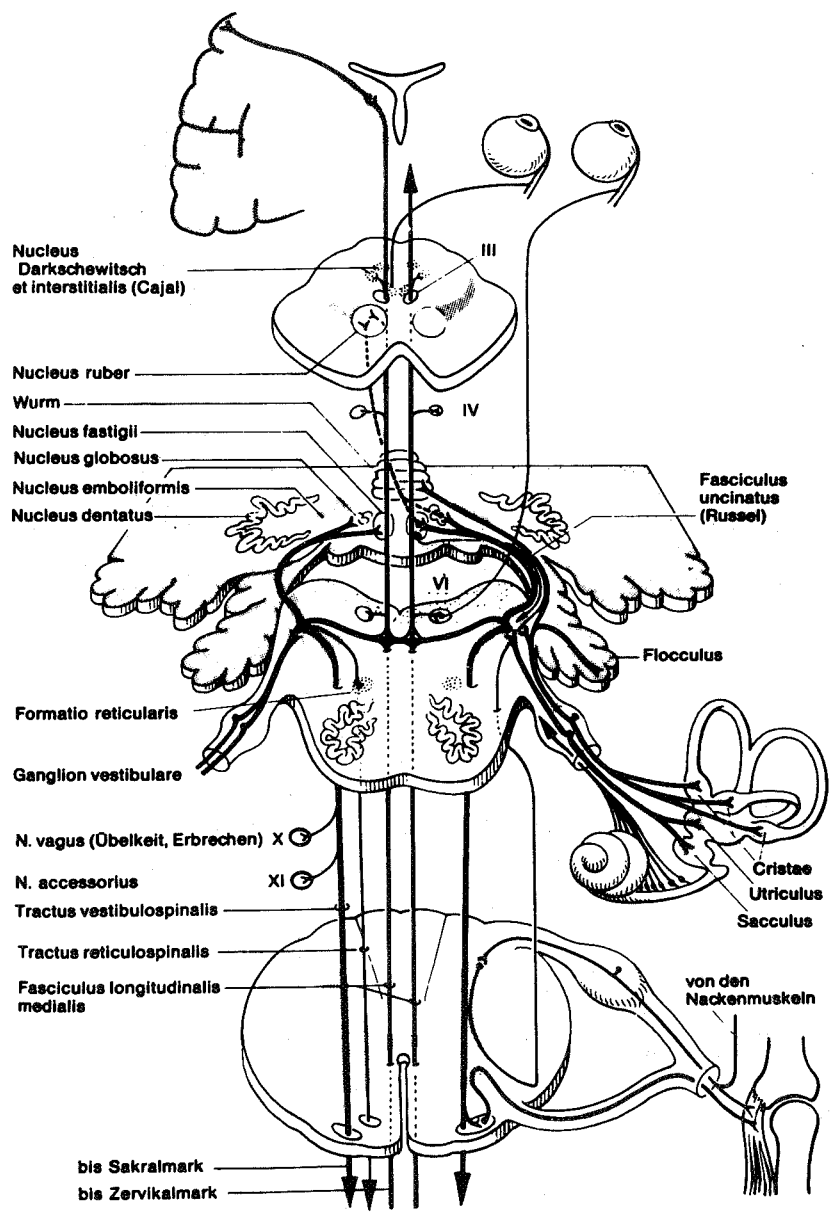


Figure 2.- Combined action of the equilibrium sense nerves.

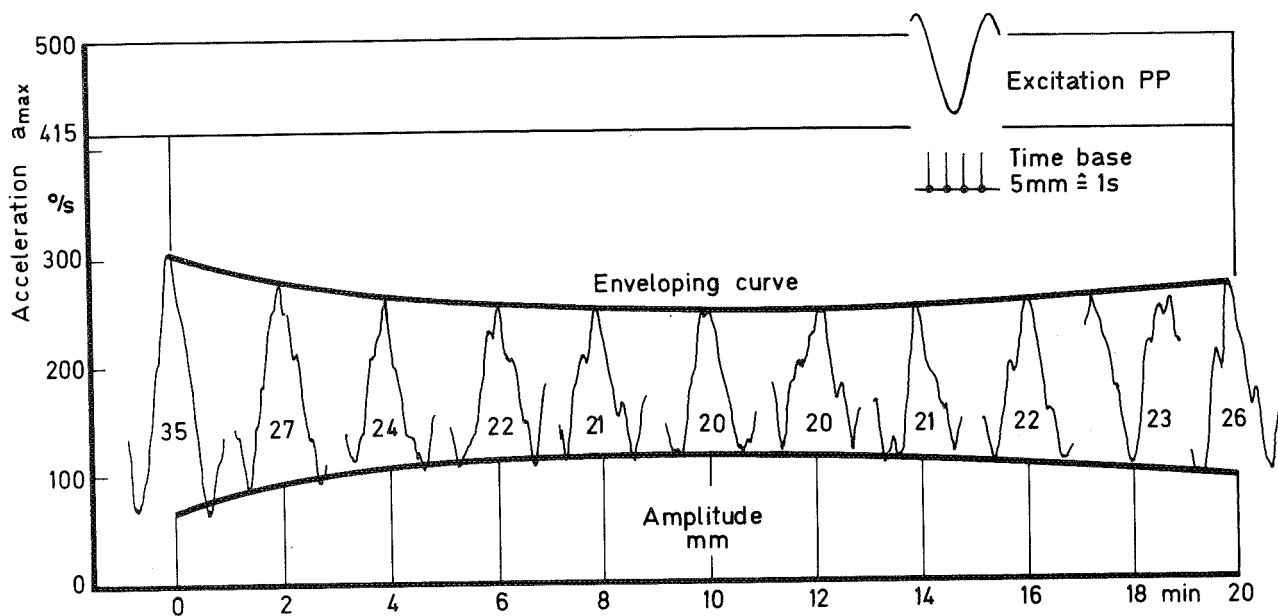


Figure 3.- Time history of amplitude of body oscillation. After a decrease in the beginning it increases again later.

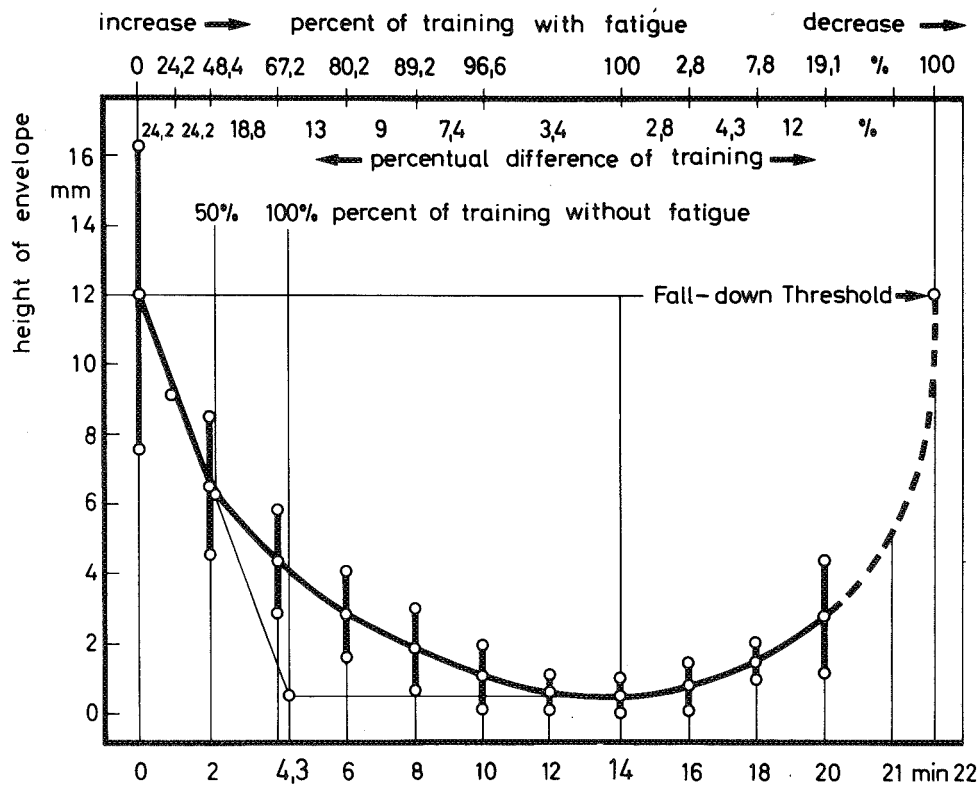


Figure 4.- Envelope of short-term training. It shows 100% effect of training after 4,3 minutes, lasting for 10 more minutes.



Figure 5.- Test person on the scales. She is balancing on toes or heels with covered eyes and ears.

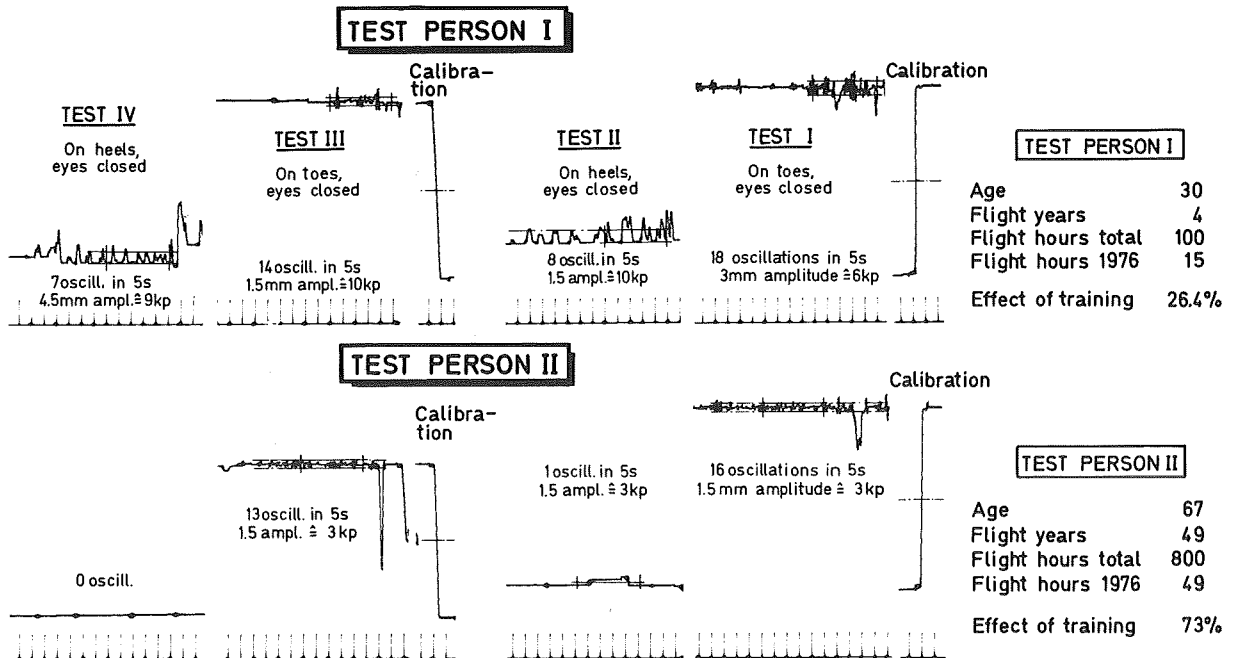
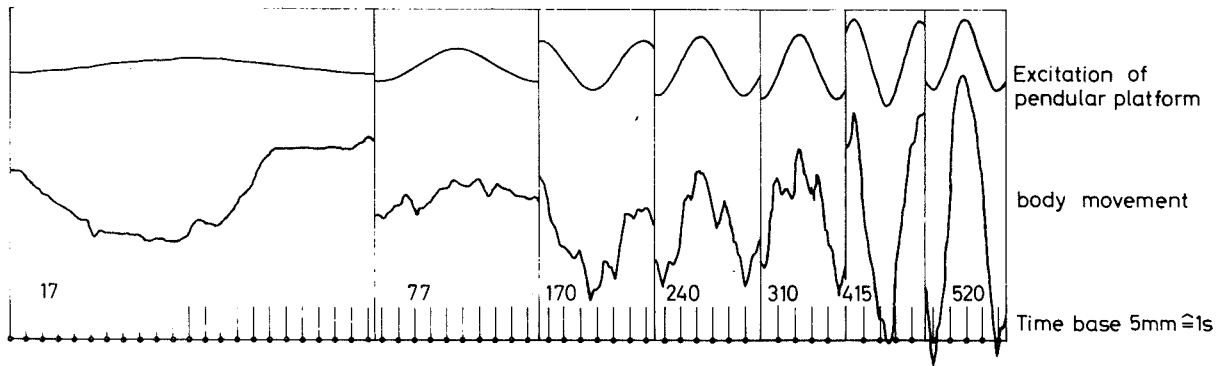
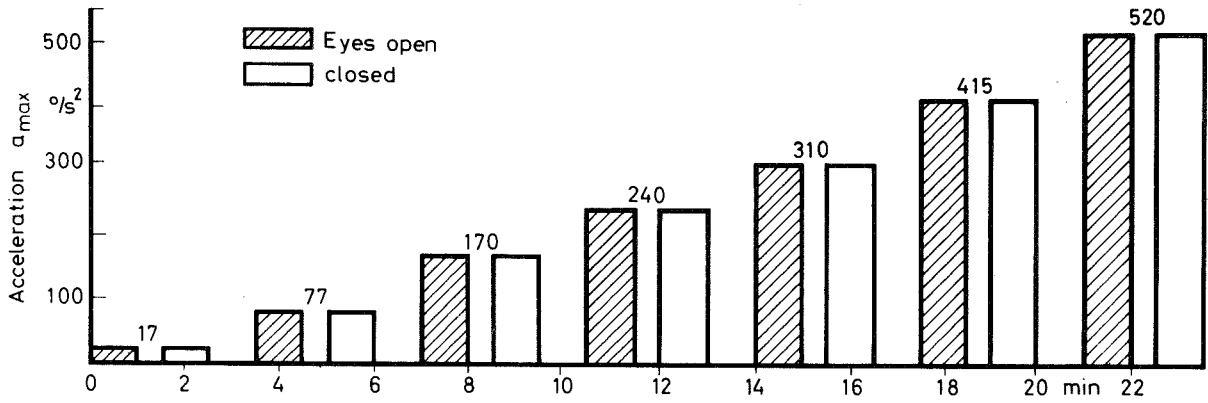


Figure 6.- Long-term training. Original recordings for two different test persons. 1 kilopond (kp) = 9.8 newtons.



SCHEME OF EXCITATION

Figure 7.- Excitation scheme. The equilibrium sense is excited according to this scheme. The eyes are open or closed, the acceleration is raised step by step with breaks between.

FORMULAS

(1) $\left[1 - \frac{\Delta G_{III}}{\Delta G_I} \right] \cdot 100 = TE \text{ [\%]}$ $\frac{III}{I}$ valid for toes

(2) $\left[1 - \frac{n_{III}}{n_I} \right] \cdot 100 = TE \text{ [\%]}$

TE = Effect of training

ΔG = Average amplitude of oscillations during 5 sec
(difference in weight on scale)

n = number of oscillations during 5 sec

For the heels divide $\frac{\Delta G_{IV}}{\Delta G_{II}}$ and $\frac{n_{IV}}{n_{II}}$ accordingly

EXAMPLES

Test-person	T O E S				H E E L S				
	ΔG_I	ΔG_{III}	n_I	n_{III}	$n_{G_{II}}$	$n_{G_{IV}}$	n_{II}	n_{IV}	
I	2,5	1,8	9	12	12	5,4	7	3	TE from (1)or(2)
	28 %		33 % *		55 %		58 %		
II	0	0	1	0	10	0	5	1	TE from (1)or(2)
	100 %		100 %		100 %		80 %		

* measurement error eliminated

Average TE from I = $\frac{28 + 55 + 58}{3} = 47 \%$

Average TE from II = $\frac{100 + 100 + 100 + 80}{4} = 95 \%$

Figure 8.- Calculations, formulas, and examples.

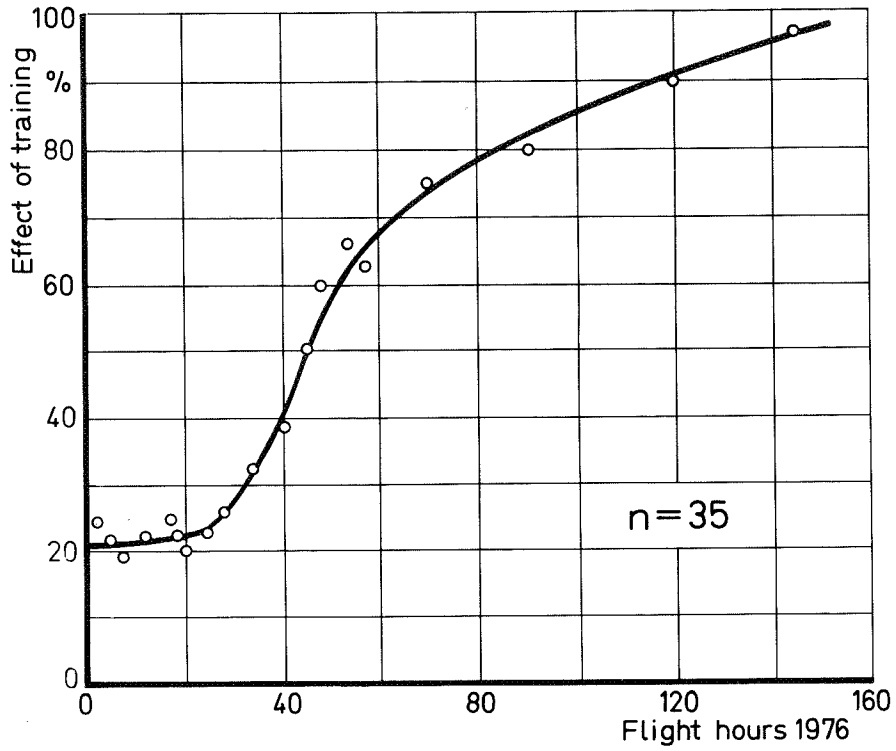


Figure 9.- Effect of training versus flight hours.

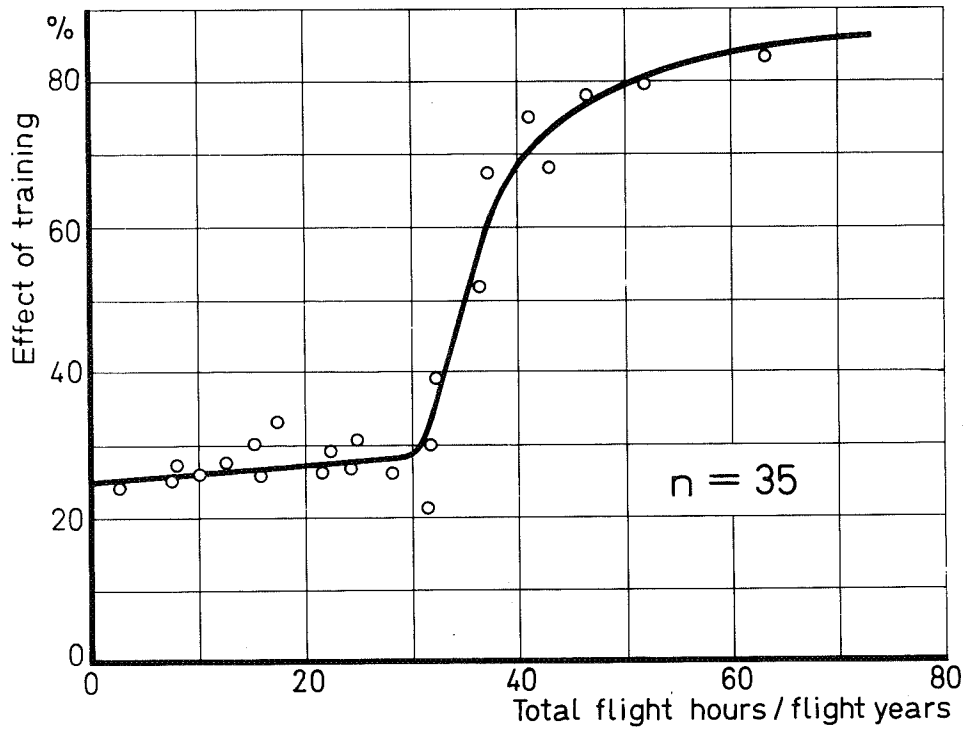


Figure 10.- Effect of training versus average flight hours per year.

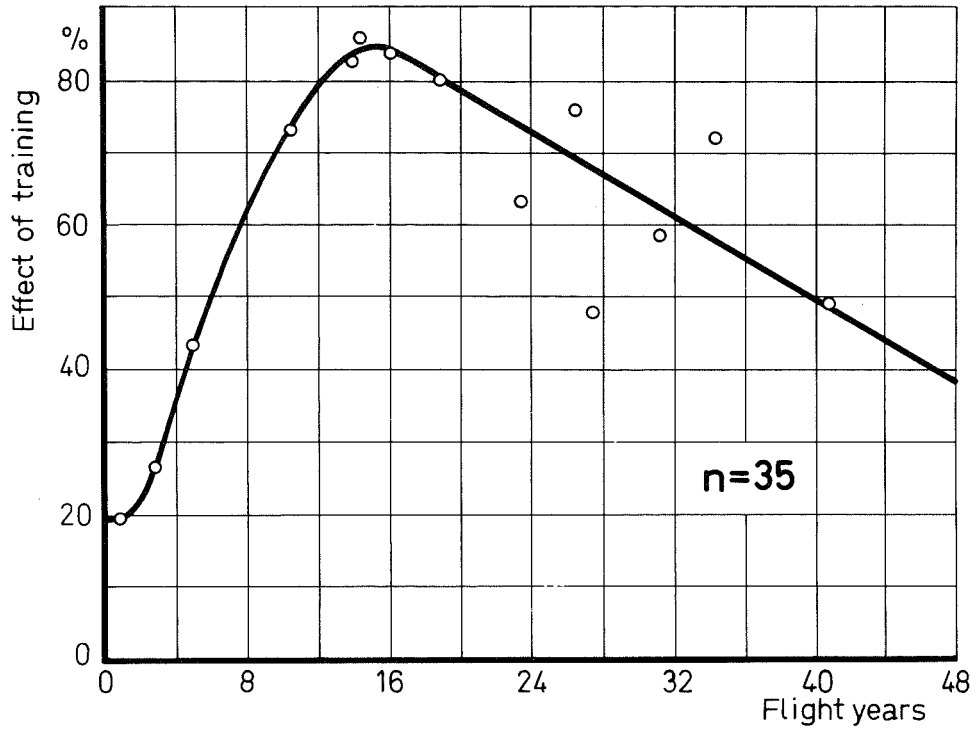


Figure 11.- Effect of training versus flight years.

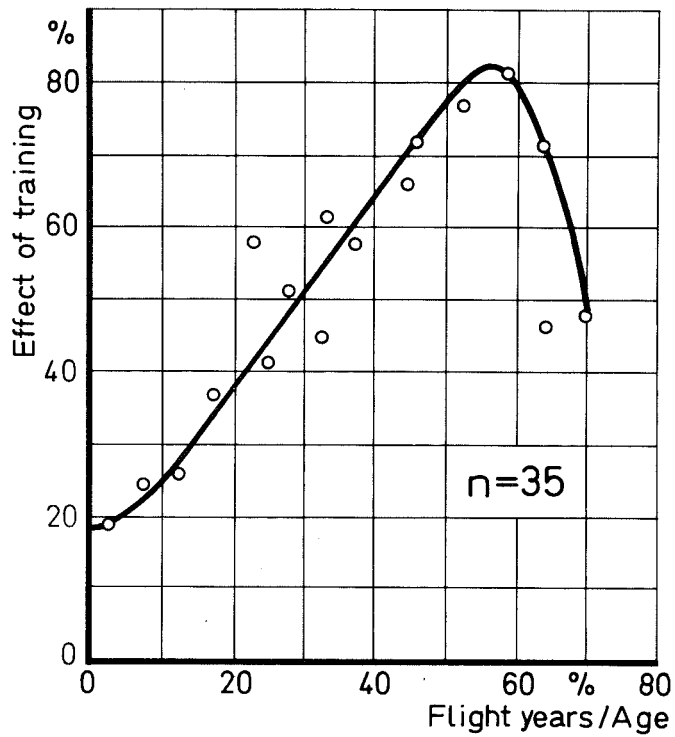


Figure 12.- Effect of training versus age related flight years.

A MONTE CARLO APPROACH TO COMPETITION STRATEGY

Michael P. Teter
Coming Glass Works

The classic MacCready approach to maximize cross-country soaring speeds has many drawbacks. Pilots race to get maximum scores, not to maximize speed over a short length of a course. Maximum scores require a consistently high average cross-country speed, but absolutely no landouts in a typical contest. If a pilot refuses to accept weak lift, he will have a good time almost regardless of the speed at which he flies. This presumes that he will make it around the course, however. Real strategy is not so simple. Variables which must be taken into account other than the strength of the next thermal are the following:

- 1) Height of clouds
- 2) Distance between thermals
- 3) Time of day
- 4) Water ballast
- 5) Present altitude
- 6) Weather changes
- 7) Lift organization
- 8) Distance to goal

This list is neither complete nor arranged in order of importance. Most competition pilots recognize these factors and attempt to take them into account in their decision making. The biggest problem, however, is how to quantitatively make trade-offs between these factors.

In an attempt to model these factors, a three-dimensional model of the atmosphere was created mathematically, and simulated sailplanes were "flown" on hypothetical tasks which consisted of a start, soaring flight to a turn point, soaring flight back, and a final glide to the goal. The solar heating curve was taken into account, and after a trigger temperature was reached, thermals were created at random whose strength varied but depended on the difference between the trigger temperature and the ground temperature. These thermals were created at ground level and had a fixed horizontal and vertical extent. The thermals were of elongated vortex ring type and their typical vertical velocity distribution is shown in figure 1. These thermals ascended at a speed equal to one-half their maximum vertical velocity component in the center of the thermal, yielding several realistic phenomena. The slowing down as the top of the thermal was reached and the dropping out of the bottom of the thermal if one was too low are two such phenomena. A shell of sink surrounded each thermal to make the total vertical movement of air zero. There were four stages in the visible life of the thermal. First they were invisible; second as their tops neared the cloud base, they became wisps. Next, as their centers reached the cloud base, they became mature clouds, and finally as their bottoms reached the cloud base, the clouds began dissipating. These four states of visibility were used for pilot decisions.

Sailplane performance was based on a quadratic polar, and the two constants were taken to be maximum L/D and speed at maximum L/D. Water ballast was taken into account by increasing the speed of maximum L/D as the square root of the wing loading, which affected both cruising speed and circling speed. The thermals were centered as they were encountered,

typically taking two circles to completely center the thermal. The final glide was started whenever the sailplane was within $2/3$ of the maximum glide angle of the final goal, but the sailplane was allowed to climb longer if time could be saved by doing so. On a typical flight, the positions and velocities of the thermals in the atmosphere, as well as those of the sailplane, were updated every second, so that a two hour flight would typically involve 7200 updates of over 100 thermals as well as the position, cruising speed, altitude, and direction of the sailplane.

The two fundamental decisions were whether or not to circle and where to head next. All circling decisions were made by a speed-ring setting, and similarly all cruising speeds through sink or lift were determined by the same setting. The decision about direction was determined by the present state of the visible clouds and the direction to the goal. All clouds were ranked according to their stage of development, distance from the sailplane, and how close they lay to the course line.

A typical day was determined primarily by the thermal strength and the cloud base. Thermal heights were correlated with strengths by using the relationships in Charles Lindsay's pamphlet on soaring meteorology. The number of thermals which were chosen to reside in the area of interest was determined by their spacing which was taken to be $2-1/2$ times their height. The actual positions were determined at random, although in some studies these positions were correlated to form cloud streets. Usually 50 sailplanes were launched through the start gate within 20 minutes of each other, each one having its strategy defined through some speed-ring setting procedure. These flights were scored by using a simple approximation to the rules for

scoring national championships. Basically, the fastest flight got 1000 points, and the rest of the finishers were scored proportionately. Those who landed out got 400 points multiplied by the fraction of the task distance completed. No relights were permitted. Usually 10 days of statistically equivalent weather were flown. This is equivalent, roughly, to one national championship flown to evaluate each strategy in each weather condition.

Several simple results became immediately apparent. First, water ballast should be carried even slightly below the speed break-even point. The reason is that the ability to cruise faster and achieve a greater fraction of the sailplane's maximum glide angle in sinking air increases the chances of completing the task. Second, the sailplane is most vulnerable to landing out when low, and for both speed reasons and greatest completion probability, the first thermal after the gate is critical. A good start enhances the score even more than the time saved since the few hundred feet difference between a good start and a mediocre start can easily be the difference between landing out and completing the course.

To illustrate a particular example, namely, the effect of setting the speed ring, a typical soaring day was chosen. Cloud base was chosen to be 6000 feet, and thermals ranged from 300 to 900 feet per minute with the average being about 600 fpm. The sailplanes were launched from 1:00 to 1:20 p.m. and had speed-ring settings ranging from 60 to 600 fpm. This was done for 10 days in which the detailed thermal locations, radii, strengths, and heights were shuffled, but on average the conditions remained the same. A 100 mile out-and-return task was flown. The effect of speed-ring setting on time to complete the task is shown in figure 2. The bars represent one standard deviation on the times. One conclusion is obvious: the higher the

setting, the faster the speed. The conclusion, however, that the way to win is to fly fast and accept only great lift is erroneous. The reason is shown in figure 3. The percent of task completions drops off rapidly with a ring setting above 240 fpm. The fundamental trade-off between task completion and speed is obvious. Figure 4 shows that most days were won by pilots who flew with a ring setting of 360 fpm, but the total contest was won by a pilot who flew at a ring setting of 180 fpm. The reason for this is that each of the pilots who flew at higher settings landed out at least once during the 10 days. No one who flew at a ring setting of greater than 500 fpm made it around the course even once. The statistical results shown in figures 2 and 3 were then used to predict the distributions of winners of 1250 separate 1, 5, and 10 day contests made up of 64 pilots. The pilots were split into groups of 8, each group flying at 1 of 8 speed settings ranging from 60 fpm to 480 fpm. Figure 5 shows the results. In general, the longer the contest, the more conservative the winner. This is in keeping with the words of George Moffat who felt that to win a contest, you must first keep from losing it. The greatest probability of winning a single day lay in a speed-ring setting of 420 fpm, but the chances of landing out are nearly 80%. For a 5 day contest, the greatest chance of winning came with a ring setting of 300 fpm. This corresponds to most regionals. For a 10 day contest, the greatest probability of winning in this model lies in a setting of 180 fpm. The optimum strategy would lie in that setting which over an infinite amount of time would give the best average. Due to the extremely heavy penalty for landing out, this strategy is conservative. It makes no difference whether a pilot averages 950 over 9 days and lands out once for 200 points, or whether he averages 875 over the 10 day contest by flying

more conservatively. Unfortunately, the optimum long range strategy lies between 800 and 850 points per day which is too little to win a short contest. Basically, to win a championship, whether it be regional or national, a pilot must take risks in excess of optimum long range strategy and have a little luck. The crucial assumption here is that all pilots are equally capable, but that there is an even distribution of conservatism and rashness expressed by a speed-ring setting. In reality, there are many different levels of ability in any single contest and no one flies 80 knots all the way into the ground. Nevertheless in some diluted form, it is felt that the conclusion is valid. One must push and be a little lucky in order to win. The shorter the contest, the harder one must push.

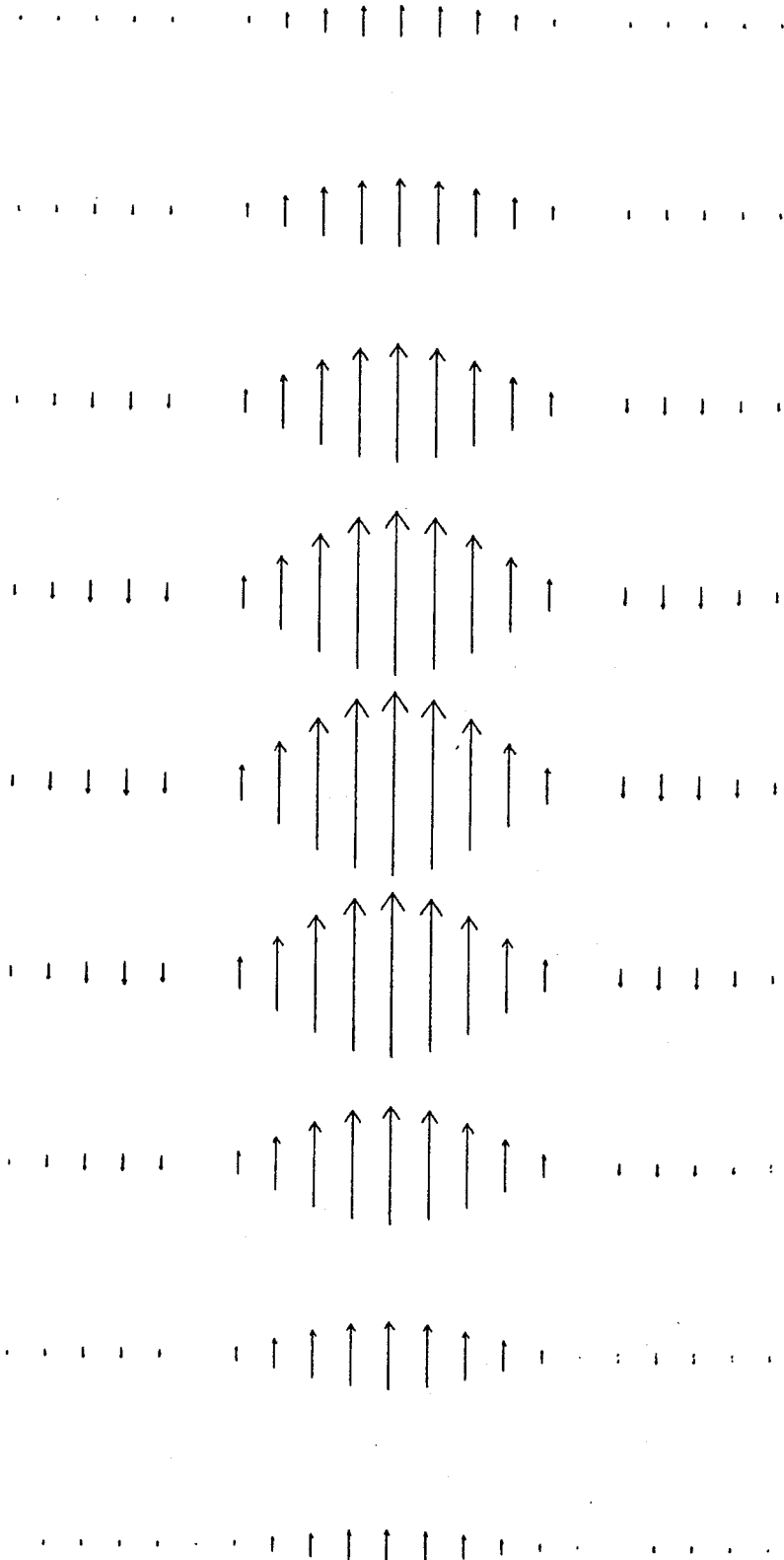


Figure 1.- Thermal structure.

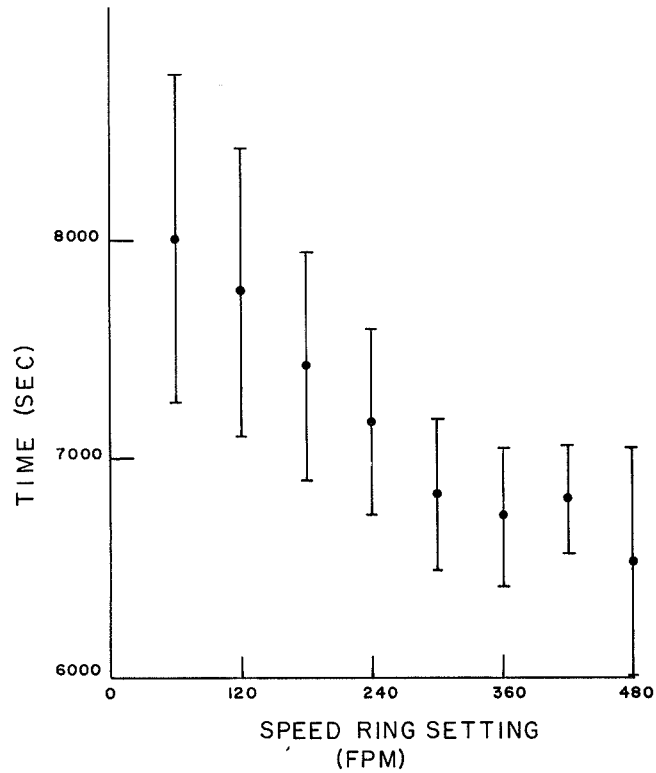


Figure 2.- Effect of speed-ring setting on time to complete the task.

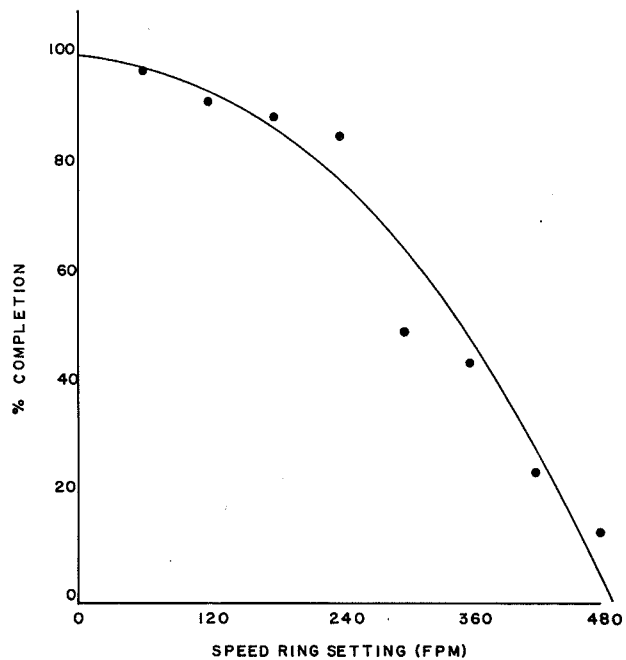


Figure 3.- Trade-off between task completion probability and speed-ring setting.

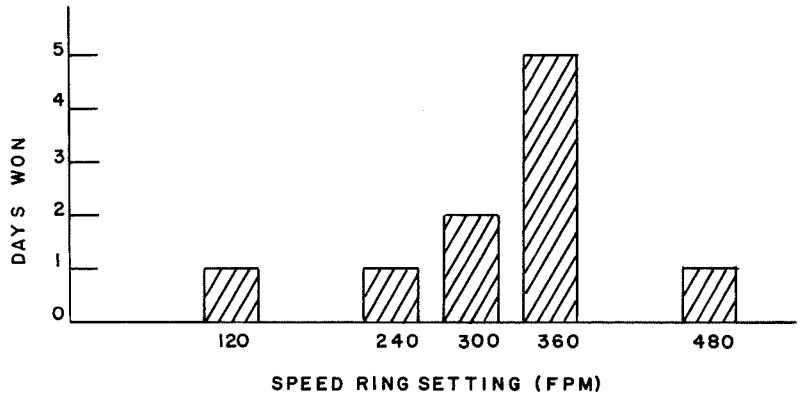


Figure 4.- Effect of speed-ring setting on number of days won.

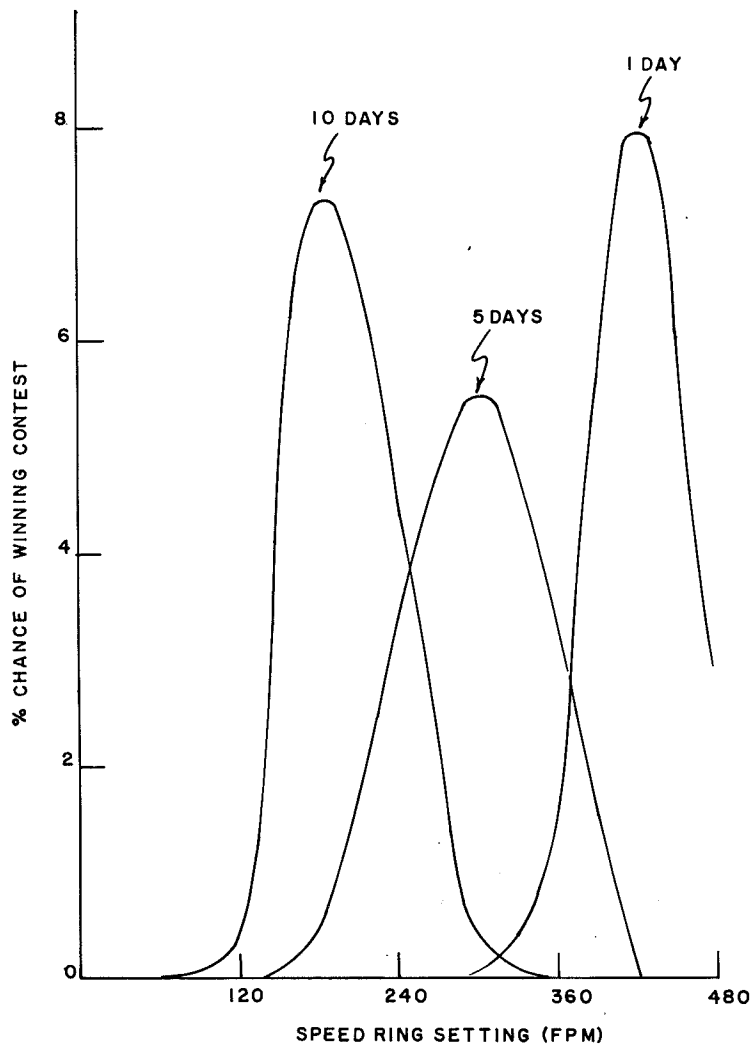


Figure 5.- Effect of speed-ring setting on statistical chance of winning.

Page intentionally left blank

A GENERAL METHOD FOR THE LAYOUT OF AILERONS AND ELEVATORS
OF GLIDERS AND MOTORPLANES

Manfred Hiller
Institute A for Mechanics
University of Stuttgart

SUMMARY

A method is described which allows the layout of the spatial driving mechanism of the aileron for a glider or a motorplane to be performed in a systematic manner. In particular, a prescribed input-output behaviour of the mechanism can be realized by variation of individual parameters of the spatial four-bar mechanisms which constitute the entire driving mechanism. By means of a sensitivity analysis, a systematic choice of parameters is possible. At the same time the forces acting in the mechanism can be limited by imposing maximum values of the forces as secondary conditions during the variation process.

INTRODUCTION

The driving mechanism of the aileron and of the elevator of a glider or a motorplane is realized by a series-connection of spatial four-bar mechanisms, which transfer the movement of the control stick into the movement of the aileron. Generally, the relation between the movements is nonlinear. In the past, the layout of driving mechanisms has been performed mostly by means of the well known graphical techniques for plane mechanisms, treating parts of the spatial mechanism as plane problems. Today, as the driving mechanisms are getting more and more complicated, these techniques are no longer providing satisfying results (refs. 1 and 2).

Replacing the graphical techniques by a numerical method for the optimal layout of spatial transfer mechanisms, a given design can be modified in the desired way. The individual spatial four-bar mechanisms of the train are regarded as transfer elements, which can be treated separately. By means of a steepest descent method, the angular displacement of the stick and the aileron can be adjusted iteratively to a prescribed input-output behaviour. Thereby, individual parameters have to be chosen for variation (ref. 3).

The proposed method has been applied successfully to the layout of the driving mechanism of the aileron for the experimental glider fs-29*, with the desired differentiation of the displacement of the aileron. Two main experi-

* fs-29, an experimental glider with variable wing geometry, developed by the Akademische Fliegergruppe, University of Stuttgart, 1975.

ences showed that some improvements of the method are still necessary:

1. During the variation process, the loads acting in the mechanism may exceed maximum values, particularly if somewhere in the train for a certain position the angle between a crank and the corresponding coupler is either close to zero or close to 180 degrees. Considering prescribed maximum values of the loads as secondary conditions during the variation process, the acting loads can be limited.
2. Primarily, the choice of the parameters to be varied is arbitrary. Submitting the initial values of the geometrical data of the mechanism to a sensitivity analysis, a more systematic choice of the parameters is possible.

OPTIMAL LAYOUT OF SERIES-CONNECTED SPATIAL FOUR-BAR MECHANISMS

In a train of p series-connected spatial four-bar mechanisms, a single spatial four-bar mechanism consists of two rigid cranks \underline{r} and \underline{s} with skewing axes of rotation \underline{u} and \underline{w} , and of the coupler \underline{d} , which is hinged to the cranks (figure 1). The bottoms of the vectors \underline{r} and \underline{s} are connected by the vector \underline{l} . The whole system has only one degree of freedom, and a rotation of the input-crank \underline{r} about an input-angle β produces a unique rotation of the output-crank \underline{s} about the output-angle γ . The rotations of the cranks \underline{r} and \underline{s} can be described by the pairs

$$(\underline{u}, \beta) \tag{1}$$

$$(\underline{w}, \gamma) \tag{2}$$

consisting of the vectors which describe the axes of rotation, and of the rotation angles. With respect to an initial position $\underline{r}_0, \underline{s}_0$ for the rotations of the cranks \underline{r} and \underline{s} , the following homogeneous vector functions are valid:

$$\underline{r} = T(\underline{u}, \beta) \underline{r}_0 \tag{3}$$

$$\underline{s} = U(\underline{w}, \gamma) \underline{s}_0 \tag{4}$$

where $T(\underline{u}, \beta)$ and $U(\underline{w}, \gamma)$ are the tensors of rotations:

$$T(\underline{u}, \beta) = \cos\beta I + (1-\cos\beta)\underline{u}\underline{u} + \sin\beta C \quad (5)$$

$$U(\underline{w}, \gamma) = \cos\gamma I + (1-\cos\gamma)\underline{w}\underline{w} + \sin\gamma D \quad (6)$$

Here, I is the unit matrix, $\underline{u}\underline{u}$ and $\underline{w}\underline{w}$ are the dyadic products of the axis-vectors, while the skew-symmetric matrices C and D are composed by the axis-vectors \underline{u} and \underline{w} . The unchangeable length of the coupler

$$\underline{d}^2 = \underline{d}_0^2 \quad (7)$$

yields the following algebraic equation for the output-angle γ :

$$a\cos\gamma + b\sin\gamma = c \quad (8)$$

with

$$a = (\underline{\ell}-\underline{r})^T (I-\underline{w}\underline{w})\underline{s}_0 \quad (9)$$

$$b = (\underline{\ell}-\underline{r})^T D\underline{s}_0 \quad (10)$$

$$c = a - (\underline{s}_0+\underline{\ell})^T (\underline{r}_0-\underline{r}) \quad (11)$$

Therefore, the output-angle γ is a nonlinear function of the input-angle β , and of the describing vectors \underline{u} , \underline{r} , $\underline{\ell}$, \underline{w} , \underline{s} :

$$\gamma = f(\beta, \underline{u}, \underline{r}, \underline{\ell}, \underline{w}, \underline{s}) \quad (12)$$

By a series-connection of several spatial four-bar mechanisms, a spatial transfer mechanism is realized (figure 2). The j -th four-bar mechanism is described by the vectors

$$\underline{u}_j, \underline{r}_j, \underline{\ell}_j, \underline{w}_j, \underline{s}_j \quad j = 1, \dots, p \quad (13)$$

and by the following correspondence of angles

$$\gamma_j = \beta_{j+1} \quad j = 1, \dots, p \quad (14)$$

The output-angle γ_j is a nonlinear function of the input-angle β_1 and of the vectors given by equation (13):

$$\gamma_j = f(\beta_1, \underline{u}_i, \underline{r}_i, \underline{\ell}_i, \underline{w}_i, \underline{s}_i) \quad \begin{matrix} i = 1, \dots, j \\ j = 1, \dots, p \end{matrix} \quad (15)$$

By variation of a set of arbitrary chosen components of the vectors $\underline{u}_j, \underline{r}_j, \underline{\ell}_j, \underline{w}_j, \underline{s}_j$, the input-output behaviour of the kinematical train can be changed in such a way that to a given number of m input-angle positions β_1 , the output-angles γ_j can be adjusted to prescribed values γ_{sj} . The variation of the parameters follows from a steepest descent method, minimizing iteratively the least-squares error

$$[\underline{y}(\underline{x}) - \underline{y}_s]^T [\underline{y}(\underline{x}) - \underline{y}_s] \quad (16)$$

where the set of parameters is summarized in the parameter-vector \underline{x} of dimension n , the prescribed output-angles in the nominal-value vector \underline{y}_s of dimension m , and the actual output-angles are summarized in the vector \underline{y} .

Due to the r -th iteration step, we have an improvement of the parameter-vector $\underline{x}^{(r-1)}$

$$\underline{x}^{(r)} = \underline{x}^{(r-1)} + \underline{\xi}^{(r)} \quad (17)$$

where the improvement $\underline{\xi}^{(r)}$ is given by the solution of the algebraic equation

$$A^{(r-1)T} A^{(r-1)} \underline{\xi}^{(r)} + A^{(r-1)T} \underline{d}^{(r-1)} = \underline{0} \quad (18)$$

Here, $A^{(r-1)}$ is the Jacobian matrix of partial derivatives of the nominal-value vector with respect to the parameter-vector, during the r -th iteration step. For the vector $\underline{d}^{(r-1)}$,

$$\underline{d}^{(r-1)} = \underline{y}^{(r-1)} - \underline{y}_s \quad (19)$$

The proposed method enables an optimal adjustment of the actual output-angles to the set of prescribed nominal values with respect to the least-squares error, with only few iteration steps necessary for convergence. To make the iteration method applicable, a set of kinematically compatible data at the beginning of the iteration process is required.

EXTENDED METHOD CONSIDERING MAXIMUM LOADS AS SECONDARY CONDITIONS

Regarding only slow motions of the transfer mechanism, the inertial forces of the system may be neglected, and the loads acting in the hinges and the bearings can be calculated statically. Furthermore, in real systems the dead loads of the cranks and the couplers may be neglected, because they are small in comparison to the acting forces. The hinged articulations between the cranks and the couplers are regarded as ideal constraints, and consequently the coupler forces are directed along the coupler itself.

Cutting the j -th four-bar mechanism in a train of p series-connected spatial four-bar mechanisms, the coupler force of the preceding four-bar mechanism acts as an input-load, whereas the output-load is the coupler force of the succeeding four-bar mechanism. Thus, we have a propagating flux of forces passing through the whole train (figure 3). For the coupler force of the j -th four-bar mechanism, we obtain

$$\underline{f}_{r,j} = \frac{\underline{f}_{s,j-1} (\underline{s}_{j-1} \times \underline{d}_{j-1}) \cdot \underline{w}_{j-1}}{\underline{d}_{j-1} (\underline{d}_j \times \underline{r}_j) \cdot \underline{u}_j} \underline{d}_j \quad (20)$$

which is a function of the coupler force of the preceding four-bar mechanism, and of the geometrical data of the $(j-1)$ -th and the j -th four-bar mechanism, respectively (see ref. 4). From equation (20) it follows that according to the numerator, the geometry of the preceding four-bar mechanism is responsible for the zeros of the coupler force, while the geometry of the regarded four-bar mechanism is responsible for the poles of the coupler force, according to the denominator.

The engineering design of a spatial transfer mechanism is often characterized by prescribed constraints, which can be either geometrical boundaries due to limitations in the available space, or which can be restrictions for the permissible loads in the mechanism. During the iteration process, these constraints may be violated, due to the variation of the parameters. Considering the constraints as secondary conditions in the iteration method, this can be avoided. In case of permissible loads, the corresponding secondary conditions are inequalities which have to be considered in a specific way. In the following, the restriction of the coupler force which is of most importance will be discussed in more detail.

Generally, the coupler force, designated as \underline{f}_j , is a nonlinear function of the input-angle β_1 , and of the describing vectors of the four-bar mechanisms, according to equation(20):

$$\underline{f}_j = \underline{f}_j(\beta_1, \underline{u}_i, \underline{r}_i, \underline{l}_i, \underline{w}_i, \underline{s}_i) \quad \begin{matrix} i = 1, \dots, j \\ j = 1, \dots, p \end{matrix} \quad (21)$$

During the iteration process, the coupler forces will change, due to the variation of the designated parameters. If the residual components of the describing vectors are regarded to be constant, the coupler force depends only on the input-angle β_1 , and on the parameter-vector \underline{x} :

$$\underline{f}_j = \underline{f}_j(\beta_1, \underline{x}) \quad j = 1, \dots, p \quad (22)$$

Now, it may happen that individual coupler forces exceed maximum values for certain positions of the train, particularly if somewhere in the train the angle between a crank and the corresponding coupler is either close to zero or close to 180 degrees. Thereby, only the magnitude of the coupler force is of interest, for its direction is given by the direction of the coupler. Furthermore, compressive forces are more important than tension forces. If f_{j0} is the permissible value of the j -th coupler force, the difference between the actual and the permissible force is given by

$$g_j(\beta_1, \underline{x}) = f_j(\beta_1, \underline{x}) - f_{j0} \quad j = 1, \dots, p \quad (23)$$

and the following secondary condition is valid:

$$g_j(\beta_1, \underline{x}) \leq 0 \quad j = 1, \dots, p \quad (24)$$

Hence, the iteration method may be split into two parts. As long as equation (24) is not violated, the iteration process operates in the way described above. The r -th iteration step is given by equation (17):

$$\underline{x}^{(r)} = \underline{x}^{(r-1)} + \underline{\xi}^{(r)}$$

If equation (24) is violated during the r -th iteration step for at least one index j (input-angle β_1 fixed), we have

$$g_j(\beta_1, \underline{x}) > 0 \quad j \in \{1, \dots, p\} \quad (25)$$

Consequently, the parameter-vector $\underline{x}^{(r)}$ has to be corrected. In a first step, the intersection point \underline{x}_s of the corrective vector $\underline{\xi}^{(r)}$ with the surface of separation $g_j(\beta_1, \underline{x})=0$ has to be determined. In a second step, the vector $\underline{\xi}^{(r)}$ can be separated in two components:

$$\underline{\xi}_1^{(r)} = \underline{x}_s - \underline{x}^{(r-1)} \quad (26)$$

$$\underline{\xi}_2^{(r)} = \underline{x}^{(r)} - \underline{x}_S \quad (27)$$

Then, the component $\underline{\xi}_2^{(r)}$ has to be projected into the tangential plane of the surface $g_j(\beta_1, \underline{x})=0$, at point \underline{x}_S . Thus, we have the new corrective vector for the r -th iteration step (figure 4):

$$\underline{x}'^{(r)} = \underline{x}^{(r-1)} + \underline{\xi}_1^{(r)} + \underline{\xi}_{2t}^{(r)} \quad (28)$$

which is the most favorable correction referring to the secondary condition (24). If

$$g_j(\beta_1, \underline{x}'^{(r)}) < 0 \quad j = 1, \dots, p \quad (29)$$

the iteration process continues with the next step. If, on the other hand

$$g_j(\beta_1, \underline{x}'^{(r)}) > 0 \quad j \in \{1, \dots, p\} \quad (30)$$

the vector $\underline{x}'^{(r)}$ has to be corrected again. Starting from point $\underline{x}'^{(r)}$, and proceeding against the gradient $\partial g_j(\beta_1, \underline{x})/\partial \underline{x}$, we arrive after the second correction at point $\underline{x}''^{(r)}$, for which

$$g_j(\beta_1, \underline{x}''^{(r)}) \leq 0 \quad j = 1, \dots, p \quad (31)$$

is valid (figure 5), and the iteration process will be continued with the next step. By means of the described correcting procedure, the variation of the parameter-vector \underline{x} occurs in the neighbourhood of the surface of separation

$$g_j(\beta_1, \underline{x}) = 0 \quad j = 1, \dots, p \quad (32)$$

if the secondary condition (24) is violated. Until now, the input-angle β_1 was assumed to be fixed. Actually, we have an assignment of m input-angles β_1 to m prescribed output-angles γ_j , and consequently, the secondary condition (24) has to be checked for every input-angle position β_1 . In practical cases, the coupler forces will exceed their maximum values only for small domains of angular positions, due to the kinematical reasons mentioned above, so that the secondary condition (24) has to be examined only for individual angular positions.

PARAMETER SENSITIVITY AND CHOICE OF PARAMETERS

Primarily, the choice of the set of parameters for the iteration process is arbitrary. In practical applications, one difficulty arises from the questions, which parameters shall be chosen, and how many parameters shall be varied? As each component of the five vectors

$$\underline{u}_j, \underline{r}_j, \underline{\ell}_j, \underline{w}_j, \underline{s}_j$$

which describe a spatial four-bar mechanism, may serve as parameters, we have a set of 15 available parameters for every four-bar mechanism. Accordingly, the number of parameters increases in a train of series-connected four-bar mechanisms. By means of a systematic sensitivity analysis applied to the initial data of the train, before starting the iteration, it is possible to get some information about the kinematical behaviour with respect to variations of individual components of the vectors involved.

Designating the indicated four-bar mechanism with index-number j_0 , where the changed vectors are

$$\hat{\underline{u}}_{j_0}, \hat{\underline{r}}_{j_0}, \hat{\underline{\ell}}_{j_0}, \hat{\underline{w}}_{j_0}, \hat{\underline{s}}_{j_0} \quad (33)$$

the output-angles of the train are given on the one hand by

$$\gamma_j = f(\beta_1, \underline{u}_i, \underline{r}_i, \underline{\ell}_i, \underline{w}_i, \underline{s}_i) \quad \begin{array}{l} i = 1, \dots, j \\ j = 1, \dots, j_0 - 1 \end{array} \quad (34)$$

and on the other hand by the new values

$$\hat{\gamma}_{j_0} = f(\beta_1, \hat{\underline{u}}_{j_0}, \hat{\underline{r}}_{j_0}, \hat{\underline{\ell}}_{j_0}, \hat{\underline{w}}_{j_0}, \hat{\underline{s}}_{j_0}) \quad (35)$$

$$\hat{\gamma}_j = f(\beta_1, \underline{u}_i, \underline{r}_i, \underline{\ell}_i, \underline{w}_i, \underline{s}_i) \quad \begin{array}{l} i = j_0 + 1, \dots, j \\ j = j_0 + 1, \dots, p \end{array} \quad (36)$$

Thus, the changed vectors (equation (33)) are not only influencing the transfer behaviour of the four-bar mechanism with index-number j_0 , but also the behaviour of all subsequent four-bar mechanisms, while the preceding four-bar mechanisms remain unchanged.

The difference

$$\Delta\gamma_j = \hat{\gamma}_j - \gamma_j \quad j = j_0, \dots, p \quad (37)$$

serves as a measure for the sensitivity of the transfer behaviour of the kinematical train against changes in its vectors.

For a complete sensitivity analysis, it is necessary to examine the influence of the individual components separately. Moreover, the vector components have to be changed in the same way, to enable the comparison between different sensitivities. Among the different possibilities of changing the vector components, the method where the ratio of change remains constant has proved to be the most successful. If in a certain vector one component is equal to zero, another component which is not equal to zero serves as reference value. The difference angle $\Delta\gamma_j$ is plotted versus the input-angle β_1 , and for the j -th and all subsequent four-bar mechanisms we have a family of 15 curves each, which are representing the sensitivity of the j -th four-bar mechanism. By means of the plotted curves, a more systematic choice of the parameters for the variation process is possible.

The sensitivity analysis has been performed on the basis of the initial data of the kinematical train. During the iteration process, the sensitivities of the selected parameters, as well as the sensitivities of the residual components involved will change, because of their nonlinear interdependence. Therefore, it is suitable to subject the whole system to another sensitivity analysis at the end of the iteration process. It might also be taken into consideration to control the sensitivity of the system during the iteration process, but the required numerical effort is considerable.

The advantages of the proposed sensitivity analysis consist not only in a more systematic choice of parameters for the optimal layout of the transfer mechanism, but at the same time it enables an estimation of the deviations in the transfer behaviour, which arise from manufacturing defects or from bearing play in the hinges.

PROGRAM SYSTEM

For application, a sophisticated and user-oriented program system has been developed, the more important aspects of which are:

1. The determination of the kinematical transfer behaviour and of the range of kinematical compatibility of the train, by a stepwise change of the input-angle β_1 .
2. The determination of the transfer behaviour of the coupler forces for a given input load, by a stepwise change of the input-angle β_1 .

3. The determination of the output-angles and of the coupler forces, as well as the influences caused by the changes of parameters.
4. A systematic analysis of the individual four-bar mechanisms, concerning domains of kinematical compatibility and poles in the coupler forces, as well as angular positions, for which the train becomes unstable.
5. A systematic sensitivity analysis of the kinematical train, which enables on the one side a systematic choice of parameters for variation, and which provides on the other side information about the influence of inaccuracies on the transfer behaviour of the train.

APPLICATIONS

In the following, the application of the described method to the driving mechanism of the aileron for the glider fs-29 will be discussed in more detail. The fs-29 is an experimental glider developed at the University of Stuttgart. Due to telescoping wings, the wing span of the glider can be varied during flight. The driving mechanism of the aileron consists of 10 series-connected spatial four-bar mechanisms. By means of the variation method in its original version, the driving mechanism has been laid out successfully, assigning desired aileron deflections to given stick positions. But a large number of computer runs were necessary, trying various sets of parameters (consisting of 2 or 3 parameters). The parameters were components of the cranks \underline{r}_j and \underline{s}_j in the neighbourhood of the aileron. Flight tests showed that for certain positions of the mechanism the coupler forces exceeded permissible values. By application of the extended variation method, these disadvantages can be avoided.

The numbering of the series-connected four-bar mechanisms starts with the stick, as the input-movement of the stick produces the output-movement of the aileron. Table 1 shows the initial data of the driving mechanism (all distances in meters). The data of the involved four-bar mechanisms (except the four-bar mechanisms 8, 9, 10) are given in the same cartesian coordinate system: x-axis \equiv axis of pitch, y-axis \equiv axis of yaw, z-axis \equiv axis of roll. The required four assignments of stick position to aileron deflection are shown in table 2. The transfer behaviour of the coupler forces will be tested by a unit input-load acting on the stick. Figure 6 and figure 7 show the input-output behaviour of the individual four-bar mechanisms as a function of the stick deflection β_1 . Before starting the variation process, a sensitivity analysis for the four-bar mechanisms 7, 8, 9, and 10 has been performed. The sensitivities of the cranks \underline{r}_9 , \underline{s}_9 , and \underline{r}_{10} , \underline{s}_{10} , respectively, are shown in figure 8 and figure 9. (The influence of \underline{r}_9 , \underline{s}_9 on four-bar mechanism 10 is not displayed.) Satisfactory optimization results are obtained by combinations of parameters with high and low sensitivity, from which the parameter combina-

tion $r_{9,1}$, $r_{10,1}$ has been selected. Here, $r_{9,1}$ and $r_{10,1}$ are the x-components of the cranks \underline{r}_9 and \underline{r}_{10} , respectively.

The behaviour of the aileron deflection γ_{10} as a function of the stick position β_1 is shown in figure 11. The approximation of the prescribed values of table 2 is within an accuracy of 0.6 degrees. (The curve $\gamma_9(\beta_1)$ is given by figure 10.) Due to the variation process, the coupler force f_9 has completely changed its behaviour (see figure 12). However, the maximum values can be considerably reduced by prescribing maximum limiting values of the coupler forces as secondary conditions, as shown in figure 13. In this case, the accuracy of the required assignment is reduced, but still sufficient.

During flight, the input-output displacement propagates from the stick to the aileron, whereas, looking to the forces, the aerodynamic forces on the aileron are the input-loads, which have to be balanced by the pilot through the stick. In this case, the application of the variation method gets more complicated, because the transfer mechanism has to be investigated in both directions (see ref. 4). Figure 14 shows an example, where critical values of the coupler force in the seventh four-bar mechanism have been reduced. The input-load at the aileron has been the constant moment $\underline{m}_A = (23.34, 0, 0)$ [Nm].

CONCLUSIONS

The layout of spatial transfer-mechanisms consisting of series-connected spatial four-bar mechanisms can be performed more effectively if the graphical techniques are replaced by a numerical method. Within this method, the individual four-bar mechanisms are treated analytically as transfer elements. By variation of selected parameters, the input-output behaviour of the train can be adjusted to prescribed values. The acting loads in the mechanism can be limited, considering maximum values of the loads as secondary conditions during the variation process. The effectiveness of the proposed method has been demonstrated at the layout of the driving mechanism for the aileron of a glider.

REFERENCES

1. Beyer, R.: Technische Kinematik. Ambrosius-Verlag, Leipzig, 1931.
2. Hall, A. S.: Kinematics and Linkage Design. Prentice-Hall, Englewood Cliffs, N.J., 1961.
3. Eppler, R.; Hiller, M.: Numerische Behandlung von Gelenkvierecken mit vorge-schriebenem Ausgang. DLR-Forschungsbericht 75-132, pp. 53-66, 1975.
4. Hiller, M.: Ein Verfahren zur optimalen Auslegung von mechanischen Ruderan-trieben bei Segelflugzeugen und Motorsportflugzeugen. Zeitschrift für Flug-wissenschaften und Weltraumforschung (ZFW), May 1979.

TABLE 1.- INITIAL DATA OF AILERON DRIVING MECHANISM
OF THE EXPERIMENTAL GLIDER, fs-29

four-bar mechanism	\underline{r}_j [m]	\underline{u}_j	$\underline{\ell}_j$ [m]	\underline{s}_j [m]	\underline{w}_j
1	0.0000 0.0430 0.0150	0.0000 -0.0190 0.2000	0.1250 0.0400 -0.0450	0.0000 -0.0062 0.0596	0.0000 -0.3875 -0.0400
2	0.0800 0.0000 0.0000	0.0000 -0.3875 -0.0400	0.0000 -0.0200 -0.8810	0.0000 0.0650 -0.0100	1.0000 0.0000 0.0000
3	0.0000 0.0610 -0.0210	1.0000 0.0000 0.0000	0.0000 -0.0960 -0.3820	0.0000 0.0580 0.0060	1.0000 0.0000 0.0000
4	0.0000 0.0400 -0.0430	1.0000 0.0000 0.0000	-0.0060 -0.2430 -0.1490	-0.0800 0.0000 0.0000	0.0000 0.0590 -0.1000
5	0.0000 -0.0690 -0.0400	0.0000 0.5900 -0.1000	3.0600 -0.0570 0.1120	0.0000 -0.0080 0.1350	0.0000 1.0000 0.0000
6	0.0900 -0.0070 -0.0665	0.0000 1.0000 0.0000	0.1150 -0.0510 -0.0090	-0.0250 0.0590 -0.0150	-1.0000 0.0000 0.0000
7	0.0000 0.0420 -0.0270	-1.0000 0.0000 0.0000	0.0000 0.0290 -0.0900	0.0000 -0.0125 0.0480	1.0000 0.0000 0.0000
8	0.0020 -0.0170 0.0470	0.0810 0.0000 -0.0030	-0.0480 0.0220 0.0510	0.0500 0.0000 -0.0015	-0.0030 0.0000 -0.0835
9	0.0220 -0.0490 0.0120	-0.0030 0.0000 -0.0835	0.5860 -0.0200 -0.0640	-0.0480 0.0280 0.0510	0.0000 -1.0000 0.0000
10	0.0400 0.0000 -0.0020	0.0000 1.0000 0.0000	0.0500 0.0400 -0.0740	0.0000 -0.0405 0.0045	-1.0000 0.0000 0.0000

TABLE 2.- INPUT/OUTPUT ANGULAR RELATIONSHIPS FOR STICK
AND AILERON OF fs-29 GLIDER

input-angle at stick	β_1 [°]	-22.1	-12.7	14.1	26.4
output-angle at aileron	γ_{10} [°]	-25.0	-12.6	8.9	15.0

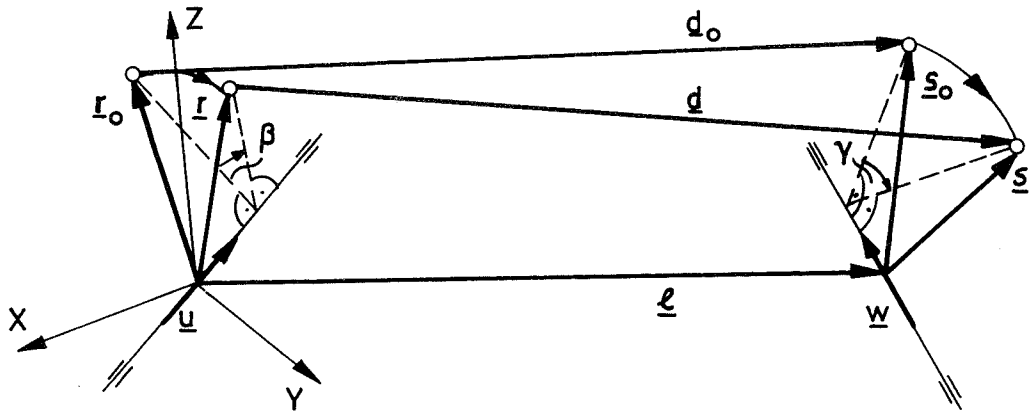


Figure 1: The spatial four-bar mechanism.

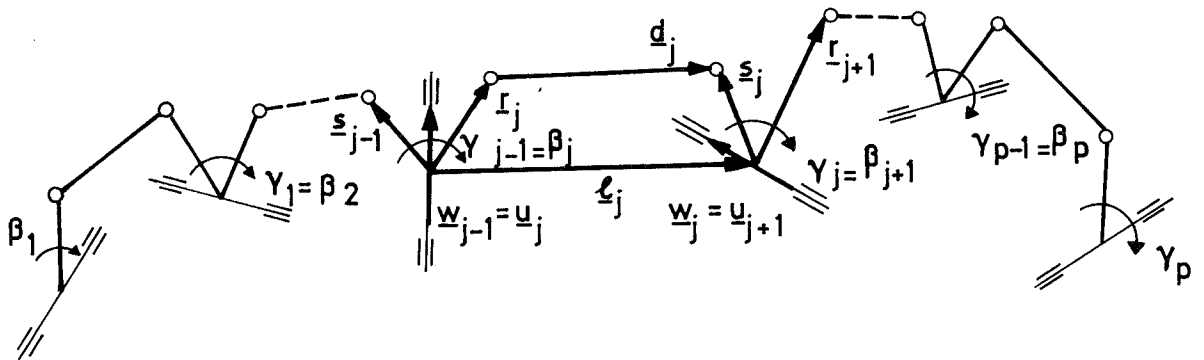


Figure 2: The spatial transfer mechanism.

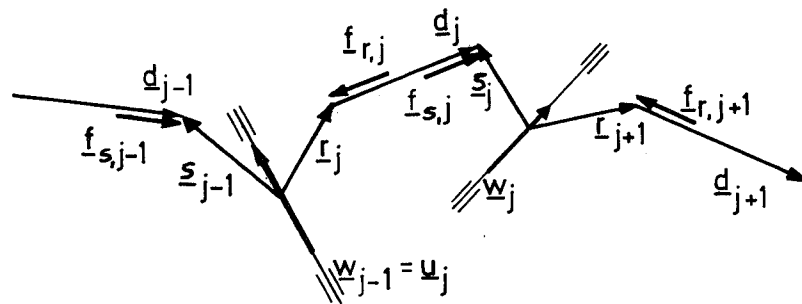


Figure 3: Coupler force.

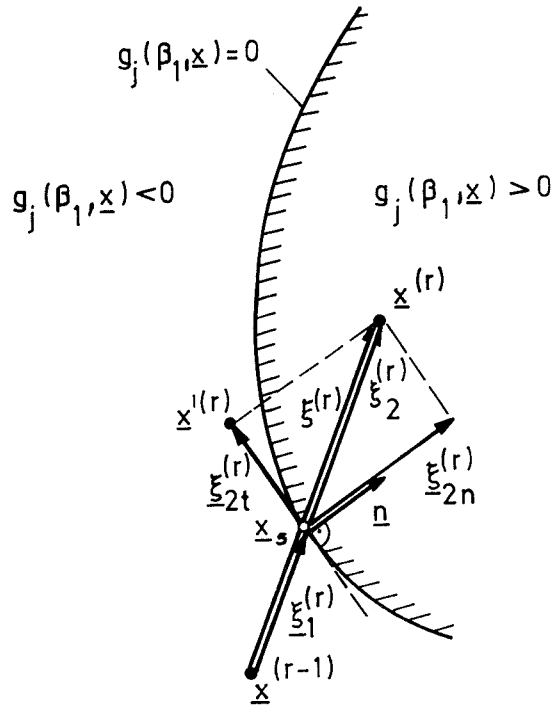


Figure 4: Correction step 1 for secondary condition.

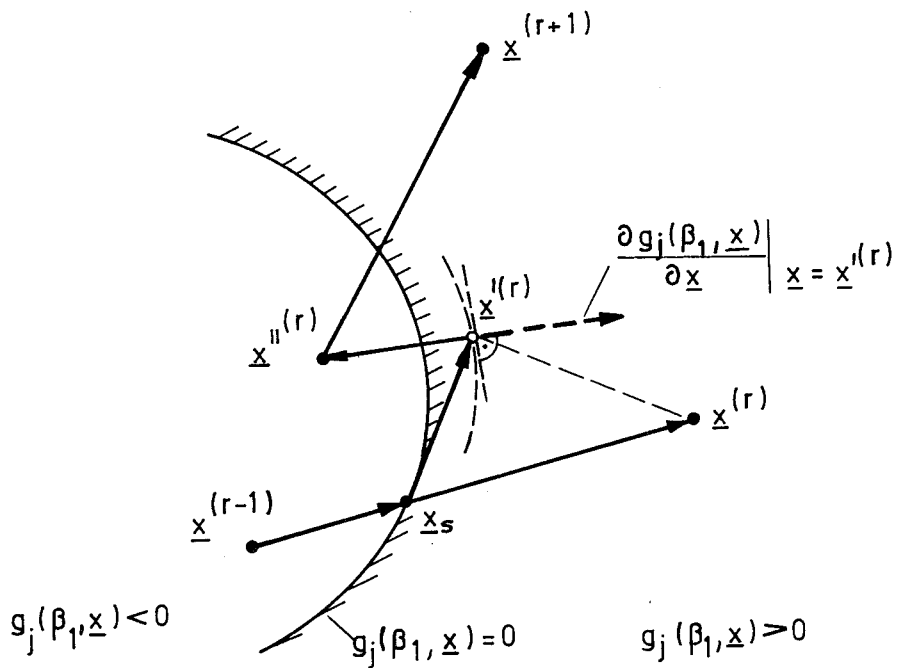


Figure 5: Correction step 2 for secondary condition.

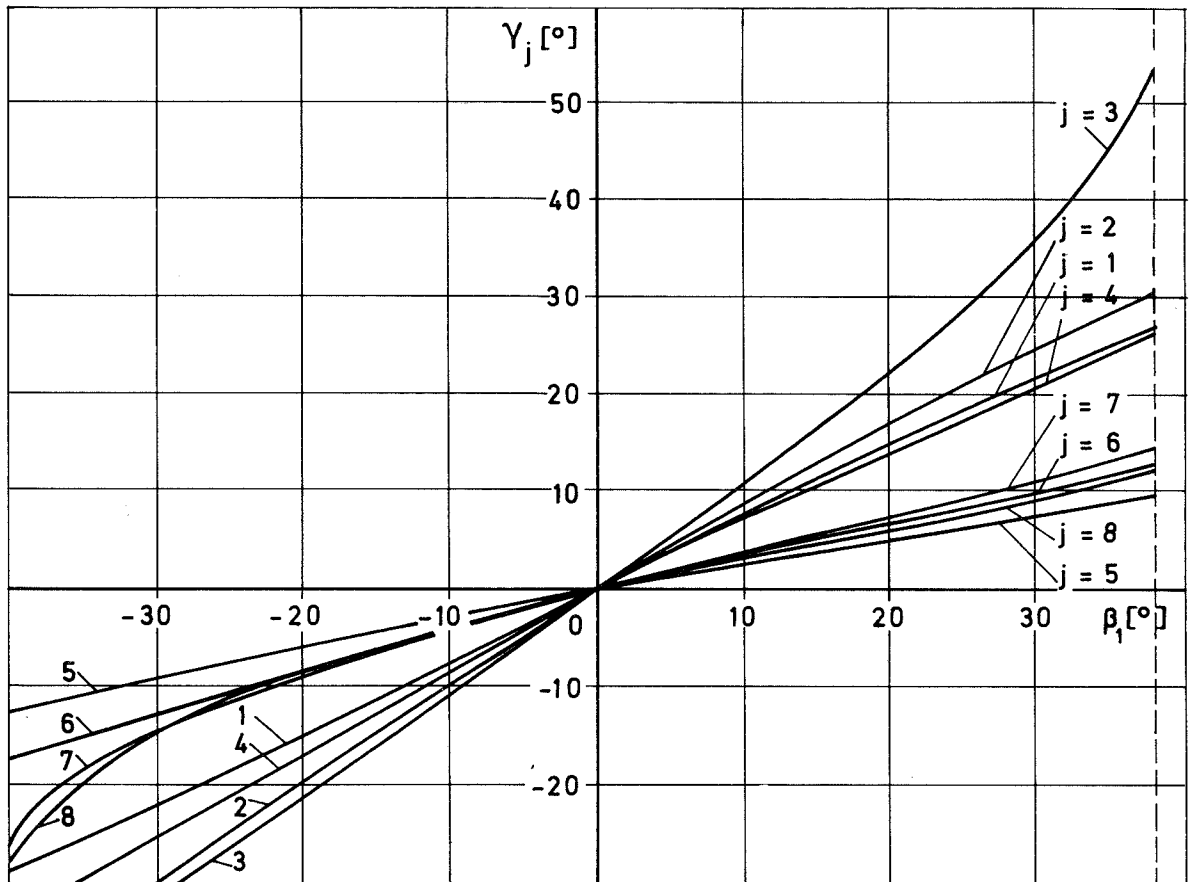


Figure 6: Input-output behaviour of four-bar mechanisms 1 to 8.

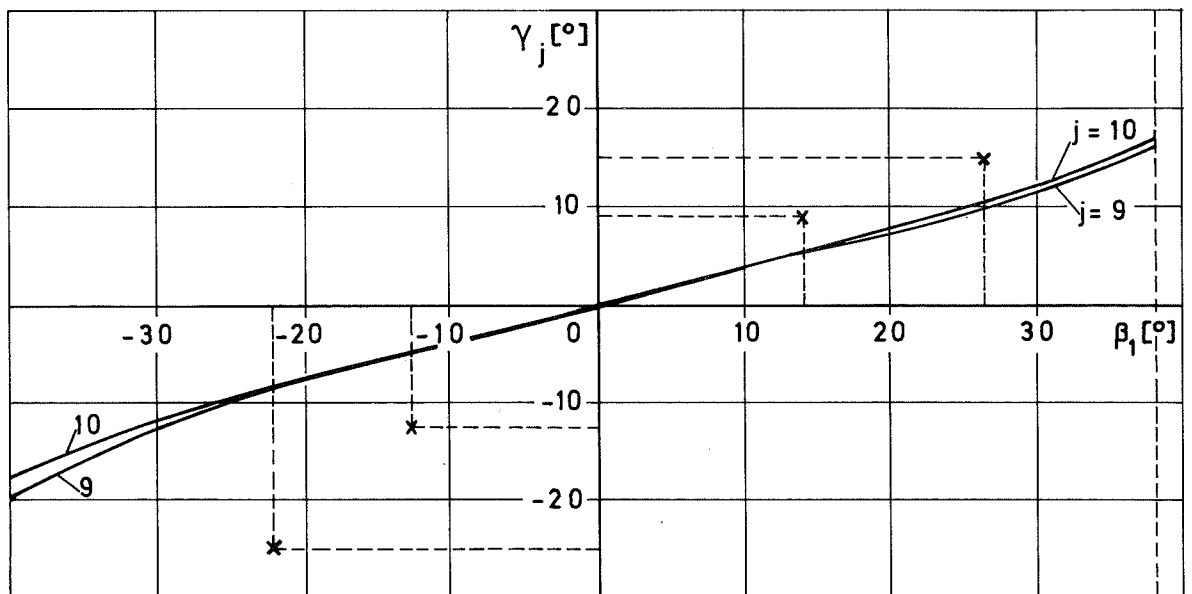


Figure 7: Input-output behaviour of four-bar mechanisms 9 and 10.

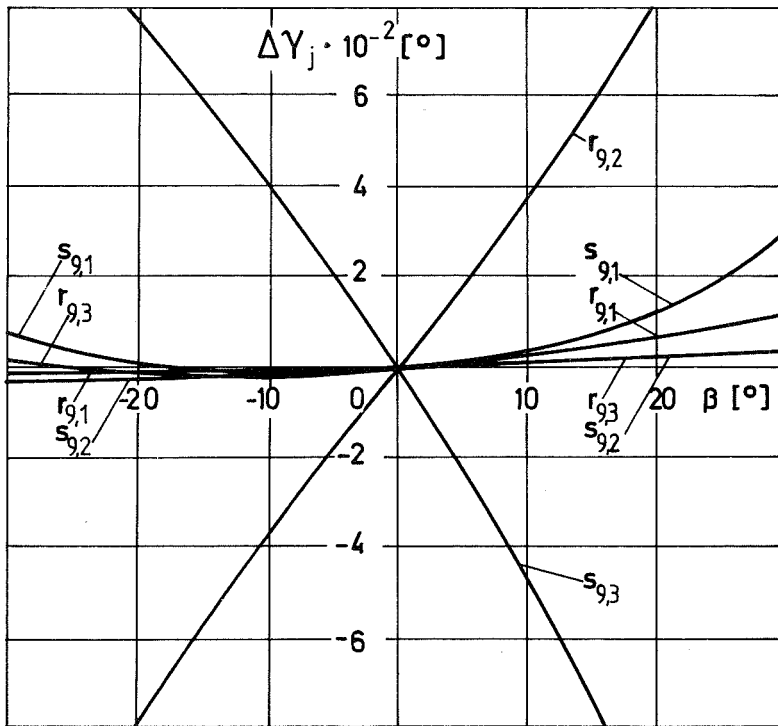


Figure 8: Sensitivity of the cranks \underline{r}_9 and \underline{s}_9 .

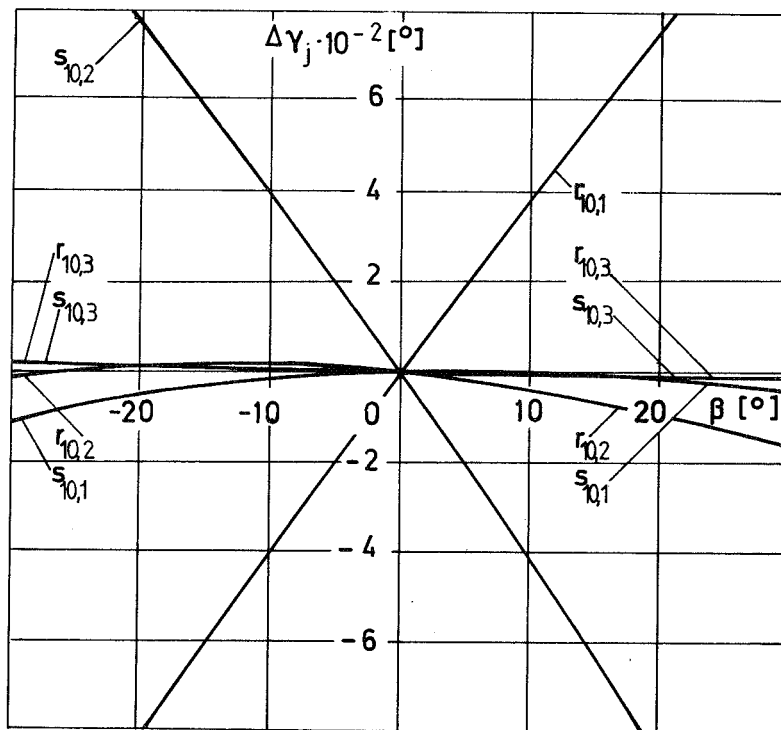


Figure 9: Sensitivity of the cranks \underline{r}_{10} and \underline{s}_{10} .

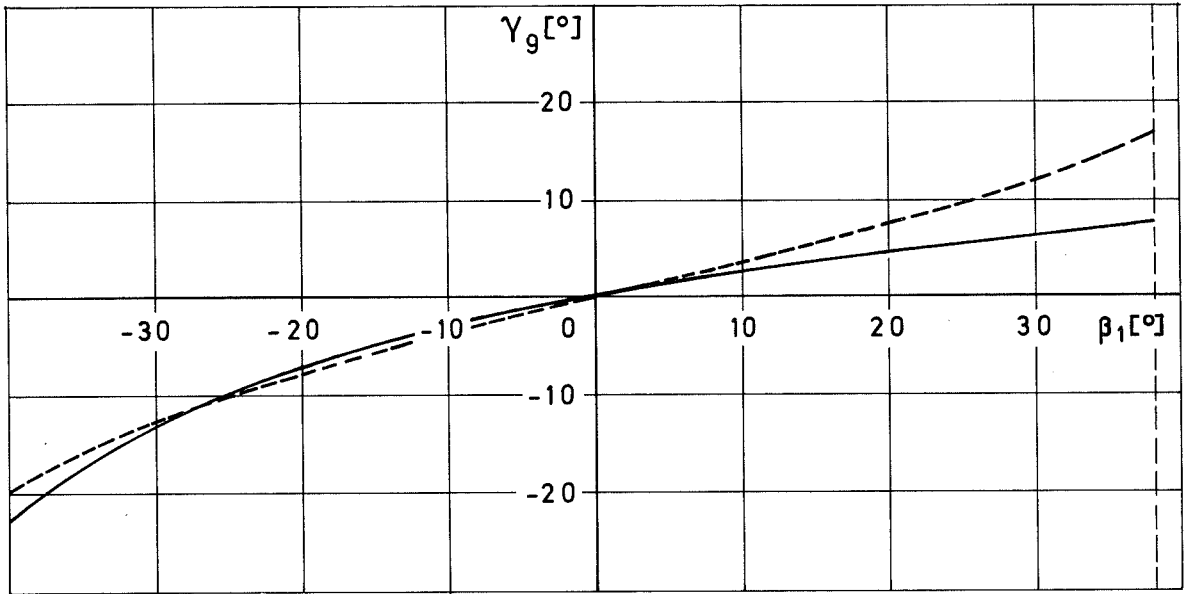


Figure 10: Output-angle γ_9 before (---) and after (—) variation.

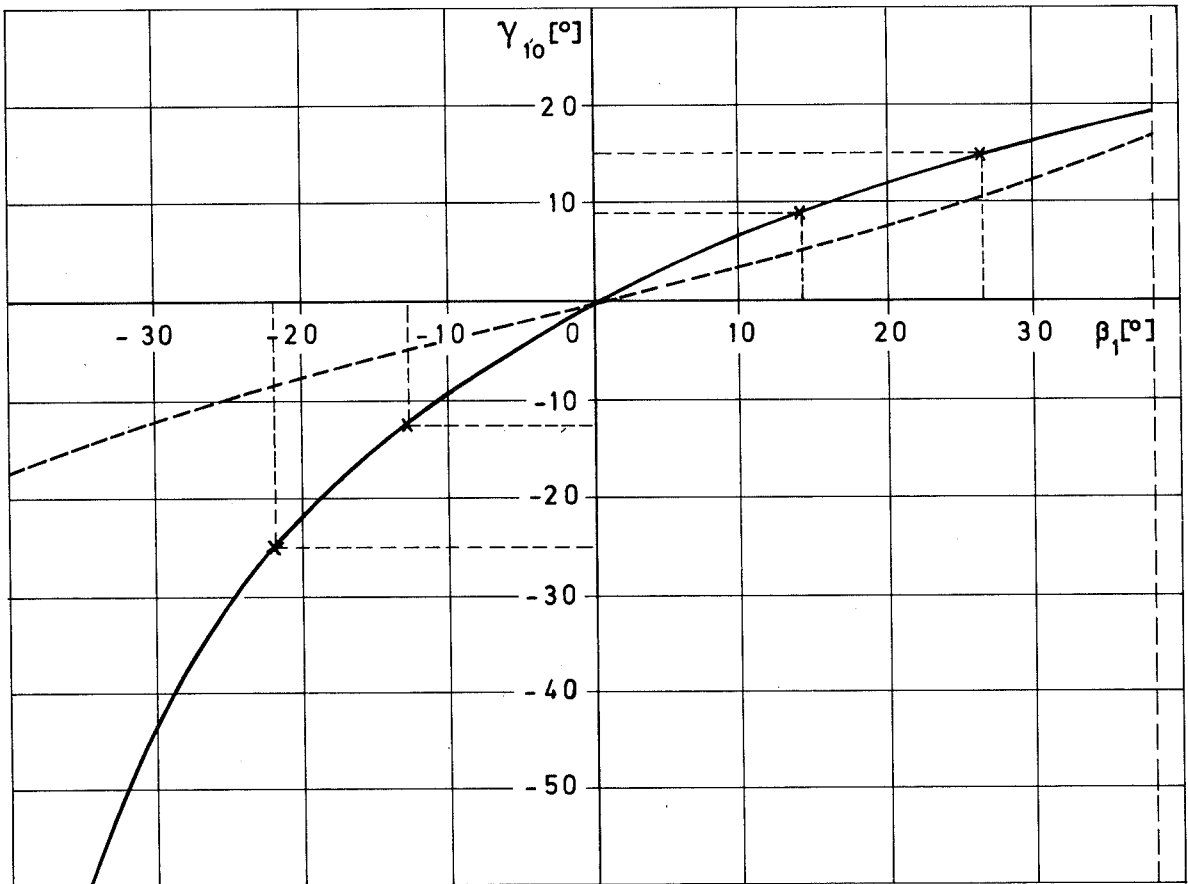


Figure 11: Aileron deflection γ_{10} before (---) and after (—) variation.

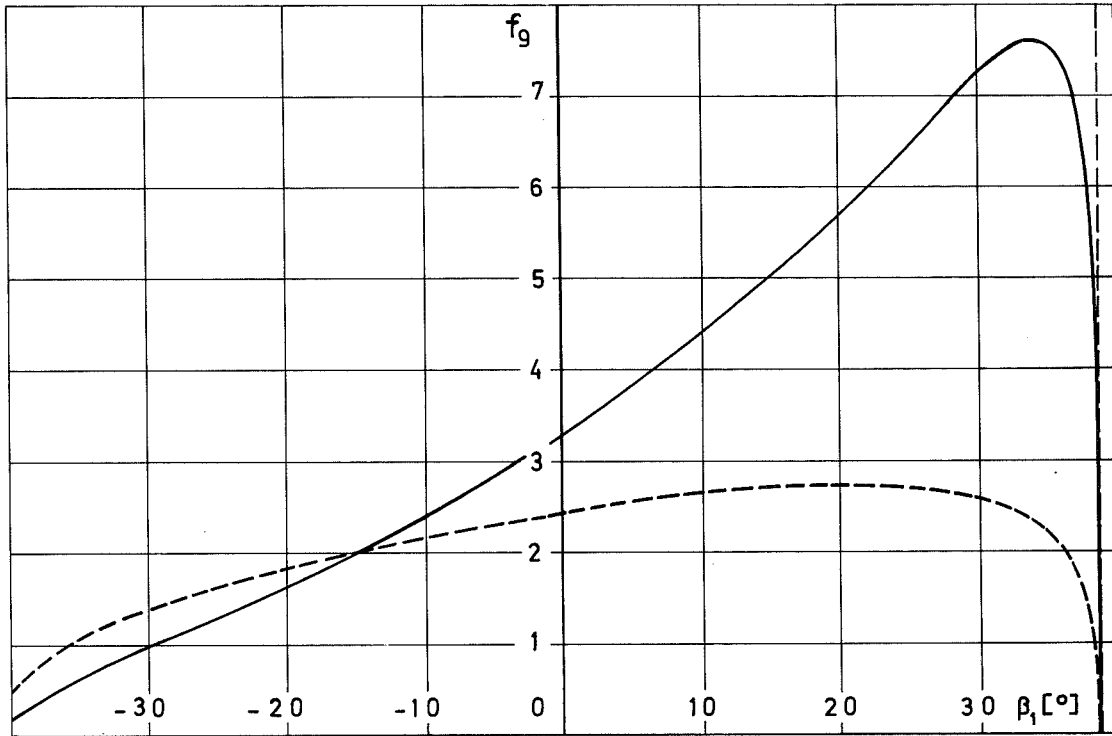


Figure 12: Coupler force f_g before (---) and after (—) variation.

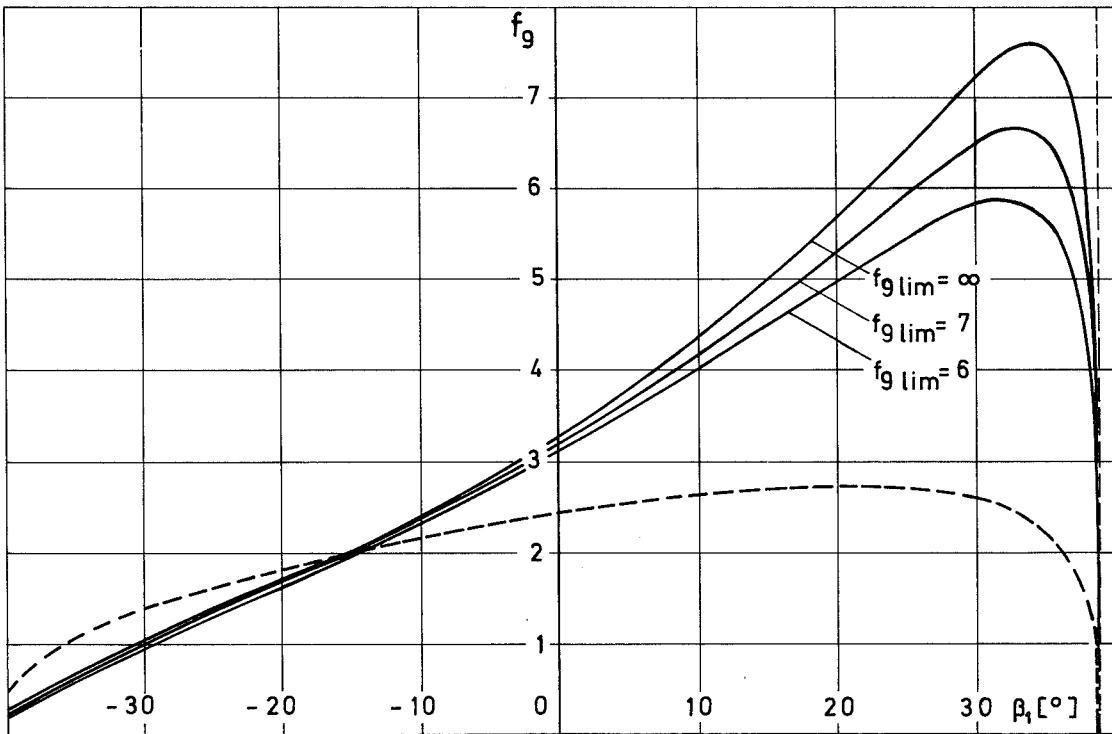


Figure 13: Limited coupler force f_g .

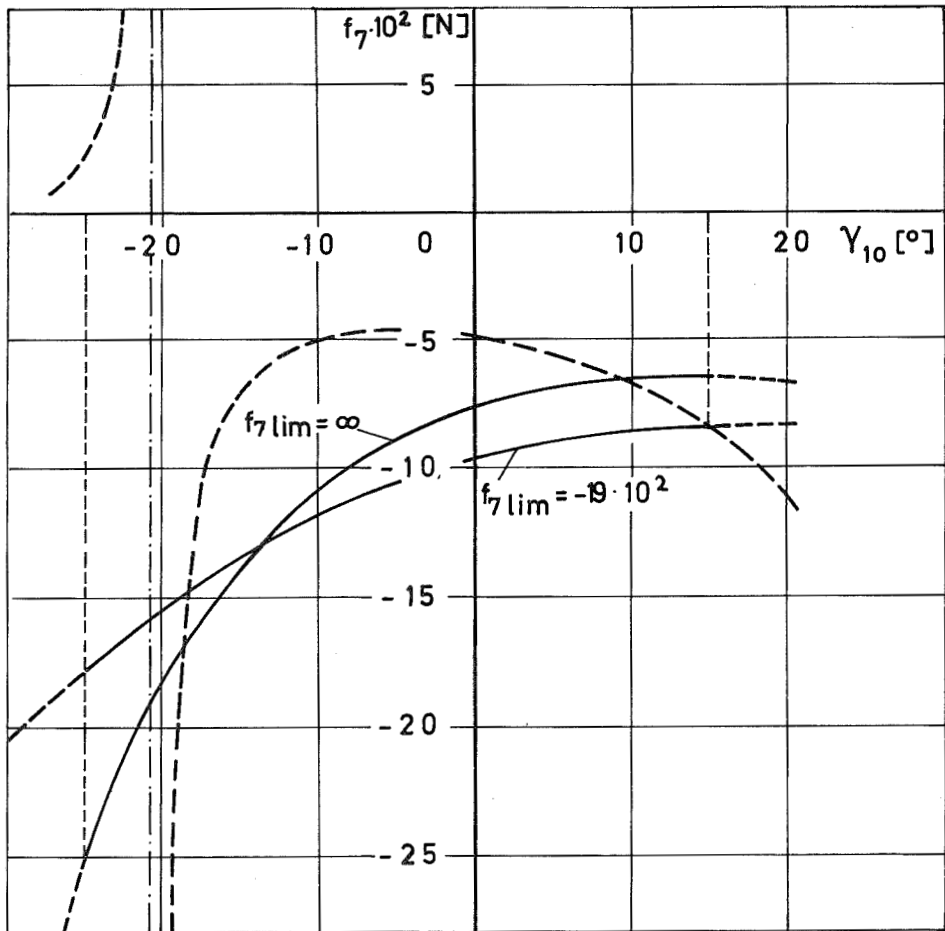


Figure 14: Coupler force f_7 before (---) and after (—) variation.

EXPERIMENTAL INVESTIGATION INTO THE FEASIBILITY
OF AN "EXTRUDED" WING

Piero Morelli and Giulio Romeo
Politecnico di Torino, Italy

SUMMARY

Research work in the Politecnico di Torino and realizations (fabrications) of extruded aluminium alloy structures during the past years is briefly reviewed. The design criteria and the realization of the main structure of a sailplane wing made of a few extruded profiles longitudinally connected one to the other are then illustrated. Structural tests recently carried out are reported upon.

INTRODUCTION

Early research work and the first realizations on the M-300 sailplane prototypes were reported upon in reference 1. Figure 1 illustrates the cross section of the M-300 extruded structures: first and second realization of the ailerons (a,b), tailplane (c), wing spar (d). An aluminium alloy AlMgSi TA16 (A.A. 6063-T6) was employed for the extrusion except for the spar, which was of A.A.7075.

In more recent years the same structural concept was adopted by the firm Caproni Vizzola Costruzioni Aeronautiche, manufacturer of the two-seater sailplane Calif A-21S (ref.2 and 3). Figure 2 illustrates some of the parts of this glider which were realized by extrusion using the same aluminium alloy mentioned above: airbrake (a), flap (b), aileron (c), elevator (d), and leading edge of the wing central part (e). The aileron and elevator extruded profiles incorporate the hinge (A). In the aileron leading edge lodging is provided (B) for the counterweight, uniformly distributed along the span for static and dynamic balance.

In the M-300 and Calif extruded structures the original wall thickness of 1.8 to 2.0 mm was reduced to design values of .5 to .8 mm by chemical milling of the outer surface.

All these structures are basically ribless. They proved light and largely adequate in strength and stiffness.

One of the M-300 prototypes is still active. The Calif two-seater has been series produced with the extruded parts mentioned here since 1975, except the extruded airbrake which was introduced in 1978.

Advantages and limitations of the extruded structures were discussed in references 1, 2, 3. They are briefly summarized here.

Main advantages are:

1. Reduction of manhours required to realize the structure, mainly during the assembling stage.
2. Reduction of cost in a series production when the cost of the expensive extrusion dies can be distributed over a high number of pieces.
3. Correct reproduction of section contours with consequent aerodynamic benefit.

The practical limitations are principally the following:

1. The extruded profile has necessarily a constant cross section. Through suitable mechanical and chemical operations, however, it is possible to achieve a certain degree of cross section variation along the beam axis.
2. The maximum linear dimension and net area of the profile section are limited by the power of the available extrusion press.
3. The difficulty of extruding increases with high strength aluminium alloy such as 2024 or 7075.
4. A minimum wall thickness is imposed by the extrusion process, which is sometimes excessive in relation to the strength and weight/strength ratio required.

A wide field of possible applications seem to exist notwithstanding these limitations, particularly for gliders and light powered aircraft.

A glider has been conceived, which is similar to the M-300 from which it is derived and is suitable for a wide use of extruded structures, whose locations are indicated by the shadowed areas in figure 3.

The realization of the central part of the wing of this glider is the aim of the research work started a few years ago at the Politecnico di Torino, after the completion of the first stage which led to the realization of the above described M-300 extruded parts.

THE DESIGN OF AN "EXTRUDED" WING

The wing illustrated in figure 3 is 15 m span with rectangular-trapezoid planform, the central rectangular part being extended over 9 m.

It is a three-piece wing: the central part is a flat single piece connected to the fuselage by a 4-point attachment; the outer trapezoid panels are attached to the ends of the central part and give the wing the required dihedral angle.

The central part is conceived as a combination of extruded profiles: a possible typical cross section is illustrated in figure 4 (airfoil FX 67-K-170/17), which is purely indicative of the basic idea. Corresponding to the airfoil maximum thickness a box structure can be seen which carries practically all bending loads and a good portion of the shear/torsion loads. The other two thin walled extruded profiles are riveted to the central box and contribute to the shear/torsion strength and stiffness of the whole structure. The extruded profile at the trailing edge is a flap.

The wing structure is intended as basically ribless, as far as tests will confirm that ribs can be eliminated.

In order to provide the central box with the required bending strength and stiffness under the prescribed loading conditions (according to the OSTIV Airworthiness Requirements, ref.4) a cellular structure was adopted for the dorsal and ventral panels. This multi-cell structure was tentatively designed to prevent general and local elastic instability.

The central box is made of two profiles joined by riveting the two halfwebs along the span (A.A. 6061-T6).

The large bending deformation, typical of a high aspect ratio sailplane wing, combined with the absence of ribs makes the problem of resisting the "crushing" loads a basic one. One of the main objectives of the testing program is to ascertain how far the webs alone are capable of withstanding the crushing loads.

The central box section is reduced along the span by chemically etching the outer surface of each of the two profiles so that the original wall thickness of the skin panels is decreased from 2.3 mm down to .8 mm at a spanwise station about 2.65 m from the wing centerline. This thickness is then kept constant over the rest of the wing.

Figure 5 shows the reduction of skin thickness along the span in two possible ways. A step reduction (above) or a continuous tapering (below) can be realized, the latter requiring, however, additional equipment for chemical milling at variable time of immersion.

Figures 6 and 7 show the central box cross sections at the wing root and at a spanwise station from 2.65 m on.

EXPERIMENTAL PROGRAM AND RESULTS

Several problems are to be faced in the realization of a wing as described in the preceding paragraph.

A preliminary experimental investigation was considered necessary in order to check the following points:

1. The capability of the cellular panels to withstand the high design compression

stresses without incurring local instability phenomena at low load factors.

2. The capability of the box structure to withstand the design bending moments and, in particular, the crushing loads due to bending deformation.
3. The capability to obtain the central box profiles by extrusion of a suitable material at an acceptable degree of accuracy and reasonable cost.
4. The feasibility of satisfactory chemical milling in relation to the particular aluminium alloy adopted for the extrusion.

With reference to points 1 and 2, it was decided to check the general design of the central box structure, and of the cellular panels in particular, by realizing a "simulated" extruded structure and submitting it to pure compression and pure bending tests. The cross section of the simulated structure in figure 8 shows its conventional construction through Z-stringers and metal sheet, both of dural, connected by rivets.

Notwithstanding the difference in material and some geometrical features these tests gave some valuable indications (ref.2) so that the realization of the expensive extrusion dies could be undertaken with reasonable confidence.

The two extruded profiles were then obtained, having the cross section shown in figure 6.

Several attempts were necessary, with modification of the die, before an acceptable degree of accuracy of the section contour was achieved.

The aluminium alloy employed on the first extruded profiles was not satisfactory (inadequate values of the yield and rupture stress). A different aluminium alloy was then used of higher strength but, perhaps, rather poor plastic characteristics.

It should be remarked here that, in our Italian situation, the choice of materials for extrusion is extremely limited. In fact, since our factories are not furnishers of the aircraft industry, the supply of a small quantity of extrusions such as required for research can only be made of a material of current use, i.e. having rather low strength characteristics.

Pure bending tests were planned and carried out on several specimen, 1000 mm long, of the real extruded structure using the bending test machine of the Istituto di Progetto di Aeromobili - Politecnico di Torino.

Figure 9 shows the testing equipment. Figures 10 and 11 show the deflection curves measured on specimens with wall thickness of 2.3 and .8 mm, i.e. having the cross sections illustrated in figure 6 and 7, respectively.

Figure 12 shows the typical failure in compression due to bending which occurred on one of the $t=.8$ mm specimen.

The results of these tests were encouraging, although of still limited vali-

dity for two main reasons:

1. Since the ends of the specimen are rigidly attached to the test machine, only a rather short central portion of the structure is free from their restraining influence. Therefore, the capability of the structure to withstand the crushing loads cannot be fully evaluated.
2. Shear is not present.

Testing on a full scale structure was therefore planned.

A test structure was prepared corresponding to the central box of the rectangular part of the sailplane wing illustrated in figure 3.

The span of this test specimen was 7.67 m, less than the 9.0 m span of the wing rectangular part, due to limitations of the available equipment for chemical milling.

The skin thickness was reduced spanwise through chemical milling by .3 mm steps from 2.3 down to .8 mm as shown on the upper part of fig. 5. Two extensions were added at both ends of the structure to allow the application of concentrated loads corresponding to the actual distributed load carried by the outer portions of the wing (see figure 13).

The spanwise wing lift and mass distributions were evaluated and then replaced by ten concentrated loads, giving a good approximation of the bending moment and shear distribution (see figure 13).

Figure 14 shows the structure under the load corresponding to load factor $n=8$.

The incremental load was 2,413 N corresponding to a unity load factor increment. The ultimate load was 24,074 N corresponding to a rather high ultimate load factor of 9.975.

The structural failure occurred at a load factor $n=8.72$.

As shown by figure 15, the dorsal cellular panel between the fittings, simulating the wing-fuselage attachments, collapsed under the combined effects of compression and crushing loads. In this area both webs were largely cut out to allow the connection of the fittings to the structure.

Figure 16 shows the deflection curves of the whole structure at load factors of 2, 4, 6 and 8. It can be seen that, at high load factors, the deflection of the left wing becomes a little higher if compared with the other wing. This is presumably due to the growing elastic buckling of the dorsal panel caused by the large cut-outs of the wing central part where the failure finally occurred (fig. 15).

The deflections at different stations are plotted versus load factor in figure 17.

Strain gage measurements showed: a) a slight elastic buckling of both webs in their longitudinally compressed part at load factors above $n=4$; b) no buckling whatever of the dorsal panels along the span; and c) a maximum local normal stress of 235 N/mm^2 at $n=8$ on both dorsal and ventral panels.

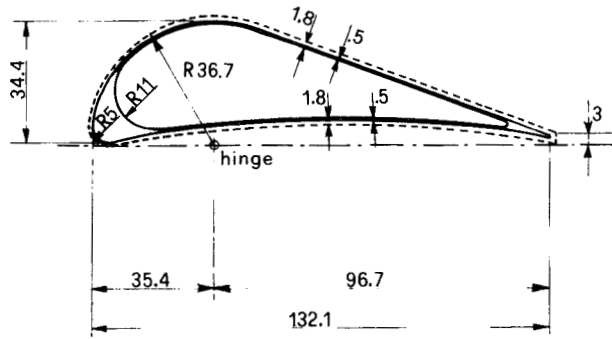
CONCLUSIONS

The failure under bending having occurred at a very high load factor ($n=8.72$) and in the central part of the structure where the webs can be easily reinforced, the result of this first static test can be considered successful. There is a reasonable confidence that, after reinforcement of the web cut-outs in the central portion of the structure, the residual load factor increment $\Delta n=9.975-8.720=1.255$ will be attained.

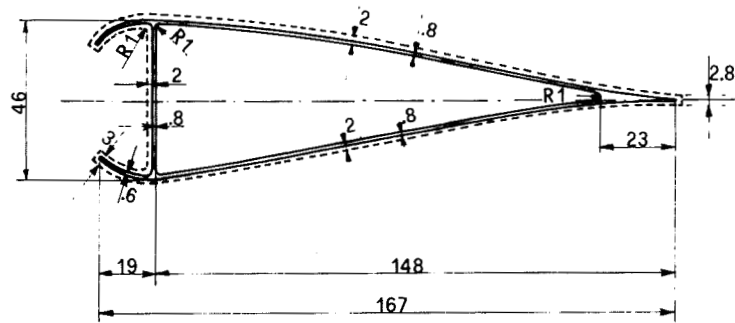
Although torsion static strength and fatigue life are to be demonstrated before a structure of this type can be assessed to be adequate for a sailplane wing, the result of the actual shear/bending test should probably be considered of basic importance as it practically demonstrates the feasibility of a ribless structure made of a few extruded profiles longitudinally connected one to the other.

REFERENCES

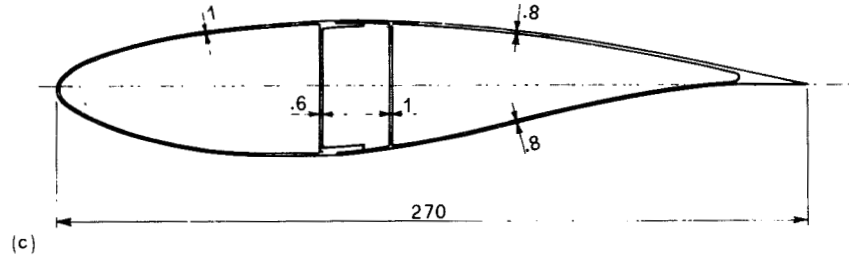
1. Morelli, P.: Extruded Light Alloy Aircraft Structures. Proceedings of the 1st International Symposium on the Technology and Science of Motorless Flight. M.I.T., Cambridge, U.S.A., October 1972.
2. Romeo, G.: Realizzazione per estrusione di strutture aeronautiche - Ricerca su struttura alare estrusa. Prestampa AIDAA n.60, IV Congresso Nazionale dell'Associazione Italiana di Aeronautica e Astronautica, Milano, September 1977.
3. Romeo, G.: Progress on Extruded Structures. 16th OSTIV Congress, Chateauroux, France, July 1978.
4. OSTIV Airworthiness Requirements for Sailplanes, September 1976.



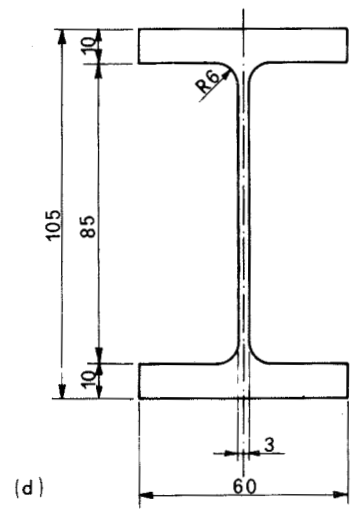
(a)



(b)



(c)



(d)

FIG.1- M-300 EXTRUDED STRUCTURES

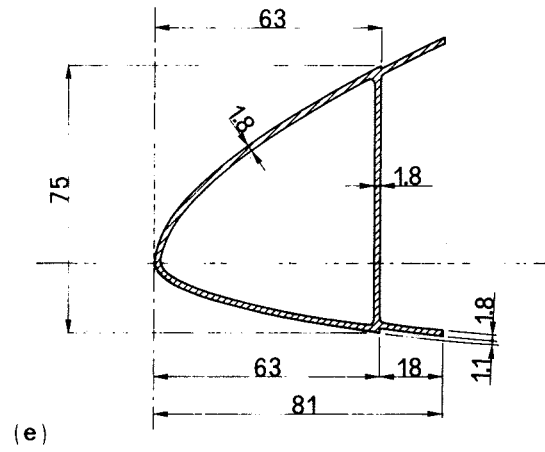
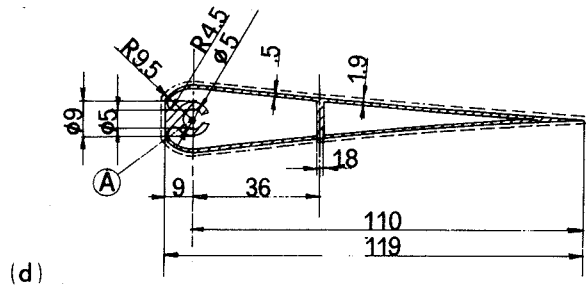
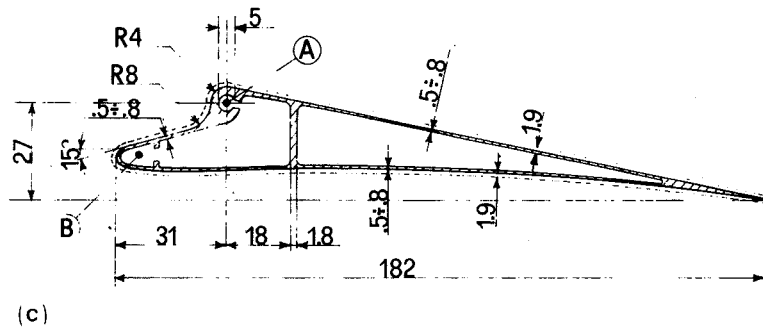
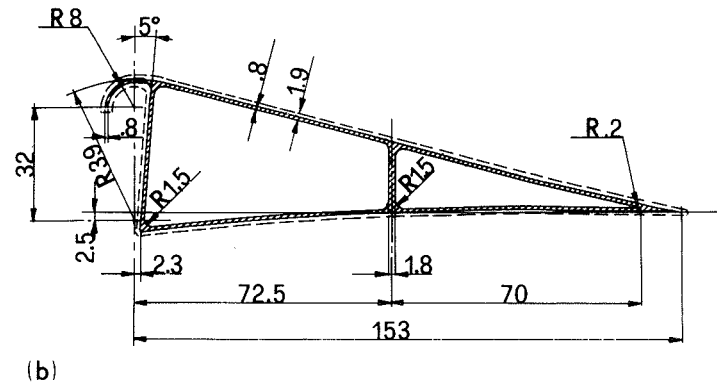
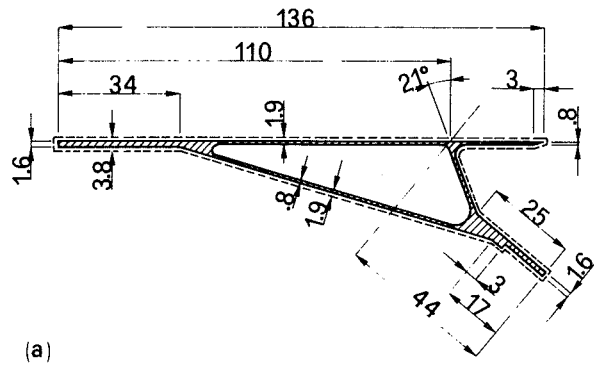


FIG.2 - CALIF A-21S EXTRUDED STRUCTURES

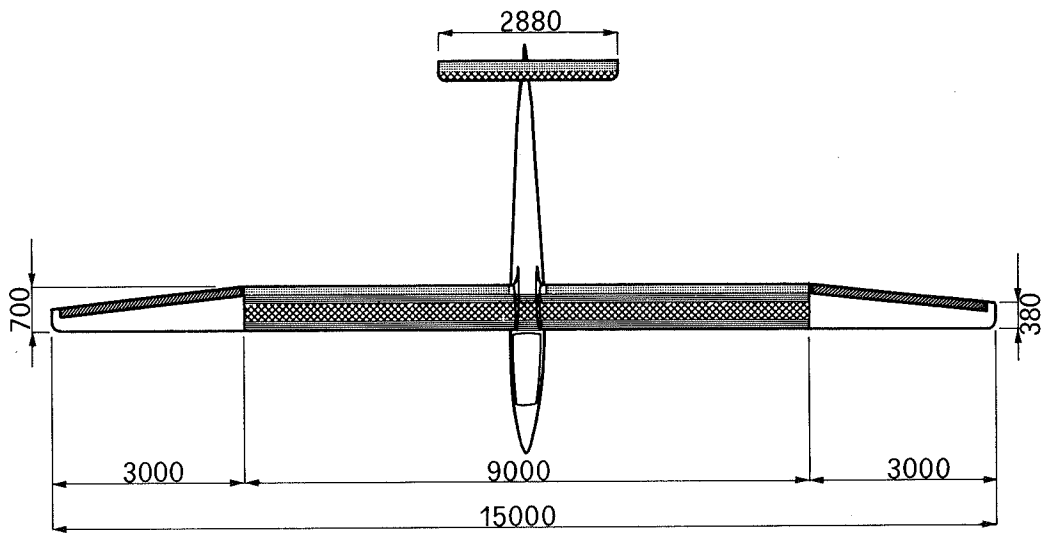


FIG.3 – GLIDER DESIGNED FOR WIDE USE OF EXTRUDED STRUCTURES

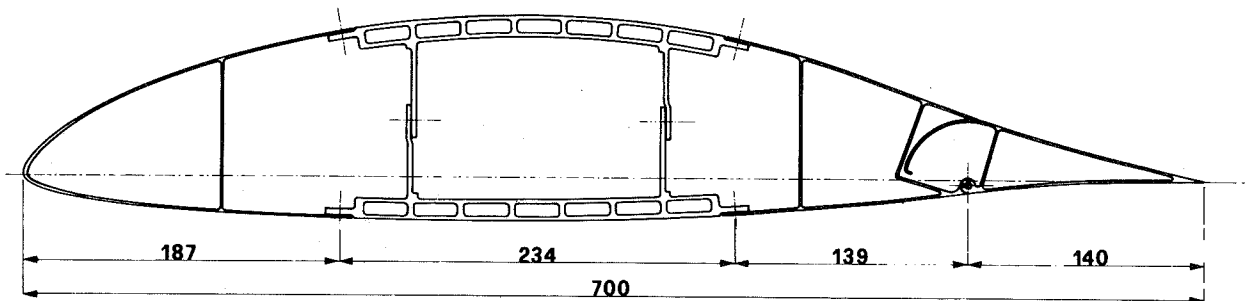


FIG.4 – TYPICAL CROSS SECTION OF AN "EXTRUDED" WING

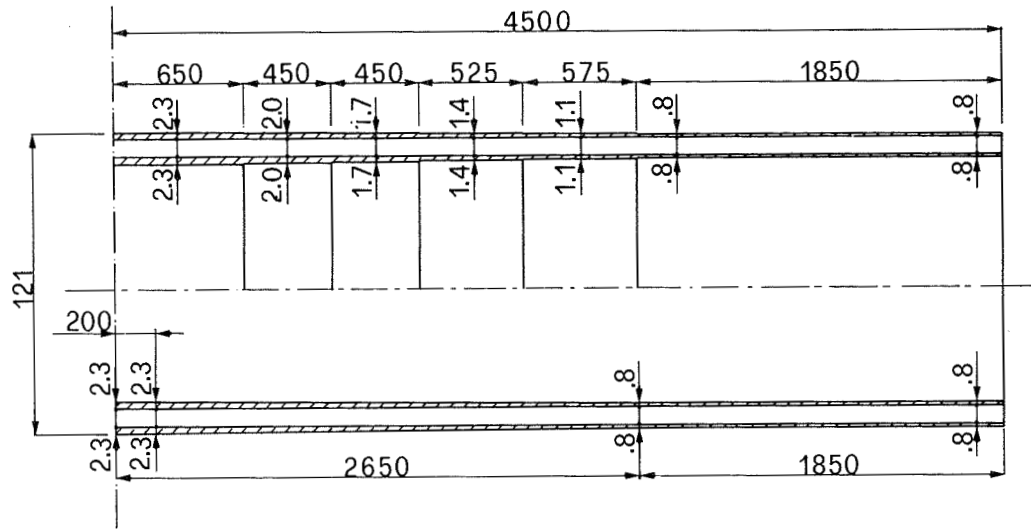


FIG.5 - SKIN THICKNESS REDUCTION ALONG THE SPAN

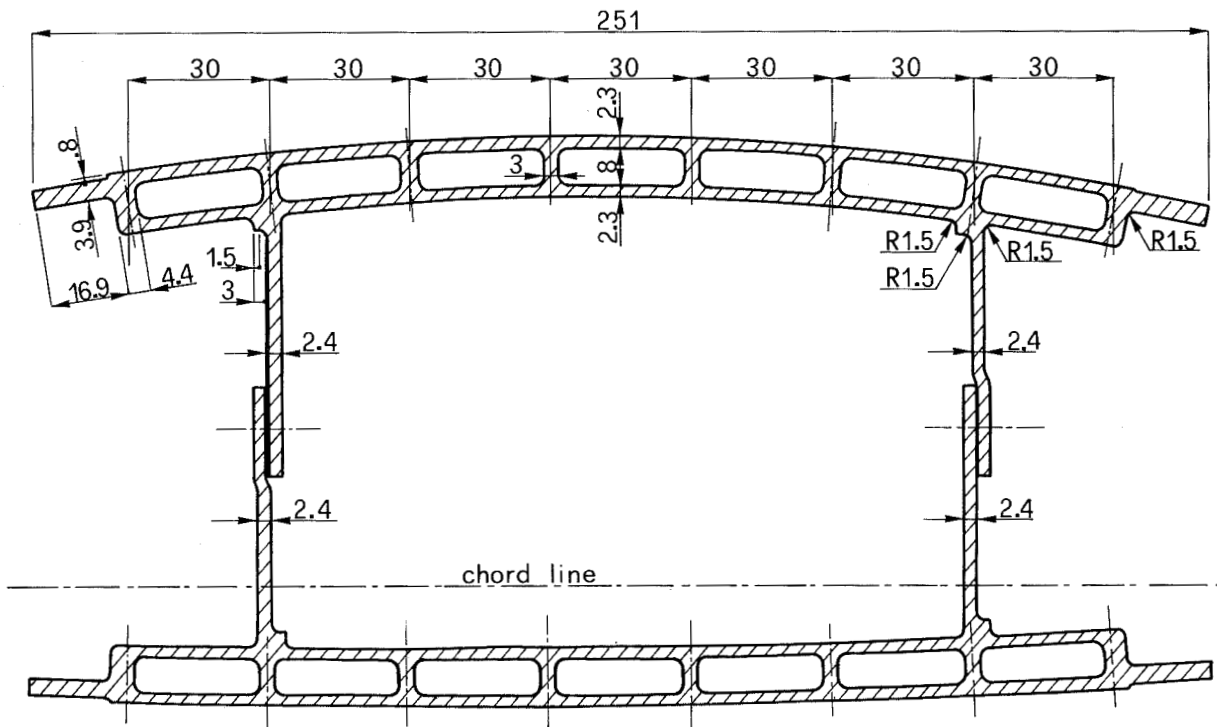


FIG.6 - CENTRAL BOX ROOT SECTION

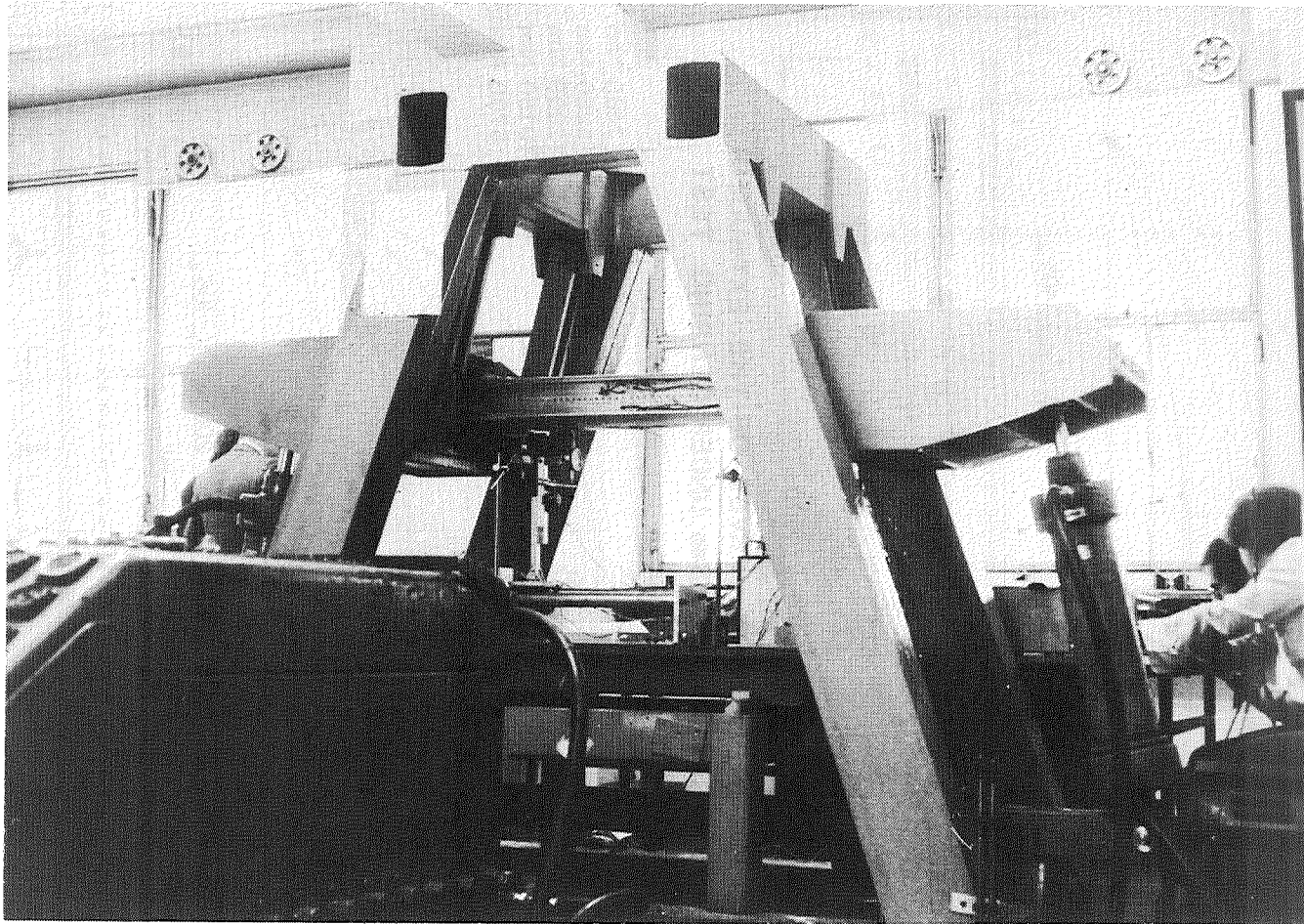


FIG.9 - EXTRUDED SPECIMEN TESTED AT BENDING MACHINE

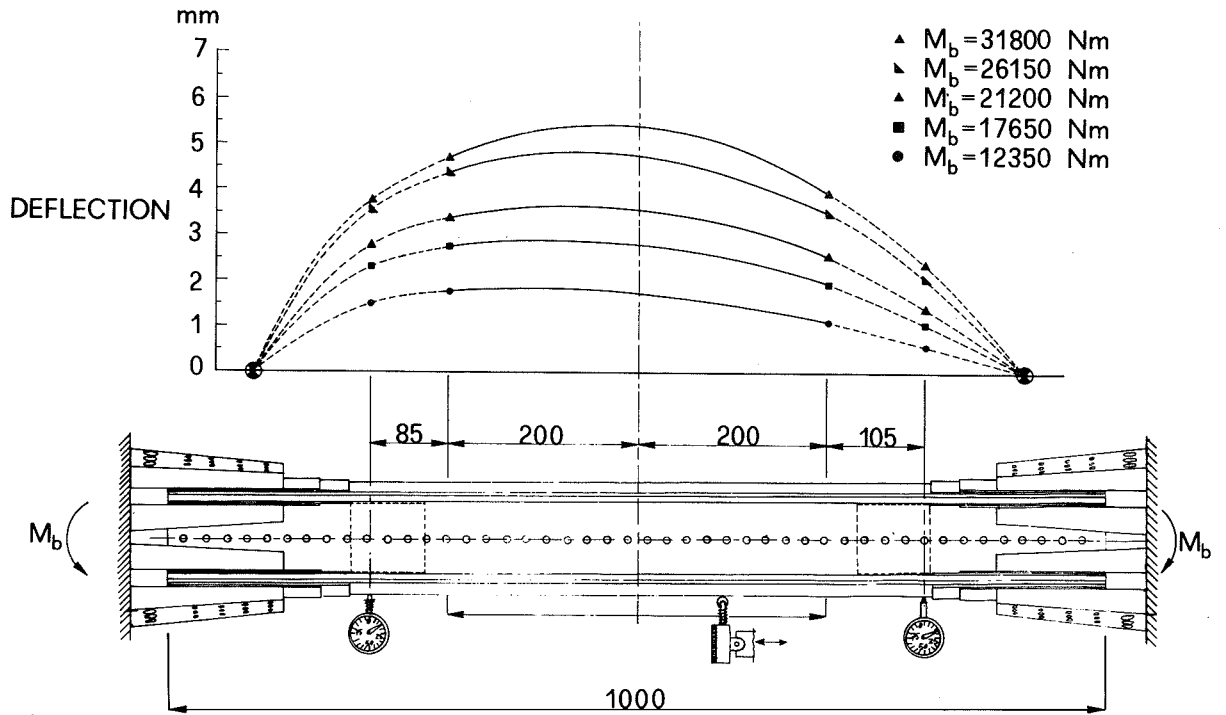


FIG.10 - DEFLECTION CURVES OF THE EXTRUDED SPECIMEN $t=2.3\text{mm}$ UNDER BENDING TEST

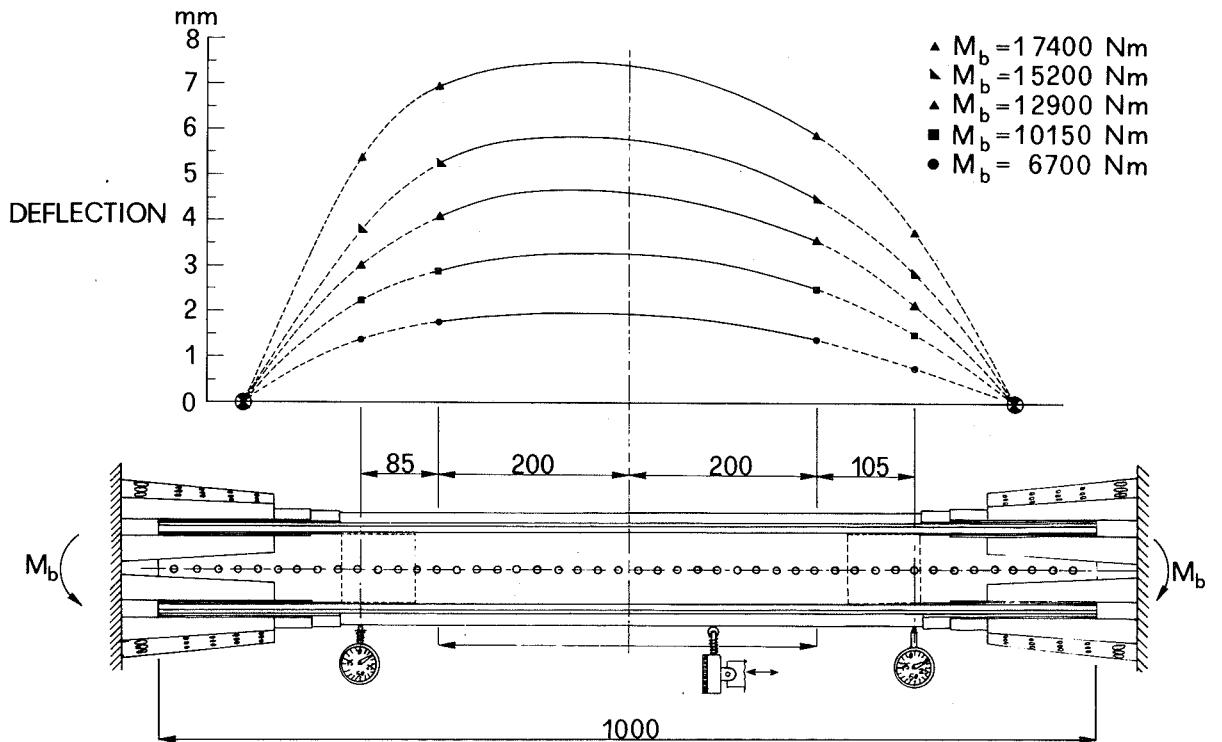


FIG.11 - DEFLECTION CURVES OF THE EXTRUDED SPECIMEN $t=.8\text{mm}$ UNDER BENDING TEST

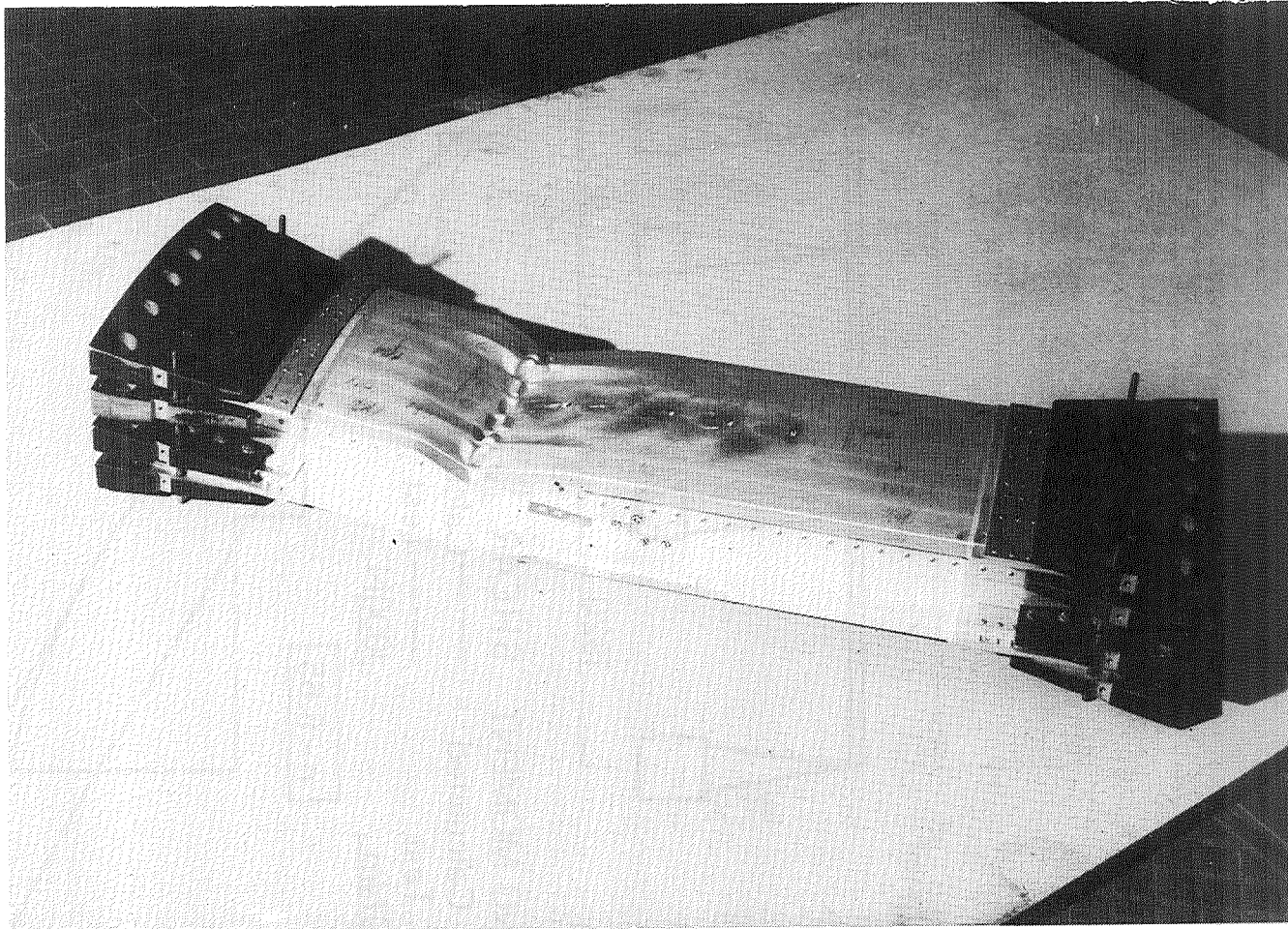


FIG.12 - BENDING FAILURE OF THE $t=.8$ EXTRUDED SPECIMEN

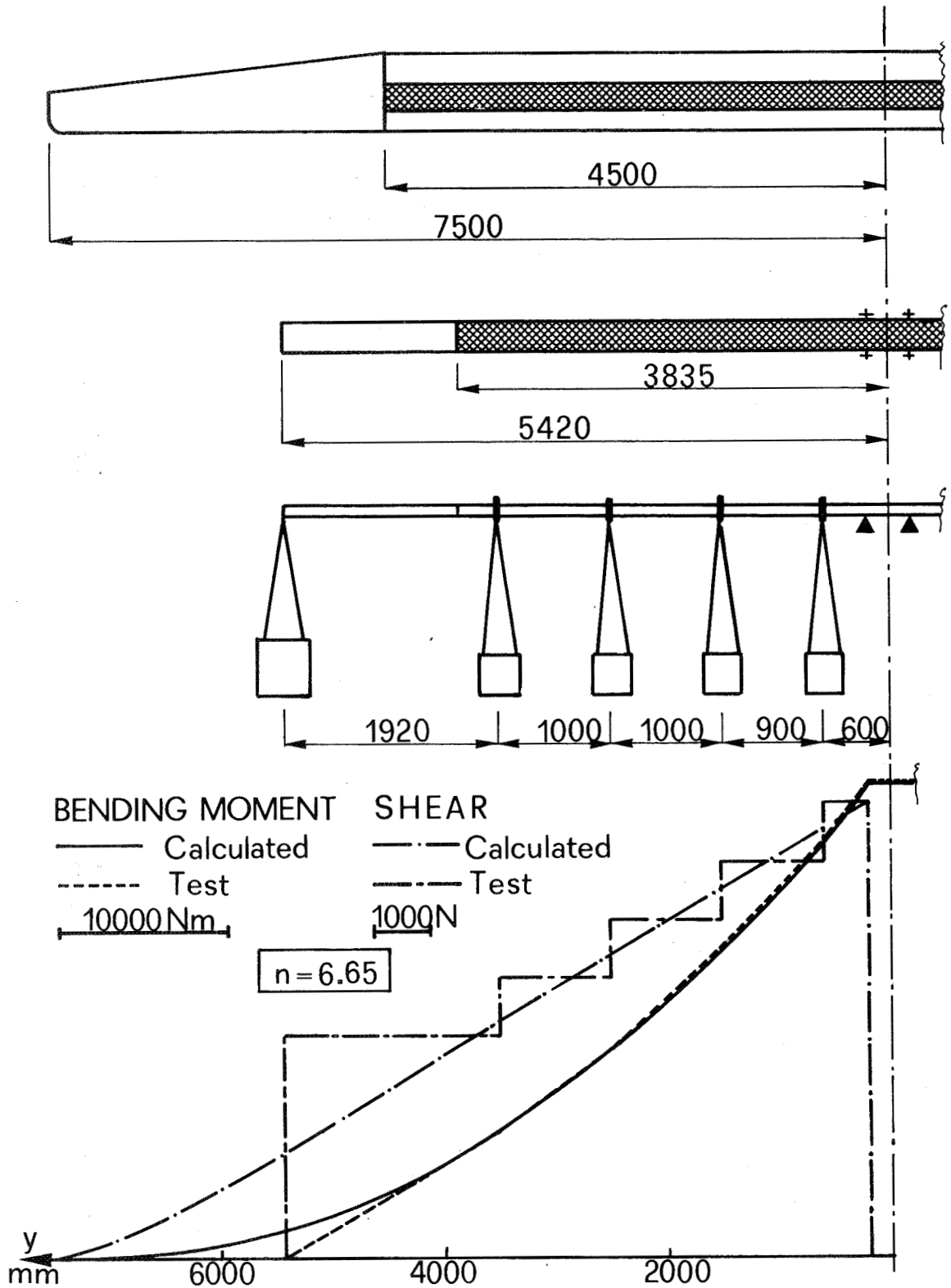


FIG.13 – LOAD DISTRIBUTION ON TEST STRUCTURE

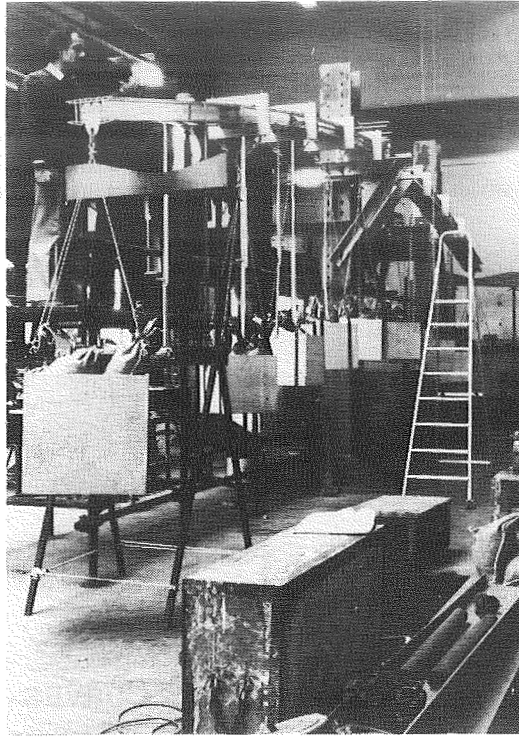


FIG.14- STRUCTURE AT LOAD FACTOR $n=8$

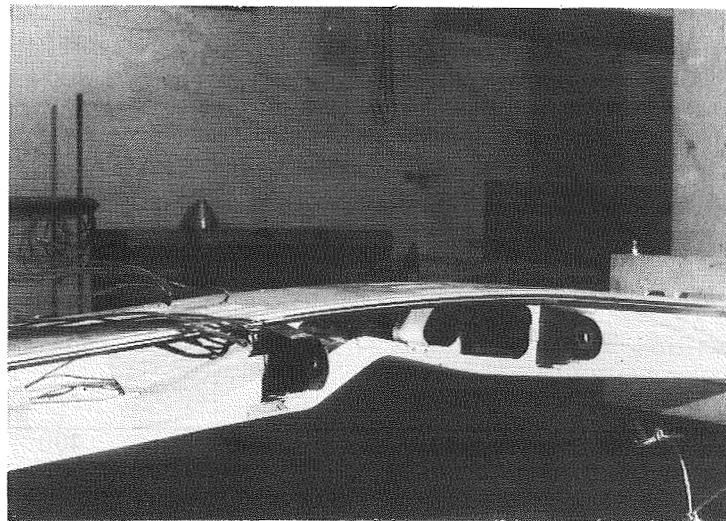


FIG.15 - STRUCTURE FAILURE

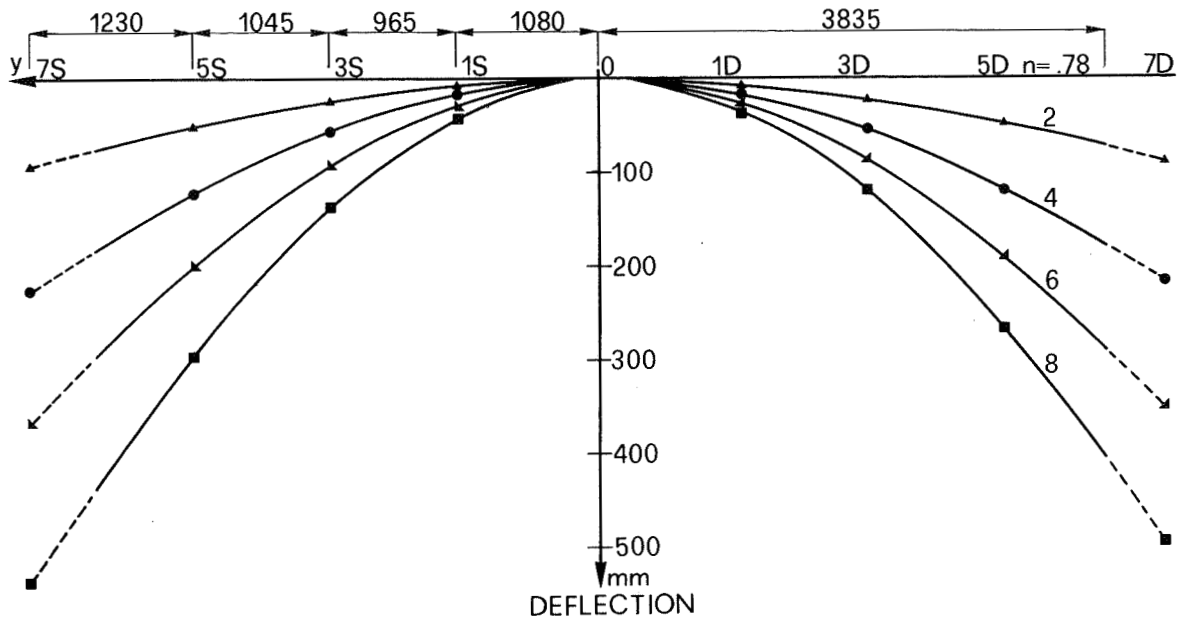


FIG.16 - DEFLECTION CURVES

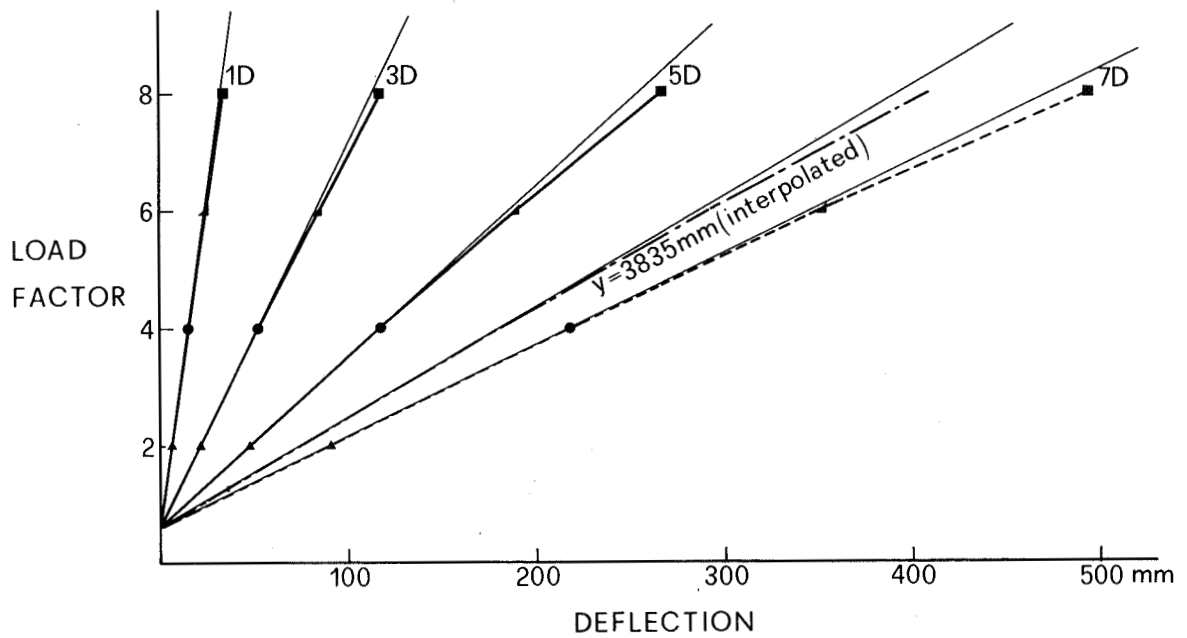


FIG.17 - DEFLECTION VS. LOAD FACTOR

TREATMENT OF THE CONTROL MECHANISMS OF LIGHT AIRPLANES

IN THE FLUTTER CLEARANCE PROCESS

Elmar J. Breitbach*
Langley Research Center

SUMMARY

Recently, it has become more and more evident that many difficulties encountered in the course of aircraft flutter analyses can be traced to strong localized nonlinearities in the control mechanisms. To cope with these problems, more reliable mathematical models paying special attention to control system nonlinearities may be established by means of modified ground vibration test procedures in combination with suitably adapted modal synthesis approaches. Three different concepts are presented in detail.

INTRODUCTION

At first glance the flutter clearance of soaring and light airplanes does not seem to raise any serious problems which cannot be solved by means of today's aeroelastic tools. This is true even for the determination of the unsteady aerodynamic loads as long as cases with large aspect ratios at comparably low speeds are considered. The elastodynamical characteristics can be determined by using common experimental or analytical methods if structural linearity can be assumed to be a proper approximation. However, as experience has shown, the control mechanisms of light airplanes¹ are generally nonlinear to such a large extent that setting up a dependable mathematical model requires special attention, including modifications to standard linearized procedures.

In the first part of this paper some of the most frequently occurring types of control-system nonlinearities are described. To get an idea of the influence of some typical nonlinearities on the aeroelastic stability the results of wind tunnel flutter tests on a nonlinear wing aileron model are presented. After that, it is shown in detail how the aeroelastic equations of light airplanes with localized nonlinearities may be formulated by using various suitably modified ground vibration test (GVT) procedures all based on the well-known modal synthesis approach. The shortcomings as well as the usefulness of the different concepts are discussed.

*NRC-NASA Senior Resident Research Associate.

¹Light airplanes as used in this paper include both powered and unpowered vehicles where the power to the flight control system is supplied by the pilot without electrical or hydraulic boost through a system of cables, pulleys, push-rods, bellcranks, or other mechanical linkages.

SYMBOLS

a, b	hinge axis coordinates of control surfaces and tabs, respectively
A, B, C	mass, damping, and stiffness matrices, respectively, defined in terms of geometrical displacements
$\Delta A, \Delta B, \Delta C$	matrices of mass, damping, and stiffness changes, respectively, defined in terms of geometrical displacements
C_e	equivalent linear stiffness of a nonlinear force deflection diagram, defined in equations (1) and (2)
e, f	center-of-gravity coordinates of control surfaces and tabs, respectively
F	force or moment acting on a control surface or tab
g	column matrix of constraint functions g_l
h	bending deflection of the quarter-chord line of lifting surface
I_v, I_{tv}	mass moments of inertia per span unit of control surface and tab, respectively, referred to the center of gravity
I_{Rx}, I_{Ry}, I_{Rz}	mass moments of inertia of control surface referred to the main axes of inertia
l	span width coordinate
m_R	control-surface mass
m_v, m_{tv}	mass per unit span of control surface and tab, respectively
M, D, K	generalized mass, damping, and stiffness matrices, respectively
$\Delta M, \Delta D, \Delta K$	generalized matrices taking into account mass, damping, and stiffness changes, respectively
P	column matrix of external forces
q, p	column matrices of generalized coordinates
Q	column matrix of generalized forces
t	time
T	inertia energy
u	column matrix of geometrical deflections
U	stiffness energy

V flight speed
 W damping energy
 X,Y transformation matrices, defined in equations (53) and (55)
 α rotation about the quarter-chord line of lifting surface
 β control-surface rotation about the hinge line
 γ tab rotation about tab hinge line
 η rotation of a control surface referred to its center of gravity
 θ damping loss angle
 λ column matrix of Lagrange's multipliers λ_l
 Λ diagonal matrix of the square values of the normal circular frequencies
 Φ, Ψ modal matrices
 ω circular frequency
 I unity matrix
 O zero matrix
 $j = \sqrt{-1}$ imaginary unit

Subscripts:

A,B,C,R,v,t substructures indices
 l constraint index, $l = 1, 2, \dots, \sigma$
 r normal mode index
 σ, ϵ indices referring to σ constraints and ϵ independent coordinates
 NL index referring to nonlinear properties
 L index referring to linear properties

Superscripts:

T transposed matrix
 A,B indices referring to substructures A and B
 ', " real, imaginary part

GENERAL REMARKS

Sources of Control-System Nonlinearities

Aeroelastic investigations are usually carried out on the basis of simplified linearized mathematical models. In many cases this approach has been adequate to ensure sufficient flutter safety margins for light airplanes. However, in the last few years, it has become evident that disregarding nonlinear phenomena can lead to hazardously misleading results. For example, it is shown in reference 1 that so-called concentrated or localized nonlinearities in control systems have a significant effect on the flutter behavior. Nonlinearities of this kind may be produced by such things as

- (1) Backlash in the joints and linkage elements
- (2) Solid friction in control-cable and pushrod ducts as well as in the hinge bearings
- (3) Kinematic limitation of the control-surface stroke
- (4) Application of special spring tab systems provided for pilot handling relief

The most critical parts of a control mechanism where localized nonlinearities may arise are shown schematically in figure 1.

An aeroelastic investigation may become even more complicated if it is necessary to account for items such as the following:

- (1) Preload changes due to maneuver loads and specially trimmed flight attitudes
- (2) Changes in friction and backlash over an airplane's lifetime
- (3) Additional mass, stiffness, and damping forces randomly activated by the pilot

Coping with all these difficulties requires special measures throughout the flutter clearance process. First, the ground vibration test (GVT) used to determine the elastodynamical coefficients of the flutter equations has to be modified so that a consistent and superpositionable set of orthogonal, or well-defined nonorthogonal, normal modes can be measured.

In reference 2 a proposed experimental approach employs a high frequency auxiliary excitation superimposed upon the much lower sinusoidal excitation to be tuned to the several normal frequencies. Thus, "slip-stick" effects and related nonlinearities in the control mechanisms can be minimized. The method requires additional test and control devices capable of exciting all controls simultaneously.

Of course, the simplest solution appears to be to build control-surface mechanisms without either friction or backlash. However, aside from a consider-

able increase in manufacturing costs, there is no guarantee that such an ideal condition could be kept unchanged for the lifetime of an airplane. Moreover, a frictionless control system is not necessarily equivalent to better handling qualities, because friction helps give the pilot the "feel" of flying the airplane.

From an experimentalist's standpoint, there are some simpler, but effective, methods using special modal coupling and modal superposition approaches. A detailed presentation of some of these methods is given in the subsequent sections of this paper. They will be referred to as Concepts I, II, and III.

Illustrative Examples of Control-System Nonlinearities

To get a realistic impression of control-mechanism nonlinearities, the force deflection diagrams $F(\beta)$ of the rudder and aileron system (antisymmetrical and symmetrical case) of a soaring airplane (ASW-15, A. Schleicher, Poppenhausen, W. Germany) are shown in figures 2(a), 3(a), and 4(a). Using the principle of the energetic equivalence (refs. 1 and 3) the stiffness and damping properties of a nonlinear force deflection diagram can be approximated by the so-called equivalent complex stiffness:

$$C_e(\beta) = C_e'(\beta) + j C_e''(\beta) \quad (j = \sqrt{-1}) \quad (1)$$

The coefficients $C_e'(\beta)$ and $C_e''(\beta)$, representing stiffness and damping, respectively, can be calculated from

$$\left. \begin{aligned} C_e'(\beta) &= \frac{1}{\pi\beta} \int_{\phi=0}^{2\pi} F(\beta \cos \phi, -\beta\omega \sin \phi) \cos \phi \, d\phi \\ C_e''(\beta) &= \frac{1}{\pi\beta} \int_{\phi=0}^{2\pi} F(\beta \cos \phi, -\beta\omega \sin \phi) \sin \phi \, d\phi \end{aligned} \right\} \quad (2)$$

where the circular frequency $\omega = 2\pi f$ (where f is frequency in hertz) and the integration variable $\phi = \omega t$. Damping can also be expressed by the loss angle

$$\theta_e(\beta) = \frac{C_e''(\beta)}{C_e'(\beta)} \quad (3)$$

The functions $C_e^I(\beta)$ and $C_e^{II}(\beta)$ corresponding to the force deflection diagrams of figures 2(a), 3(a), and 4(a) are plotted in 2(b), 3(b), and 4(b), respectively. Figure 3(b) shows that the antisymmetric aileron hinge stiffness in the range of the normal aileron stroke varies between 390 N-m and 44 N-m. Because of the stiffness variation, the normal frequency of the antisymmetrical aileron vibration (wing assumed to be fixed) varies over a wide range, between 2.4 Hz and 7.4 Hz. At least two other antisymmetric normal modes lie in this frequency range and are consequently characterized by highly amplitude-dependent portions of aileron vibrations. Similar effects can also be observed for the symmetric aileron mode and for the rudder vibration.

The effects of strong nonlinearities on the flutter behavior have been demonstrated in some wind-tunnel tests carried out on a nonlinear wing-aileron mode in the low-speed wind tunnel of DFVLR Göttingen. The nonlinear flutter boundaries for a backlash-type and for a spring-tab-type aileron hinge stiffness are shown in figure 5. Unlike the flutter boundaries of linear systems, both curves are characterized by a considerable dependence of the critical flutter speed on the aileron amplitude. Thus, the flutter boundary of the spring-tab-type system varies between $V = 12.5$ m/s and $V = 24$ m/s. The backlash-type system shows a flutter boundary variation between $V = 13.5$ m/s and $V = 20$ m/s. More detailed information, especially about the geometric and elastodynamic data of the wing-aileron model, is presented in reference 1.

MATHEMATICAL MODELING USING MODAL SYNTHESIS CONCEPTS

As mentioned previously, the determination of the elastodynamic characteristics by means of GVT can be affected severely by localized nonlinearities in the control mechanisms. It will be shown in the following discussion that the uncertainties resulting from these nonlinear effects can be avoided by applying experimental-analytical concepts based on the well-known modal synthesis approach.

Each of these concepts can be used to set up the aeroelastic equations of the actual airplane including all control-mechanism nonlinearities. The nonlinear force deflection diagrams of the different controls can be determined by static or dynamic tests.

Three different concepts will be presented. They may be briefly described as follows:

Concept I: Measurement of a set of orthogonal normal modes with the control surfaces rigidly clamped; separate determination of the control-surface normal modes with the rest of the airplane rigidly fixed.

Concept II: GVT on a configuration artificially linearized by replacing the nonlinear control-mechanism elements by linear and lightly damped dummy devices; thus, a set of orthogonal normal modes for the entire system is available.

Concept III: Measurement of a set of orthogonal normal modes with the control surfaces removed; separate determination of the normal modes of the control surfaces in uncoupled condition.

Concept I

The governing equations of motion of an aeroelastic system, formulated in terms of physical coordinates, can be written in matrix notation as follows:

$$A\ddot{u} + B\dot{u} + Cu = P \quad (4)$$

where

- A mass matrix
- B damping matrix
- C stiffness matrix
- u column matrix of the physical displacements; \dot{u} and \ddot{u} are first and second derivatives with respect to time t
- P column matrix of external forces, for instance, unsteady aerodynamic forces

It is obvious that parts of the matrices B and C are nonlinear because of the localized nonlinearities of the controls.

Controls without tabs.- If the GVT is carried out with the controls rigidly clamped to the adjacent structure, a set of n largely linear normal modes Φ_{Ar} can be measured and combined in the modal matrix

$$\Phi_A = [\Phi_{A1}, \Phi_{A2}, \dots, \Phi_{Ar}, \dots, \Phi_{An}] \quad (5)$$

The modes satisfy the orthogonality condition

$$\left. \begin{aligned} \Phi_A^T A \Phi_A &= M_A \\ \Phi_A^T C \Phi_A &= \Lambda_A M_A = K_A \end{aligned} \right\} \quad (6)$$

where

- M_A diagonal matrix of the generalized masses M_{Ar}
- K_A diagonal matrix of the generalized stiffnesses $K_{Ar} = \omega_{Ar}^2 M_{Ar}$

Λ_A diagonal matrix of the square values of the circular normal frequencies ω_{Ar}

The generalized damping matrix D_A (not necessarily diagonal) is defined by

$$D_A = \Phi_A^T B \Phi_A \quad (7)$$

Next, assuming that the control surfaces are rigid in the frequency range of interest, a number of additional control-surface rotation modes with the adjacent main structure at rest can be determined and combined in the modal matrix

$$\Phi_B = [\Phi_{B1}, \Phi_{B2}, \dots, \Phi_{Bv}, \dots, \Phi_{Bm}] \quad (8)$$

The physical displacements of the complete structure are related to the generalized coordinates by

$$u = \Phi q \quad (9)$$

where the column matrix of the generalized coordinates q_r and q_v is

$$q = [q_A^T, q_B^T]^T \quad (10)$$

and

$$\Phi = [\Phi_A, \Phi_B] \quad (11)$$

The basic idea of this modal superposition is outlined in figure 6. Substituting equation (9) into equation (4) and premultiplying it by Φ^T yields

$$M\ddot{q} + D\dot{q} + Kq = Q \quad (12)$$

where

$$\left. \begin{aligned}
 M &= \begin{bmatrix} M_A & M_{AB} \\ M_{BA} & M_B \end{bmatrix} & Q &= \Phi^T P \\
 D &= \begin{bmatrix} D_A & 0 \\ 0 & D_B \end{bmatrix} & K &= \begin{bmatrix} K_A & 0 \\ 0 & K_B \end{bmatrix}
 \end{aligned} \right\} \quad (13)$$

The matrices M_A , K_A , and D_A measured in a GVT are defined in the equations (6) and (7). The diagonal matrices M_B , D_B , and K_B contain the generalized masses, damping values, and stiffnesses of the control-surface rotation modes. In the case of nonlinear hinge stiffness and damping, the matrix elements of K_B and D_B are

$$K_{Bv} = C'_{ev}(\beta) \beta_{va}^2 \quad D_{Bv} = \frac{C''_{ev}(\beta)}{\omega} \beta_{va}^2 \quad (14)$$

where $C'_{ev}(\beta)$ and $C''_{ev}(\beta)$ can be determined from equation (2). The term β_{va} denotes the control rotation in the action line of the control actuator force. The matrix M_B can be determined by calculation or measurement taking into account not only the control-surface mass but also the moving mass of such attached hardware as pushrods, cables, and control stick. The elements of the coupling matrix

$$M_{AB} = M_{BA}^T = \Phi_A^T A \Phi_B \quad (15)$$

can be found by integration over surfaces S_{Bv} of the controls

$$M_{AB,rv} = \int_{S_{Bv}} \{ e_{v\gamma} m_{v\gamma} h_r \beta_{v\gamma} + [I_{v\gamma} + e_{v\gamma} m_{v\gamma} (a_{v\gamma} + e_{v\gamma})] \alpha_r \beta_{v\gamma} \} d\ell \quad (16)$$

where the following terms correspond to the v th control with tab locked to the control

- m_v mass of the control surface per unit span
- I_v mass moment of inertia per unit span referred to the center of gravity
- e_v distance between center of gravity and hinge axis (see fig. 7)
- a_v distance between hinge axis and the quarter-chord point (see fig. 7)

All these data as well as the amplitudes h_r , α_r , and β_v (see fig. 7) are functions of the span coordinate ℓ . In case of an ideal locking of the con-

trols, neither hinge stiffness forces nor hinge damping forces are generated in the normal modes Φ_{Ar} . Hence,

$$\left. \begin{aligned} K_{AB} &= K_{BA}^T \equiv 0 \\ D_{AB} &= D_{BA}^T \equiv 0 \end{aligned} \right\} \quad (17)$$

Extension to controls with tabs.— The above procedure can easily be extended to systems with controls and tabs (spring tabs, trim tabs, or geared tabs) by introducing the tab movement as a separate degree of freedom. For this special case the main GVT configuration is characterized by controls locked to the adjacent airplane structure and tabs locked to the controls. This leads to the same set of normal modes Φ_{Ar} as defined in equation (5). Furthermore, the degrees of freedom of the controls are separately determined with the main structure at rest and with tabs locked to the controls. The resulting normal modes are identical to the ones defined by equation (8). Finally, in a third step the tab modes Φ_{Cv} are determined with both the main structure and the controls at rest. This concept is schematically illustrated in figure 8. In accordance with this, u can be expressed as a series expansion of the normal mode sets Φ_A , Φ_B , and Φ_C

$$u = [\Phi_A, \Phi_B, \Phi_C] q \quad (18)$$

where

$$q = [q_B^T, q_B^T, q_C^T]^T \quad (19)$$

Replacement of u in equation (4) by equation (18) and premultiplication by Φ^T leads to an equation similar to equation (12). Because of the additional tab degrees of freedom the matrices M , D , K , and Q have the extended form

$$\left. \begin{aligned} M &= \begin{bmatrix} M_A & M_{AB} & M_{AC} \\ M_{BA} & M_B & M_{BC} \\ M_{CA} & M_{CB} & M_C \end{bmatrix} & Q &= \Phi^T P \\ D &= \begin{bmatrix} D_A & 0 & 0 \\ 0 & D_B & 0 \\ 0 & 0 & D_C \end{bmatrix} & K &= \begin{bmatrix} K_A & 0 & 0 \\ 0 & K_B & 0 \\ 0 & 0 & K_C \end{bmatrix} \end{aligned} \right\} \quad (20)$$

The matrices M_A , M_B , $M_{AB} = M_{BA}^T$, K_A , K_B , D_A , and D_B are identical to the matrices defined in equations (6), (7), (14), (15), and (16). The matrices K_C and D_C can be determined in the same way as K_B and D_B by measuring the nonlinear force deflection diagrams of the tabs and using equation (2) to calculate

$$K_{CV} = C_{eV}^i(\gamma) \gamma_{Va}^2 \quad D_{CV} = C_{Va}''(\gamma) \gamma_{Va}^2 \quad (21)$$

The term γ_{Va} denotes the tab rotation in the line where the force acting on the tab is applied. The matrix M_C can be determined by test or calculation. The elements of the coupling matrix

$$M_{AC} = M_{CA}^T = \Phi_A^T A \Phi_C \quad (22)$$

can be found by integration over the tab surface S_{CV}

$$M_{AC,rv} = \int_{S_{CV}} \{f_v m_{tv} h_r \gamma_v + [I_{tv} + f_v m_{tv} (b_v + f_v)] \alpha_r \gamma_v\} d\ell_t \quad (23)$$

where the following terms correspond to the v th tab (part of the v th control)

- m_{tv} mass of the tab per unit span
- I_{tv} mass moment of inertia per unit span referred to the center of gravity
- f_v distance between the tab hinge axis and the tab center of gravity (see fig. 7)
- b_v distance between the tab hinge axis and the control hinge axis (see fig. 7)

The quantities I_{tv} , m_{tv} , f_v , and b_v as well as h_r , α_r , and γ_v (see fig. 7) are functions of the tab span coordinate ℓ_t . The elements of the coupling matrix

$$M_{BC} = M_{CB}^T = \Phi_B^T A \Phi_C \quad (24)$$

between the control surfaces and the appertaining tabs can be calculated by integration over the tab surface S_{CV}

$$M_{BC,vv} = \int_{S_{CV}} [I_{tv} + m_t f_v (b_v + f_v)] \beta_v \gamma_v d\ell_t \quad (25)$$

Provided that the normal modes Φ_{Ar} can be measured with ideally locked control and tab hinges, neither hinge damping forces nor hinge stiffness forces are generated in Φ_{Ar} . This leads to

$$\left. \begin{aligned} K_{AC} = K_{CA}^T &\equiv 0 & K_{BC} = K_{CB}^T &\equiv 0 \\ D_{AC} = D_{CA}^T &\equiv 0 & D_{BC} = D_{CB}^T &\equiv 0 \end{aligned} \right\} \quad (26)$$

Concept II

As described in references 1, 6, and 7, the replacement of the control nonlinearities by artificial linear stiffnesses results in a modified linearized test configuration represented in matrix notation by

$$A_L \ddot{u} + B_L \dot{u} + C_L u = P \quad (27)$$

which is formulated in terms of physical displacements. The governing dynamic equations of the unchanged nonlinear system can be written in the same form as equation (4) by subdividing the matrices A, B, and C as follows:

$$\left. \begin{aligned} A &= A_L - \Delta A_L + \Delta A_{NL} \\ B &= B_L - \Delta B_L + \Delta B_{NL} \\ C &= C_L - \Delta C_L + \Delta C_{NL} \end{aligned} \right\} \quad (28)$$

The term $\Delta A_{NL} - \Delta A_L$ represents the difference in the mass distribution between the artificial linear system and the real nonlinear system; ΔB_L and ΔC_L define the damping and stiffness properties of the artificial linear elements; ΔB_{NL} and ΔC_{NL} describe the damping and stiffness properties of the replaced nonlinear elements. Development of the arbitrary displacement vector u in a series expansion of the measured normal modes Φ_{Lr} of the linearized system yields

$$u = \Phi_{Lr}^T q \quad (29)$$

Inserting this modal transformation into equation (4), premultiplying by Φ_L^T , and taking into account equation (28) results in generalized equations of motion in the same form as equation (12), but with the mass, damping, and stiffness matrices now defined as

$$\left. \begin{aligned} M &= M_L - \Delta M_L + \Delta M_{NL} \\ D &= D_L - \Delta D_L + \Delta D_{NL} \\ K &= K_L - \Delta K_L + \Delta K_{NL} \end{aligned} \right\} \quad (30)$$

The matrices M_L , D_L , and K_L are measured in a GVT on the linearized system. Furthermore,

$$\left. \begin{aligned} \Delta M_{NL} - \Delta M_L &= \Phi_L^T (\Delta A_{NL} - \Delta A_L) \Phi_L \\ \Delta D_{NL} - \Delta D_L &= \Phi_L^T (\Delta B_{NL} - \Delta B_L) \Phi_L \\ \Delta K_{NL} - \Delta K_L &= \Phi_L^T (\Delta C_{NL} - \Delta C_L) \Phi_L \end{aligned} \right\} \quad (31)$$

For simplicity, consider only one control surface. For the v th control surface, the modal matrix Φ_L degenerates to the row matrix

$$\Phi_{vL} = [\beta_{v1}, \beta_{v2}, \dots, \beta_{vr}, \dots, \beta_{vn}] \quad (32)$$

and $\Delta B_{NL} - \Delta B_L$ and $\Delta C_{NL} - \Delta C_L$ degenerate to the 1×1 matrices

$$\left. \begin{aligned} \Delta B_{NL} - \Delta B_L &= \frac{C_e''(\beta)}{\omega} - B_L \\ \Delta C_{NL} - \Delta C_L &= C_e'(\beta) - C_L \end{aligned} \right\} \quad (33)$$

where the nonlinear stiffness and damping values $C_e'(\beta)$ and $C_e''(\beta)$ can be determined again by applying equation (2) to the measured nonlinear force deflection diagram. The damping and stiffness matrices B_L and C_L , respectively, of the artificial linear element can be measured by means of simple tests. The matrix $\Delta M_{NL} - \Delta M_L$ can also be calculated by using the modal matrix as defined in equation (32), provided the two parts of the 1×1 matrix $\Delta A_{NL} - \Delta A_L$ can be defined as moments of inertia by referring the removed mass of the nonlinear system, as well as the additional mass resulting from the artificial linearization, to the hinge angle β .

Concept III

The aeroelastic equations of an airplane can also be established by means of both a set of normal modes measured in a GVT with controls removed and rigid-body and some elastic normal modes of the several controls (see fig. 10) determined experimentally or by fairly simple calculations. The equations of motion of the coupled system can be set up by means of Lagrange's equations

$$\frac{\partial}{\partial T} \left(\frac{\partial T}{\partial \dot{q}_r} \right) + \frac{\partial U}{\partial q_r} + \frac{\partial W}{\partial \dot{q}_r} = \sum_{\ell=1}^{\sigma} \lambda_{\ell} \frac{\partial g_{\ell}}{\partial q_r} \quad (34)$$

$$(r = 1, 2, \dots, n_A, n_A + 1, \dots, n_B, \dots, n_i, \dots)$$

where

$$\left. \begin{aligned} 2T &= M\dot{q}^2 \\ 2U &= Kq^2 + \Delta K q^2 \\ 2W &= D\dot{q}^2 + \Delta D \dot{q}^2 \end{aligned} \right\} \quad (35)$$

The matrices ΔK and ΔD in equation (35) take into account the elastic coupling between control surfaces and main structure by means of the real hinge stiffness and hinge damping elements. The term on the right side of equation (34) is formulated in terms of Lagrange's undetermined multipliers λ_{ℓ} which correspond to a number of σ constraint conditions

$$g_{\ell} (q_1, q_2, \dots, q_r, \dots, q_{n_i}) = 0 \quad (\ell = 1, 2, \dots, \sigma) \quad (36)$$

They express compatibility in those coupling points, where the controls can be assumed to be rigidly fixed to the main structure. Application of equation (34) to equations (35) and (36) yields

$$M\ddot{q} + (D + \Delta D)\dot{q} + (K + \Delta K)q - \Psi^T \lambda = 0 \quad (37)$$

where the elements of the $r \times \ell$ matrix Ψ^T are

$$\Psi_{\ell r}^T = \frac{\partial g_{\ell}}{\partial q_r} \quad (38)$$

Confining the further derivation to the coupling of only two systems, A and B (main structure and control surface) results in the following generalized mass, stiffness, and damping matrices of the uncoupled system:

$$\left. \begin{aligned} M &= \begin{bmatrix} M_A & 0 \\ 0 & M_B \end{bmatrix} & D &= \begin{bmatrix} D_A & 0 \\ 0 & D_B \end{bmatrix} \\ K &= \begin{bmatrix} K_A & 0 \\ 0 & K_B \end{bmatrix} \end{aligned} \right\} \quad (39a)$$

where the submatrices are

$$M_i = \Phi_i^T A_i \Phi_i \quad K_i = \Phi_i^T C_i \Phi_i \quad D_i = \Phi_i^T B_i \Phi_i \quad (i = A, B) \quad (39b)$$

The matrices A_i , B_i , and C_i describe mass, damping, and stiffness of the subsystems A and B in terms of geometrical coordinates; Φ_i is the modal matrix of subsystem i . The elements of the diagonal matrices M_i and K_i and of the damping matrices D_i , which are not necessarily diagonal, can be determined by GVT or, as in the case of the controls, by calculation, also.

According to reference 7 the generalized coupling matrices ΔK and ΔD can be written as follows:

$$\Delta K = \Phi_{AB}^T C_{AB} \Phi_{AB} \quad \Delta D = \Phi_{AB}^T B_{AB} \Phi_{AB} \quad (40)$$

When the main structure and control surface are coupled by one single complex hinge stiffness C_e in the action line of the control force, we obtain

$$\Phi_{AB} = \left[\begin{array}{ccc|ccc} \text{A} & \text{A} & & & & \\ \alpha_{a1} & \alpha_{a2} & \dots & \alpha_{an} & & \\ \hline & & 0 & & & 0 \\ & & & & \alpha_{a,n+1}^B & \alpha_{a,n+2}^B & \dots & \alpha_{an}^B \end{array} \right] \quad (41)$$

$$C_{AB} = C'_e \begin{bmatrix} 1 & -1 \\ -1 & 1 \end{bmatrix} \quad B_{AB} = \frac{C''_e}{\omega} \begin{bmatrix} 1 & -1 \\ -1 & 1 \end{bmatrix} \quad (42)$$

The angles of rotation α_{ar}^A and α_{ar}^B are defined in figure 9. For the special case of coupling two systems A and B the compatibility condition for σ physical degrees of freedom can be expressed by the constraints

$$g_\ell = u_\ell^A - u_\ell^B = 0 \quad (\ell = 1, 2, \dots, \sigma) \quad (43)$$

If u_ℓ^A and u_ℓ^B are expressed in a series of the normal modes of the systems A and B, then

$$g_\ell = \sum_{r=1}^{n_A} u_{\ell r}^A q_r - \sum_{r=n_A+1}^{n_B} u_{\ell r}^B q_r = 0 \quad (44)$$

or in matrix notation

$$g = \Psi q = 0 \quad (45)$$

The aeroelastic equations of motion are defined now by the $n_A + n_B = m$ generalized coordinates. Due to the σ constraints there remains a number of $\epsilon = m - \sigma$ independent generalized coordinates in terms of which the aeroelastic equations have to be formulated. To do this, the term Ψ^T in equation (37) has to be rearranged rowwise so that

$$\Psi^T \rightarrow \bar{\Psi}^T = \begin{bmatrix} \Psi_\epsilon \\ \Psi_\sigma \end{bmatrix} \quad (46)$$

where Ψ_σ is a nonsingular $\sigma \times \sigma$ matrix. The matrices M , K , D , ΔK , and ΔD with respect to both their columns and rows and the column matrix q have to be rearranged in the same sense. The rearranged equations can be written as

$$\bar{M}\ddot{\bar{q}} + (\bar{D} + \Delta\bar{D})\dot{\bar{q}} + (\bar{K} + \Phi\bar{K})\bar{q} = \bar{\Psi}^T \lambda \quad (47)$$

where

$$\bar{q} = [p^T, q_\sigma^T]^T \quad (48)$$

The new structure of the matrices \bar{M} , \bar{D} , \bar{K} , $\Delta\bar{D}$, and $\Delta\bar{K}$ is shown in the following equation using \bar{M} as an example

$$\bar{M} = \begin{bmatrix} M_{\epsilon\epsilon} & M_{\epsilon\sigma} \\ M_{\sigma\epsilon} & M_{\sigma\sigma} \end{bmatrix} \quad (49)$$

Thus, λ can be determined as follows

$$\begin{aligned} \lambda = (\bar{\Psi}^T)^{-1} & \left\{ [M_{\sigma\epsilon}, M_{\sigma\sigma}] \ddot{\bar{q}} + ([D_{\sigma\epsilon}, D_{\sigma\sigma}] + [\Delta D_{\sigma\epsilon}, \Delta D_{\sigma\sigma}]) \dot{\bar{q}} \dots \right. \\ & \left. + ([K_{\sigma\epsilon}, K_{\sigma\sigma}] + [\Delta K_{\sigma\epsilon}, \Delta K_{\sigma\sigma}]) \bar{q} \right\} \quad (50) \end{aligned}$$

From equations (45) and (46) it follows that

$$q_\sigma = -\Psi_\sigma^{-1} \Psi_\epsilon p \quad (51)$$

Inserting equation (50) into the first ϵ rows of equation (47) and taking into account equation (51) results in the following equation

$$\begin{aligned} & (M_{\epsilon\epsilon} - M_{\epsilon\sigma} X - X^T M_{\sigma\epsilon} + X^T M_{\sigma\sigma} X) \ddot{p} \\ & + \left\{ D_{\epsilon\epsilon} + \Delta D_{\epsilon\epsilon} - (D_{\epsilon\sigma} + \Delta D_{\epsilon\sigma}) X - X^T (D_{\sigma\epsilon} + \Delta D_{\sigma\epsilon}) + X^T (D_{\sigma\sigma} + \Delta D_{\sigma\sigma}) X \right\} \dot{p} \\ & + \left\{ K_{\epsilon\epsilon} + \Delta K_{\epsilon\epsilon} - (K_{\epsilon\sigma} + \Delta K_{\epsilon\sigma}) X - X^T (K_{\sigma\epsilon} + \Delta K_{\sigma\epsilon}) + X^T (K_{\sigma\sigma} + \Delta K_{\sigma\sigma}) X \right\} p = 0 \quad (52) \end{aligned}$$

where

$$X = \Psi_\sigma^{-1} \Psi_\epsilon \quad (53)$$

It can easily be shown that equation (52) can be transformed to the more convenient equation

$$Y^T \bar{M} \ddot{Y} + Y^T (\bar{D} + \Delta \bar{D}) \dot{Y} + Y^T (\bar{K} + \Delta \bar{K}) Y = 0 \quad (54)$$

$$\text{where } Y = \begin{bmatrix} I \\ -X \end{bmatrix} \quad (55)$$

with the unity matrix I . It should be mentioned that a nonsingular matrix Ψ_G can be determined optimally by applying common mathematical tools for the determination of the linear independence of a given number of vectors, as described, for example, in reference 8. These methods are also applicable to cases with the number of constraints higher than the rank of matrix Ψ_G . Practical applications to structural dynamics problems are presented in reference 9.

It is obvious that the unsteady aerodynamic forces cannot immediately be calculated on the basis of the separate normal mode sets of the several substructures (main structure and control surfaces). However, this problem can easily be solved as follows:

(1) Couple the controls to the main structure using the above described procedure. In doing so, the actual nonlinear stiffnesses C_e are replaced by linear stiffnesses chosen to be an average representative of the nonlinear ones.

(2) Calculate the normal mode characteristics of this linearly coupled system and calculate the unsteady aerodynamic forces based on this set of normal modes.

(3) In the case of hinge stiffness variations or nonlinear flutter calculations, the combination of concepts III and II described subsequently may be used.

Combined Application of Concepts I, II, and III

A detailed examination of the possibilities offered by the three concepts makes it obvious that sometimes their combined application may be very beneficial. Four possible variations can be outlined as follows:

Combination of Concept III and Concept II:

(1) Apply Concept III, taking into account linear and lightly damped hinge coupling elements.

(2) Calculate the normal mode characteristics of the linearly coupled system.

(3) Vary the linear coupling elements or introduce the nonlinear coupling elements by means of Concept II.

Combination of Concept III and Concept I:

(1) Apply Concept III with a completely rigid coupling including the control hinge degrees of freedom resulting in a configuration with rigidly locked controls.

(2) Take into account the control degrees of freedom according to Concept I by adding a separate set of control normal modes with the main structure at rest.

Combination of Concept II and Concept I:

(1) Test the aircraft structure with controls removed as a basic configuration.

(2) Establish analytically a second configuration with the controls rigidly locked to the main structure by applying Concept II. This can be achieved by adding modal mass coupling matrices ΔM to the equations of motion of the basic configuration similar to those defined in equation (31).

When a single control surface is considered the coefficients of the mass coupling matrix ΔM can be written as

$$\Delta M_{rS} = \Phi_{Rr}^T \Delta A_R \Phi_{RS} \quad (56)$$

where

$$\Phi_{Rr}^T = [u_{xr}, u_{yr}, u_{zr}, \eta_{xr}, \eta_{yr}, \eta_{zr}] \quad (57)$$

The column matrix Φ_{Rr} represents the translational and rotational displacements at the coupling point of the main structure in relation to the XYZ axis system (see fig. 10). If the center of gravity of the control lies outside the coupling point, $(x_S, y_S, z_S) = (s_x, 0, s_z)$, the inertia matrix ΔA_R can be written in the form

$$\Delta A_R = \begin{bmatrix} m_R & & & 0 & m_R s_z & 0 \\ & m_R & & -m_R s_z & 0 & m_R s_x \\ & & m_R & 0 & -m_R s_x & 0 \\ \hline 0 & -m_R s_z & 0 & I_{Rx} + m_R s_z^2 & 0 & -m_R s_z s_x \\ m_R s_z & 0 & -m_R s_x & 0 & I_{Ry} + m_R (s_z^2 + s_x^2) & 0 \\ 0 & m_R s_x & 0 & -m_R s_x s_z & 0 & I_{Rz} + m_R s_x^2 \end{bmatrix} \quad (58)$$

where

m_R mass of the control surface
 I_{Rx}, I_{Ry}, I_{Rz} mass moments of inertia of the control surface in relation to its center of gravity

(3) Take into account the control degrees of freedom according to Concept I by adding a separate set of control normal modes with the main structure at rest.

Combination of Concept II and Concept III:

(1) Test the aircraft structure with rigid control dummies in locked condition as a basic configuration. The rigid dummies are used to determine a better basic set of normal mode shapes representing the dynamic deformations of the coupled system than can be determined in the test configuration with removed controls. This procedure can best be described as convergence acceleration by means of interface loading.

(2) Establish analytically a second configuration with the dummy controls removed. This can be achieved in accordance with Concept II by subtracting a modal mass coupling matrix ΔM as defined in equation (56) from the equations of motion of the basic configuration.

(3) Apply Concept III coupling the elastic controls to the main structure.

COMPARATIVE CONSIDERATIONS

The concepts presented offer a number of possibilities to incorporate the control systems of light airplanes, which in general are affected by strong concentrated nonlinearities, into the flutter analysis. Special emphasis is placed on the mathematical modeling of the elastomechanical system based on GVT. It is obvious that a final evaluation of the applicability and accuracy of the different concepts is rather difficult because, up to the present time, only Concept I has been applied to some extent to real airplane structures. Only little experience with the other concepts is at hand. Thus, Concept II has recently been employed in the course of the flutter clearance process of the soaring airplane ASW-15. Flutter calculations based on this concept predicted tail flutter at about 200 km/hr. That result was verified by flight flutter tests, where the airplane showed nonlinear flutter in a speed range from 175 to 220 km/hr, starting with comparably small amplitudes at 175 km/hr and increasing to very high amplitudes far beyond the regular rudder stroke at higher speeds. This behavior in concurrence with substantial alterations of the flutter modes is symptomatic of highly nonlinear flutter cases. A more detailed consideration of this special problem exceeds the subject of this paper and should be reserved for further investigations.

It is also worth mentioning that the ground vibration test carried out in accordance with this concept took far less test time than a normal test on the unchanged structure (reduction of about 80%).

The first comparative investigation of the Concepts I, II, and III has been the special concern of reference 10, where results are reported for a simple plate-type wing-aileron model with largely linear elastodynamical properties. Although this model cannot be considered representative in all respects of the elastodynamical behavior of real airplanes, it seems to be opportune to use the results of this investigation together with the present experience with the Concepts I and II as a basis for a preliminary assessment concerning the advantages and the weak points of different methods. For this purpose a selected number of criteria is used taking into consideration several requirements such as

- (1) Test effort required
- (2) Numerical effort required
- (3) General applicability
- (4) Physical consistency

Table 1 shows in a condensed form how the criteria are met by the several concepts.

CONCLUDING REMARKS

It has been known for many years that the flutter clearance of light airplanes can be highly afflicted by uncertainties stemming from strong localized nonlinearities in the control mechanisms. It is shown that the establishment of more reliable and accurate mathematical models for the flutter analysis requires modified ground vibration test procedures combined with suitably adapted modal synthesis approaches. Three basic concepts with several variations have been described in detail. They offer a diverse choice of tools for carrying out both approximately linearized and nonlinear flutter investigations.

A comparative consideration has been made as to the capacity as well as the drawbacks of the different concepts. However, because of lack of practical experience with Concepts II and III, it is not possible at present to make a conclusive evaluation.

REFERENCES

1. Breitbach, E.: Effects of Structural Non-Linearities on Aircraft Vibration and Flutter. AGARD Report No. 665, Sept. 1977.
2. Dat, R.; Trétout, R.; and Lafont, J. M.: Essais de Vibration d'une Structure Comportant du Frottement Sec. La Rech. Aérospatiale, No. 3, 1975, pp. 169-174.
3. Bogoljubow, N. N.; and Mitropolski, J. A.: Asymptotische Methoden in der Theorie der nichtlinearen Schwingungen. Akademie-Verlag, Berlin, 1965.
4. Scanlan, R. H.; and Rosenbaum, R.: Introduction to the Study of Aircraft Vibration and Flutter. MacMillan Co., 1951.
5. Küssner, H. G.; and Göllnitz, H.: Theorie und Methode der Flatterrechnung von Flugzeugen unter Benutzung des Standschwingungsversuchs. AVA-Forschungsbericht 64-01, 1964.
6. Küssner, H. G.; and Breitbach, E.: Bestimmung der Korrekturglieder der Bewegungsgleichungen bei Änderungen eines elastomachanischen Systems. AVA-Report 69 J 01, 1969.
7. Breitbach, E.: Investigation of Spacecraft Vibrations by Means of the Modal Synthesis Approach. ESA-SP-121, Oct. 1976, pp. 1-7.
8. Courant, R.; and Hilbert, I.: Methoden der mathematischen Physik I. Heidelberg Taschenbücher, Springer-Verlag, 1968.
9. Walton, W. C.; and Steeves, E. C.: A New Matrix Theorem and Its Application for Establishing Independent Coordinates for Complex Dynamical Systems With Constraints. NASA TR R-326, 1969.
10. Hüners, H.: Berücksichtigung der Ruderfreiheitsgrade im Flatternachweis von Flugzeugen. DFVLR-Report IB 253-78 J 07, 1978.

TABLE 1.- COMPARATIVE CONSIDERATION OF CONCEPTS I, II, AND III

Criterion		Concept I	Concept II	Concept III
Test effort	Preparation time	Low - locking the several controls and tabs	Medium - replacement of the real hinge stiffnesses by linear ones	Medium - removal of the controls
	Test time	Very low - no angle measurements	Low - angle measurement in the hinge stiffness points	Low/medium - angle measurement in coupling points, several substructures
	Test equipment	Low - regular number of accelerometers, no angle measurements	Medium - more accelerometers in the hinge stiffness points	Medium/high - high number of accelerometers at coupling points, several substructures
	Measuring accuracy	Regular accuracy sufficient	Higher accuracy required - angle measurement	Higher accuracy required - angle measurement
Numerical effort	Elastodynamical equations	Low/medium - integration over mass distribution of controls	Low - very simple determination of coupling matrices	Medium - calculation of normal modes of coupled system necessary
	Unsteady aerodynamic forces	Low - most normal modes without hinge angle	Low/medium - all normal modes affected with hinge angles	Low/medium - all normal modes affected with hinge angles
Physical consistency and general application	Convergence	Good - for controls without resonances in the frequency range of interest	Excellent - statically indeterminate coupling included	Good - can be improved by interface loading, statically indeterminate coupling included
	Type of controls	Restricted to controls without resonances in the frequency range of interest, small size	No restrictions - controls can be very flexible and large	No restrictions - controls can be very flexible and large
	Nonlinearities	No restrictions - low number of nonlinear coupling terms	No restrictions, but higher number of nonlinear coupling terms	No restrictions, but higher number of nonlinear coupling terms

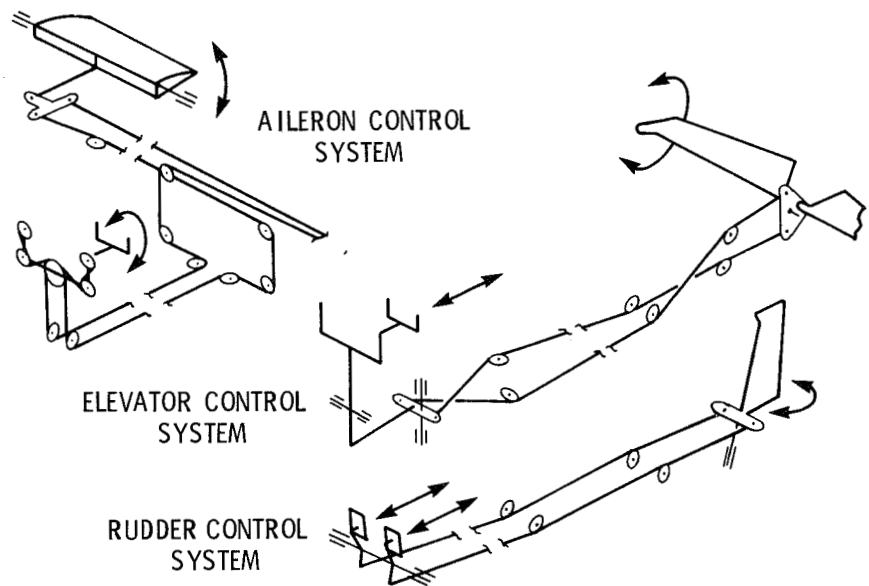
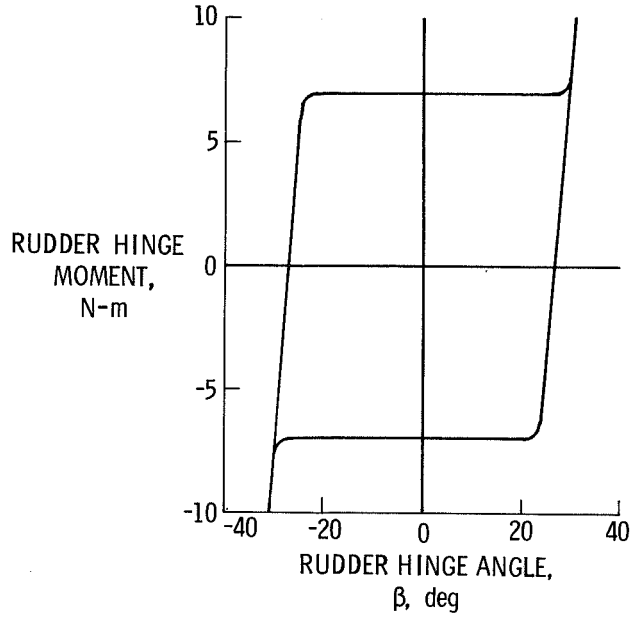
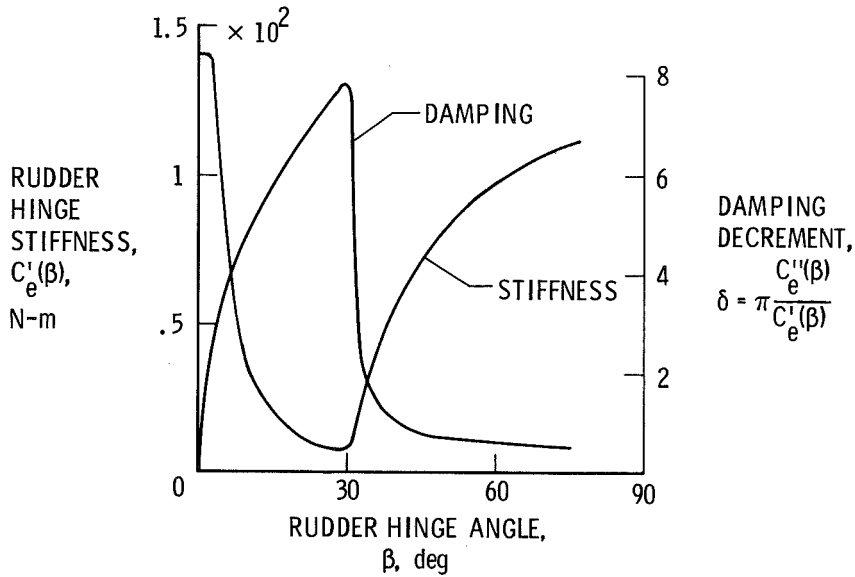


Figure 1.- Schematical sketch of the control system of a light airplane.

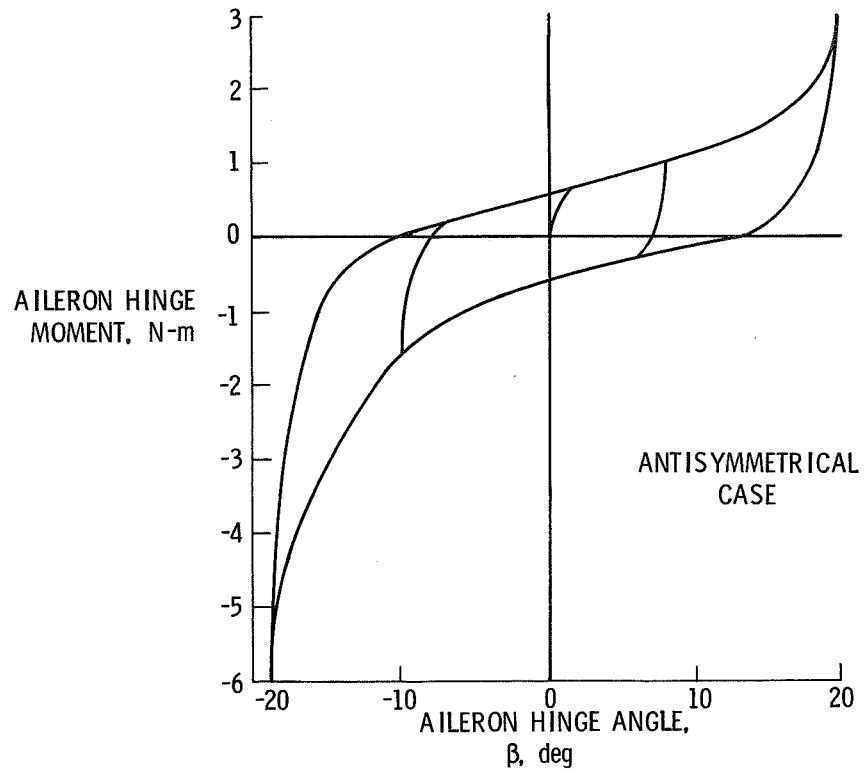


(a) Force deflection diagram.

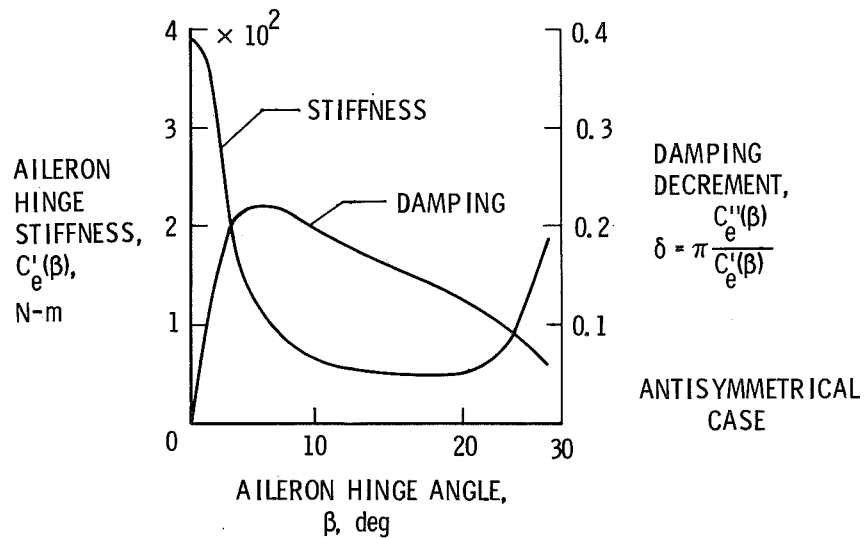


(b) Hinge stiffness and damping versus hinge angle.

Figure 2.- Force deflection diagram and stiffness and damping for the rudder system of a soaring airplane.

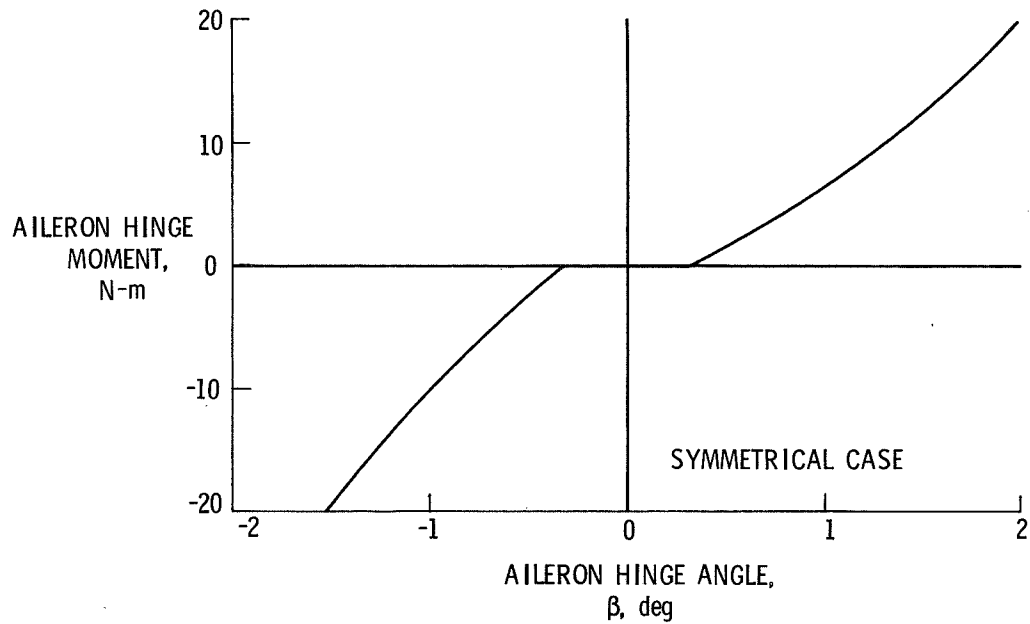


(a) Force deflection diagram.

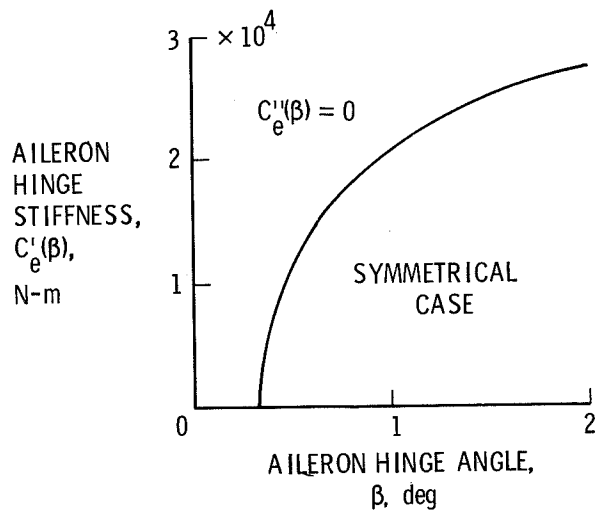


(b) Hinge stiffness and damping versus hinge angle.

Figure 3.- Force deflection diagram and stiffness and damping for the aileron system of a soaring airplane. Antisymmetrical case.



(a) Force deflection diagram.



(b) Hinge stiffness and damping versus hinge angle.

Figure 4.- Force deflection diagram and stiffness and damping for the aileron system of a soaring airplane. Symmetrical case.

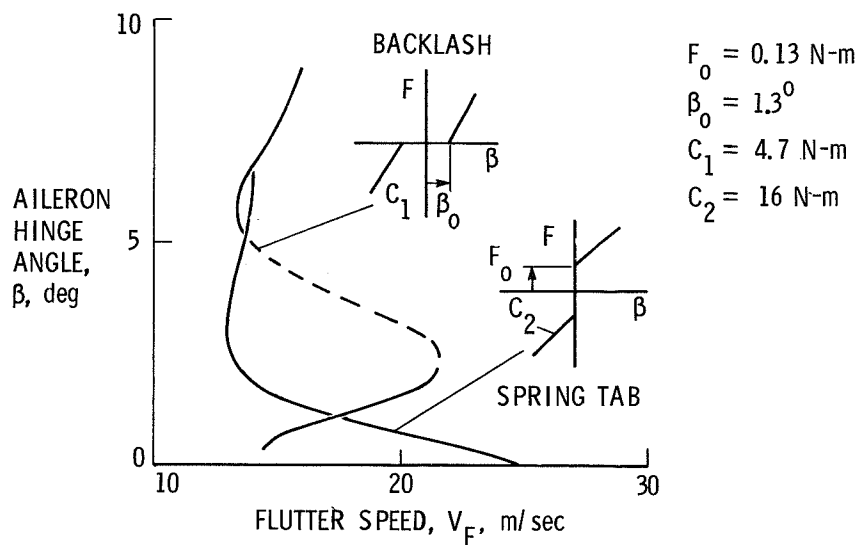


Figure 5.- Measured flutter boundary of a nonlinear model.

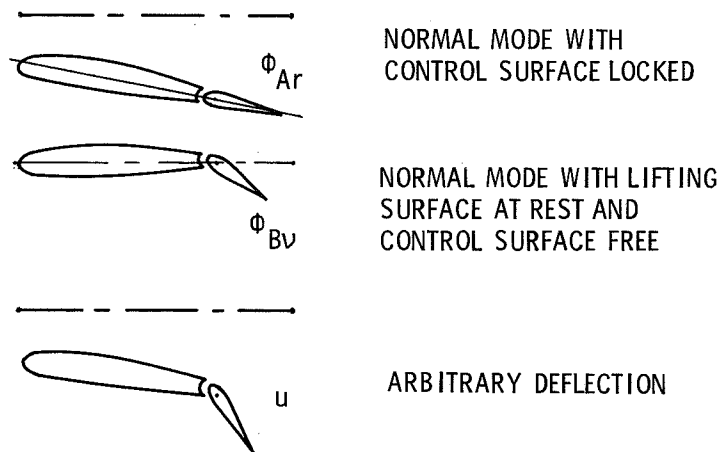


Figure 6.- Modal superposition according to concept I. Controls without tabs.

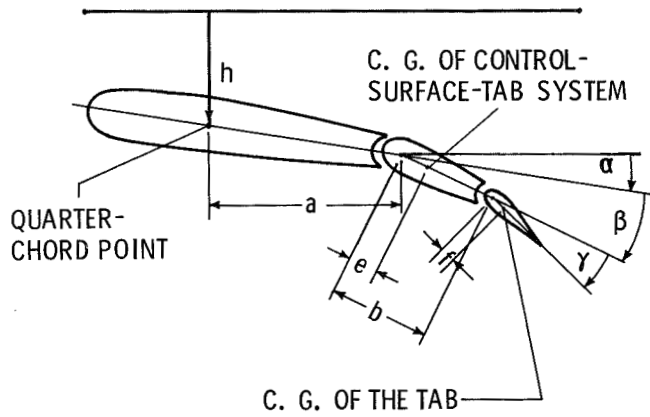


Figure 7.- Lifting surface with control surface and tab.

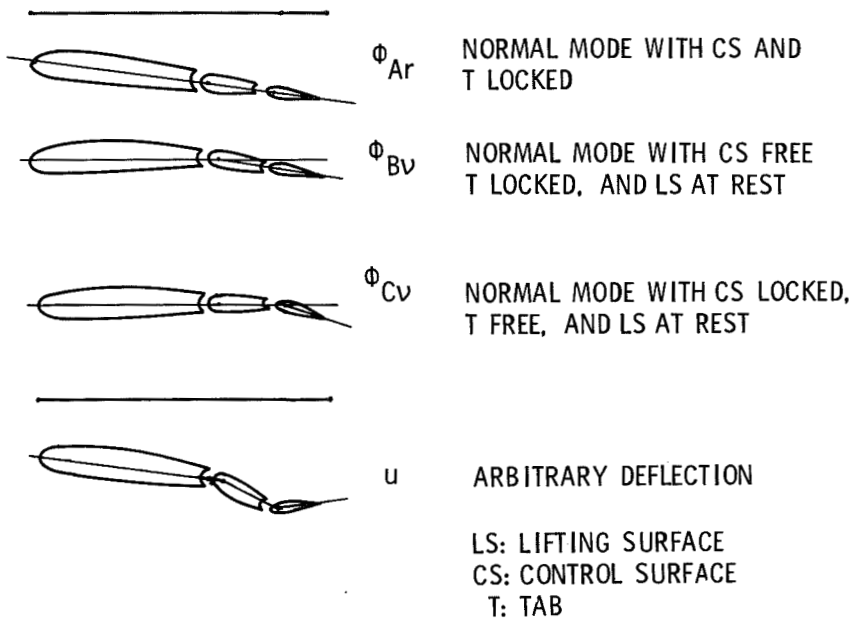


Figure 8.- Modal superposition according to concept I. Controls with tabs.

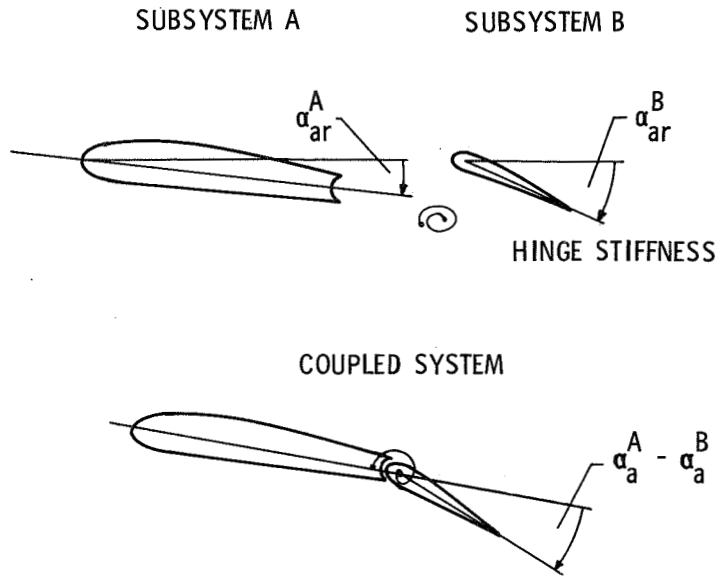


Figure 9.- Modal coupling of a wing control surface system according to concept III.

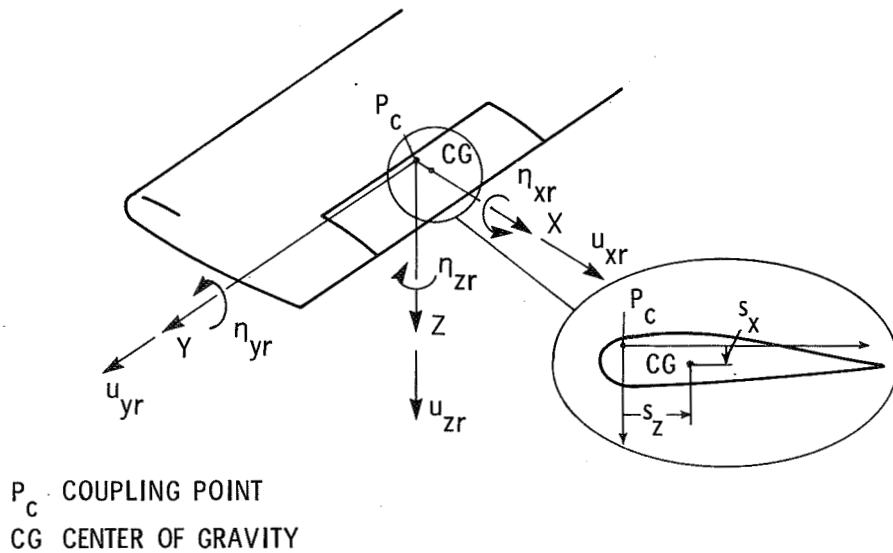


Figure 10.- Modal coupling according to a combination of concepts I and II.

ADVANCED COMPOSITES IN SAILPLANE STRUCTURES:

APPLICATION AND MECHANICAL PROPERTIES

Dieter Muser

Research Center Stuttgart
Deutsche Forschungs- und Versuchsanstalt
für Luft- und Raumfahrt e.V.

SUMMARY

Advanced Composites in Sailplanes mean the use of carbon and aramid fibers in an epoxy matrix. Weight savings are in the range of 8 to 18% in comparison with glass fiber structures. The laminates will be produced by hand-layup techniques and all material tests shown here have been done with these materials. These values may be used for calculation of strength and stiffness as well as for comparison of the materials to get a weight-optimum construction. Proposals for material-optimum construction are mentioned.

TECHNICAL HISTORY

The first fiber-reinforced glider, a Phoenix developed by Prof. Eppler, made its maiden flight in 1957. Now, more than 4000 gliders with glass-fiber-reinforced structures are in the air all over the world. Increasing the wing loading permitted increases in maximum speed, but structural demands increased the weight also.

A large span enabled the constructors to build planes with lift to drag ratios of about 50 (ASW 17: 48.5, Nimbus 2: 49) and sinking speeds of 0.50 m/s (1.64 ft/s). But it was not possible to realize wing spans with more than 22 meters without a very soft wing structure. This was possible when carbon fibers were used in the center wing section of the Akaflieg Braunschweig SB 10 in 1972 (fig. 1). With a maximum wing span of 29 meters, this glider has the best glide ratio of 53 and a sinking speed of 0.41 m/s (1.35 ft/s). But the price of carbon fibers was very high at this time and so this material was used only in another prototype, the Akaflieg Stuttgart fs-29 in 1975. To realize the old dream to vary the span during flight, it was absolutely necessary to use carbon fibers in the outer moving part of the wing and in the spar of the inner wing section. When the Akaflieg Braunschweig built the first all-carbon glider in 1977/78, they used carbon fibers to reduce weight and to stiffen the wing, so that all flaps move only very slightly and the pilot is able to handle them. And this was the year when carbon fibers were used in a larger volume in different types of commercial gliders.

WEIGHT SAVINGS

Weight and stiffness problems occur especially, and so it is not surprising that most of the new flap gliders use carbon fibers in the spar. The wings of some of the often-built gliders are shown in figure 2. All the planes use a spar with carbon-fiber-reinforced epoxy and the weight savings are in the range of about 11 to 14%. When carbon fabric is also used instead of some glass fiber fabric layers, weight savings increase up to 17.4% compared with the fully equipped wing or up to 24.3% compared with the wing structure itself.

In the matter of fuselages, weight saving rates are lower (fig. 3), because there is a higher weight percent of controls and of the landing gear. When carbon is only used in fuselage stringers, weight savings are about 8%. If some glass layers are replaced by aramid or carbon fabric, the range will increase to about 15%.

But these values are not the maximum weight savings which can be realized. Looking at specific tension strength of reinforced epoxy laminates in figure 4, mass reductions of 50% by substitution of aramid fibers and of 40% by substitution of carbon fibers are possible, when bare structures are considered.

MATERIAL PROPERTIES

All material properties shown in the following figures are test results of hand-laminated systems. Most of the tests have been undertaken at room temperature and normal outdoor humidity.

Resins were of the epoxy type, such as Rütgers-Bakelite L02/SL or L20/SL or CIBA XB 2878. These resin systems are normally cured for glider purpose at room temperature for 24 hours and postcured at 60° C (140° F) for 15 to 20 hours. They have shown better interface characteristics with carbon and aramid fibers and also higher temperature stability than the older Shell Epikote systems.

The fiber types are mentioned in each figure. The carbon is usually untwisted T300 B produced by TORAY. Fabric types which have been used have the following characteristics:

Carbon-UD:	TORAY	2002	130 g/m ²
Carbon fabric:	Interglas	03040	200 g/m ² linen
Aramid-UD:	Interglas	98616	170 g/m ²
Aramid fabric:	Interglas	98612	170 g/m ² twill
Glass-UD:	Interglas	92145	220 g/m ²
Glass fabric:	Interglas	92125	276 g/m ² twill

Material tests have been done in a lot of different works (refs. 1 to 5). But all laminates have been prepared under the same conditions and have been tested at the same test facilities.

To use advanced composites - i.e., carbon- and aramid-fiber-reinforced epoxy laminates - in spar flanges for gliders and lightweight planes, tensile strength and modulus are the most important characteristics to consider. Figure 5 shows a small advantage of Kevlar 49 compared with carbon and E-glass especially when UD-laminates are intended to be used for a wet lamination process. For torsion shells, fabrics under diagonal orientation are normally used. Therefore Kevlar and carbon have the same qualities.

But as spar flanges may also be loaded under compression, aramid fibers are not usable for this purpose. Because of its chainlike molecular structure, this material has only about 20% of tension strength capacity under compression load (fig. 6).

In all highly loaded structures the shells are also carrying loads. To calculate the load distribution between the shell and spar, it is necessary to know the elastic moduli of the materials used (fig. 7).

A conventional structure has a carbon spar, laminated with rovings or UD-tapes and a $\pm 45^\circ$ reinforced shell. So the very stiff spar will carry most of the bending loads, while the shell with only 10% stiffness in carbon or 3 to 4% in aramid or glass fiber fabric will carry only a small part of the bending forces. This is valid only when the laminate areas of the spar and the shell are in the same range. Due to the higher allowed stresses in carbon compared with glass, the cross sections of spars decrease while the shell area remains constant. So the load-carrying ratio is pushed to the side of the shell and the wing stiffness increases.

On the other hand, shear moduli of 45° laminates are higher than those of 0° or 90° laminates (fig. 8). As the shear area of the shell is much higher than the area of the spar, most of the torsion and shear loads are carried by the shell.

Figure 9 shows the shear strength of epoxy laminates found by tube-torsion tests. This test method generates the highest shear values, as there is no problem with force introduction into test specimens. Carbon laminates with $\pm 45^\circ$ fiber orientation show the highest values compared with aramid or glass fibers. Woven materials also produce higher values than nonwoven unidirectional layers oriented under $\pm 45^\circ$. These layers are better to handle and to orient.

Interlaminar shear strength (fig. 10) of carbon laminates is higher than in glass or aramid fiber laminates. The epoxy resins used most in combination with aramid and carbon fibers in Germany are the Rütgers-Bakelite L20 and CIBA XB 2878. There are only small differences in material strength, not only in interlaminar shear strength, so that these resins may be substituted one for the other. Both resins have fulfilled the airworthiness requirements issued by the Luftfahrtbundesamt.

It is not necessary to use only laminate angles of 0° , $0^\circ/90^\circ$ or $\pm 45^\circ$, which are based on production experiences to save material and time during fabrication. When different angle-ply laminates are used, the tensile modulus can be calculated as shown in figure 11 for UD-tapes in a symmetric laminate.

For gliders, temperatures of 54° C (129° F) in structures with a white surface are normally not exceeded. But the coefficients of thermal expansion should be considered (fig. 12). Additional stresses may occur in some material combinations. This is also valid when carbon is bonded to aluminium or steel. In this matter there must be also anticorrosion coatings to provide corrosion protection without any adhesive system. Stainless steels should be used in this case.

As shown before, aramid fibers are not very useful for primary structures. Especially when weight savings are necessary in some parts of planes, aramid fibers in combination with carbon fibers can be used to increase the impact resistivity.

The low impact energy of pure carbon (fig. 13) can be improved by combination with aramid fibers (fig. 14). The highest gains can be reached with a 36% carbon fiber weight ratio in an aramid-carbon-hybrid laminate (ref. 4), where carbon is the surface material. Such a material combination may be used in fuselages, especially in the cabin area, to provide large impact resistance in case of an accident.

If such hybrid laminates should be subjected to high loadings too, Poisson's ratio of the combined materials must be considered (fig. 15). In case of large differences in Poisson's ratio, secondary stresses perpendicular to the loading direction will be generated.

The investigation of fatigue usually ends at 10^6 to 10^7 load cycles. In case of the hand-laminated, room-temperature-cured epoxy laminates normally used, there are only limited valid test results available. The published results are normally valid for prepreg systems (fig. 16). Larger differences between prepreg resin systems and room-temperature-curing systems at operation temperatures of planes are not expected and the test results can be extrapolated to these laminates. Fatigue strength of carbon epoxy (about 600 N/mm²) is much higher than of glass fiber epoxy (about 200 N/mm²). But more tests have to be run with the new resin systems, because the normally used Shell Epikote/Laromin has poorer quality in combination with carbon fibers.

Special tests on wing spars have been carried out with different fiber resin systems (fig. 17 and ref. 5). A loading spectrum of various operation loads has been run with about 6 million load cycles or 9000 hours flight simulation for glass fiber spars. As the lifetime of fiber-reinforced gliders is higher than expected, an increased program for carbon spars with a safe life simulation of 12 000 hours has been run. Residual strengths of different spars indicate the safe life value of 600 N/mm² at the maximum demanded operation temperature of 54° C (129° F) (refs. 6, 7).

A new problem appears when carbon fibers are used in airplane structures. Lightning damage may occur to unprotected carbon-fiber-reinforced plastic (CFRP) up to total failure of a 6-mm laminate in an area of 80 mm diameter, corresponding to a strike of 200 kA (fig. 18 and refs. 8 to 10). The whole carbon-reinforced area must be protected with an aluminium mesh. The weight gain is small, because mesh weight is only 100 g/m². Damage is reduced to failure of the surface layers.

Different applications combining all material qualities are possible. For fuselage tubes, fiber winding technology is possible and has already been tested (figs. 19, 20, and ref. 11).

For wing structures a combination of carbon spars, carbon torsional shell, and aramid trailing edge box may be the weight optimal structure (fig. 21). In the cockpit region hybrid shells of aramid and carbon fabric may fulfill the accident requirements, while the carbon spars carry most of the bending loads.

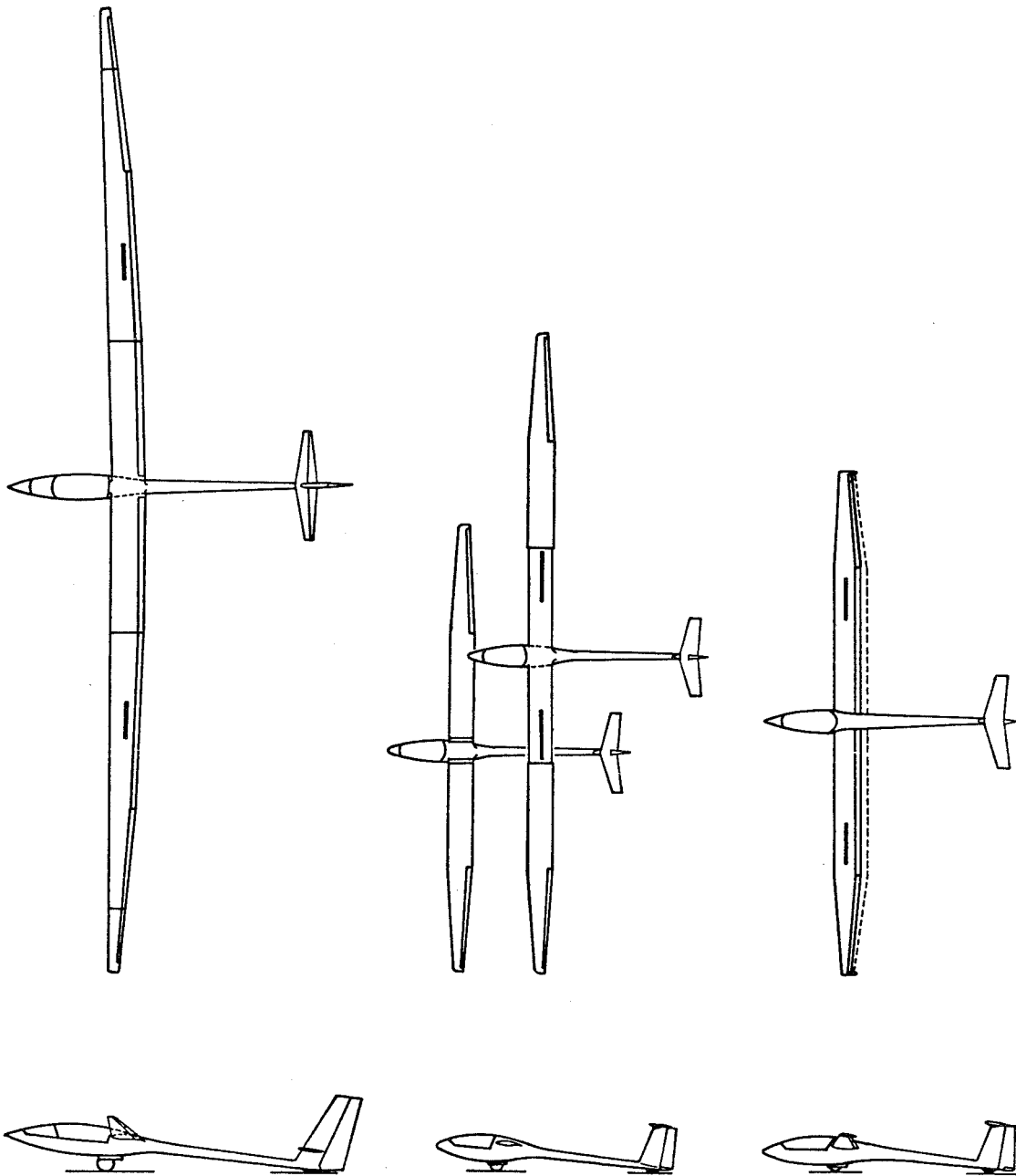
Comparing prices, a decrease is still observed and a more severe decrease is expected when automotive industries start using these fibers or new production technologies are developed. Also new manufacturing methods, such as winding or prepreg application, have to be introduced to the sailplane industry to make the new materials cost-competitive with the "old" glass fiber.

ABBREVIATIONS

CFRP	carbon-fiber-reinforced plastic
GFRP	glass-fiber-reinforced plastic
SFRP	synthetic-fiber-reinforced plastic

REFERENCES

1. Hald, H.: Versuche zur Festigkeit von Gewebe - Laminaten. DFVLR Stuttgart, IB 454-79/4 (1979).
2. Schmid, T.: Biegefestigkeiten von Gewebe - Laminaten. DFVLR Stuttgart, IB 454-79/5 (1979).
3. Kensch, Chr.; Muser, D.: Neuere Werkstoffentwicklungen und Fertigungstechniken für den Segelflugzeugbau. DFVLR Stuttgart, IB 454-77/17 (1977).
4. Hector, B.: Untersuchungen symmetrischer Mischlamine. Studienarbeit Institut für Flugzeugbau, Universität Stuttgart, May 1976.
5. Hinz, B.: Statische und dynamische Biegeversuche an CFK-Holmen mit kastenförmigem Querschnitt. DFVLR Stuttgart, IB 454-78/2 (1978).
6. LBA: Richtlinien zur Führung des Festigkeitsnachweises für Bauteile aus Kohlenstofffaser verstärkten Kunststoffen von Segelflugzeugen und Motorseglern. Luftfahrtbundesamt (LBA) Braunschweig, March 1978.
7. Niederstadt, G.: Kriterien und Beispiele für die Wahl von Verbundwerkstoffen mit Fasern hoher spezifischer Eigenschaften. In: Kohlenstoff- und aramidfaserverstärkten Kunststoffen, VDI-Verlag, Düsseldorf 1977.
8. Molly, J. P.: Blitzschutzuntersuchungen und Auslegung des Blitzschutzsystems für das GROWIAN - Rotorblatt. DFVLR Stuttgart, IB 454-78/11 (1978).
9. Skouby, C. D.: Relative Behaviour of Graphite/Epoxy and Aluminium in a Lightning Environment. Annual Book of SAMPE, Volume 23, 1977.
10. Hendricks, C. L.: Lightning Protection Techniques for Graphite/Epoxy Aircraft Structures. Annual Book of SAMPE, Volume 23, 1977.
11. Speth, J. F.: Faserverbund-Rumpfröhre. Studienarbeit Institut für Flugzeugbau, Universität Stuttgart, January 1976.



TYPE	SB 10	fs-29	SB 11
SPAN m	29	13 - 19	15
WEIGHT N	5800	3700	2600
1. FLIGHT	1972	1975	1978
FIBER	SIGRI	T 300	VARIOUS

Figure 1.- CFRP in prototypes.

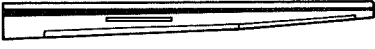
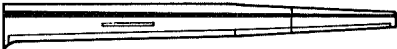
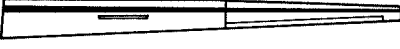
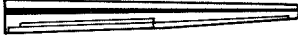
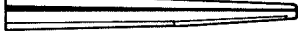
980	860		12,2	Slingsby T59
1375	1225		10,9	ASW 17
1150 COMPLETE WING	950		17,4	Nimbus 2
820 STRUCTURE	620		24,3	
650	540		16,9	Mini-Nimbus
700	600		14,3	PIK 20 D
GFRP	CFRP		[%] WEIGHT- SAVING	
WEIGHT [N]				

Figure 2.- Material substitution in sailplane wings.

1250	1150	8	25	C		ASW 17
940	830	11,7	20	C/S		Mini-Nimbus
1020	905	11,2	50 1	C		ASW 19 SB 11
930	790	15,0	1	C/S		LS 3
GFRP WEIGHT	C/SFRP WEIGHT	WEIGHT SAVING	PROD. UNITS			TYPE
[N]		[%]				

Figure 3.- Material substitution in fuselages.

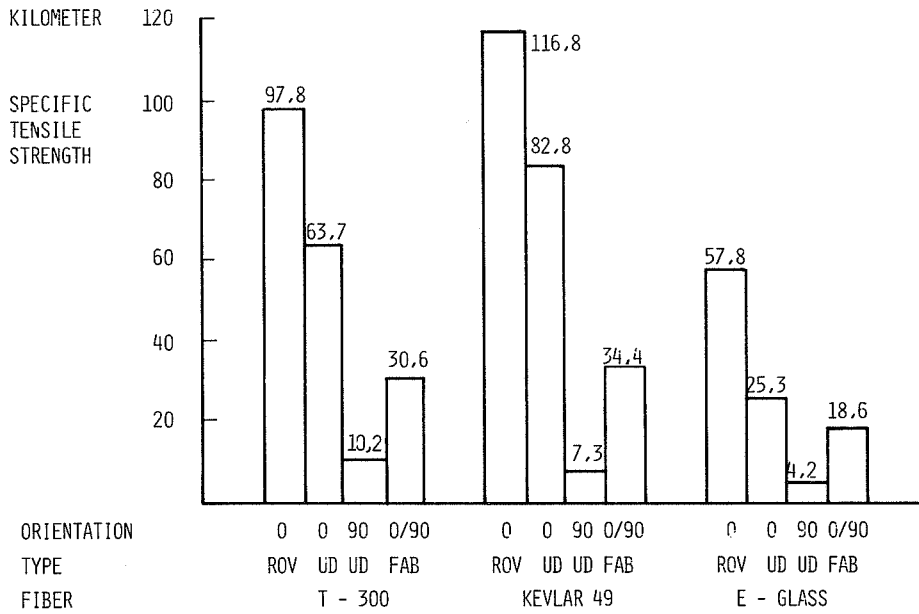


Figure 4.- Specific tension strength of epoxy laminates.

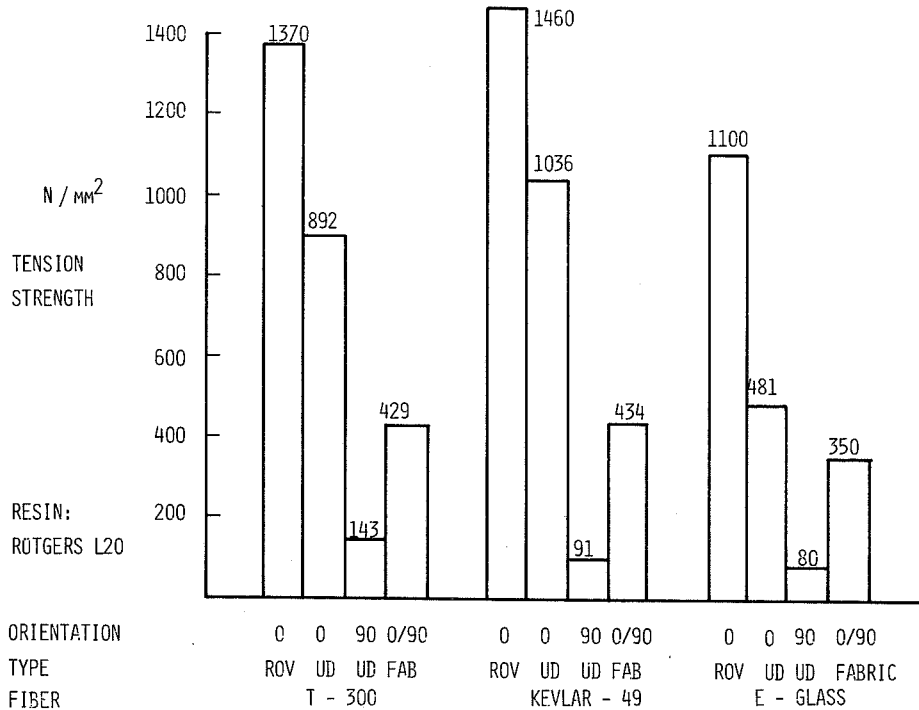


Figure 5.- Tension strength of epoxy laminates.

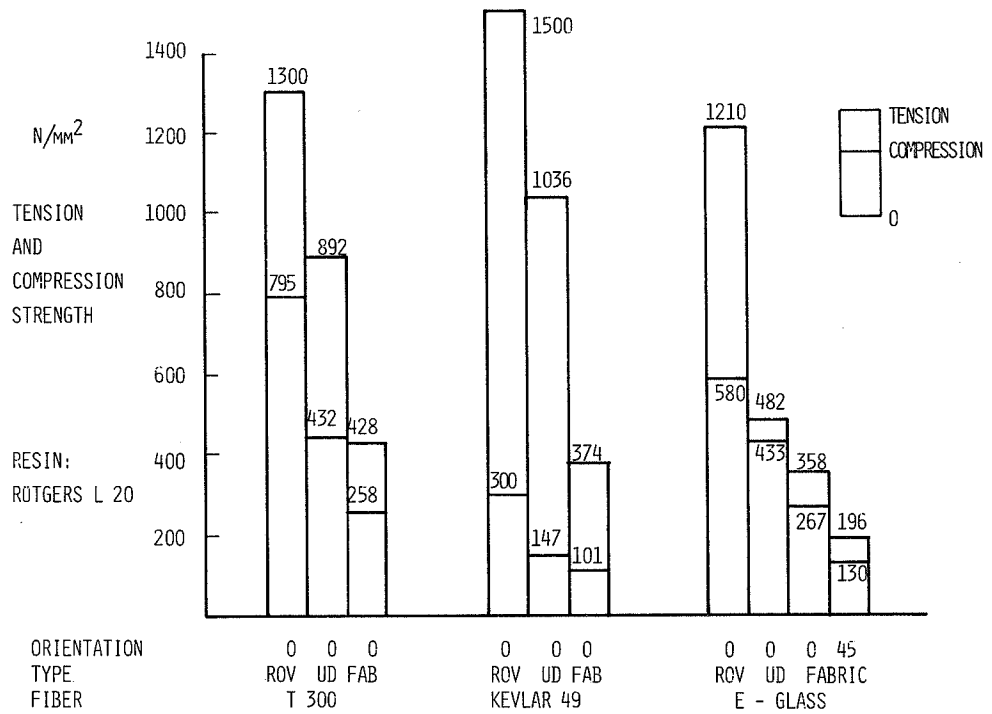


Figure 6.- Tension and compression strength.

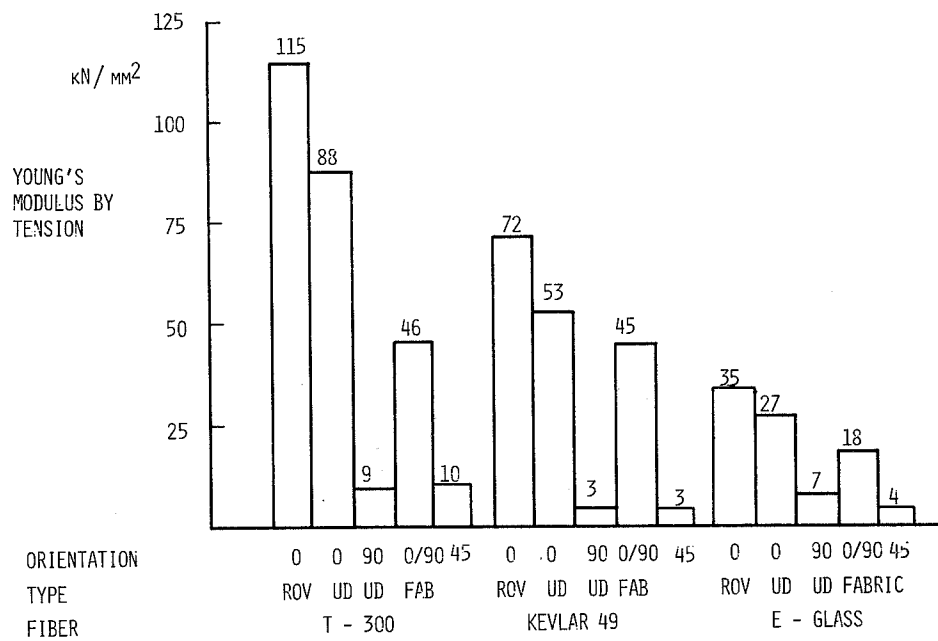


Figure 7.- Young's modulus of epoxy laminates.

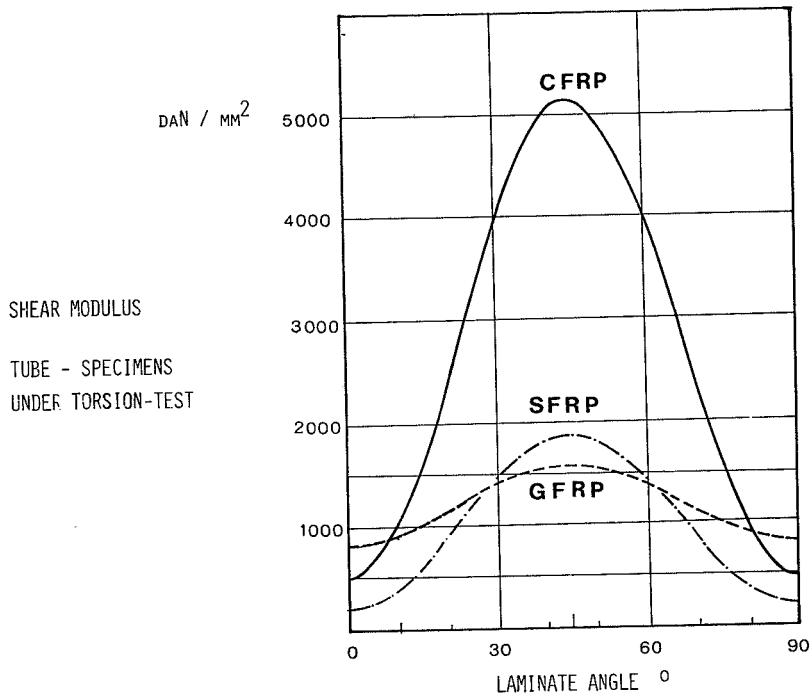


Figure 8.- Shear modulus of epoxy laminates.

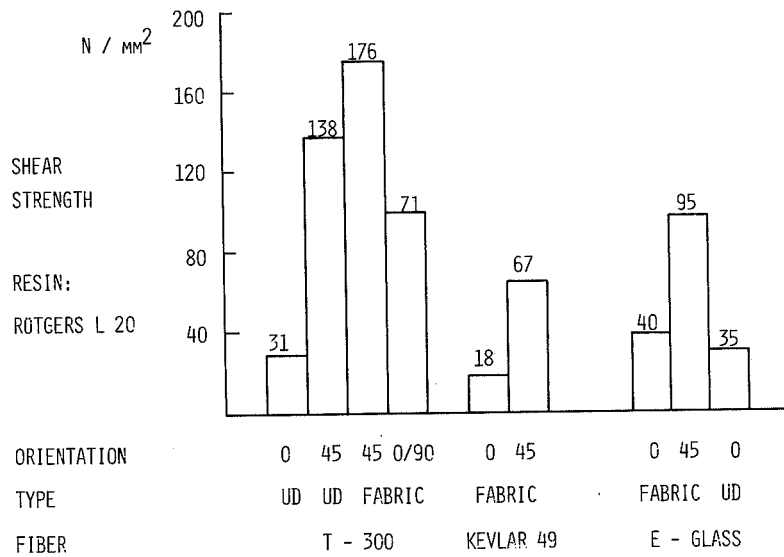


Figure 9.- Shear strength of epoxy laminates.

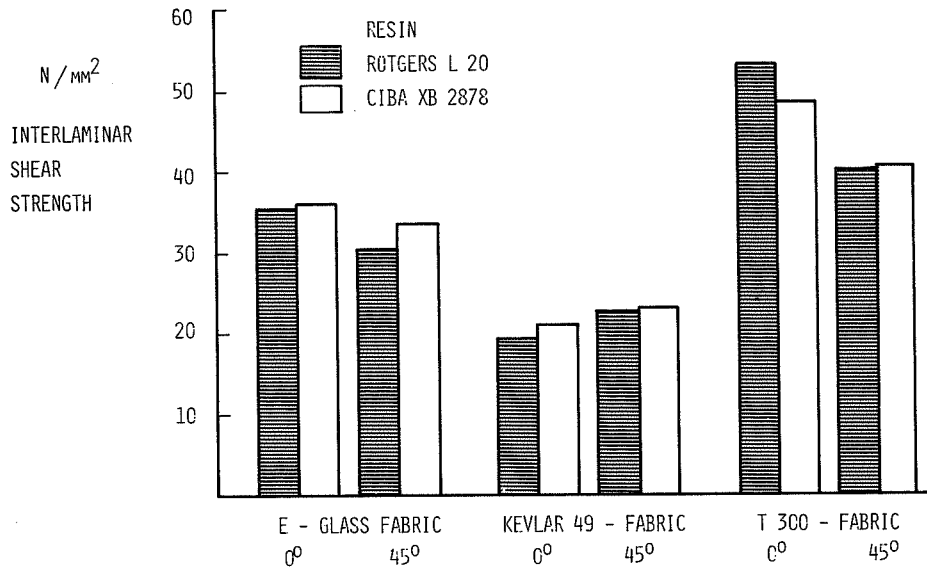


Figure 10.- Interlaminar shear strength.

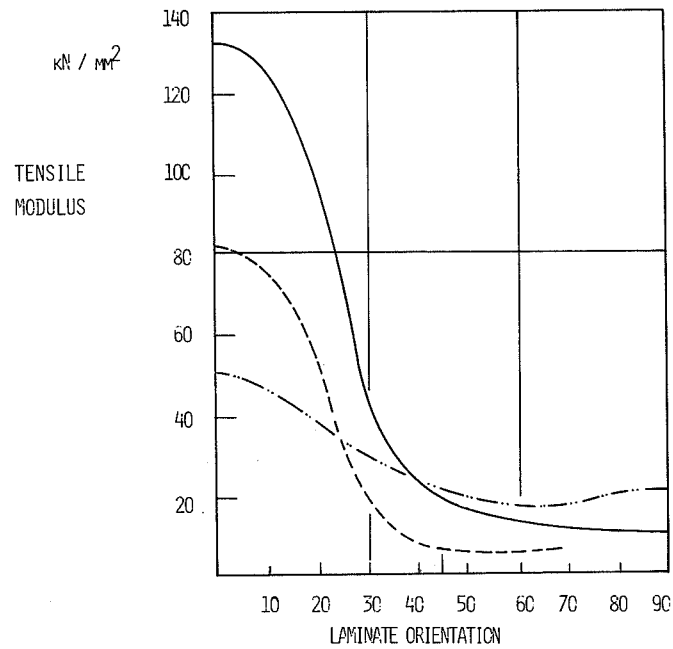


Figure 11.- Tensile modulus of angle-ply laminate.

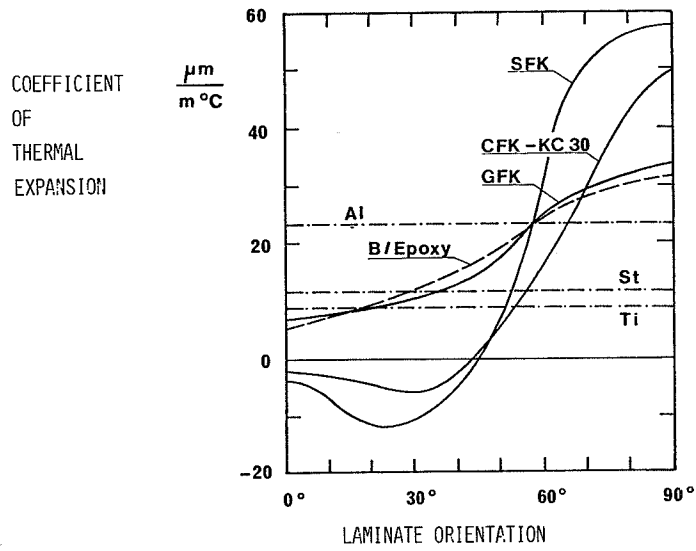


Figure 12.- Coefficient of thermal expansion.

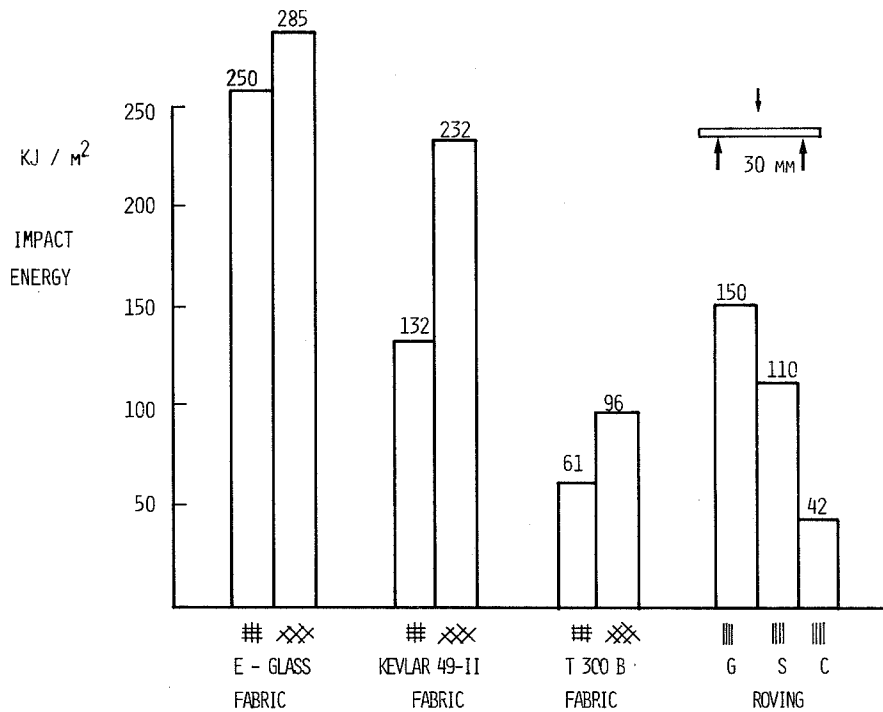


Figure 13.- Impact energy of epoxy laminates.

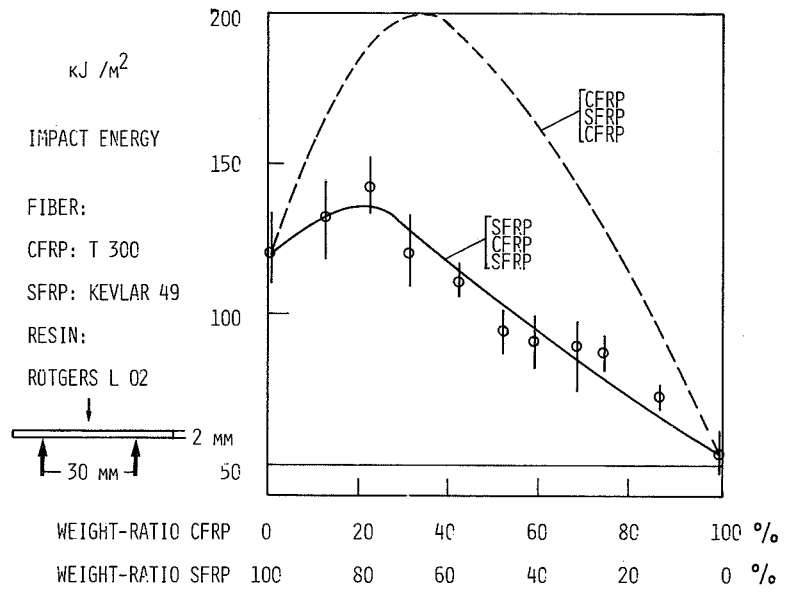


Figure 14.- Impact energy of hybrid laminates.

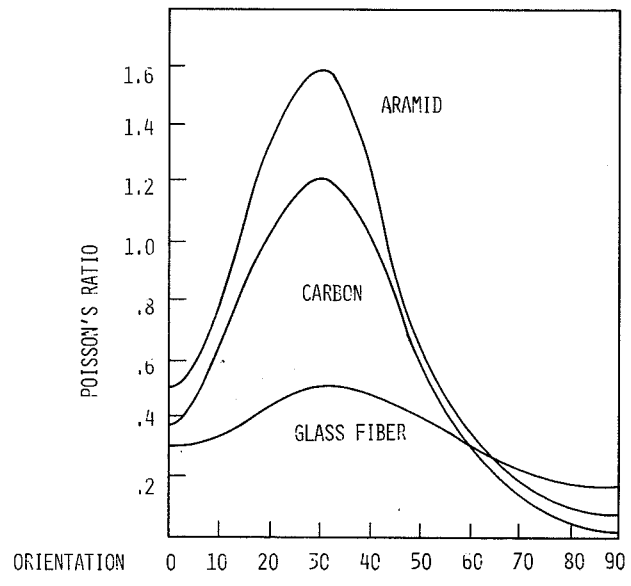


Figure 15.- Poisson's ratio of epoxy laminates.

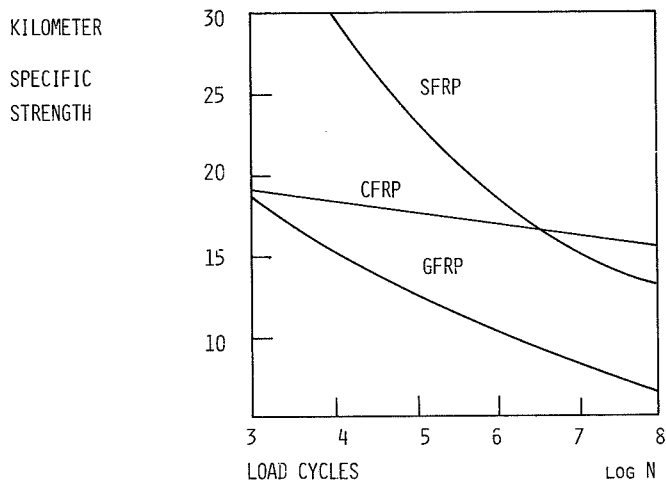


Figure 16.- Specific fatigue strength of 0° laminates.

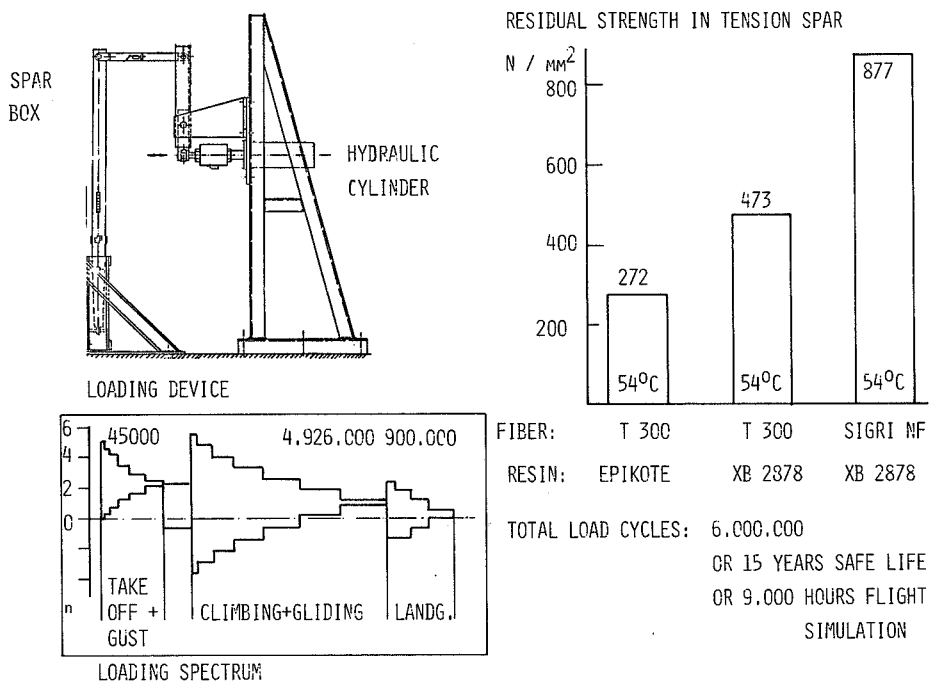


Figure 17.- Dynamic tests on CFRP glider spar box.

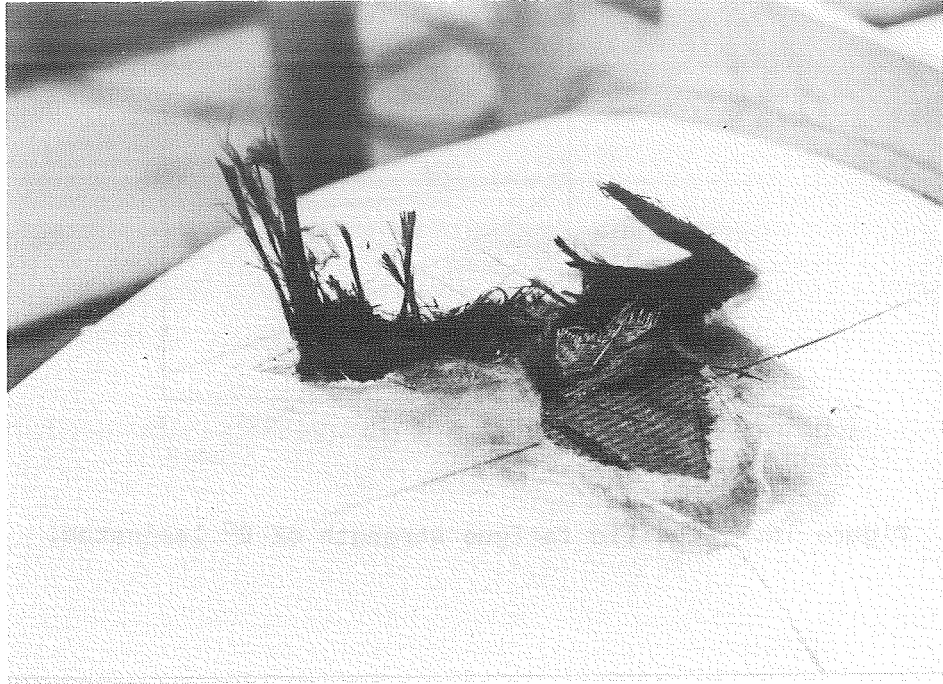


Figure 18.- Lightning damage of an unprotected carbon-reinforced wing structure.



Figure 19.- Carbon fiber winding of a fuselage tube with hybrid structure.

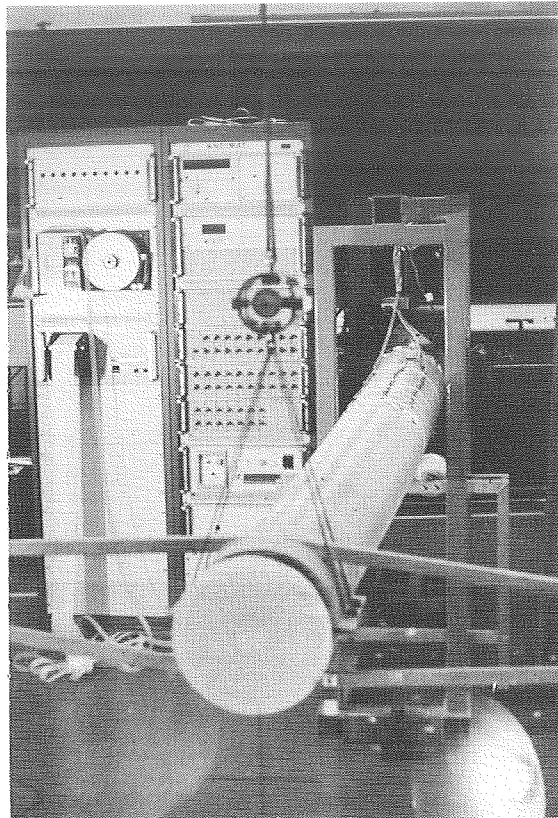


Figure 20.- Hybrid fuselage tube under bending load.

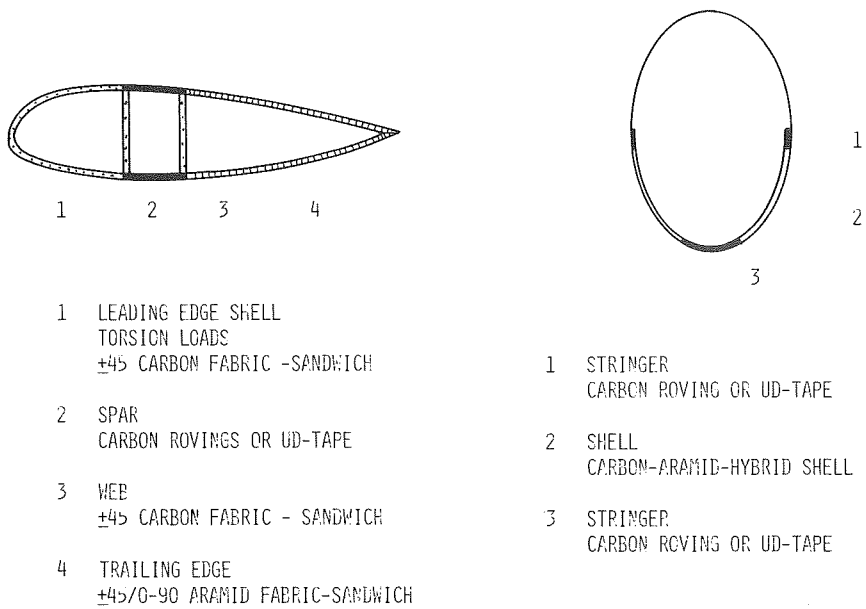


Figure 21.- Proposals for lightweight structures.

Page intentionally left blank

THE ULTRALIGHT SAILPLANE

by

J. H. McMasters

Boeing Commercial Airplane Company

Seattle, Washington

SUMMARY

The increasing cost of traditional soaring has led to a search for less expensive alternatives. During the past decade, the rise in the popularity of hang gliding, together with advances made in other branches of ultralight weight aircraft design (e.g., human powered aircraft), has demonstrated the possibility of development of a "new" category of soaring device - the "ultralight sailplane." As presently envisioned, the ultralight sailplane is intermediate in size, cost and performance between current hang gliders (defined here as a "sailplane" having a foot launch/landing capability) and the lower end of the traditional sailplane spectrum (as represented by the Schweizer 1-26, "Duster" and "Woodstock"). In the design of an ultralight sailplane, safety, low cost and operational simplicity are emphasized at the expense of absolute performance. The present paper presents an overview of the design requirements for an ultralight sailplane. It is concluded that by a judicious combination of the technologies of hang gliding, human powered flight, conventional soaring and motor gliding, an operationally and economically viable class of ultralight, self-launching sailplanes can be developed.

INTRODUCTION

The purpose of the present paper is to summarize and place in context the technical design trade-offs, performance potential and operational characteristics of a category of ultralight sailplanes which would combine several desirable characteristics of present hang gliders, sailplanes and motorgliders into a viable, low-cost alternative or supplement to all three. There are few modern examples of the ultralight sailplane envisioned here, and a central purpose of this paper is to establish the existence of an "ecological niche" for such devices.

The remarkable rise in the popularity of hang gliding during the past decade has paralleled an increase in both cost and regulation of traditional sport aviation (powered and unpowered). This has led to a rebirth in interest in a range of ultra-light weight sport aircraft. The wretched safety record and generally low performance (by modern sailplane standards) of hang gliders has resulted in substantial controversy within organizations like the Soaring Society of America (SSA) regarding the wisdom and desirability of associating

themselves in any way with the vital new sport of "ultralight soaring." To many participants in traditional soaring, the term "ultralight sailplane" is taken as synonymous with the expletive "hang glider," which conjures visions of wretched wood and fabric (or bamboo and plastic) anachronisms. This lack of discrimination among the possible types of ultra-light weight soaring devices is unfortunate and is as wrong-headed as considering "soaring" to be synonymous with fiberglass racing sailplanes and contest flying.

Despite its obvious liabilities, hang gliding has several attractive features, not least of which are low cost and simplicity (both in construction and in operation). In view of its advantages, and a surprisingly benign regulatory environment, hang gliding has gone its own way, largely oblivious to the outcries of its critics. Progress has been rapid and separate organizations have been formed to provide goals and a measure of self regulation. At present, hang gliding is represented by the US Hang Glider Association (USHGA), its British counterpart, the BHGA, and, within the Federation Aeronautique Internationale (FAI), by the Commission International du Voile Libre (CIVL).

Several authorities (including the FAA) have attempted to define the term hang glider and identify it as only one element of a larger "ultralight" matrix. Attempts to rigorously define classes of vehicles whose development is at a rudimentary stage are often inadequate and frequently degenerate into a sort of pointless legal exercise. Regarding the problem of "disassociating" the hang glider from other types of soaring device, it must be acknowledged that all but the crudest of modern hang gliders are capable of soaring under favorable conditions, and there appears to be no satisfactory way to ignore these devices when discussing the broad spectrum of possible soaring activities.

Despite the difficulty of formulating adequate general definitions, the following simple morphology is considered adequate for purposes of the subsequent discussion:

- Hang Glider - An airplane whose dominant mode of flight is gliding or soaring, wherein the pilots legs serve as the primary launching and/or landing gear.
- Ultralight Sailplane - Any "lightweight" (by Schweizer 1-26 standards) sailplane capable of steady controlled flight at a (zero wind) minimum speed below 15 m/s (~30kt).

SOURCES

While few modern examples of the sort of ultralight sailplane to be discussed here exist, its possible development must draw heavily on the wealth of data and experience gained in other branches of low-speed and motorless flight. Prior to discussing the prospects for synthesizing this information into a "new" whole, it is advisable to indicate some sources of such information.

A definitive technical history of soaring, charting its evolution from the notions of Cayley and Rayleigh, through the experiments of Lilienthal and the Wrights, the early experience at the Wasserküppe, and the fundamental transition which occurred as ridge soaring gave way to cross-country thermal and wave soaring, has yet to be written. Along the way, the classic ultralight sailplane (perhaps epitomized by the Darmstadt D28 "Windspiel") was discarded as competition sailplane performance rose to its present dramatic levels. Serious hang gliding died with Lilienthal. The brief summary of this evolution presented by Zacher (ref. 1) remains the single best semi-technical source of information on developments up to the advent of the current range of fiberglass sailplanes, and a popularized overview has been presented by Dwiggins (ref. 2). Modern sailplane developments are covered extensively in the various journals devoted in whole or part to soaring (e.g., Soaring, Sailplane and Gliding, AeroRevue, Technical Soaring). Possible future trends have been discussed recently in references 3 through 5.

The history and technology of hang gliding has been documented in several sources (refs. 6, 7, 8) and an excellent survey article by MacCready (ref. 9) describes technical and operational trends for a range of unpowered hang glider type vehicles. Developments in this branch of ultralight aviation have been very rapid and the interested reader should consult publications specifically devoted to this sport (e.g., Hang Glider, nee' Ground Skimmer; Glider Rider). Perhaps the most important development in "hang gliding" since publication of ref. 9 has been the rapid rise of powered (self launching) hang gliders (ref.7), both rigid and flexible winged.

Good sources of information on related areas of ultralight aircraft development (e.g., human powered aircraft) are contained in refs. 10 through 12. Specific background information for the present paper has been published in references 3, 8, 13 through 16. To place the subsequent discussion in quantitative perspective, the characteristics of twelve ultralight aircraft and small sailplanes are presented in Table 1.

PRELIMINARY ANALYSIS

In order to discuss the specific design requirements for an "ultralight sailplane" which could represent a true alternative to either the traditional sailplane or the modern hang glider, it is necessary to examine the possible performance ranges of existing low-speed "aircraft." For this purpose it is instructive to examine the variation of maximum aerodynamic efficiency (maximum lift-drag ratio) with the flight speed at which these values are achieved for aircraft operating below 40m/s (~80kt). Such a plot, with the apparent (approximate) bounds of the feasible indicated, is shown in Figure 1.

Lift-drag ratio by itself is not an adequate index of soaring performance, and Figure 2 has therefore been prepared to show the approximate ranges of minimum sink rate as functions of horizontal speed for some of the same categories of device shown in Figure 1. The foot launching capability limitation on cross-country speed for hang gliders is clearly shown in Figure 2.

Figures 1 and 2 show that there exists a rather large void area between the performance ranges of current hang gliders and sailplanes. This is presumably the performance range or "ecological niche" of the ultralight sailplane. While Figures 1 and 2 provide few clues to the size-performance-cost trade-offs in ultralight design, they remain instructive of the general nature of the performance spectrum to be investigated. As in Nature, if a vacant niche' exists, and good reasons for filling it exist, it will be filled - by new genera or species as necessary.

"Good" reasons for filling the ultralight niche' can be readily identified on the basis of an analysis of cost and operational penalties of traditional soaring and the performance limitations of hang gliders. Detailed cost-performance comparisons for sailplanes are always controversial, and a full discussion of the many factors involved is far beyond the scope of the present paper. However, two brief articles by Sharp (ref. 17) and Bell (ref. 18) present interesting insights into the problem of the spiralling cost of traditional soaring, and allow one to make the following observations:

1. Initial equipment cost (airframe, instruments, trailer) is a substantial portion of the cost of soaring and probably looms largest to the average pilot contemplating a first purchase.
2. There is a direct relation (with possible substantial scatter around the mean) between sailplane cost, empty weight and performance increase. Bell's analysis (ref. 18) supports the intuitive conclusion that the cost-performance relation is non-linear, with cost increasing ever more rapidly with increasing performance.
3. Over several years of utilization, the overall cost per hour of soaring dominates the cost consciousness of the enthusiast. These costs are strongly influenced (for those who neither crash nor travel frequently to national contests) by:
 - a. The requirements for aero towing (either its direct cost or the problem of availability limiting sailplane utilization).
 - b. Factors associated with fixed base operations (hangaring, tie-down, travel).

There are obvious options and alternatives to the above. Homebuilding can reduce airframe costs substantially. However, many lower cost/performance sailplanes for which plans or kits are presently available suffer from a level of structural complexity which limits their appeal to homebuilders due to the large amount of construction time involved. Further, these aircraft, once built, remain traditional sailplanes carrying the full burden of operating costs associated with any performance level sailplane (fiberglass or otherwise). In principle, motor gliders (or self launching sailplanes) could reduce direct operating costs (e.g., towing, outlandings), and increase

utilization. Motor gliding has not yet become a popular alternative in this country, due to a number of factors besides the philosophical difficulties of mating an engine to a "motorless" soaring machine. If soaring performance comparable to unpowered equivalents is sought (e.g., PIK 20E, Motor Nimbus), equipment cost becomes very high. If simplicity or cost reduction is sought in a conventional sailplane weight vehicle, power requirements become excessive and/or performance deteriorates dramatically. All too frequently, a device resembling the mooncalf off-spring of a dalliance between a Piper "Cherokee" and a Ka6 results. Finally, commercial motor glider development has been plagued for decades by the problem of availability of low-cost, reliable, light-weight, licensable engines.

Current hang gliding (powered or unpowered) may provide an alternative to sailplane soaring for some, but many more conservative individuals are put-off by the safety record of the sport, the apparent flimsiness of the equipment, and the lack of suitable instruction or flying sites in their area. Extremely light weight structures and ultra-low speeds are intrinsic characteristics of the hang glider, the resulting compromises in performance and crash protection made in exchange for the freedom and low cost of basic foot launched hang gliding being cheerfully accepted by its proponents. To many accustomed to 1-26 durability and performance, hang gliding is no alternative at all.

The latest bold extrapolation in hang gliding involves fitting "anything airworthy" with a "chainsaw" engine. This development has caused very serious concern, even among many of those who have been stout advocates of basic hang gliding. The sometimes crude, often unenlightened "cut-and-try" nature of some of these retrofits to marginal or inappropriate airframes seems a sure route to disaster. The obvious appeal is undeniable, however.

It should also be noted here that several designs for "low-cost" sailplanes have recently appeared. Only two of these, however, (the powered version of "Monerai" and the American "Eaglet", cf. Table 1) seriously address both the problems of reducing airframe cost (through reduced size and complexity) and operating cost (by incorporating a self launching capability). Both the "Eaglet" and the "Monerai" remain relatively sophisticated by contemplated ultralight standards and their appeal as a true alternative to conventional sailplanes remains to be fully demonstrated.

In view of the preceding discussion, it appears that the ecological niche' for a safe, ultralight, low-cost sailplane indeed exists and is not adequately filled by other available types of soaring equipment. As hang gliding matures and the cost of traditional soaring continues to increase, it seems unlikely that overlap between the two sports will occur (thus leaving the ultralight niche' intact), and the requirements for the ultralight alternative will increase. If the favorable prognosis for the ultralight sailplane is valid, why do so few examples of this type of machine exist at present?

The reasons for the "vacancy" in the ultralight sailplane niche' have several historical roots, but it may be conjectured that basically its time has not yet come (or returned). Soaring in the US (unlike Europe) is not a major branch of sport aviation. Potential domestic manufacturers of conventional sailplanes are faced with a limited market and the huge expense of complying with existing airworthiness certification requirements. Ultralights like the "Windspiel" became "obsolete" in the early 1930's, and domestic sailplane designers have remained enthralled with the challenges of developing high performance racing sailplanes (or more affordable imitations) ever since. The low priority of soaring due to its limited commercial potential has also resulted in a lack of the research necessary to maintain a strong modern data base from which designs can compete efficiently with European (largely German) manufacturers.

As racing sailplane performance and cost have spiralled upward together, an alternative presented itself on the extreme low end of the soaring spectrum in the form of a rebirth in interest in hang gliding. Here, at least, no technology gap existed between domestic and foreign manufacturers. In the absence of any direct government regulations on hang gliding, this turn from the sublime to the ridiculous has flourished. Hang gliding development has brought with it a whole new set of challenges to designers, and remarkable progress has been made very largely on a cut-and-try basis. As developments on both ends of the soaring spectrum mature and stabilize, the time may again become ripe to turn attention to the middle range of ultralight sailplanes, and a class of machines as different from the "Windspiel" as the Rogallo is from the box kite may emerge.

Regardless of the route future soaring developments take, it appears that there is a valid place for an ultralight sailplane in the overall scheme. It can be argued that both the "Eaglet" and "Monerai" are commendable half measures of what may eventually be possible, and a large gap still remains between these machines and the 1-26 on one side and the motorized Mitchell Wing (ref. 19) on the other. The technology exists to design a good ultralight and the last stumbling block to its early realization appears to be lack of a definite goal for its development. Ann Welch's article (ref. 15), advocating establishment of an internationally recognized "Ultralight Class" (100 kg empty weight limit) for record and competition purposes, discusses what may be wanted, provided the rules are not too confining, and the resulting machines represent clear alternatives to either present hang gliders or pseudo-racing sailplanes.

AN ULTRALIGHT SAILPLANE

On the basis of the preceding discussion it is now possible to define in more detail the concept and design requirements of a "typical" ultralight sailplane.

Concept

This light weight (empty weight less than about 1300 N~300 lbs.) sailplane is intended for local and limited cross-country soaring. The aircraft may be suitable for home construction from a limited number of prefabricated components. Launching is to be by means of other than aero towing (e.g., bungee, winch or self-launched by an air restartable engine).

Design Priorities

In order of importance:

1. Safety (benevolent launch and flight characteristics, no unusual demands on pilot skill, adequate structural strength and controllability over the entire flight envelope, crash protection for the pilot).
2. Simplicity (in both construction and operation).
3. "Low cost" (in both construction and operation).
4. Performance (adequate mild thermal soaring capability, adequate penetration into winds up to 15 m/s~30 kt).

Additional Constraints

1. The machine should be transportable on nothing more elaborate than a simple boat type trailer, towed by a compact car.
2. The machine should break down into components which allow convenient storage at the owner's residence.
3. There should be minimum requirements for, or limitation due to, special launching sites (e.g., a hill of sufficient slope and height).
4. No completely adequate airworthiness standards (U.S. or international) presently exist for this category of ultralight aircraft. Until such standards are formulated, the OSTIV Airworthiness Standards for Sailplanes should be used as a guide.

A tentative concept for the type of machine which might meet these requirements is shown in Figure 3, together with an existing "first generation" version.

TECHNICAL CONSIDERATIONS

A detailed technical discussion of ultralight design trade-offs is beyond the space limitations of the present paper. Such a study is in preparation by the author, and, in the interim, some additional technical references up-dating those in ref. 8 are presented. Although absolute performance is not the primary design goal of the ultralight sailplane, it remains necessary to examine carefully several areas of performance compromise involved in meeting primary design objectives (e.g., safety, low-cost, simplicity).

Aerodynamic Requirements

In general, sailplane aerodynamic preliminary design optimization is performed assuming a "glider" operating in rectilinear flight, with central emphasis placed on the achievement of a high lift-to-drag ratio (minimum glide angle) at a "desired" forward speed. Around this pivot point in the performance polar, low sink rates at both low (for climb) and high (cross-country) speeds are juggled until a satisfactory "racer" has been defined. If thermal soaring is envisioned, only towards the end of the analysis is sink rate in a banked turn seriously considered. It has recently been argued by Eppler (ref. 20) and Irving (ref. 21) that emphasis on analysis of the rectilinear portion of the glide may lead to non-optimum sizing (selection of wing area and aspect ratio) of 15m span sailplanes which must both thermal efficiently and achieve good high speed performance. Under a variety of conditions (ballast levels and thermal models assumed), a racing sailplane optimized for minimum sink rate in a turn and a high forward speed in the region around 2-3 m/s rate of sink should have a somewhat lower than customary aspect ratio. In the 15 m examples considered, this means larger area. In these examples, absolute rectilinear L/D suffers somewhat, but average cross-country speed (in the MacCready sense) increases.

For somewhat different reasons, the ultralight sailplane presents the same two-point optimization problem confronted by the classic thermal soaring racer, with rectilinear maximum L/D being of importance only insofar as it reflects minimum sink rate (at an arbitrary bank angle) and high speed (penetration) capability. High speed penetration capability is basically a safety objective, and only secondarily a desirable performance objective in the ultralight. Minimum sink rate is the fundamental performance objective. An indication of banked turn performance is shown in Figure 4.

Unfortunately, the banked turn, minimum sink rate, optimum sizing problem is a great deal more complex than the simple rectilinear flight problem. For further discussions, the papers by Marsden (ref 22, 23) and Cone (ref. 24), in addition to those by Eppler (ref. 20) and Irving (ref. 21), should be consulted. Any serious ultralight design must also consult the report by Shenstone and Scott-Hall (ref. 25).

While ultralight detailed aerodynamic wing design should follow conventional sailplane practice (although aspect ratios may be substantially lower), the selection of suitable airfoil sections presents a major problem due to the general lack of experimental data for appropriate sections optimized at sufficiently low Reynolds number. Existing data is surveyed in refs. 26 through 34. The airfoil selection and design problem is further complicated by the strong coupling between high-lift/low-drag aerodynamic and simple, light weight wing structural requirements. Modern laminar sailplane sections are generally inapplicable to an airplane wherein the structure is unlikely to support laminar flow much beyond 30-40% of the wing chord. In this light, the experience with sailplanes of 1930-40 vintage (refs. 25, 27) provide a far better guide to airfoil selection and performance than do those of the 1970's.

Aerodynamically, the ultralight is an excellent candidate for a fully flapped wing (preferably involving flaps with a high degree of Fowler motion). Unfortunately, this desirable feature directly conflicts with the simplicity requirement, and cannot be advised for early generations of such aircraft. Further data on this topic can be found in references 35 through 39.

Aerodynamic Constraints

The basic first order equations of sailplane motion (cf. refs. 22, 24, 40) show that both minimum sink rate and maximum L/D are (for equal weight vehicles) most powerfully influenced by wing span. High speed performance is largely one of profile/parasite (viscous dependent) drag which increases as the square of the flight speed. Further, whereas weight and/or wing loading increase helps high speed performance, it seriously erodes minimum sink performance. Overall, then, for a racing sailplane the trend should be towards large span (to regain low-speed performance) and high wing loading and extreme aerodynamic "cleanliness" to maximize high speed performance. In addition, a better match between desired low- and high-speed performance can be had by use of flaps.

This simplistic view ignores important aspects of the low-speed thermalling (banked turn) mode, however; these effects may be particularly important in attempts to transfer the above recipe to an ultralight. Increasing span leads to increasing wing weight. Drag cleanup and flaps are contrary to structural simplicity. Most important is the "low-speed turn problem" which puts the ultralight in closer kinship with the vulture and the HPA than the racing sailplane, and may ultimately establish a practical upper bound on wing span, just as aeroelastic effects at high speed ultimately limit the span of high-performance sailplanes.

In a steady turn, the radius is a purely kinematic function proportional to the square of the sailplane's velocity and the reciprocal of the tangent of the bank angle. For an ultralight type vehicle (vulture, hang glider), the normal thermalling speed may be decreased to the point where the wing span

becomes a significant percentage of the turn radius. As discussed in refs. 41-43, this situation results in substantial gradients of velocity (and hence dynamic pressure and Reynolds number) across the span, and a corresponding distortion of the untrimmed span loading accompanied by an outboard shift in the center of lift which tends to steepen the turn. To counteract this overbanking tendency, powerful trimming devices (ailerons and rudder) and dihedral are required, and/or the bank angle or wing span must be limited. Regardless of other precautions, the depressed Reynolds number over the inboard semi-span during a turn may aggravate any tendency towards tip stall with the danger of a subsequent spin. The vulture's solution to this problem (ref. 24) is worth noting, since it represents a marvelous example of the coupling between structural strength/stiffness, high-lift aerodynamics and minimization of trim drag.

Structures and Weight

Surprisingly little good information on ultralight structural techniques exists. The best sources relate to human powered aircraft, the structures of which are generally complex. Of all the aspects of ultralight development, structural weight reduction and simplification are in most need of major effort. The author's favorite sources on these topics are references 44 through 48.

Launching

Provision of an alternative to aero towing for launching an ultralight sailplane is central to the operational simplicity concept. The success of the motorized hang glider makes the notion of a motorized self-launching ultralight sailplane an attractive idea. The key to success here lies in availability of reliable "engines" (internal combustion or otherwise). It should also be noted that either the canard or the flying wing configuration seem natural for a powered ultralight due to the ease of low drag integration of an engine into the design. Some information on suitable engine/propeller combinations are contained in references 49 and 50.

CONCLUSIONS

An evaluation of the requirements for an inexpensive alternative to conventional soaring has shown that an "ecological niche" apparently exists for an ultralight sailplane intermediate in performance and weight between modern hang gliders and traditional sport sailplanes. There appear to be no serious constraints on the economic or operational viability of such a device. Four factors appear to be central to progress towards its early realization:

1. Development of simple structural techniques for minimum time and cost construction of wings of adequate aerodynamic quality, strength and stiffness.
2. Availability of reliable, light weight, low powered and low-cost engines to provide a self launching capability, and/or development of "minimum" non-aero tow launching methods.
3. Establishment of suitable goals for ultralight sailplane performance and design (e.g., national or international recognition of an Ultralight Class for record or competition purposes).
4. Clarification of the relationship of hang gliding (powered or unpowered), ultralight sailplanes and government (FAA) regulation. Whether regulated by the government or not, a suitable set of airworthiness standards for "ultralights" needs to be developed.

As a final thought, it can be argued that the single most important factor which made the modern hang glider renaissance flourish as it has was the structural and aerodynamic model presented at the outset by the Rogallo wing. The utter simplicity of this concept completely outweighed its very modest performance. As it turned out, this performance was quite good enough to launch a new sport and its supporting industry. The great progress in hang gliding since a few visionaries began diving off sand dunes in bamboo and plastic monstrosities has been accomplished very largely by cut-and-try, further tribute to the basic simplicity of the initial concept. It now remains for some individual to make the same sort of creative leap which could usher in the modern ultralight sailplane.

REFERENCES

1. Zacher, H., "The Shape of High Performance Sailplane Technical Development," The World's Sailplanes, Vol. II, edited by B. S. Shenstone and K. G. Wilkinson, OSTIV Publication, 1963.
2. Dwiggin, D., On Silent Wings, NY: Gossett and Dunlap, 1970.
3. McMasters, J. H. and Nash-Webber, J., "Some Technical Extrapolations," Soaring, January 1977, pp. 21-28.
4. Carmichael, B. H., "On Predicting the Future of Soaring Flight," Soaring, April 1977, pp. 25-30.
5. Brain, V., "The Next 25 Years - An Overview," Soaring, January 1977, pp. 14-19.
6. McMasters, J. H. and Cole, C. J., "Ecoflight Is Here," Lifestyle No. 3, February 1973. (Available from The Mother Earth News, P.O. Box 70, Hendersonville, NC 28739.
7. Gustafson, D., "Powered Hang Gliders and Such," Sport Aviation, August 1978, pp. 10-14.
8. McMasters, J. H., "Some Opportunities for Progress in Ultralight Aeronautics," Soaring, June 1975, pp. 22-26.
9. MacCready, P. B. Jr., "Developments in Ultralight Gliding," Soaring, June 1976, pp. 23-29.
10. McMasters, J. H. and Palmer, G. M., "At the Threshold of Man Powered Flight," Aeronautics and Astronautics, September 1977, pp. 60-70.
11. Reay, D. A., The History of Man-Powered Flight, NY: Pergamon Press, 1977.
12. McMasters, J.H. and McLean, J. D., "The Formulation Flight of Human Powered Aircraft Across the English Channel in the Spring," presented at the XVI OSTIV Congress, Chateauroux, France, July 1978. (See also Soaring, June 1978, pp. 16-22).
13. McMasters, J. H., "Four Ultralight Questions," Soaring, July 1977, pp. 14-15.
14. McMasters, J. H., "Ultralight Survey Results," Soaring, December 1977, pp. 27-30.
15. Welch, A., "The Orphans," Soaring, July 1978, p. 14.

16. Worthington, G., "Wheels vs. Foot Launching," Soaring, July 1978, p. 15.
17. Sharp, T., "The Myth of Cheap Soaring," Soaring, August 1977, p. 27.
18. Bell, D., "A Look at the Used Sailplane Market," Soaring, January 1978, p. 31.
19. Patmont, S., "Free at Last," Soaring, August 1978, pp. 12-13.
20. Eppler, R., "The Optimum Design and Wing Section of a 15m Glider Without Flaps," Sailplane and Gliding, June/July 1977, pp. 110-117.
21. Irving, F., "Computer Analysis of the Performance of 15m Sailplanes," in Motorless Flight Research - 1972, J. L. Nash - Webber ed., NASA CR 2315, November 1973.
22. Marsden, D. J., "Circling Performance of Sailplanes," OSTIV Pub. XI, 1970.
23. Marsden, D. J., "Gemini - A Variable Geometry Sailplane," AIAA Paper 74-1035, September 1974. (Proc. 2nd Int. Symposium Low-Speed and Motorless Flight).
24. Cone, C. D. Jr., "The Design of Sailplanes for Optimum Thermal Soaring Performance," NASA TN D-2052, January 1964.
25. Shenstone, B. S. and Scott-Hall S., "Glider Development in Germany," NACA TM 780, 1937.
26. McMasters, J. H., "Low-Speed Airfoil Bibliography," Tech. Soaring, Vol. 3, No. 4, Fall 1974, pp.40-42.
27. Riegels, F. W., Airfoil Sections, London: Butterworth, 1961.
28. Jacobs, E. N. and Sherman, A., "Airfoil Section Characteristics as Affected by Variations of the Reynold Number," NACA TR 586, 1937.
29. Liebeck, R. H., "Design of Subsonic Airfoils for High Lift," Jour. of Aircraft, September 1978, pp. 547-561.
30. Henderson, M. L., "Inverse Boundary-Layer Technique for Airfoil Design," Proceed. of the NASA Advanced Technology Airfoil Research (ATAR) Conference, NASA CP-2045, March 1978.
31. Wortman, F. X., "Airfoil Design for Man-Powered Aircraft," Proceed. of the 2nd Royal Aero. Soc. MPA Group Symposium, February 1977. (Roy. Aero. Soc., 4 Hamilton Place, London W1V 0BQ, England)

32. Eppler, R., "Turbulent Airfoils for General Aviation," Jour. of Aircraft, February 1978, pp. 93-99.
33. Hiscocks, R. D., "Airfoils," Soaring, November-December 1951.
34. McGhee, R. J. and Beasley, W. D., "Effects of Thickness on the Aerodynamic Characteristics of an Initial Low-Speed Family of Airfoils for General Aviation Applications," NASA TMX-72843, December 1976.
35. Smith, A. M. O. "High Lift Aerodynamics," Jour. Aircraft, Vol. 12, No. 6, June 1975, pp. 501-530.
36. Bingham, G. J. and Noonan, K. W., "Low-Speed Aerodynamic Characteristics of NACA 6716 and NACA 4416 Airfoils with 35% Chord Single-Slotted Flaps," NASA TMX 2623, 1974.
37. Wortmann, F. X., "The Sailplane," Aero-Revue, June 1971. (Also OSTIV Publ. XI).
38. Wenzinger, C. J. and Harris, T. A., "Wind Tunnel Investigation of an NACA 23012 Airfoil with Various Arrangements of Slotted Flaps," NACA TR 664, 1939.
39. Feifel, W., "Combination of Aileron and Flap Deflection on Minimum Induced Drag Roll Control," presented at XVI OSTIV Congress, Chateauroux, France, July 1978.
40. Falk, T. J. and Matteson, F. H., Sailplane Aerodynamics, American Soaring Handbook Vol. 9, LA: SSA, 1971.
41. McMasters, J. H., "The Prospects for Man-Powered Flight," Tech. Soaring, Vol. 1. No. 2, October 1971.
42. McMasters, J. H., "The Optimization of Kremer Competition Man Powered Aircraft," Proceed. of the 2nd Internat. Sym. on the Tech. and Sci. of Low-Speed and Motorless Flight, September 1974.
43. Phillips, W. H., "Analysis and Experimental Studies of the Control of Hang Gliders," AIAA Paper 74-1030, September 1974.
44. Czerwinski, W., "Dominant Factors in Light Weight Design," Can. Aero. Space J., January 1967, pp. 9-22.
45. Czerwinski, W., "Man-Powered Flight, Its Purpose and Future," AIAA Paper 70-879, July 1970.
46. Wimpenny, J. C., "Structural Design Considerations in Man-Powered Aircraft," Aero J., May 1975, pp. 198-207.

47. Pazmany, L. et. al., "Potential Structural Materials and Design Concepts for Light Airplanes," NASA CR-1285, March 1969.
48. Stender, W., "Sailplane Weight Estimation," OSTIV Publication, June 1969.
49. "Dyad 280, A Self-Launch Engine," Soaring, December 1977, pp. 31-34.
50. Rautio, J., "15-Meter Motorglider Performance Calculations," Soaring, December 1978, p. 3.
51. Rogers, B., "1974 Sailplane Directory," Soaring, August 1974.
52. Hoose, S. (ed), "1978 Sailplane Directory Supplement," Soaring, August 1978, pp. 21-44.
53. Simons, M. "The D38 Windspiel," Soaring, February 1972, pp. 35-36.
54. Zacher, H. "Flugmessungen mit Segelflugzeugen von 12 bis 13m Spannweite," OSTIV Publication IX (1965, pt. 2).
55. Maupin, J. "Woodstock," Soaring, May 1978, pp. 38-39. Also, Soaring, June 1978, p. 3.
56. Hall, S., "The Vector I," Soaring, August 1975.
57. Foreman, J. M., "Monerai," Soaring, June 1978, pp. 14-15.
58. Haig, L., "American Eaglet," Soaring, March 1976, pp. 16-19.
59. Worthington, G., "Getting Acquainted With the American Eaglet," Soaring, March 1978, pp. 10-14.
60. Mitchell, D., "The Mitchell Wing," Soaring, June 1977, pp. 26, 40.
61. Allen, W. A., "Hoist on Your Own Canard," Pop. Mech., Sept. 1978, pp. 56-57.
62. Price, C. B., ed., "USHGA Hang Glider Directory," Ground Skimmer (now Hang Glider), December 1975.
63. McMasters, J. H., "An MPA Prediction," Soaring, April 1977, p. 3.
64. Johnson, D., et. al., "The 1977 Supershops - A Consumer Report," Glider Rider, May 1977, pp. 27-30, (P. O. Box 6009, Chattanooga, TN 37401).

Table 1. Aircraft Characteristics

Type	Wing Span m (ft)	Wing Area m ² (ft ²)	Aspect Ratio	Weights		Wing* Loading N/m ² (psf)	Estimate L/D max.	Ref.
				Empty N (lb)	Loaded* N (lb)			
Schweizer 1-26	12.2 (40.0)	14.87 (160.0)	10.0	1826 (410)	2628 (590)	176.6 (3.69)	21.6	51
Darmstadt D28b "Windspiel"	12.0 (39.4)	11.4 (122.6)	12.6	704 (158)	1506 (338)	132 (2.76)	23.5	1, 53, 54
Maupin "Woodstock"	11.9 (39.0)	9.73 (104.7)	14.5	1047 (235)	1849 (415)	190 (3.96)	24	52, 55
Hall "Vector I"	10.4 (34.0)	11.6 (125)	9.25	668 (150)	1470 (330)	127 (2.64)	17	52, 56
Monett "Monerai"	11.2 (36.7)	7.3 (78.5)	17.2	1025 (320)	1826 (410)	250 (5.22)	30	52, 57
Haig/American "Eaglet"	11.0 (36.0)	6.7 (72.0)	18.0	713 (160)	1515 (340)	226 (4.72)	26.5	52, 58, 59
Marske "Monarch"	12.8 (42.0)	17.3 (186)	9.5	980 (220)	1782 (400)	103 (2.15)	20	52
Hill "Super- floater"	9.76 (32.0)	12.3 (132)	7.8	401 (90)	1203 (270)	98 (2.05)	12	52, 62
Mitchell Wing	10.4 (34.0)	12.6 (136)	8.5	347 (78)	1149 (258)	91 (1.90)	14	52, 60
Aviafibre Canard 2FL	13.5 (44.4)	9.1 (98)	20	423 (95)	1225 (275)	94 (1.96)	28	61
Bennett "Phoenix 8"	11.3 (37.1)	17.9 (193)	7.15	254 (57)	1056 (237)	59 (1.23)	8	62, 64
Nihon U. "Stork B"	21.0 (68.9)	21.7 (233.5)	20.3	354 (79.4)	1155 (259.4)	53 (1.11)	28	12, 63

*Weight assumes pilot plus equipment weight of 800 N ~ 180 lb.

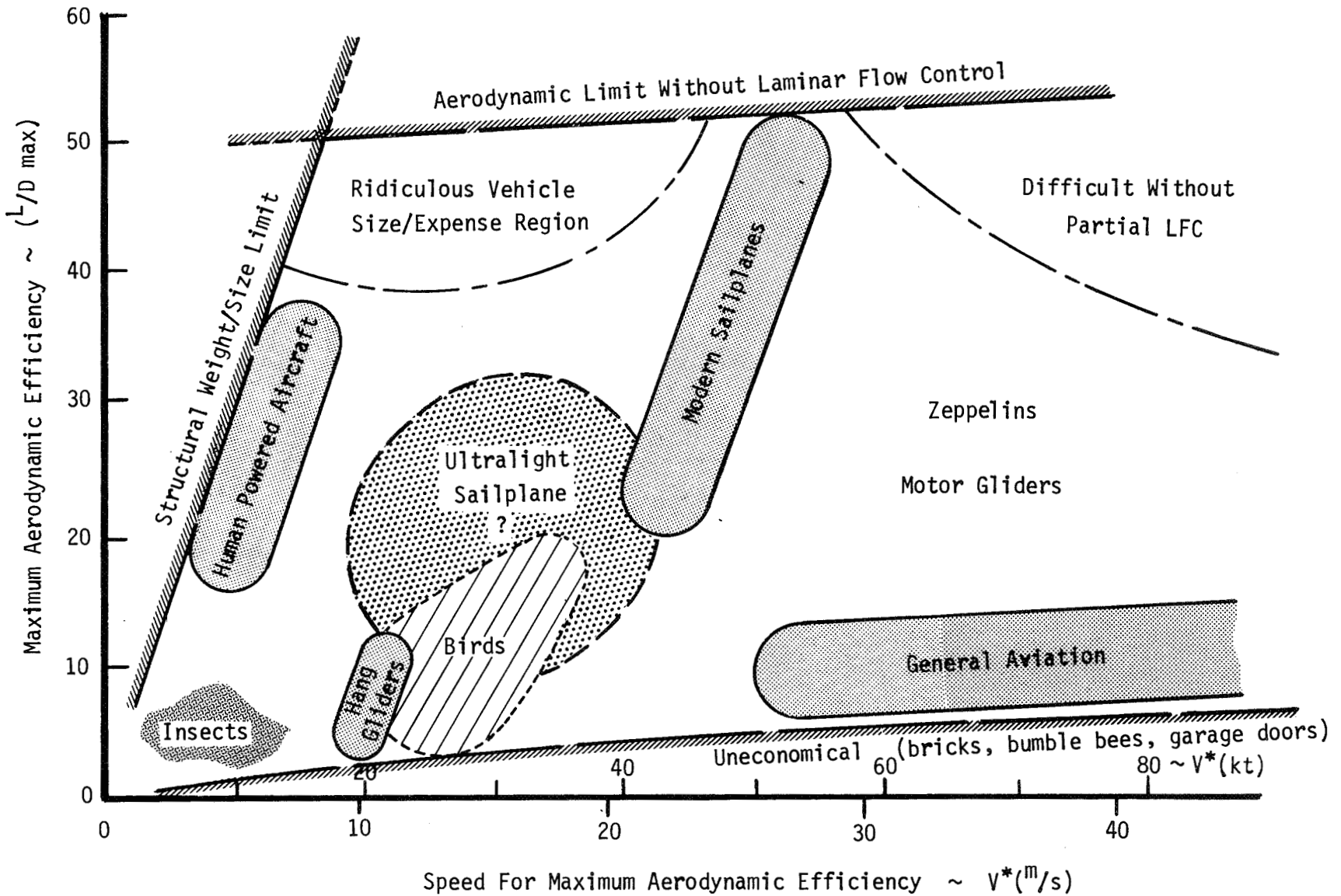


FIGURE 1. APPROXIMATE BOUNDARIES OF THE FEASIBLE/ECONOMICAL LOW-SPEED FLIGHT SPECTRUM

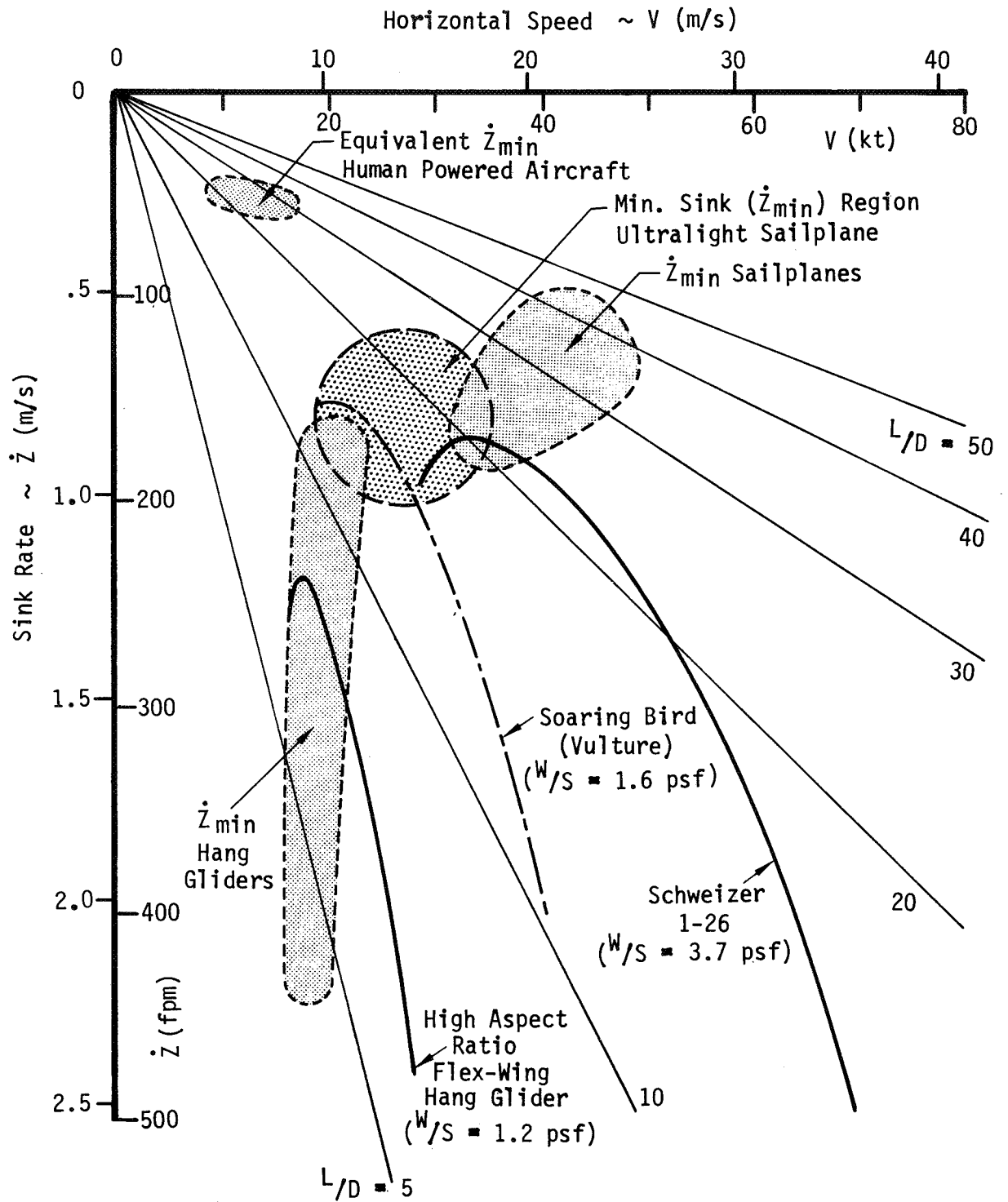
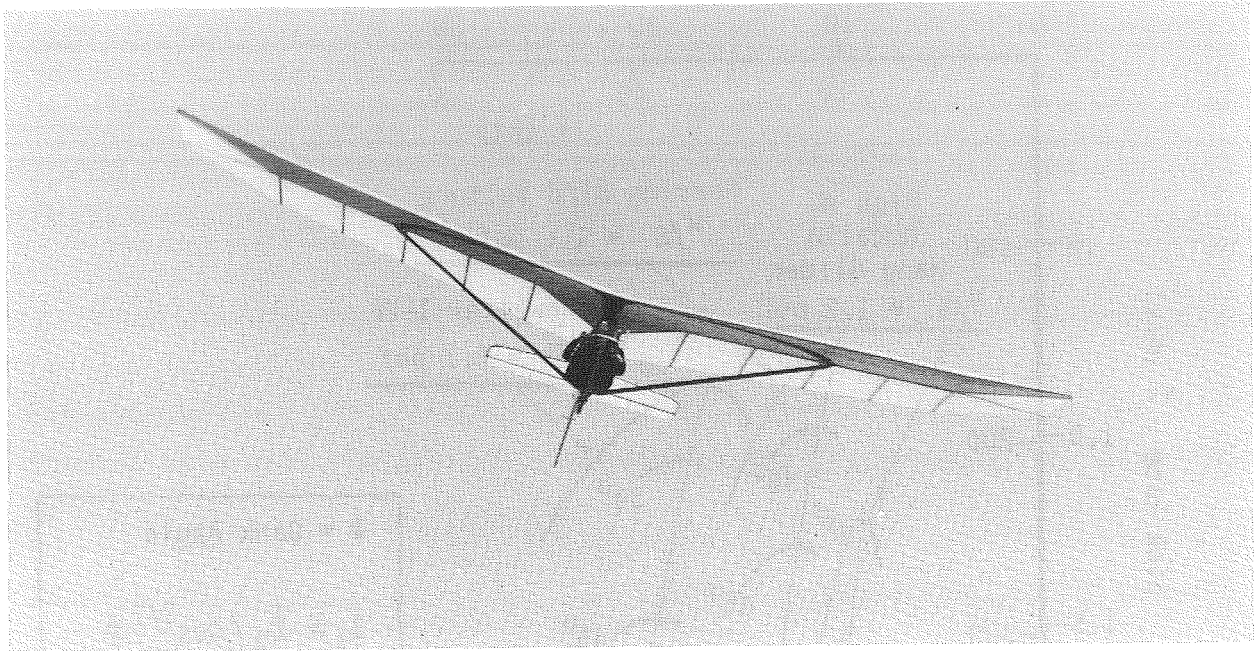


FIGURE 2. SINK RATE PERFORMANCE COMPARISON



KLAUS HILL "SUPERFLOATER"

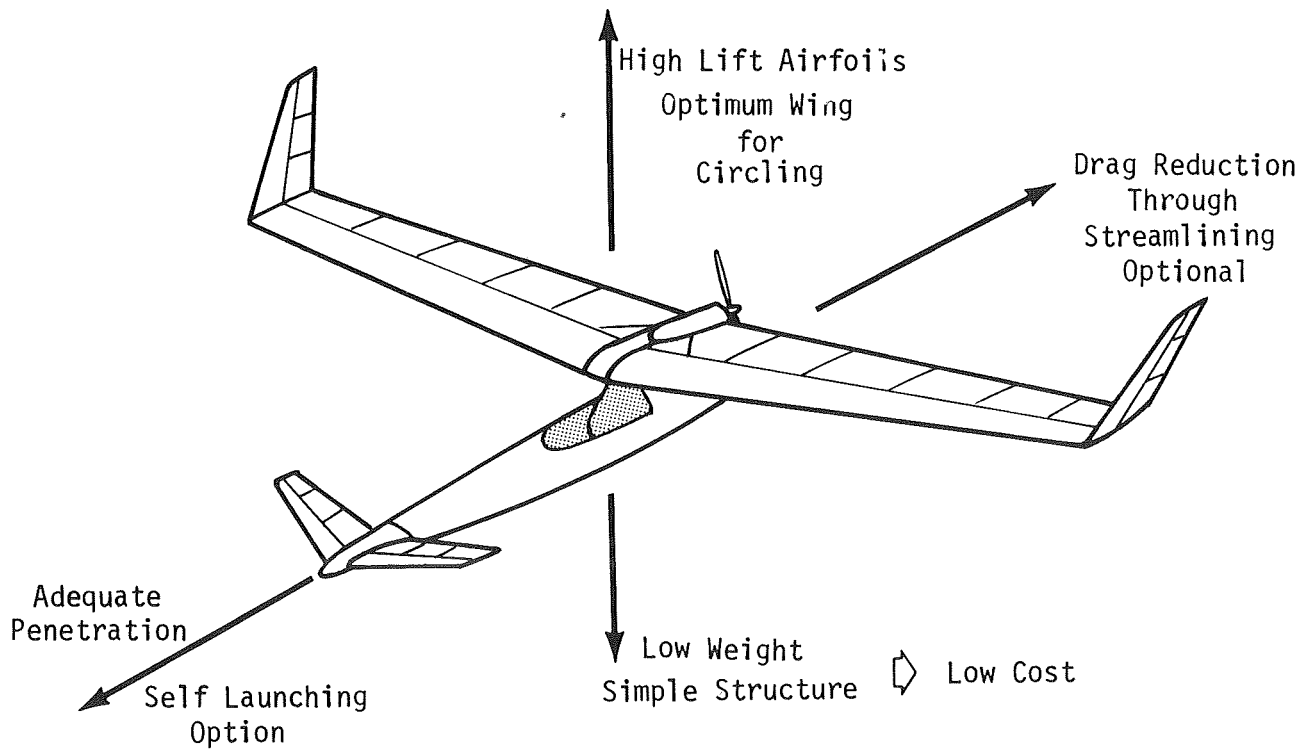


FIGURE 3. TYPICAL ULTRALIGHT SAILPLANES

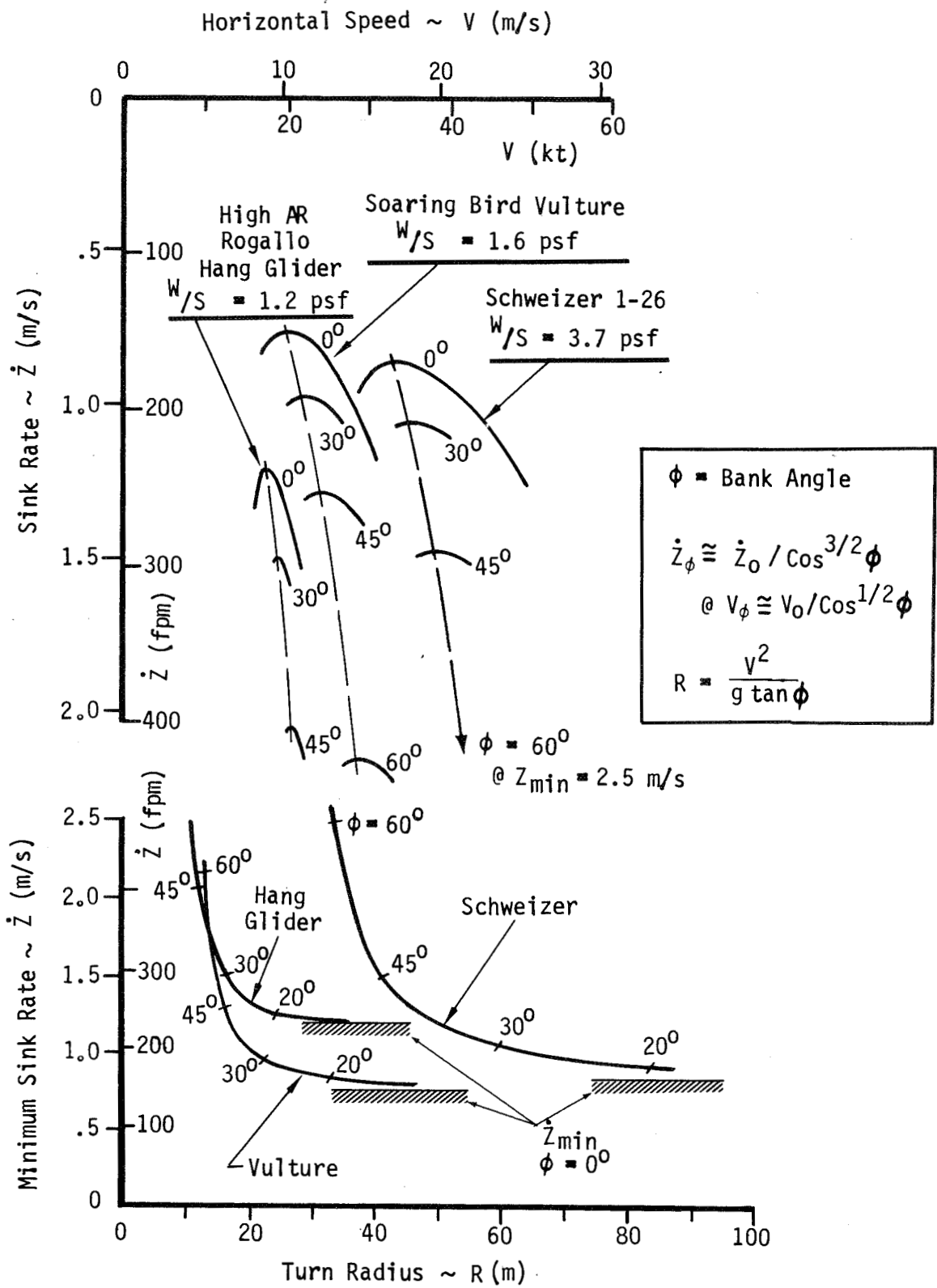


FIGURE 4. TYPICAL GLIDER TURN PERFORMANCE

ANALYTICAL AND SCALE MODEL RESEARCH AIMED AT IMPROVED HANG GLIDER DESIGN

Ilan Kroo and Li-Shing Chang
Stanford University

SUMMARY

A program of research on the aerodynamics, aeroelasticity, and stability of hang gliders has recently begun at Stanford University with support from NASA. The research consists of a theoretical analysis which attempts to predict aerodynamic characteristics using lifting surface theory and finite-element structural analysis as well as an experimental investigation using 1/5-scale elastically similar models in the NASA Ames 2 m x 3 m (7' x 10') wind tunnel. Experimental data will be compared with theoretical results in the development of a computer program which may be used in the design and evaluation of ultralight gliders.

This paper describes the goals and general procedures of the investigation begun in January 1979.

INTRODUCTION

In recent years the performance and variety of hang glider designs have increased dramatically. Flight conditions and demands that are placed on hang gliders are very different from those encountered by older designs. Whereas lift-to-drag ratios of 3 were common not long ago, some present designs achieve glide ratios of close to 10 and have been flown cross country for 160 km (100 mi) at altitudes as high as 6000 m (19,000 ft.) (Ref. 1). In addition to (often turbulent) thermal flying, increased controllability has made limited aerobatic maneuvers possible. Several years ago the results of NASA wind tunnel studies of the Rogallo wing (Ref. 2-7) in the 1960's could be used to obtain some idea of the characteristics of new designs. Although not all flight regimes and relevant parameters were thoroughly investigated, the data that did exist proved useful. The hang glider has evolved, however, to the point that these original investigations can no longer be applied. The flight characteristics of modern hang gliders (Ref. 8) with spans extending to 31 m (36 ft.), aspect ratios from 5 to 7.6 and sails with low billow and sweep, cannot be estimated from these data for the high billow (4-5 degrees), low aspect ratio (2.5) "standards". Information on the aerodynamic characteristics of present designs is almost entirely qualitative, deduced from limited flight tests of new designs.

Many problems that have been encountered might have been prevented had such data been available. Pitch-down divergence at low angles of attack continues to be an important problem. Thirty percent of fatalities in 1976 involved full-luffing dives from altitudes in excess of 60 m (200 ft.) (Ref. 9) although recovery is theoretically possible in less than 15 m (50 ft.) (Ref. 10). Statistics from hang gliding accidents in 1977 and 1978 show that, despite a more

thorough testing program pursued by the industry in the last few years, such instabilities are all too common even up to the present time.

Work was begun in January 1979 on a program of research aimed at providing quantitative tools for use in the design and evaluation of modern hang gliders. The investigation consists of two concurrent and closely integrated phases:

- 1) Basic force and moment measurements will be made on scale models in one of the 2 m x 3 m wind tunnels at NASA Ames Research Center. Models are being constructed that will reproduce the geometric, elastic, and aerodynamic properties of a representative class of modern glider.
- 2) A computer program, based on the best available analytic tools from potential aerodynamics and finite-element structural methods, for predicting the measured airloads with static aeroelastic corrections is being developed. After refinement by comparison with the tests, this program will be promulgated for the analysis of future glider designs.

As this research is to be conducted over the next two years, this paper describes the goals and general approach of the project with results to be published at a later date.

WIND TUNNEL TESTS

Models

Planned wind tunnel tests consist of measurements of the basic forces and moments on a group of 1/5-scale models at Reynold's numbers very close to the full scale value.

Although there exist today a wide variety of hang glider designs and it is no longer possible to test a "standard" configuration and use the results to predict universal characteristics for these aircraft, sufficient similarity does exist so that certain characteristics may be determined from tests on a limited number of models and applied to many other designs with similar features. In this way, good approximations to the properties of such gliders may be obtained from tests on a small group with different, but carefully selected, geometries. The models selected span a wide range of glider types, from the older Rogallo-type "standards" to more recent "intermediate" and high performance designs. (See Table 1). The effect on overall aerodynamic characteristics of various wing tip geometries, sail planforms, and camber and twist distributions common to many gliders will be determined from tests on this group of models.

The importance of elastic scaling has been demonstrated recently (Ref. 11). The flight characteristics of gliders are seen to vary considerably with changes in loading. This is caused by the flexibility of the frame and deformation of the sail of these ultralight gliders. For this reason, it is important that scale models be constructed in such a way as to remain geometrically similar to full size gliders under corresponding loads.

Another key assumption underlying the design of flexible models is the attainment of full-scale Reynolds' number, Re . This is because rather complex

separated-flow effects are anticipated at the larger values of α and β . Since available wind tunnels operate at essentially sea-level conditions, it follows that any resultant force, F_m , experienced by the model must equal the corresponding F_f at full scale. (Mach number effects are negligible at these "microsonic speeds.")

Force equality can be reasoned from the fact that:

$$Re_m = Re_f$$

where the product of speed and typical length, $V\ell$, must be the same at both scales. With air densities:

$$\rho_m = \rho_f$$

and forces proportional to $\rho V^2 \ell^2$, then:

$$F_m = F_f$$

The combination of equal force and equal strain requirements lead to difficulties in the construction of elastically scaled models. Consider that both the model and full scale gliders are constructed of tubes and cables of approximately circular cross sections of radius r , supporting the fabric sails. Since r should be proportional to ℓ for aerodynamic similarity, the strains in these tubes are proportional to $Fr\ell/EI$ or to Fr^2/EI , with EI the familiar bending rigidity. The severe requirement on model construction is to ensure

$$\left(\frac{r^2}{EI}\right)_m = \left(\frac{r^2}{EI}\right)_f$$

For a typical glider, assembled of thin-walled aluminum tubes, this quantity is of the order 10^{-7} N^{-1} ($4 \times 10^{-7} \text{ lb.}^{-1}$). If the same construction and material were employed on the model, one would get

$$\left(\frac{r^2}{EI}\right)_m = \left(\frac{\ell_f}{\ell_m}\right)^2 \left(\frac{r^2}{EI}\right)_f$$

This factor of 25 at one-fifth scale is quite unacceptable. Since weight is not believed to be a very significant factor, the situation can be alleviated by going to solid-section cylinders of stiffer material on the model. Models constructed of steel in this manner approach the desired stiffness:

$$\left(\frac{r^2}{EI}\right)_m = 3.4 \left(\frac{r^2}{EI}\right)_f$$

It appears that the requirement of equal strains, therefore, can only be met by some relaxation of the Reynolds number requirement. The following values correspond to the model construction above:

$$\frac{Re_m}{Re_f} = .53$$

This difference is not large and can be reduced further with the use of tubes and cables of slightly larger than scaled radii.

Especially for newer hang glider designs with low billow, it is important to duplicate the stretching of the fabric sail as well as the bending of frame elements. This requirement may be seen approximately as follows.

Requiring equal strains in the model and full-scale glider sails, $\epsilon_m = \epsilon_f$, for geometric similarity implies that

$$\epsilon = \frac{\sigma}{E} = \frac{p(x)dx}{E dA} = \frac{p(x)dx}{Et dx} = \frac{F}{Et\ell}$$

is the same at both scales. Now since $\ell_m = \frac{1}{5} \ell_f$ and from above we have let $F_m = 1/3.4 F_f$ we require that $(Et)_m = 1.8 (Et)_f$. This can be achieved with the appropriate choice of Dacron fabric. Values of Et for Dacron sails are given in reference 24, from which it can be seen that the proper $(Et)_m$ may be achieved with two layers of material slightly lighter than that used $_m$ on full-scale gliders.

Data Reduction

From measurements of the basic forces and moments on these models, the following performance coefficients and static stability derivatives can be calculated.

$$C_L \quad C_D \quad C_m \quad C_{m_\alpha} \quad C_{\ell_\beta} \quad C_{n_\beta}$$

Data will be obtained generally at angles of attack, α from -45° through stall and at sideslip angles β to $\pm 20^\circ$. Tests will be conducted at various pressures to obtain data on the presumably significant variation of these quantities with the dynamic pressure, q (elastic effects). Test results will be corrected for jet blockage and wall effects.

Much of this data could be used immediately for design purposes with little intermediate manipulation. With the use of data on pitching moment coefficient the longitudinal equations of motion may be numerically integrated to show the effectiveness of "weight-shift" control, including required bar pressures (stic forces), under various flight conditions. Stall, dive recovery, and other aspects of longitudinal motion will be analyzed. A similar analysis for lateral motion, taking account of the unusually large coupling between longitudinal and lateral modes associated with hang gliders, will also be carried out. At the present time, the first wind tunnel model is being constructed at the machine shop facilities at Stanford. The frame will have two possible nose

angles and by attaching different sails many configurations may be tested. Although a final list of configurations to be tested has not yet been determined, a tentative group of test models is described in table 1.

THEORETICAL ANALYSIS

In conjunction with the testing program, theoretical aerodynamic and aeroelastic methodology is being applied toward the development of a computer program which will undertake to predict some or all of the quantities measured in the experimental portion of the project.

Several theoretical treatments of "parawing" aerodynamics were published in the 1960's (e.g. Ref. 12-14). Lifting surface theory was used to predict lift and moment of various parawing configurations with the assumption of a particular mode shape (generally taken to be a portion of a right circular cone). Induced and profile drags and the effects of rigid leading edges were treated. Recent experimental work (Ref. 11) has shown, however, that changes in sail shape with angle of attack and dynamic pressure are extremely important, especially for current hang glider designs. Thus, not only is the assumption of conical canopy shape no longer valid, but no rigid analytic assumption of mode shape can be used.

The approach taken in the present analysis consists of two major parts:

- 1) The determination of airloads for a prescribed mode shape, and
- 2) The flexible structural response to this calculated loading, resulting in a new approximation for canopy shape.

The iterated procedure, shown schematically in Fig. 1, is used to obtain a solution for pressure distribution without the need for specifying the exact sail shape initially.

From these predicted airloads, force and moment coefficients may be calculated and compared with experimental results.

Aerodynamics

Linearized, steady, lifting-surface theory for incompressible flow is used in the prediction of aerodynamic loads on the glider. Under such conditions the flow over the glider satisfies Laplace's equation: $\nabla^2\phi = 0$ which may be solved with the use of vortex-lattice or kernel-function methods. The approach taken here utilizes the former method described by Woodward and Rubbert (Refs. 15,16) with a code by Nathman (Ref. 17) used at Stanford's computing facilities.

The sail is divided into finite elements as shown in Fig. 2. Each element is idealized as a flat panel of constant doublet strength, K , defined as the discontinuity in potential between the upper and lower surfaces,

$$K = \phi_l - \phi_u$$

As shown in the appendix, this leads to the following expression for the velocity induced at points outside this surface

$$\{V\} = \frac{1}{4\pi} [C]\{K\}$$

where $[C]$ is the aerodynamic influence matrix described in the appendix. The doublet strength for each panel is chosen so that the flow at the surface of the glider is tangent (zero sail porosity). This condition is satisfied if the normal velocity induced by the system of doublets just cancels the free-stream normal velocity:

$$[C_n]\{K\} = -4\pi \{n \cdot V_\infty\}$$

Since the surface normals and influence matrix may be computed from the assumed sail geometry and since the free-stream velocity is given, the value of K can be calculated over the surface.

Once K is known, the vorticity on the surface is given by:

$$\gamma = n \times \nabla K$$

and the loading:

$$\Delta p(x) = \rho V \times \gamma$$

These pressures are then used to calculate the desired force and moment coefficients according to standard definitions (cf. Ref. 18). The procedure is summarized in Fig. 3.

Figs. 4-6 show the preliminary results of this theory applied to some simple planforms for which experimental data is available. (Ref. 19,20). Agreement is close although effects of leading edges and deviation from conical geometry are not considered.

It should be noted that these results are the predictions of the aerodynamic portion of the program only. A rigid mode shape is assumed and so agreement with experiment can only be expected at intermediate α . The combination of this portion of the program and the structural analysis described below is presently underway and results are not yet available.

This analysis does not include the effect of pilot, cable or frame interference. It applies only to unseparated flow and does not include viscous effects. Corrections to the first stage of the analysis, taking these effects into account, are being studied and can, hopefully, be implemented in later work.

Structural Analysis

The sail and frame of a hang glider constitute a rather flexible structure assumed to be in a state of quasi-static equilibrium. Tension members, axially loaded beams, bending members, and membrane surfaces are all involved, with clearly defined modal connections. It is evident that the finite-element method of static, structural analysis is the only feasible way of representing and balancing the complete system of internal and external loads.

The approach taken here involves an analysis of the glider frame by classical methods and modelling of the sail as a membrane with very small flexural rigidity. The procedure is diagrammed in Fig. 7.

An incremental loading technique as described by Turner et al. (Ref. 21) is used to predict the response of the entire structure to the given applied load. The pressure distribution given by the aerodynamic portion of the analysis is broken down into small increments and the change in shape due to this incremental load is calculated. This is done by expressing the pressure, Δp_i , over each panel in terms of equivalent nodal loads, F_i , and calculating the displacement, D_i , of the nodes by the relation:

$$\{F\} = [S] \{D\}$$

Here, $[S]$ is a stiffness matrix, made up of a linear, elastic part $[S_e]$ which accounts for sail stretching (despite the anisotropic stretching behavior of textile materials, the glider sail is assumed isotropic for the early stage of the investigation) and a non-linear geometric part $[S_g]$ which depends on the geometry and initial tension. The addition of this geometric stiffness to the conventional stiffness matrix allows the non-linear strain-displacement relations associated with this large displacement problem to be incorporated in an approximate manner.

A method described by Argyris (Ref. 22) is adapted here to generate the geometric stiffness matrix. This method assumes a linear strain-displacement relationship within the elements and is considerably simpler than conventional techniques which require calculation of the strain energy (cf. Ref. 23).

At each step the geometric stiffness matrix is updated and nodal forces and incremental displacements calculated. After the step-by-step process is completed, the incremental displacements are summed to obtain a new mode shape which is then used as input to the aerodynamic program for another iteration.

A code based on this approach has been developed and is presently being checked by comparison with test cases for which analytic solutions are possible. Preliminary work indicates agreement to within a few percent in displacement although further work is needed to assure convergence in some cases.

Results from the experimental portion of the investigation will be used to establish the theoretical results' range of validity and will guide efforts to incorporate the effects of viscosity, interference, leading-edge suction, and other phenomena in the analytical portion of the research.

CONCLUDING REMARKS

The theory presented here is intended to provide a general idea of some of the methods to be used in this investigation. Much work is required before the analysis can properly take account of the complex aerodynamic and aero-elastic effects associated with modern hang gliders. At the time of this writing, the aerodynamic and structural routines have not been combined although it is expected that this will be accomplished shortly. Wind-tunnel models are presently being fabricated for tests to be conducted later this year. Results from both the theoretical and experimental parts of this research will be published as they become available.

APPENDIX

Aerodynamic Influence Matrix Calculation

Expressing the velocity perturbation potential, $\phi(P)$, at a point P, in terms of the value of ϕ and its normal derivative $\frac{\partial\phi}{\partial n}$, on the fluid boundary by Green's theorem:

$$\phi(P) = \int_s \frac{\partial\phi(P')}{\partial n_s} \left(\frac{-1}{4\pi r} \right) ds + \int_s \phi(P') \frac{\partial}{\partial n_s} \left(\frac{1}{4\pi r} \right) ds$$

where r is the distance between P and P', a point on the boundary, S.

If the sail is taken to be a 2-dimensional surface, then $n_u = -n_\ell$ and, in order that the flow be tangent to the surface,

$$\frac{\partial\phi_u}{\partial n_u} = - \frac{\partial\phi_\ell}{n_\ell}$$

so;

$$\phi(P) = \int_s (\phi_u - \phi_\ell) \frac{\partial}{\partial n_u} \left(\frac{1}{4\pi r} \right) ds = \int_s K \frac{\partial}{\partial n_u} \left(\frac{1}{4\pi r} \right) ds$$

and

$$V(P) = \int_s \nabla K \left(\frac{1}{4\pi} \right) \frac{\partial}{\partial n} \left(\frac{1}{r} \right) ds$$

If K is assumed constant over each of the panels S_j , then:

$$V(P) = \sum_j \frac{K_j}{4\pi} \left(- \int_{S_j} \nabla \frac{\partial}{\partial n} \left(\frac{1}{r} \right) ds; \right)$$

The aerodynamic influence coefficient of the region S_j on the point P_i is thus defined as:

$$C_{ij} = - \int_{S_j} \nabla \frac{\partial}{\partial n} \left(\frac{1}{r} \right) ds;$$

so:

$$V(P_i) \equiv V_i = \frac{1}{4\pi} K_j C_{ij}$$

Expressing this velocity at several points in matrix notation:

$$\{V\} = \frac{1}{4\pi} [C] \{K\}$$

REFERENCES

1. "Hang Gliding Magazine" (Formerly "Ground Skimmer"), Dec. 1973-Feb. 1979, a Monthly publication of the United States Hang Glider Association.
2. Johnson, Joseph L., Jr., "Low-Speed Wind-Tunnel Investigation to Determine the Flight Characteristics of a Model of a Parawing Utility Vehicle," NASA TN D-1255, 1962.
3. Johnson, Joseph L., Jr., and Hassell, James L., Jr., "Full-Scale Wind-Tunnel Investigation of a Flexible-Wing Manned Test Vehicle," NASA TN D-1946, 1963.
4. Naeseth, Roger L., and Gainer, Thomas G., "Low-Speed Investigation of the Effects of Wing Sweep on the Aerodynamic Characteristics of Parawings Having Equal-Length Leading Edges and Keel," NASA TN D-1957, 1963.
5. Bugg, Frank M., "Effects of Aspect Ratio and Canopy Shape on Low-Speed Aerodynamic Characteristics of 50° Swept Parawings," NASA TN D-2922, July 1965.
6. Croom, Delwin, R., Naeseth, Roger L., and Sleeman, William C., Jr., "Effects of Canopy Shape on Low-Speed Aerodynamic Characteristics of a 55° Swept Parawing with Large-Diameter Leading Edges," TN D-2551, Dec. 1964.
7. Johnson, Joseph L., Jr., "Low-Speed Force and Flight Investigations of a Model of a Modified Parawing Utility Vehicle," NASA TN D-2492, March 1965.

8. Hang Glider Design Catalog, Ground Skimmer, December 1975.
9. Wills, R.V., "Accident Summaries", Hang Gliding, 1974-1978.
10. Jones, R.T., "Dynamics of Ultralight Aircraft: Dive Recovery of Hang Gliders," May 1977, NASA TM X-73229.
11. Discussion with Robert Ormiston, NASA Ames Research Center, regarding results of full-scale tests in settling chamber of #2 7'x 10' wind tunnel at Ames, June 1977.
12. Mendenhall, M.R., Spangler, S.B., and Nielsen, J.N., "Investigation of Methods for Predicting the Aerodynamic Characteristics of Two-Lobed Parawings," NASA CR-1166, Sept. 1968.
13. Polhamus, Edward C., and Naeseth, Roger L., "Experimental and Theoretical Studies of the Effects of Camber and Twist on the Aerodynamic Characteristics of Parawings Having Nominal Aspect Ratios of 3 and 6," NASA TN D-972, 1963.
14. Nielsen, Jack N., and Burnell, Jack A., "Theoretical Aerodynamics of Flexible Wings at Low Speeds: Engineering Method for Estimating Parawing Performance, Final Report, Feb. - Nov. 1965," VIDYA-209, Dec. 1965.
15. Woodward, F.A., "Analysis and Design of Wing-Body Combinations at Subsonic and Supersonic Speeds," J. Aircraft, 5:528-34.
16. Rubbert, P.E., "Theoretical Characteristics of Arbitrary Wings by a Non-Planar Vortex Lattice Method," Boeing Co., Rep. D-6-9244, 1964.
17. Nathman, J.K., "Delta Wings in Incompressible Flow," AIAA 13th Annual Meeting, 1977.
18. Ashley, H., Engineering Analysis of Flight Vehicles, Addison-Wesley Publishing Co., Reading, Mass., 1974, (Sects. 3.1, 3.2, 8.2 etc).
19. Turnell, J.A., and Nielsen, J.N., "Aerodynamics of Flexible Wings at Low Speeds, Part IV -- Experimental Program and Comparison with Theory," VIDYA Report 172, Feb. 1965.
20. From unpublished study cited in Ref. 12.
21. Turner, M.J., Dill, E.H., Martin, H.C., and Melosh, R.J., "Large Deflections of Structures Subjected to Heating and External Loads," J. Aerospace Sci., 27:97-102, 127, 1960.
22. Argyris, J.H., Kesley, S., and Kamel, H., Matrix Methods of Structural Analysis," AGARDograph 72, Pergamon Press, Oxford, England, 1964.
23. Prezeminiecki, J.S., Theory of Matrix Structural Analysis, McGraw-Hill, New York, 1968.

24. Ormiston, Robert A., "Theoretical and Experimental Aerodynamics of an Elastic Sailwing," Ph.D. Thesis, Oct. 1969, Dept. of Aerospace and Mechanical Sciences, Princeton University, Princeton, N.J.

LIST OF SYMBOLS

Notation

[C]	Aerodynamic influence matrix (see appendix)
D	Displacement of panel nodes
E	Elasticity constant
EI	Bending rigidity
F	Force
K	Doublet strength
l	Typical length
n	Unit vector normal to surface
P	Point on surface of sail
P	Pressure
p(x)	Loading on sail per unit length
q	Dynamic pressure
Re	Reynolds number
t	Sail thickness
[S]	Stiffness matrix
V	Fluid velocity
V_{∞}	Free-stream velocity
α	Angle of attack
β	Angle of side slip
γ	Vorticity
ϵ	Strain
ρ	Fluid density
σ	Stress
ϕ	Velocity perturbation potential
C_L	Lift coefficient

C_D	Drag coefficient
C_m	Pitching moment coefficient (based on keel length and referred to the $c_r/2$ point)
C_{m_α}	Slope of pitching moment curve with respect to α
C_{l_β}	Effective dihedral (rolling moment coefficient due to yaw)
C_{n_β}	Yawing moment coefficient due to sideslip

Subscripts

e	elastic
f	full scale
g	geometric
i,j	indicies refer to individual panels
l	lower surface
m	model
n	normal component
u	upper surfaces

TABLE 1

Details of Proposed Models

<u>Configuration Number</u>	<u>Airframe</u> *	<u>Basic Design Features</u>	<u>Comments</u>
1	A	High sweep, low aspect ratio, "standard"	For comparison with more recent designs and previous wind tunnel studies
2	B	High sweep, medium aspect ratio, 2° billow "intermediate"	Comparison with standard and high performance designs; effects of "billow"
3	C	High performance medium sweep (35°) zero tip chord	Washout not fixed by tips
4	C	Same as #3 with 45° sweep	Effect of sweep on stability
5	D	High performance low billow fixed minimum twist with "floating" ribs at tips	Effect of this common tip geometry on C_m
6	E	High performance low billow high twist dihedral	Features common to many contemporary hang gliders
7	E	Same as #6 with decreased twist	Effect of twist on performance and stability
8	E	Same as #6 without geometric dihedral	Dihedral effects on lateral stability and control response
9	E	Same as #6 with "keel pocket" and large reflex at root chord	Reflex effects on longitudinal stability and lateral control
10	F	Similar to #6 with low taper planform, low twist, reflex	Common to some of the highest performance gliders.

* Some configurations can be changed with minor model modifications, which results in the need for only 6 airframes for the 10 configurations listed.

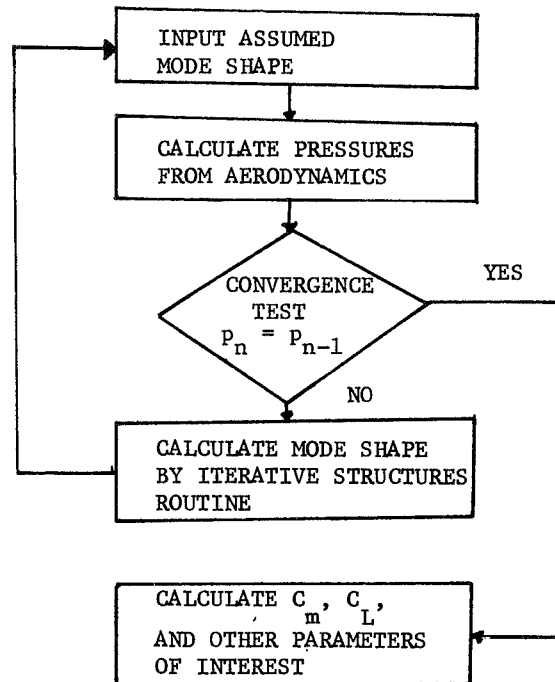


Figure 1.- Basic structure of load-prediction program.

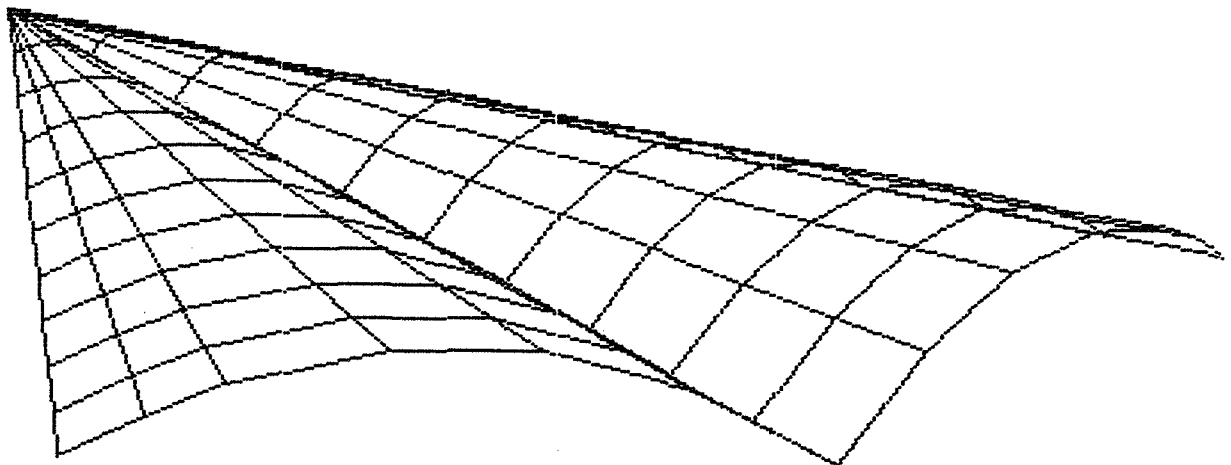


Figure 2.- Finite-element representation of hang glider sail.

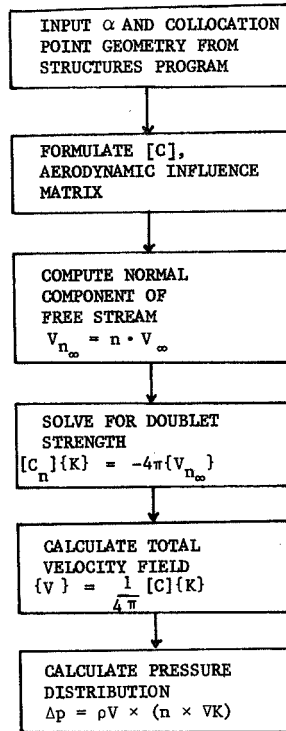


Figure 3.- Algorithm for aerodynamic analysis.

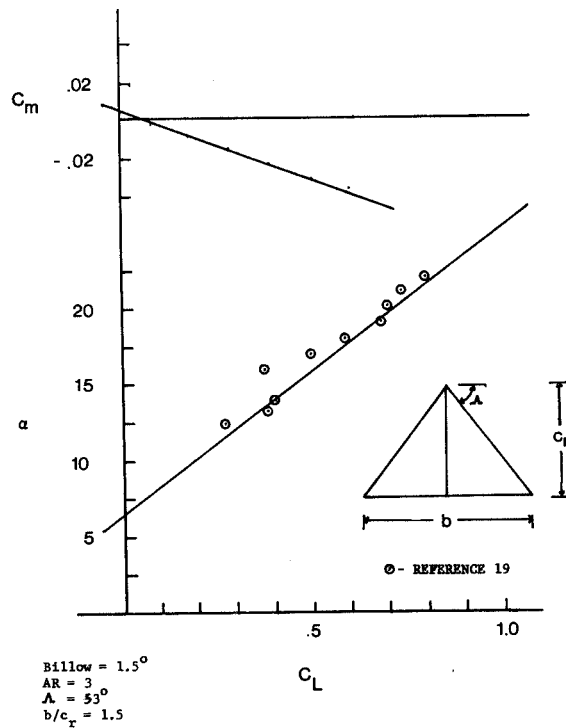


Figure 4.- Results of aerodynamic program.

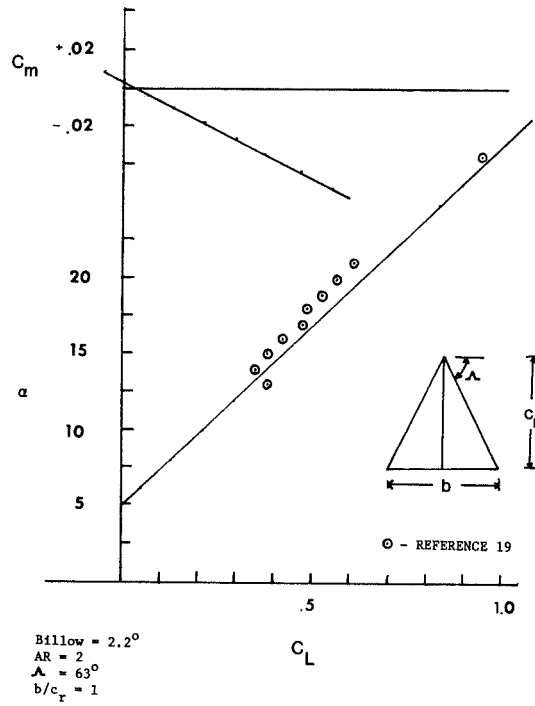


Figure 5.- Results of aerodynamic program.

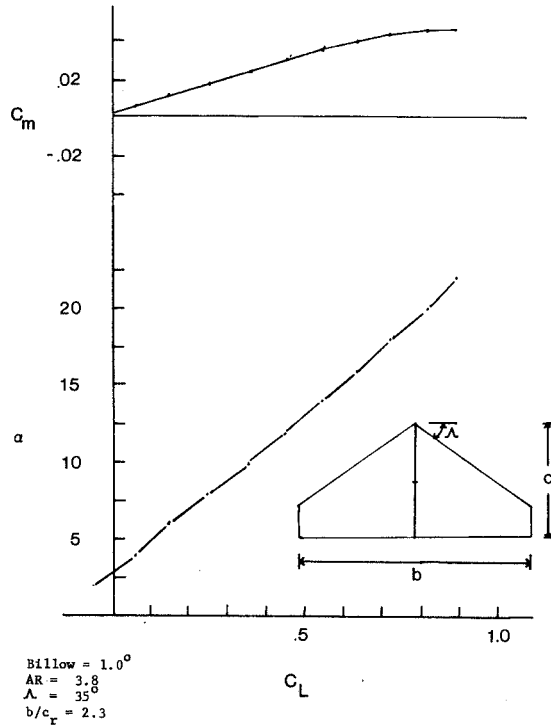


Figure 6.- Results of aerodynamic program.

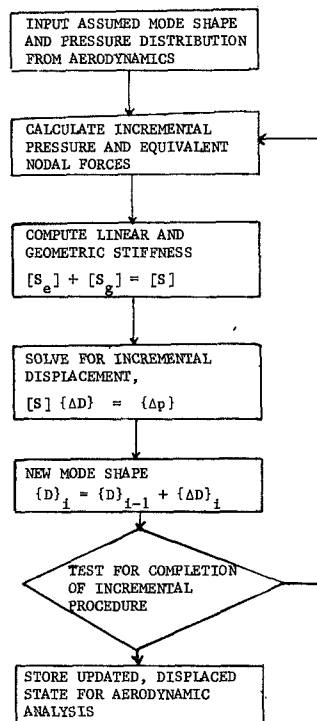


Figure 7.- Computational procedure — deflection analysis.

Page intentionally left blank

IMPROVEMENT OF HANG GLIDER PERFORMANCE

BY USE OF ULTRALIGHT ELASTIC WING

Jerzy Wolf
Aviation Institute
Warsaw, Poland

SUMMARY

The problem of the lateral controllability of the hang glider by the pilot's weight shift is considered. The influence of the span and the torsional elasticity of the wing is determined. It is stated that an ultralight elastic wing of a new kind developed by the author is most suitable for good control. The wing also has other advantageous properties.

INTRODUCTION

The main problem affecting the development of ultralight gliding is the decrease of the control effectiveness of the pilot's weight shift when the wing span increases. However, increasing the span and consequently the aspect ratio is the only way to improve the lift-drag ratio (L/D).

The important effect of the aspect ratio on the L/D for a definite type of external skeleton of the ultralight wing can be shown as indicated in figure 1 (ref. 1). Areas A, B, and C indicate the causes of the diminishing of L/D. Figure 1 shows that the induced drag A is the main price of lift production and can be diminished mainly by increasing span. Changing the unadvantageous triangular wing planform of the early flexible wings improves it to some degree and the application of final winglets makes it possible to improve it even more. Area B on figure 1 illustrates the influence of the wing profile effectiveness on the hang glider L/D, which is not very sensitive to profile shape above an aspect ratio of 5. Finally area C, the skeleton drag, constitutes the main field of the designer's activity. It is very interesting that for all wings with external skeleton (with external spars and struts (a), with external spars and cables (b), and with external cables only (c)), an optimum aspect ratio always exists. The maximum of L/D can be explained by the considerable drag increase, which for some aspect ratios exceeds the decrease of induced drag.

It has been shown in figure 1 also that the optimum aspect ratio can be a considerable one for ultralight wings. It enhances application of wings with enlarged spans. A difficulty with higher aspect ratios is that the lateral control of simple hang gliders by the pilot's body shift only is worsened.

ANALYSIS OF LATERAL CONTROL

To analyze this challenging problem, the time to bank the wing 60° was calculated (from $+30^\circ$ to -30°) as shown in figure 2. First a completely stiff wing was considered, for which the inertia forces were neglected. Next a wing completely elastic in torsion was considered, for which all the lateral aerodynamic moments were neglected. It was a soft wing, longitudinally stabilized aerodynamically, with the roll moment of inertia forces only considered. In the first case the responses on the control force moment were aerodynamic forces and in the second case solely the inertia forces. These two cases can be regarded as boundary limits on the roll rates of all real wings of hang gliders.

For the first case the following relation was found:

$$t = \frac{dC_L}{d\alpha} \frac{\psi \ell^2 L}{16rW_1 v C_L} \quad (\text{sec}) \quad (1)$$

where

C_L	lift coefficient
α	angle of incidence, deg
ψ	bank angle in figure 2, deg
ℓ	wing span, m
L	lift force ($L = W_1 + W_2$), daN
W_1	pilot weight, daN
W_2	glider weight, daN
r	mean body shift of the pilot, m
v	flight speed, m/sec
t	time to bank from -30° to $+30^\circ$, sec

and for the second case:

$$t = \sqrt{\frac{\psi m \ell^2 \pi}{8rW_1 180}} \quad (\text{sec}) \quad (2)$$

where m is the glider mass assumed to be uniformly distributed spanwise. Furthermore it was assumed that this mass grows linear as a function of the span according to the formula,

$$m = \frac{W_2}{g} \frac{\ell}{\ell^*} \quad (3)$$

where

g Earth's acceleration, m/sec^2

ℓ^* wing span, m , of hang glider weighing W_2 , daN

For the calculated practical examples the same values were assumed:

$W_1 = 75 \text{ daN}$, $W_2 = 25 \text{ daN}$, $r = 0,75 \text{ m}$, $\psi = 60^\circ$ and furthermore $dC_L/d\alpha = 0,06$,
 $v = 8 \text{ m/sec}$, $C_L = 0,7$, $\ell^* = 12 \text{ m}$.

The results of the calculation are shown in figure 3. They concern two ideal boundary cases 1 and 5 and three known types of hang gliders 2, 3, and 4. Particular curves concern the following types of ultralight wings:

- 1 - stiff wing
- 2 - Rogallo wing with flexible canopy characterized by limited washout of the wing
- 3 - sailwing or Rogallo hybrid wing of increased washout
- 4 - sailwing or hybrid Rogallo wing with automatically changing sailbillow and washout
- 5 - elastic wing of maximum arbitrary washout

In figure 3, three ranges of bank time for the mean body shift $r = 0,75 \text{ m}$ of the pilot weighing 75 daN are shown. The first range of t from 0 to 2 sec is the safe range of good manoeuvrability of the hang glider. It corresponds to practical observations of gliders and BCAR, section K, for the light airplanes (ref. 2). The second range of $t = 2$ to 4 sec is, under some weather conditions, an acceptable range of sufficient manoeuvrability. The third range, t greater than 4 sec, is dangerous for hang gliders and can be accepted only in particular cases as for man-powered airplanes at wind speed less than 2 m/sec .

In figure 3, the estimated bank time of the historical Lilienthal's gliders of 7 m span is indicated by a circle. They were controlled less effectively than contemporary hang gliders. Their bank times of 7 sec were within an unsafe range. That explains the half-century of stagnation in development of that form of gliding. Its revival was possible when the value of $r = 0,2 \text{ m}$ was increased to nearly 0,7 m when the harness for the pilot was invented.

The bank times indicated in figure 3 concern a considerably low flight speed $v = 8 \text{ m/sec}$, and it is known that the aerodynamic control effectiveness diminishes with the air speed. However this bad property does not occur in the

case of hang gliders controlled by weight shift, as was expressed by formulas (1) and (2). This problem can be presented clearly by taking into account that for the formula (1) and for the weight control the relation $C_L \sim 1/v^2$ is valid. Next for the formula (2) and aerodynamic control (when the inertia forces are the only response on the control force), the control moment $rW_1 \sim rv^2$ applies. Then we obtain relations shown in figure 4. This table shows very unadvantageous characteristics ($t \sim 1/v$) of the aerodynamic control for low speed flying devices operating near stall and being intended to operate like a parachute. On the other hand the weight control has suitable characteristics at low speeds and improves when the speed diminishes ($t \sim v$). It even can be independent of the speed ($t \neq f(v)$) in the case of the torsionally very elastic wing under consideration. Of course, this relationship remains valid if the wing is stable during stall or, in other words, if the separation is symmetrical.

DEVELOPMENT OF Z-77 HANG GLIDER

The development of an ultralight wing of this kind was very troublesome and took the author about 10 years. Initially the work concerned a wing with a cable leading edge (ref. 3) stretched by means of a pulley and a spring or rubber rope expanded along the spar tube of the skeleton. These experiments showed advantageous features of the ultralight foldable wing with the canopy fixed at one point of the tip to the wing spar and having a hinged end rib. The rib hinging on the cable or on the tube can change the angle of attack of the wing lip. The torsional elasticity allows self-adjustment of the wing to the flight conditions and good lateral control by weight shift only. Therefore it was decided to design the experimental hang glider Z-77 with a considerable span of 12 m, a rectangular wing planform, and a single central vertical stabilizer (ref. 4).

This simple flying plank arrangement was chosen as a result of the author's own wide experiments and of an analysis of positive swept flying wings. Its general properties are unstable stall for larger aspect ratios and bad dive recovery of flexible wings with soft tips and no profiled central rib. These properties create limits of a narrow speed range due to unsafe characteristics in turbulent wind conditions. It was found that the greatest chance of eliminating these undesirable properties is by application of an arrangement with slightly negative sweep of the wing. It is just the arrangement of the hang glider with reasonable application of an elastic wing characterized by one point connection of the sail tips to the skeleton, and by torsional elasticity of the wing plane.

The hang glider Z-77 was designed according to the general rule, "first safety and later the performance." The second more sophisticated rule was "do not counteract the deformation but organize and exploit it for safety and performance purposes." According to this second rule the wing bends and twists considerably around the leading edge which acts as a spanwise hinge.

The first variant of Z-77 tested in 1977 had the cable leading edge and external spar (fig. 5). Its stability and control was excellent and the only drawback was tearing of the canopy as result of contact with the wires, when

the glider was standing windward nose down on the ground. This drawback was so significant that after 15 minutes of wind pressing on the wing the sail had to be repaired.

This defect led to a modification of the construction by inserting a spar tube into the sail. Furthermore the spar was supported by only three wires so situated that the sail would not touch the wire under any conditions. In the second variant of Z-77 a double membrane airfoil (dark in the pictures) for 50% of the chord was used with duraluminium sheet profiles similar to those in the first variant.

This second variant of Z-77 (fig. 6) had an extraordinarily wide speed range and a very soft and stable stall. The glider was generally fast, considering the area of 20 m². This was the result of relatively flat self-stable profiles of the same kind as those used in single membrane version. The glider was very stable in turbulent winds and its longitudinal and lateral control was good. It participated in hang glider competition in the Zakopane-Tatra mountains in 1978. After numerous flights the next modification of the wing (fig. 7) was undertaken in order to improve its L/D above 10 which is possible for the structural arrangement used and an aspect ratio of 7.

For this purpose, new more effective special profiles were developed and the planform of the wing was slightly changed. During very many test flights, sometimes of 10 minutes duration, the glider demonstrated a very low minimum speed of 20 km/hr and a considerable lift coefficient (nearly 2). Determination of maximum speed was more difficult, but speeds of 80 km/hr were reached without any problem.

The modifications and the test flights are continuing. The main task is to improve the L/D to the possible nearly 15 while maintaining the hang glider's safety by good stability and controllability. The safety achieved is due to such properties as

- possibility of stable and controllable stall and parachuting from any altitude
- impossibility of slipping the wing and asymmetrical stall
- impossibility of spin
- controllable diving and easy recovery from dive
- very wide speed range and its safe boundaries (very important under strong wind turbulent conditions)
- possibility of immediate transition from dive to parachuting on the same straight line trajectory, losing only a dozen meters of altitude

The last of these properties is an extraordinary one and deserves some words. It was known that for the definite geometry of the glider there is one speed polar for the steady flight. But the spring wing of Z-77 is very elastic

in torsion and therefore its velocity polar is the envelope of an infinite number of polars for different twist angles of the wing. This is shown in figure 8 which explains the reasons for the wide speed range of Z-77. On the resulting polar, for the great range of the trajectory inclination angle, the two points A and B can be found for which the glide angle is the same. However, the speeds of diving and parachuting differ. For the hang glider of fixed geometry, considerable sweep or conventional horizontal tail stabilizer, a quick move from the state A to B on the straight line trajectory AB is practically impossible and occurs during pull up manoeuvre or a slack stall along the curve AB. Large span flexible wings with considerable leading edge sweep and a negligible torsional elasticity of the sail with the unelastic flexible canopy stressed between the keel and leading edge tubes behave similarly.

A completely different situation occurs when the hang glider has an elastic wing, has no horizontal tail surface or sweep, and has a low moment of inertia in pitch. Then a sudden transition from point A to B on the straight line trajectory is possible at a sufficiently large and fast increase of the incidence angle. Of course a moderate but not too slow increase of incidence angle normally results in dynamic climbing. At a slow increase of incidence angle the glider mushes according to the curve AB.

The dynamic stall and the manoeuvre of landing in a difficult situation as described and explained above is generally simple. However, technically the problem is more complicated because the torsional elasticity and the time of manoeuvre have to be suitable. These factors cause the deviation of the real trajectory from the straight line AB. Briefly, the control forces and manoeuvre time associated with insufficient elasticity exceed the physical capabilities of the pilot. On the other hand too much elasticity hinders dynamic climbing and causes pancaking of the glider. These problems and others are the subject of further research and tests of Z-77 (which has made about 400 flights to date). Moreover, Z-77 actually enables short and precise landings behind obstacles using the whole wing area as a powerful aerodynamic brake.

The actual data of Z-77 (fig. 9) are

Weight, 25 daN
Span, 12 m
Length, 5.5 m
Area, 19 m²
Speed range, 20 to 90 km/hr
Lift-to-drag ratio, 12
Profiles, special, self-stable
Maximum chord, 1.8 m
Minimum chord, 1.5 m

The hang glider Z-77, which was not described here technically, includes some essential patented improvements. The glider based on the application of the ultralight elastic wing is capable of performing the dynamic stall landing process attainable until now practically only by birds.

The ultralight elastic wing can be used for the practical investigation of the new unconventional landing technique, and for the development of the high

performance deployable flying devices (for example, hang gliders of the class 2 of FAI-CIVL regulation). This wing can be based on the application of the cable or tube leading edge arrangement. Its actual and possible future lift-drag ratio is compared in figure 10 with that of other ultralight wing types. Because of the possibility of high L/D, it is very suitable for oscillating wing propulsion of hang gliders (ref. 5) and has been practically proved and tried by the author in 1976-1977 by use of an elastic pilot harness and foot straps.

REFERENCES

1. Wolf, J.: Dlaczego sprężyste skrzydło (Why the Elastic Wing). Technika Lotnicza i Astronautyczna, Nr 10, Nr 11, 1977.
2. British Civil Airworthiness Requirements, Section K, 1974.
3. Wolf, J.: The Stretched-Membrane Sailwing. Technical Soaring, No. 4, April 1973.
4. Wolf, J.: Z-77 lotnia nowego typu (Z-77 - A New Kind of Hang Glider). Skrzydlata Polska, Nr 39, 1978.
5. Wolf, J.: The Technological Prospects for Oscillating Wing Propulsion of Ultralight Gliders. AIAA Paper No. 74-1028, presented at AIAA/MIT/SSA International Symposium on the Technology and Science of Low Speed and Motorless Flight, 1974.

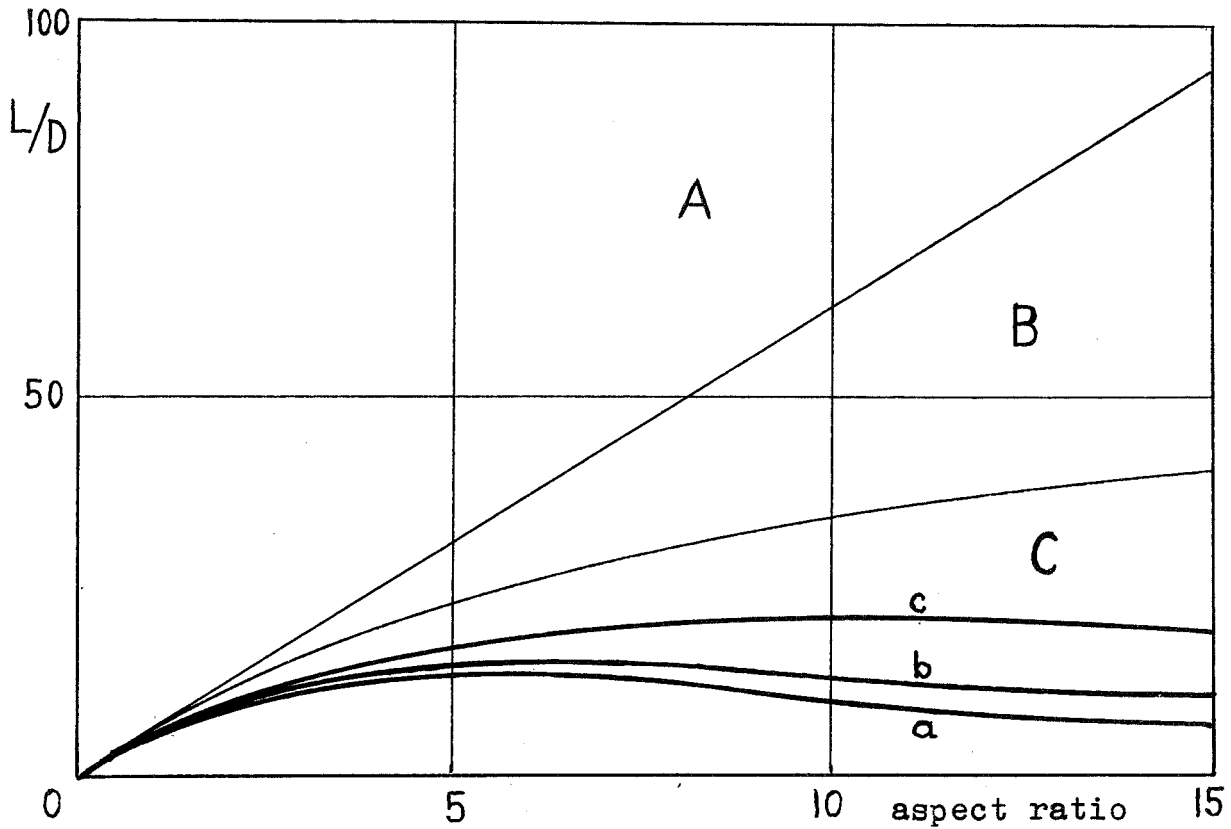


Figure 1.- Influence of the induced drag (area A), profile drag (area B), and skeleton drag (area C) on the lift/drage of the ultralight wing with external skeleton having spars and struts (a), spars and cables (b), and only cables (c).

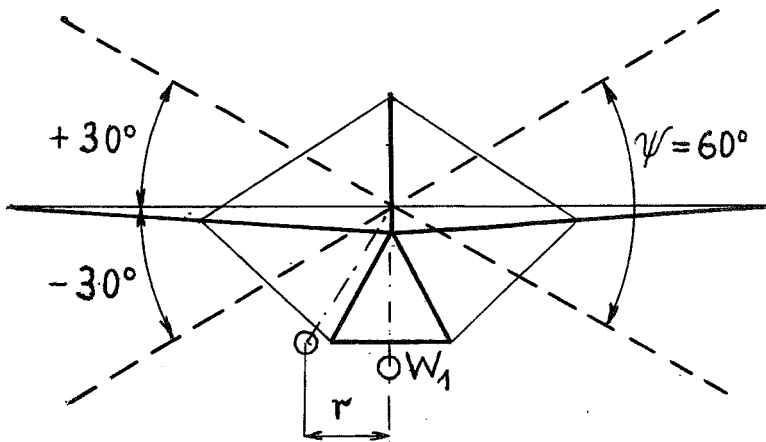


Figure 2.- Considered bank angles of the hang glider.

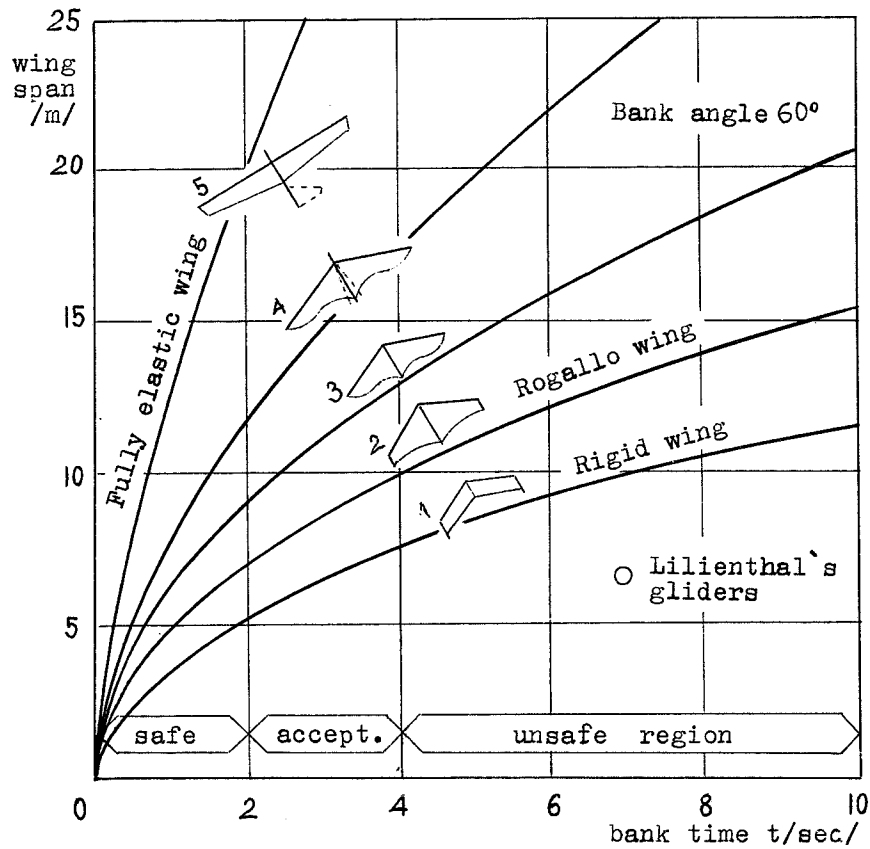


Figure 3.- The bank times t for the hang gliders controlled by mean body shift $r = 0,75$ m of the pilot weighing $W_2 = 75$ daN as a function of wing span ℓ .

		Control type	
		aerodynamic	weight shift
Wing type	rigid	$t \sim \frac{1}{v}$	$t \sim v$
	elastic	$t \sim \frac{1}{v}$	$t \neq f/v$

Figure 4.- Correlation of the bank time t with flight speed v .



Figure 5.- Experimental hang glider Z-77 (first variant) with cable leading edge elastic wing.

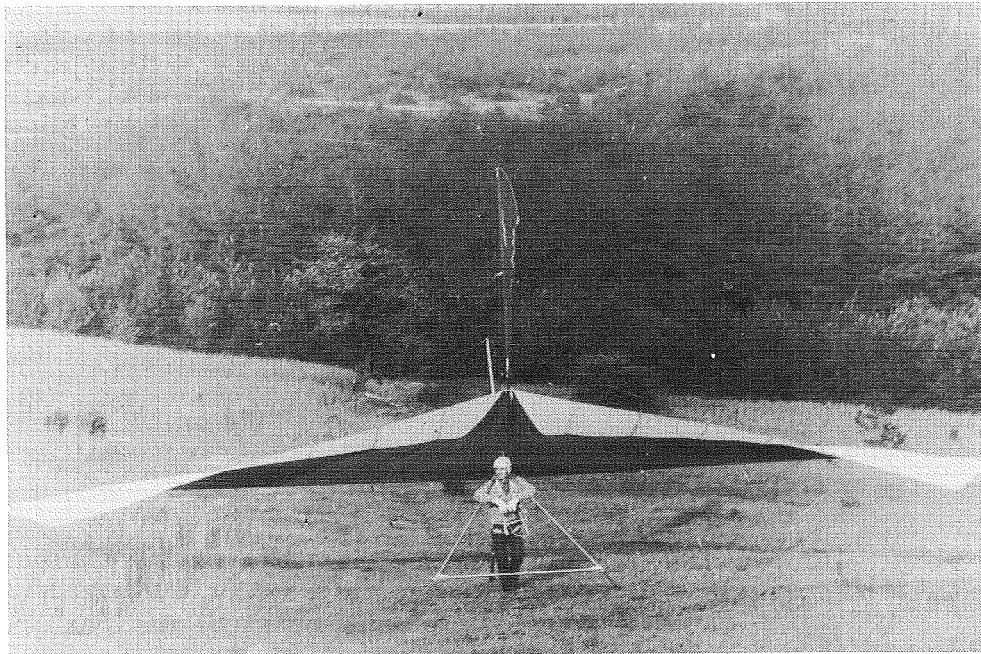


Figure 6.- Tube leading edge hang glider Z-77 (second variant) demonstrates the considerable range of the wing twist.

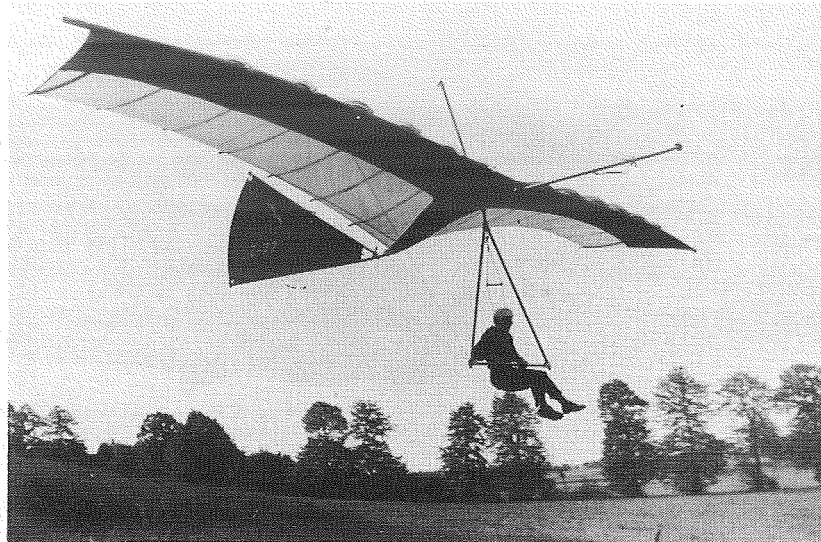


Figure 7.- Tube leading edge hang glider Z-77 (third variant) in flight.

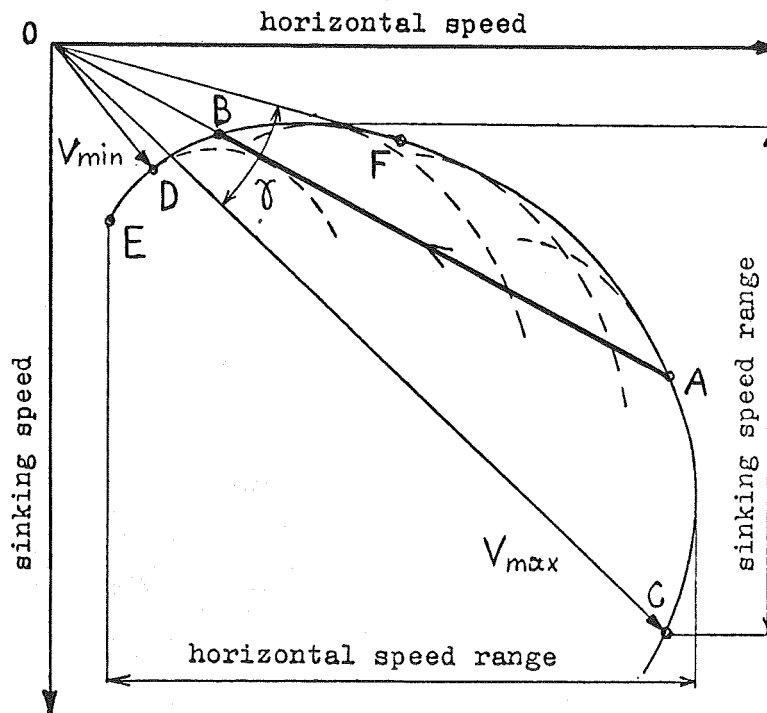


Figure 8.- Velocity polar of elastic wing hang glider. A,B - the points of polar curve for diving and parachuting on the same flight path inclination; C - the point of maximum speed; D - the point of minimum speed; E - the point of the maximum vertical parachuting; F - the point of maximum L/D; γ - the range of the flight path inclination angles for dynamic parachuting; $v_{\max} - v_{\min}$ - the range of flight speed. The velocity polars for various wing twist are shown by dashed lines.

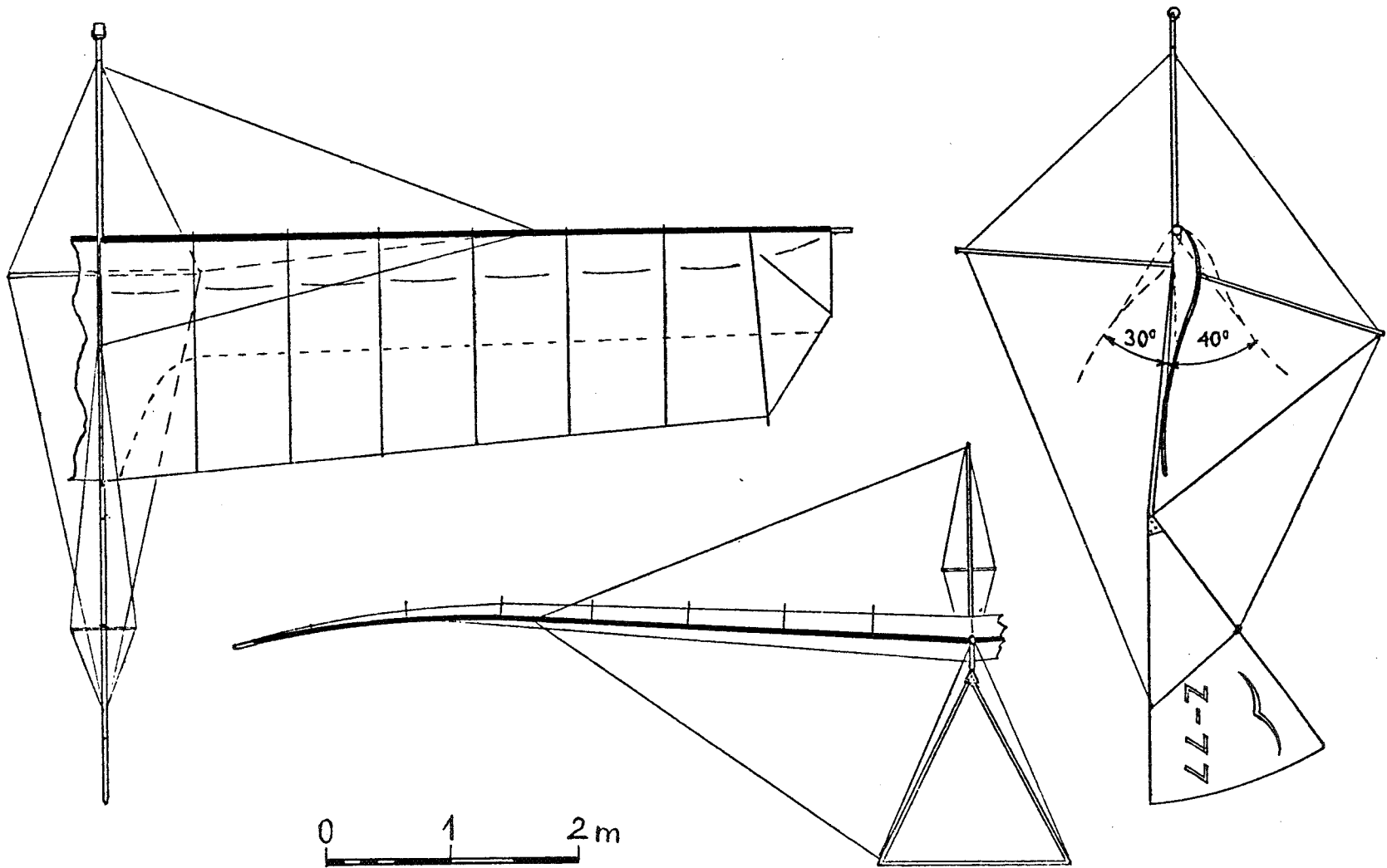


Figure 9.- Sketch of the third variant of Z-77.

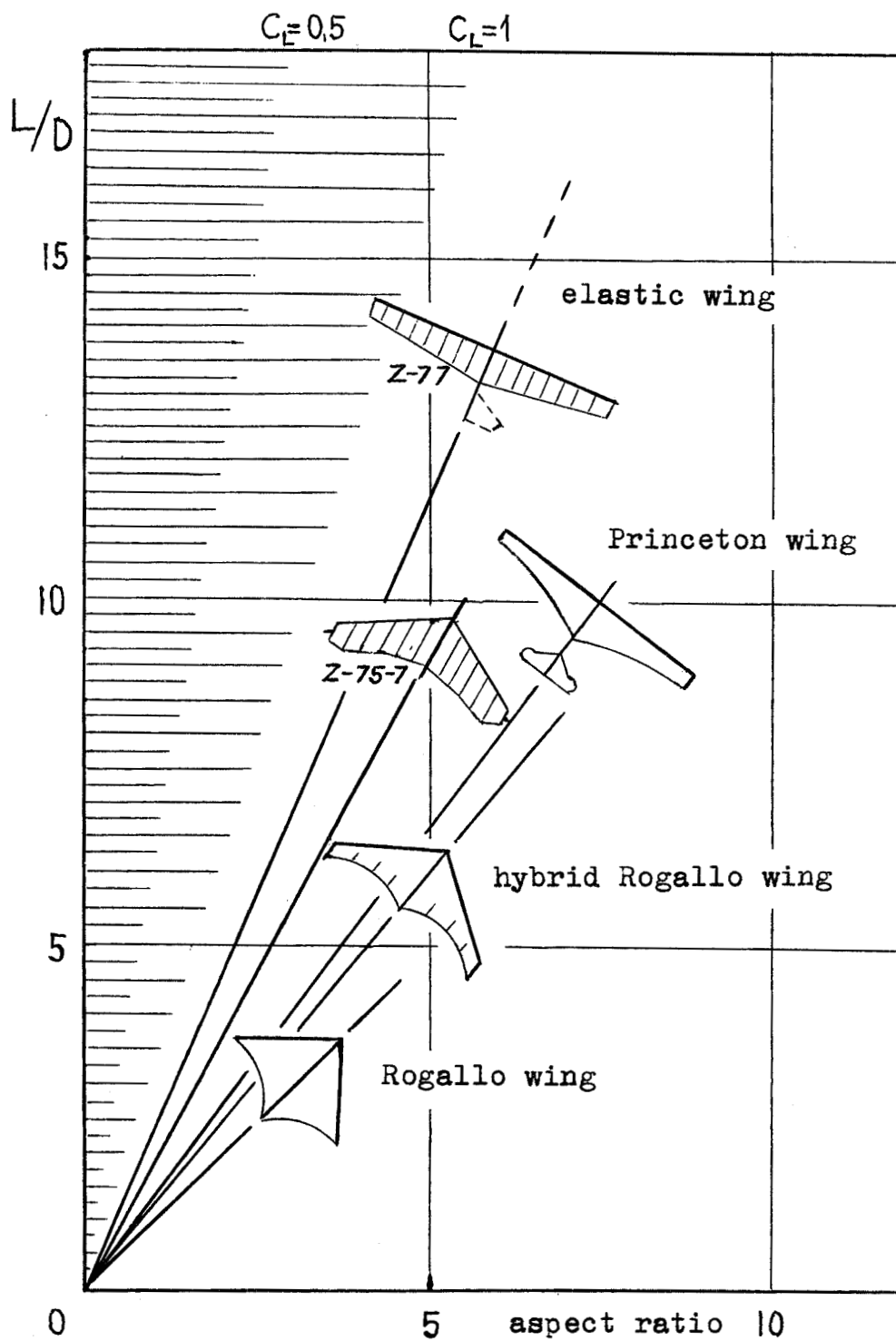


Figure 10.- Lift/drag as a function of aspect ratio for various ultralight wings.

EXPERIMENTAL STUDY OF THE FLIGHT ENVELOPE AND RESEARCH OF SAFETY REQUIREMENTS FOR HANG-GLIDERS

by Claudius LA BURTHE
Head of Aircraft Section
Aerospace Mechanics Division
Systems Department

*Office National d'Etudes et de Recherches Aéronautiques (ONERA)
92320 Châtillon (France)*



ABSTRACT

Hang gliding was born as a popular sport in France in the 70's. After a period of observation, French Officials decided that hang gliders were no longer to be considered as toys, but as a new kind of aircraft. Then, French Government funded a two years' research contract at ONERA on the safety of hang-gliders, in an attempt to set up the most adequate acceptance rules.

S1, 8 x 16 meters wind-tunnel of Chalais-Meudon near Paris, was used for two series of full scale tests, with 15 different gliders, including two-seaters, and most of them with a dummy pilot. A six component instrumentation provided lots of aerodynamic data. Flow visualization was used and showed quite unexpected air flows.

The calculated basic performances were checked in real flight by the author, with some of the same gliders as used in the tunnel.

The flight mechanics computations were then completed, providing both the flight envelopes with all sorts of limits and a fairly precise idea of the influence of several parameters, such as pilot's weight, wing settings, aeroelasticity, etc... The particular problem of luffing dives was thoroughly analysed, and two kinds of causes were exhibited in both the rules of luffing and aeroelastic effects. The general analysis of longitudinal stability showed a strong link with fabric tension, as expected through Nielsen's and Thwaites' theory. Fabric tension strongly depending upon aeroelasticity, that parameter was found to be the most effective design one for positive stability.

Lateral stability was found to be very similar in all gliders except perhaps the cylindro-conical. The loss of stability happens in roll at low angle of attack, whereas it happens in yaw at high angle. Turning performance was a bit surprising, with a common maximum value of approximately 55° of bank angle for a steady turn.

Structure calculations began on the basis of an isostatic technique which did not succeed because the leading-edges, keel, and cross-spar were separated. Then, a linear finite elements technique was used and gave very adequate results for normal loadings, since the comparison with both flight and ground tests was very satisfactory. The prediction of ultimate loadings and breaking of the structure is less precise, and would possibly require a non-linear computation because of the bendings.

During the research, all reports about significant casualties happening in France were analysed at ONERA and were of great help in the direction of the study.

The conclusions of the research are, first that none of the normal aeronautical requirements would apply to the case of hang-gliders. One good example would be the stall, which is the base of a good half of a normal aircraft certification. A hang glider would possibly require the half of the certifier's attention on its maximum diving speed. As

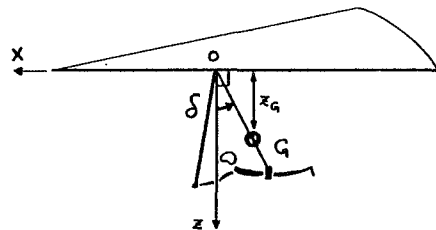
far as certification means are concerned, it is intended to make an aerodynamic-test-vehicle which would be devoted only to development and stability checks. A structural acceptance could be delivered on the basis of a calculation, plus ground-testing, using the ONERA method.

But probably the most important impact of the research in terms of hang-gliders flight safety was the dissemination of this information to French instructors and pilots.

SYMBOLS

- AOA angle of attack
- C_D drag coefficient
- C_{D0} drag coefficient at $\alpha = 0$ (linearized)
- C_L lift coefficient
- $C_{L\alpha}$ derivative : $dC_L / d\alpha$ (linearized), lift gradient
- $C_{\alpha\beta}$ rolling moment due to sideslip-coefficient
- C_M pitching moment coefficient
- C_{M0} pitching moment coefficient at $\alpha = 0$ (linearized)
- $C_{M\alpha}$ derivative $dC_M / d\alpha$ (linearized)
- $C_{M\beta}$ pitching moment due to sideslip-coefficient
- $C_{N\beta}$ yawing moment due to sideslip-coefficient
- F force exerted by the pilot on the control bar ($F > 0$ corresponds to a nose-up action)
- G center of gravity of the vehicle
- ℓ aerodynamic chord (length of the keel)
- L/D fineness ratio
- O center of the glider (at the crossing of keel and cross-par)
- O, X, Y, Z wing axes
- \vec{R} resulting aerodynamic force on the glider
- V relative air velocity
- V_{stall} stalling speed
- z_G height of center of gravity, wing axis (see fig.)
- α angle of attack (in degree)
- α_β corresponding to maximum L/D
- α_K corresponding to the kink point on $C_M(\alpha)$ curve
- α_{Luff} corresponding to onset of luffing if α decreases
- $\alpha_{min\ sink}$ corresponding to minimum sink speed
- α_V corresponding to maximum of $\sqrt{C_L^2 + C_D^2}$ (minimum flying speed)
- β sideslip
- $\Delta E\alpha = \alpha_V - \alpha_{Luff}$
- $\Delta S\alpha = \alpha_V - \alpha_K$
- δ angle between wing-axis OZ and pilot strap (see fig.) ($\delta > 0$ corresponds to a nose-up action)
- λ aspect ratio

- Δ aircraft in trim with control bar free ($F = 0$)
- \mathbb{P} luffing limit
- \mathbb{M} maneuvering limit (max length of the pilot's arms)
- \mathbb{F} force limit (25% of pilot's weight)
- \mathbb{R} loss of roll control
- \mathbb{Y} loss of yaw control



INTRODUCTION

In France, hang gliding started to be a popular sport in 1973, when a national association (FFVL) was born. There were some hundreds of people flying, almost all claiming to be instructors! As usual, some dramatic accidents focused everyone's attention on hang gliding, and fairly soon, many flying places became very crowded. Some of them were closed because of the problems created by the people watching and their motor-cars. But the aeronautical authorities were reluctant to consider them as real aircraft, and preferred initially to classify them as beach games, in order not to have to certify them.

After two years, it was clear that a new kind of aircraft was flying French skies, and something had to be done about its flying safety. The DGAC (equiv. to F.A.A.) funded a two years' research at ONERA about the flying envelope of ultralight hang-gliders, and requested advice for future specifications.

In order to avoid difficult similarity problems due to the slackness of fabric, it was decided to go through scale 1 tests in S1 Meudon wind-tunnel. The gliders used covered different shapes from the standard Rogallo to the Fledgling 1.

Somewhat unexpected results were obtained, and it was decided to check the main performances in flight, which was done successfully.

Then, the flight mechanics computations were completed, and highlighted some very interesting and specific features of these vehicles.

At the same time structural calculations were undertaken, and constantly cross-checked with in-flight and ground-test measurements.

But the determination of handling, performance and structure specifications remains difficult because of the numerous non-linearities encountered in the problem, and the difficulty of defining adequate demonstrations for the manufacturers.

AÉRODYNAMICS

Wind-tunnel testing of a sail-wing mock-up raises difficult scale effect questions. Therefore ONERA decided to use S1 Meudon, which allows scale 1 tests of hang-gliders, thanks to its 16 x 8 m elliptic facility. Nevertheless, the study is not necessarily free of Reynolds problems, as the paragliders' flying speeds places their Reynolds number in the range of 1 to 8 million. This could explain a good part of the scattering found in the tunnel results.

Two series of one month tests were performed with 15 different gliders covering the shapes shown on figure 1.

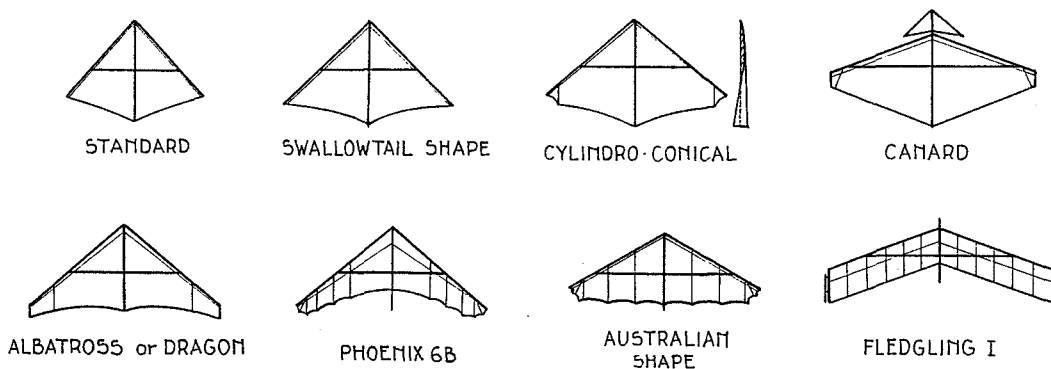


Fig. 1 - Survey of the shapes of gliders used.

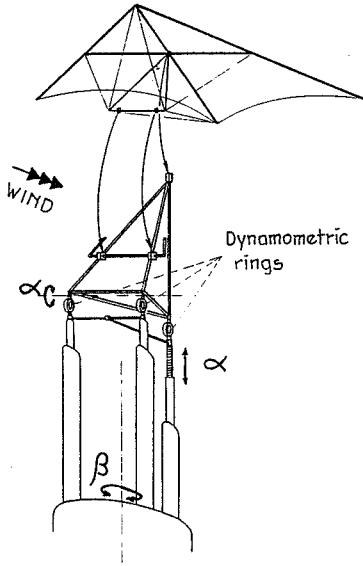


Fig. 2 - Wind tunnel arrangement.

The mounting is basically made of a tetrahedral tubing (fig. 2), fixed on three vertical masts, through three dynamometric rings. The glider is fixed by means of clutches :

- a) at its "center", on the top of the tetrahedron,
- b) at the control bar on both front struts.

The rear mast ends with a screw-jack which provides adjustment of the angle-of-attack. The whole of the mounting can rotate about a vertical axis for sideslip setting.

All tests were made under static conditions, and all measurements had to be strongly filtered because of the effects of wire and fabric vibrations.

Flow visualization revealed quite unexpected air flows, in that :
 - no wing-tip vortex was found around cruise A.O.A. ($\sim 20^\circ$),
 - a fairly high vorticing activity was found in the center-part of the wing, in spite of sweep angles ($< 45^\circ$) well below the admitted minimum value of $\sim 52^\circ$ for a vortex flow to be organised over the wing. This is almost certainly due to wing twist, which is surprisingly always near to 20° , thus preventing early separation.

Fig. 3 a) and b) show the results of visualizations respectively made with tufts and smoke, in the tunnel and in flight at all AOAs. Fig. 4 indicates the general flow around the wing at cruise angle of attack.

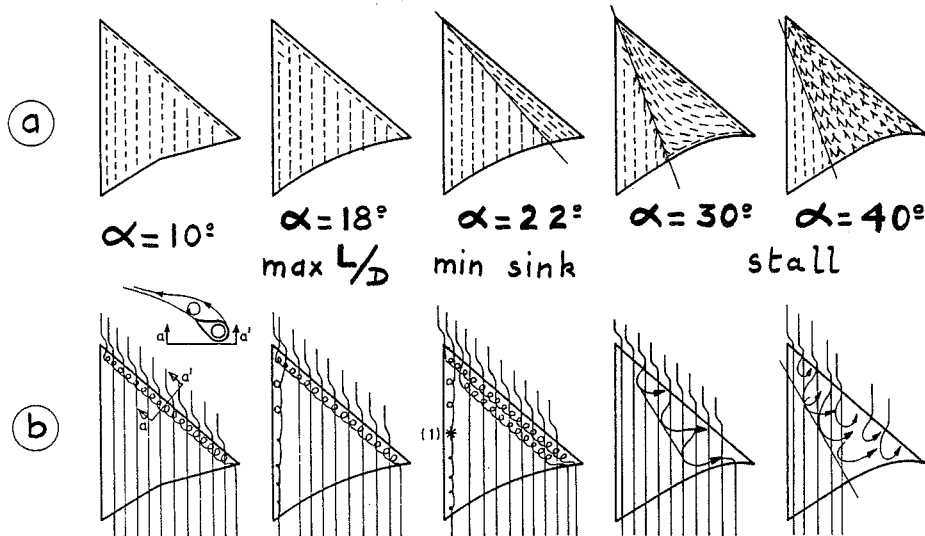


Fig. 3 - Flow visualization with tufts (a) and smoke (b).

Possible bursting
of vortex

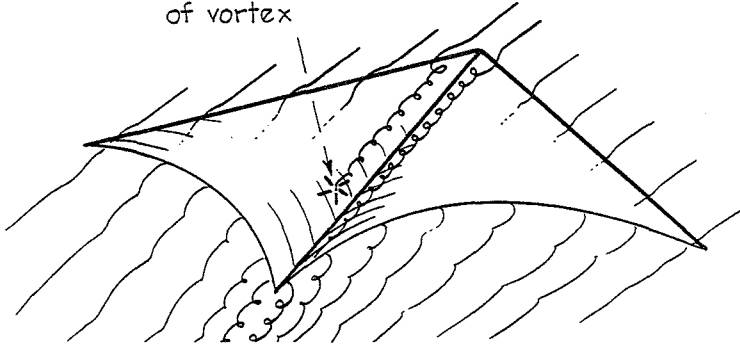


Fig. 4 - Flow visualization,
cruise A.O.A.

Two important consequences have to be mentioned. The aerodynamic loading vs. wing-span is less severe than expected through a two-dimensional theory. The flow above described remains as long as the shape of the fabric is self-adapting to the angle of attack, i.e. between luffing angle and approximately 25° . The latter characteristic provides unique capabilities to Rogallo wings in that their flying envelope is significantly increased (by an angle of 10° or more) with regard to a normal "rigid" aircraft. Fig. 5 shows the flying envelopes inferred from the following definition : the usable angles-of-attack $\Delta E\alpha$ are limited by luffing: α_{luff} and stall: α_{ν} .

	α_{luff}°	α_{ν}° L/D max	L/D max	$\alpha_{min\ sink}^\circ$	α_K°	$\Delta S\alpha^\circ$ ($\alpha_{\nu} - \alpha_K$)	α_{ν}° $\sqrt{\quad}$	$\Delta E\alpha^\circ$ ($\alpha_{\nu} - \alpha_{luff}$)
Standard	7	20	4.3	23	30	9	39	32
Swallowtail	9	23	5.5	24	30	6	36	27
Cylindro con.	9	18	4.9	24	31	-1	30	24
Canard	12	24	4.1	32	-	-	36	24
Albatross	1	16	5.5	19.5	27	0	27	26
Phoenix 6B	<6	18	5.9	21	29	3	32	>26
Australian	8	24	5.0	27	31	1	32	24
Fledgling	-5	12.5	7.6	14	-	-	20	25

Fig. 5 - Key A.O.A.s used in defining the flight envelopes.

Under these conditions, one could expect to find numerous non-linearities in the aerodynamic data. In fact, there are many, but curiously, the lift coefficient remains pretty linear against α (Fig. 6) as long as the fabric is free of luffing and far from stall conditions, which means able to adapt its own shape to the proposed angle of attack. The local linearity allows drawing a graph of $C_L\alpha$ against aspect ratio λ for all the gliders in the study (Fig. 7). Then it is possible to compare data of different origins : Fig. 8 and refs. [2, 3, 4, 5, 6].

But C_L is the only coefficient to behave so, and unfortunately the non linearities of the pitching moment C_M are very strong. Fig. 6 shows typical results obtained at constant wind speed in the tunnel. But these do not represent the actual conditions of flying, because the variations of speed induce variable loads on the aluminium structure, which is very flexible. Consequently, the shapes of the wings, mainly the billow, are modified, up to the point where it was found essential to make tunnel tests at different speeds (precisely 3 speeds in the range of 8 to 20 m/s or 18 to 45 m.p.h.). Fig. 6 shows one example of the necessary interpolation. The impact will be analysed in the discussion of longitudinal stability.

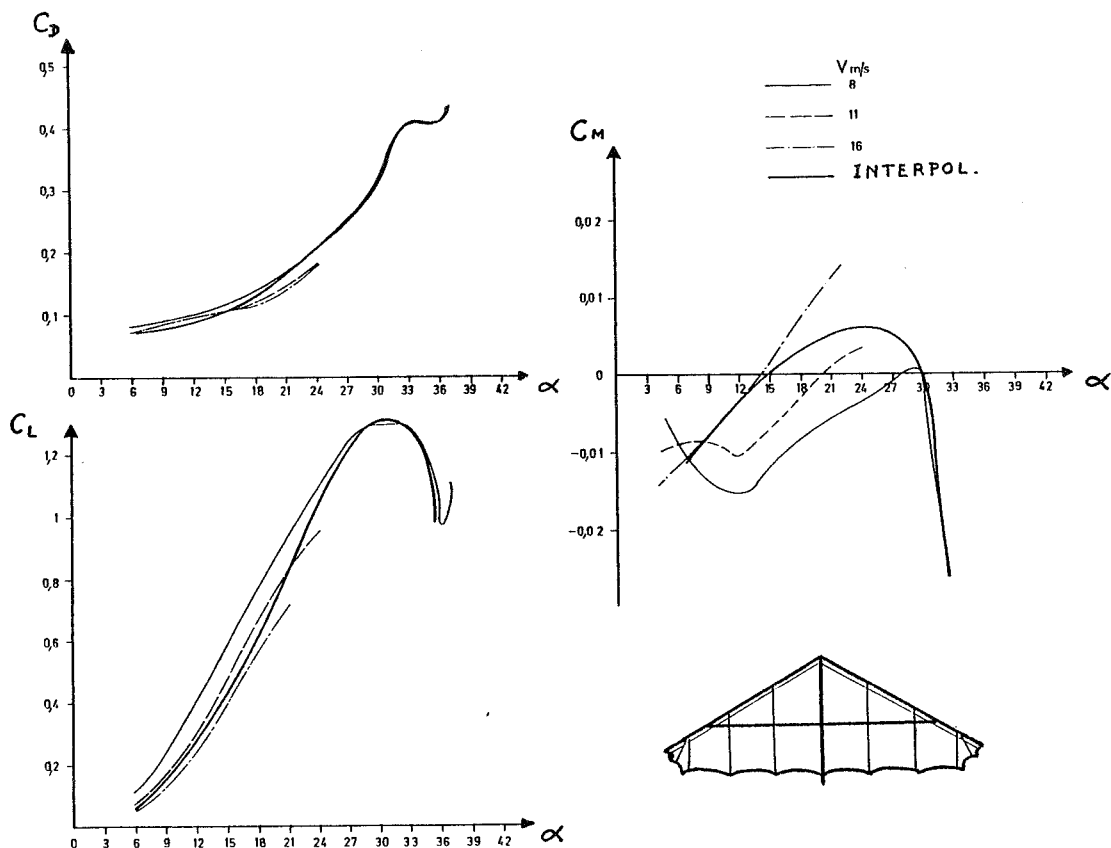


Fig. 6 - Typical tunnel results.

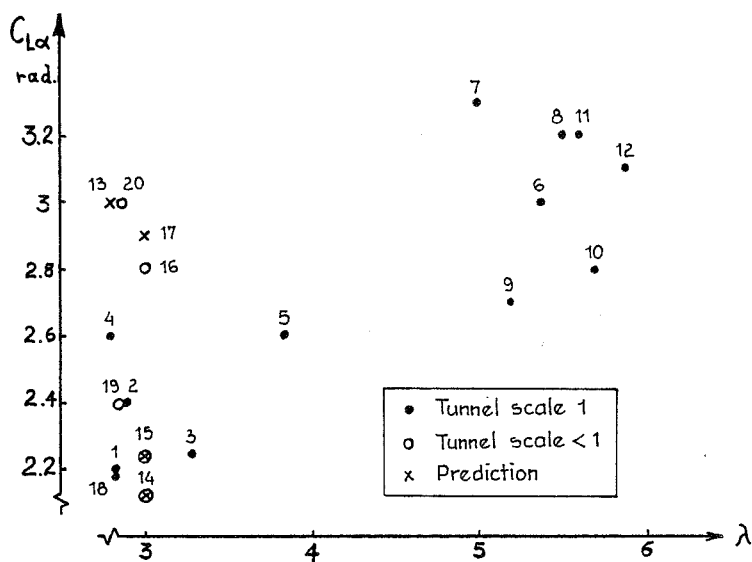


Fig. 7 - Lift gradient vs. aspect ratio.

No	Wing or Ref.	$C_{L\alpha}$	λ	
1	Standard No 1	2.2	2.83	Scale 1 W.T. tests (ONERA)
2	Standard No 2	2.4	2.88	
3	Standard No 3	2.25	3.29	
4	Swallowtail No 1	2.6	2.8	
5	Swallowtail No 2	2.6	3.84	
6	Canard	3	5.37	
7	Cylindro-con. No 1	3.3	5.0	
8	Cylindro-con. No 2	3.2	5.5	
9	Albatross	2.7	5.2	
10	Phoenix 6B	2.8	5.7	
11	Australian	3.2	5.6	
12	Fledgling	3.1	5.88	
13	Malvard [1]	3	2.8	
14	Polhamus [2]			Computation
15	Cylindrical	2.12	3	
16	Conical	2.24	3	* W.T. scale < 1
17	Naeseth [3]	2.8	3	W.T. scale < 1
18	Mendenhall [4]	2.9	3	Computation rigid wing
19	Pflugshaupt [5]	2.2	2.82	W.T. scale 1
20	ENSAÉ [6]			W.T. scale < 1
19	Rigid	3	2.83	
	Fabric	2.4	2.83	

Fig. 8 - Origins of lift gradients used in fig. 7.

The angles-of-attack limiting the flying envelope, as mentioned above, have to be discussed. The correlated analysis of the wing shape and pitching moment at low angle provides a clear explanation of the so-called luffing-dives. Fig. 9 shows how quickly and how far the center of pressure moves back when α decreases, in conjunction with a partition of the sail into two parts :

- a) one immediately downstream of the leading edges which flutters and does not provide any lift,
- b) the central part, which is inflated, and probably lifted up by the nose vortices, and which gives a local lift, applied in the rear part of the wing.

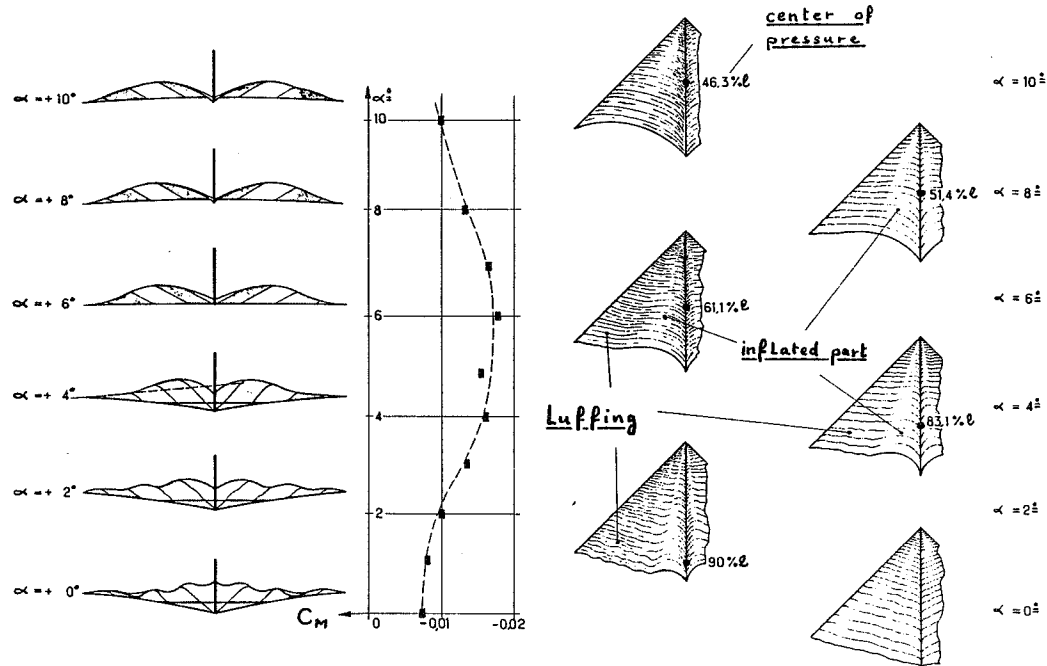


Fig. 9 - Mechanism of "aerodynamic luffing"

This phenomenon is typical of conical wings, obviously very dangerous, and of increased severity with increased length of the keel. It could explain many accidents, and will be called "aerodynamic luffing" in this paper. One must keep in mind that it happens at positive, but admittedly small, AOA, precisely when the billows are not fully inflated. It should not be confused with the cause of tumbling which is discussed below.

At negative AOA, the sails tend to invert, but are partly restrained by the cross-spar (if there is one). In that case, the shape indicated on Fig. 10 provides a very violent nose-down pitching moment which is able to launch the wing in a permanent motion, called tumbling [7].

On the other end, the stall can't be defined as precisely as on a normal aircraft, because of the very important wing twist. This will necessarily prevent abrupt flow-separation, and systematically provide a nose-down reaction of the glider. Thus a Rogallo glider may be fundamentally safe at stall. The stall conditions may be difficult to define up to the point that a reference to V_{stall} may no longer be possible. Actually, two events go along with stall. In an increase of α , one first meets a marked kink in the $C_M = f(\alpha)$ curve at α_k (discontinuity on $dC_M/d\alpha$). But lift continues to increase up to its maximum obtained at α_{γ} . Fig. 5 shows the values of $\Delta S\alpha = \alpha_{\gamma} - \alpha_k$ which are of interest in forecasting the behaviour of the glider at stall. Thus a good correlation was obtained between forecast and flight on the stalls obtained after quasi-static slow-downs, the severity of the stall being less with increased gap between both events (increased $\Delta S\alpha$). But this does not apply to most of the stalls actually occurring in flight, which are more or less dynamic ones, and often more severe than expected. A good study remains to be done on the

influence of the local magnitude of $C_{L\alpha}$ on the severity of the stall at a given $\Delta S\alpha$.

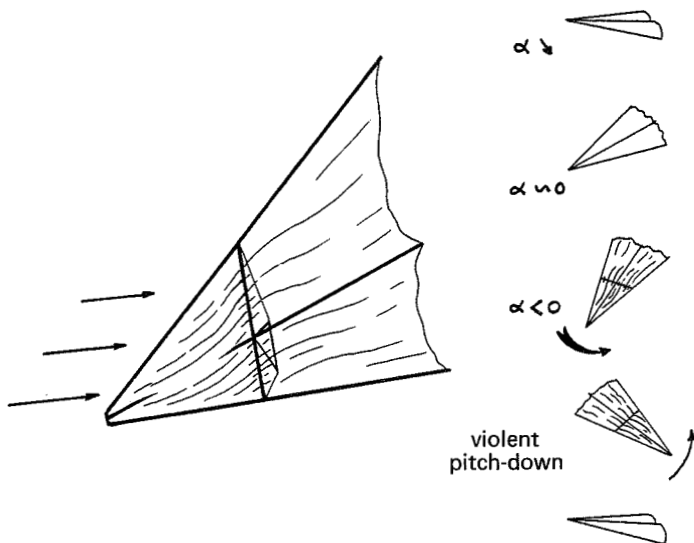


Fig. 10 - Tumbling.

FLIGHT MECHANICS

The first polar curves obtained in the tunnel provided surprisingly high minimum flying speeds, as well as scattered typical performance speeds (minimum sink and maximum L/D, as presented in fig. 5). The minimas were approximately but successfully checked in flight, using a simple but effective instrumentation, which provided through telemetry : air-speed, A.O.A., 3-axis-accelerometers, and two structural stresses (Fig. 11 and 12 give the calibrations). As an indirect consequence of that verification, we had to consider that a hang-glider is often flying in unsteady conditions, for example at take-off, landing, initiation of a turn, stall. This is due to the effects of the accelerated air-mass around the glider, which probably can't be neglected, and puts a severe limitation on the validity of quasi-static models.

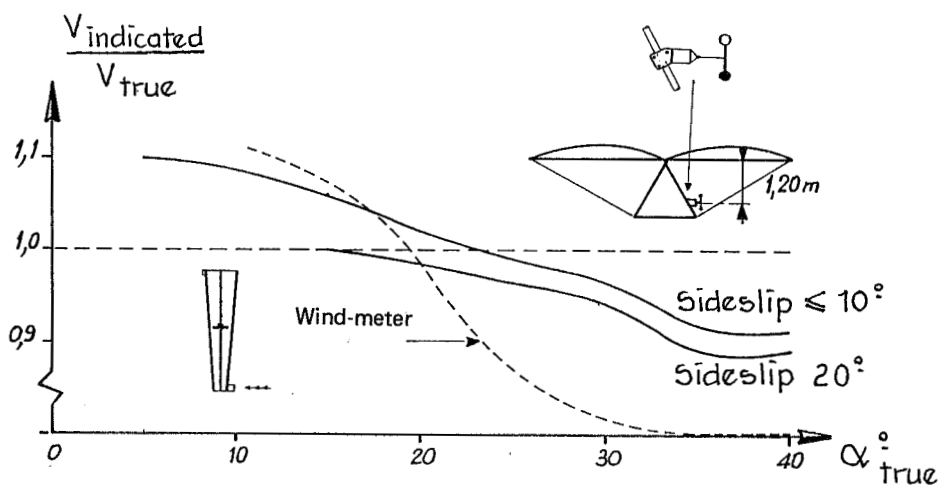


Fig. 11 - Calibration of spoon anemometer.

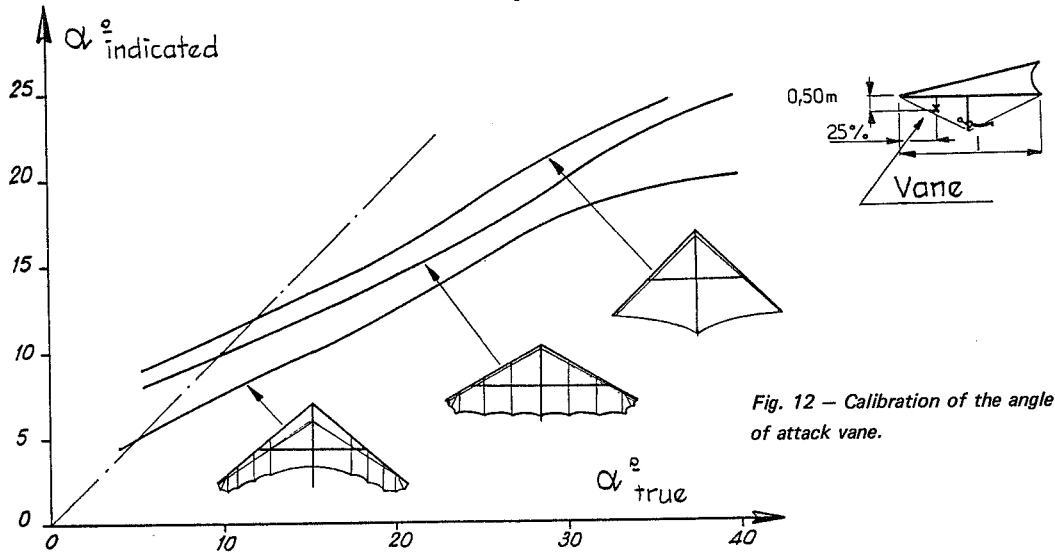


Fig. 12 - Calibration of the angle of attack vane.

The overall verification of the calculated performance allowed the estimation of the origins of drag. Fig. 13 shows the little contribution of pilot's body, but the high level of friction drag.

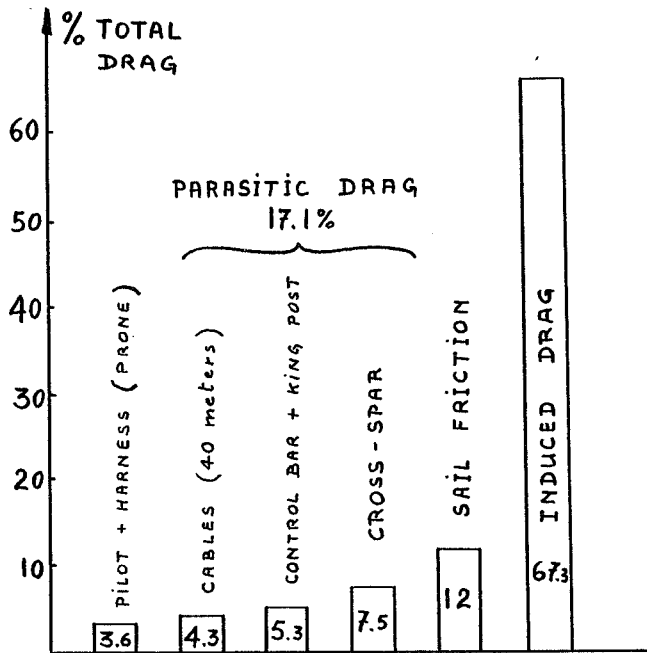


Fig. 13 - Contribution to total drag (typical wing, $C_{D0} = 0.06$, $L/D = 5$, $V = 10$ m/s).

There is no doubt that the most critical problem of hang-gliders is longitudinal stability. It was explained above that non-linearities are present everywhere in the aerodynamic data, especially if aeroelastic effects are taken into account. One consequence is that it is not possible to define an aerodynamic center, which would require constant values of $C_{L\alpha}$ and $C_{M\alpha}$. Another particular feature of hang-gliders is the lowered center of gravity, which introduces an effect of drag on longitudinal stability. Remembering the rule of positive stability which applies to a normal flying wing: $C_{M0} < 0$, it might be generalized to a hang-glider, whose aerodynamics would be linear, if

$$C_{M0} < -\frac{z_G}{l} C_{D0}$$

assuming z_G constant (the calculation has to be made in body-axis, using Lilienthal polar curve).

In order to clarify the problem, fig. 14 shows how the actual resulting aerodynamic force \vec{R} varies in body axis. The necessity of equilibrium fixes the center of gravity of the vehicle at a given location for a given α .

If the aerodynamic data C_D , C_L , C_M were linear, or at least conventional, the intersection G of \vec{R} and a circle centered in O would vary regularly. As it is not the case, the displacement of point G moves in an odd manner against α .

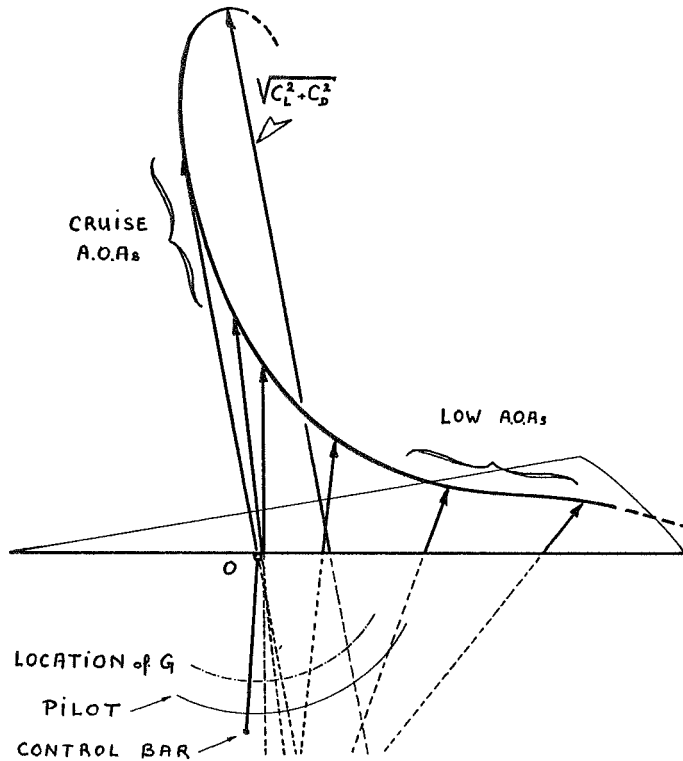


Fig. 14 - Location of resulting aerodynamic force in body axis (unstable wing).

The problem of longitudinal stability having no analytical solution, a numerical computation was performed, giving both pilot's forces F and displacements δ in body-axis against α . Analysing the significance of these curves shows that :

- a) "effort"- or "control bar free" stability $F(\alpha)$ is typical of stability about O , pilot's weight being a pure pitching moment generator, as seen on figure 15,
- b) "displacement"- or "control bar fixed" stability $\delta(\alpha)$ is typical of stability about G , as seen on figure 16.

The latter being necessarily smaller, "control bar free" stability is to be preferred as a safety criterion, which would write $dF/d\alpha$.

Computations were so organized that $F(\alpha)$ was the final result to be obtained. As it is rather easy to measure pilot forces against speeds $F(V)$ in flight, this was used as means of checking the whole of the calculations. Comparisons are shown on figure 17.

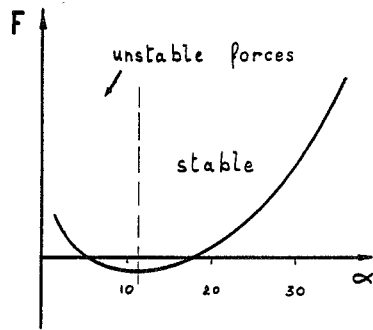
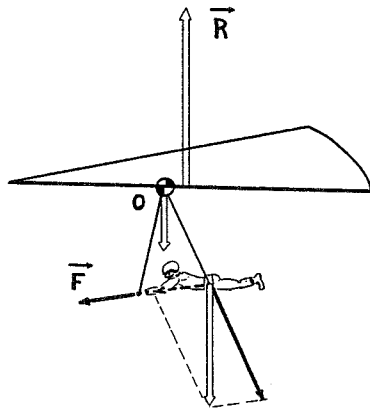


Fig. 15 - "Control bar free" stability.

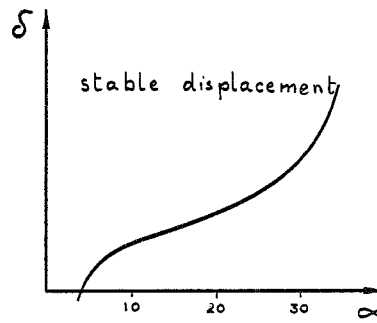
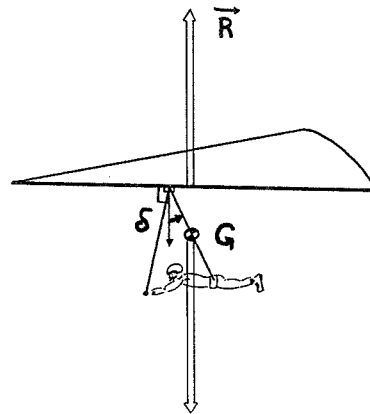


Fig. 16 - "Control bar fixed" stability.

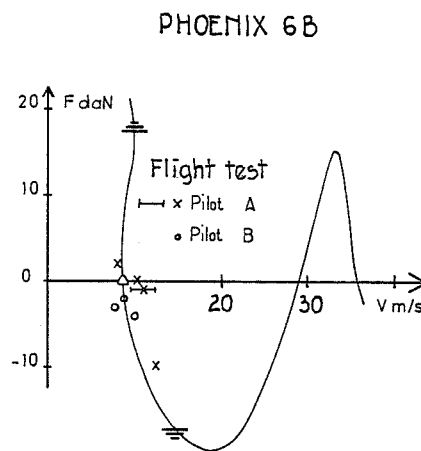
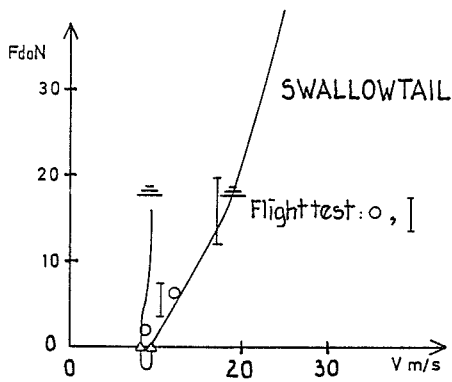


Fig. 17 - Comparison of flight test results vs. computations.

But many of the gliders in the study still presented significant instabilities at low A.O.A. in spite of having rather short keels. Looking at pitching moment curves obtained at different tunnel speeds proved that aeroelastic effects often have a negative influence on longitudinal stability at low A.O.A. Figure 18 shows this and gives a physical explanation, which was found to be applicable to a wide majority of gliders. The inwards displacement of the front part of the leading-edges loosens the fabric around the nose (fig. 19), and local lift drops dramatically, according to Thwaites' and Nielsen's theory on the behaviour of sail wings [8, 9]. This is a second explanation of the well known divergent luffing drives, and will be called "aeroelastic luffing" as opposed to the "aerodynamic luffing" described previously. Fortunately, this dangerous effect can be easily suppressed by anchoring one end of the deflectors in the middle of the bending part of the leading edges, as shown on figure 18. But, aeroelastic effects on longitudinal stability will certainly remain important, and thus become a very effective design parameter for the manufacturer.

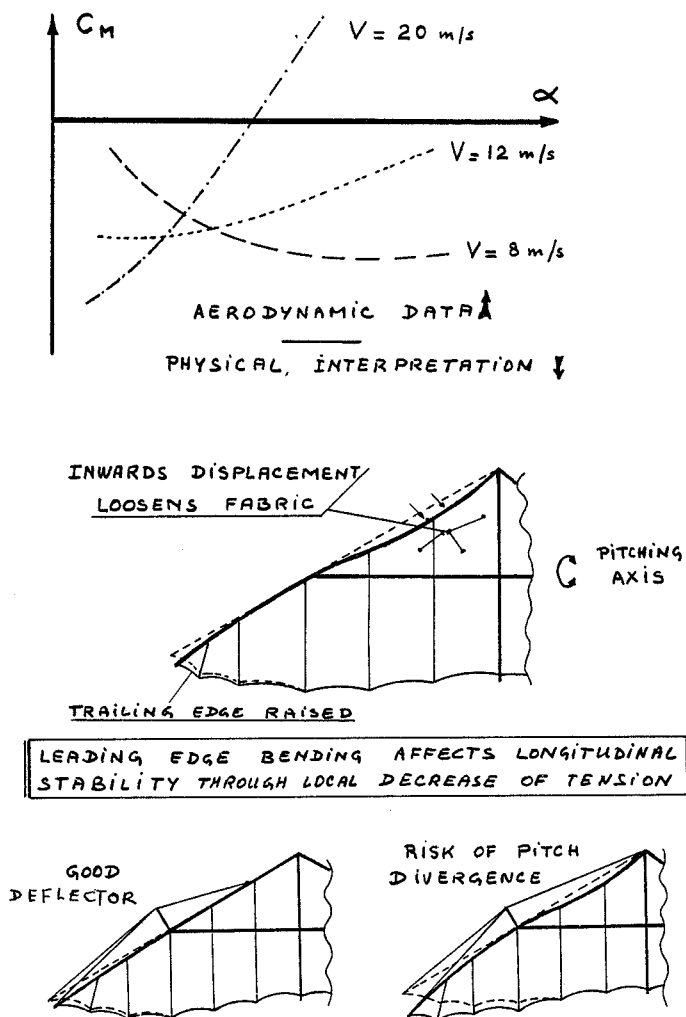


Fig. 18 - "Aeroelastic luffing".

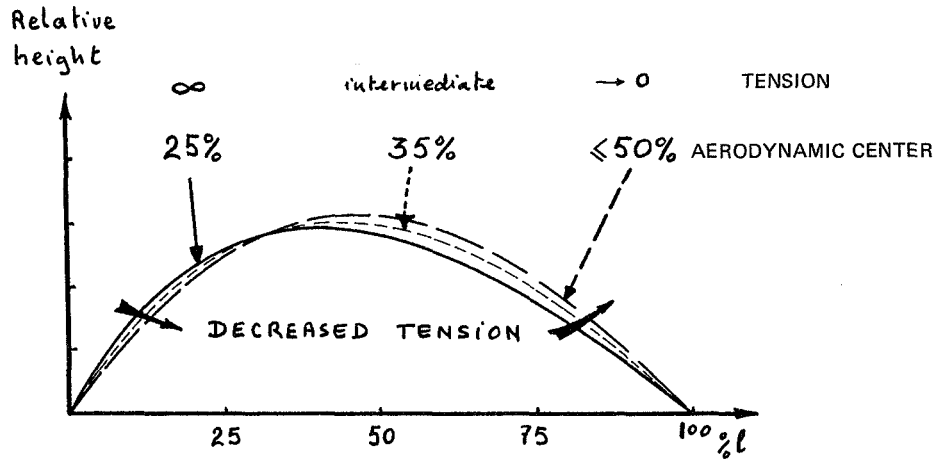


Fig. 19 - Two-dimensional theory of fabric airfoils (Thwaites & Nielsen).

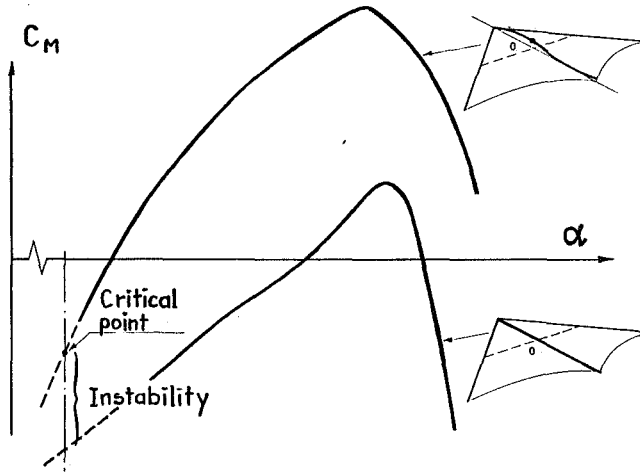


Fig. 20 - Typical effect of keel camber.

A more generalized use of Nielsen's and Thwaites' theory shows that there is a strong relationship between longitudinal stability and flying speed. Speed creates tension, and tension governs shape of the profile, as shown on figure 19. Consequently a variation of speed can result in a significant displacement of the center of pressure in the wrong direction.

Another feature is favourable to a positive longitudinal stability : the keel camber, as shown on figure 20.

Lateral stability and handling was found curiously more or less similar with all gliders in the study. It was first determined in flight that normal flying allows normal increments of 10° of sideslip, whereas ultimate manoeuvres can result in $\beta = 30^\circ$.

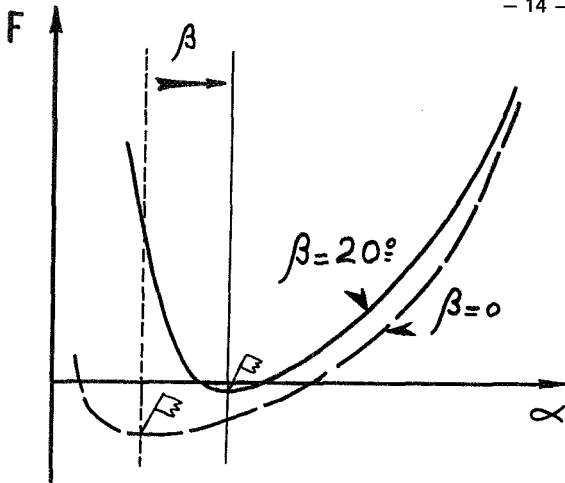


Fig. 21 - Effect of sideslip β on onset of longitudinal instability.

Laterally, the most important result is the general magnitude of $C_{M\beta}$, which corresponds to a marked pitch-down moment. Common sideslip effect is to raise the beginning of longitudinal instability by several degrees (fig. 21). This results in a modification in the shape of the forward wing due to sideslip: the fabric tends to flatten itself downstream of the leading-edge, and the application of lift moves back. The effect on the shape of the other wing is negligible in terms of camber. This results in a high risk of "tucking into a turn" when it is initiated at very low speed, and could explain several accidents.

Lateral stability itself was analysed by means of an old fashioned criterion which looks like the "spiral stability" one.

Its use demonstrated that all gliders in the study would become laterally unstable at both ends of A.O.A. envelope because of loss of yawing stability ($C_{N\beta}$) at high A.O.A., and because of loss of rolling stability ($C_{L\beta}$) at low A.O.A. It was surprising to find such a result, which can't be generalized without care.

Turning performance was also surprising. The turning equations normally used for aircraft capable of making horizontal turns are not adequate for the case of a glider-with poor L/D, which is only capable of a helicoidal motion. An adequate set of equations was used and resulted in the performances given in figure 22. Again, they are rather similar with all gliders because of the little scattering in maximum L/D. The most important ones are:

- a) it is not possible to make a steady turn if bank angle is bigger than $\sim 60^\circ$;
- b) at a given lower bank angle, there are theoretically two possibilities of making a steady turn, with two different A.O.A.s and load factors;
- c) the rate of descent, or height loss per turn is very sensitive to α at low A.O.A.

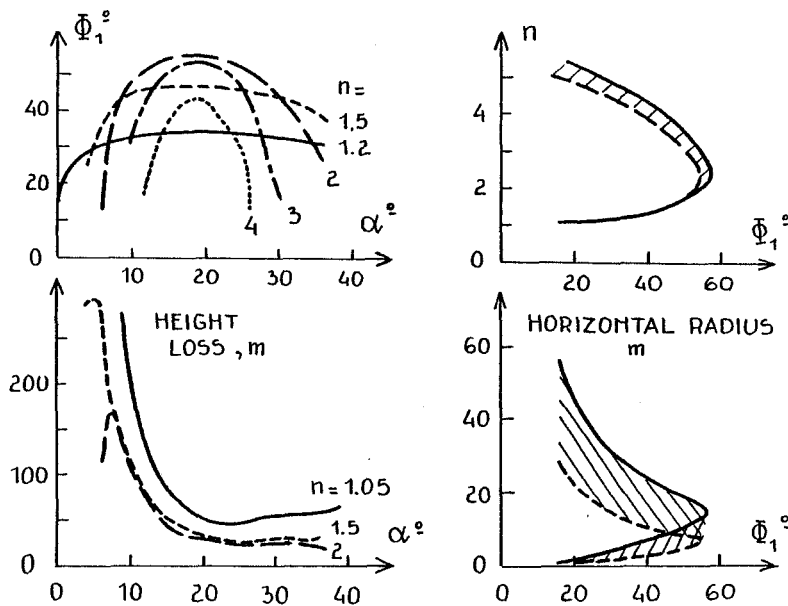


Fig. 22 - Typical wing turn performance.

Performance envelope of all gliders known.

STRUCTURE

In France, in the early years of hang-gliding, no evidence of structural failures was obtained. Some stresses were measured in flight or in the tunnel, and no critical figure was found. This was attributed to practical knowledge of the manufacturers, and also poor performance (mainly diving speed) of the gliders. Also, the demonstration made about turning performance was anything but alarming. But the gliders on the market got improved performances, and some problems were encountered. The investigation was started by an analysis of the load factors which may be applied in real flight. It appeared that a value of 2 is difficult to overshoot in steady turn, whereas a symmetric pull-out (push-out) would perhaps reach 3 or more. A typical pull-out is shown on figure 23.

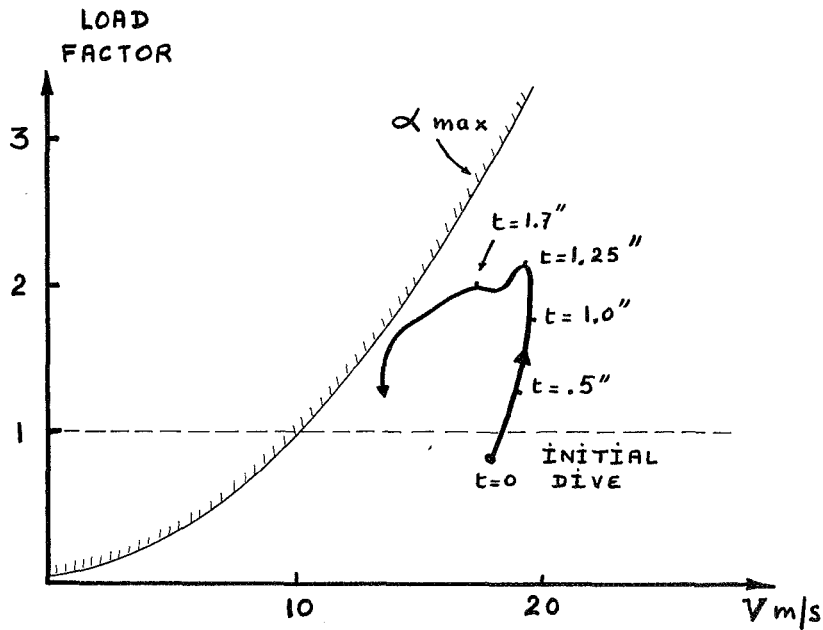


Fig. 23 - Time-history of a dive recovery.

Then structure calculations began separately on leading-edges, keels, and cross-spars. That isostatic technique did not succeed because it supposed a mandatory partition of the aerodynamic efforts. The real phenomenon required a more global approach, which was allowed by the use of a finite element program [10]. Figure 24 shows a typical result, giving both the stresses and displacements. As expected, the use of the program is easy, but the distribution of aerodynamic loading is somewhat arbitrary. An effective help was found in using sail shape identification with photography in the tunnel. Close comparison with some flight results and many ground tests gave credit to the method.

Key results are given in figure 25. But the prediction of breaking loads remains difficult, because of the scatter found in ground tests. That result will lead to a fairly high safety factor if the calculation is accepted as a design tool.

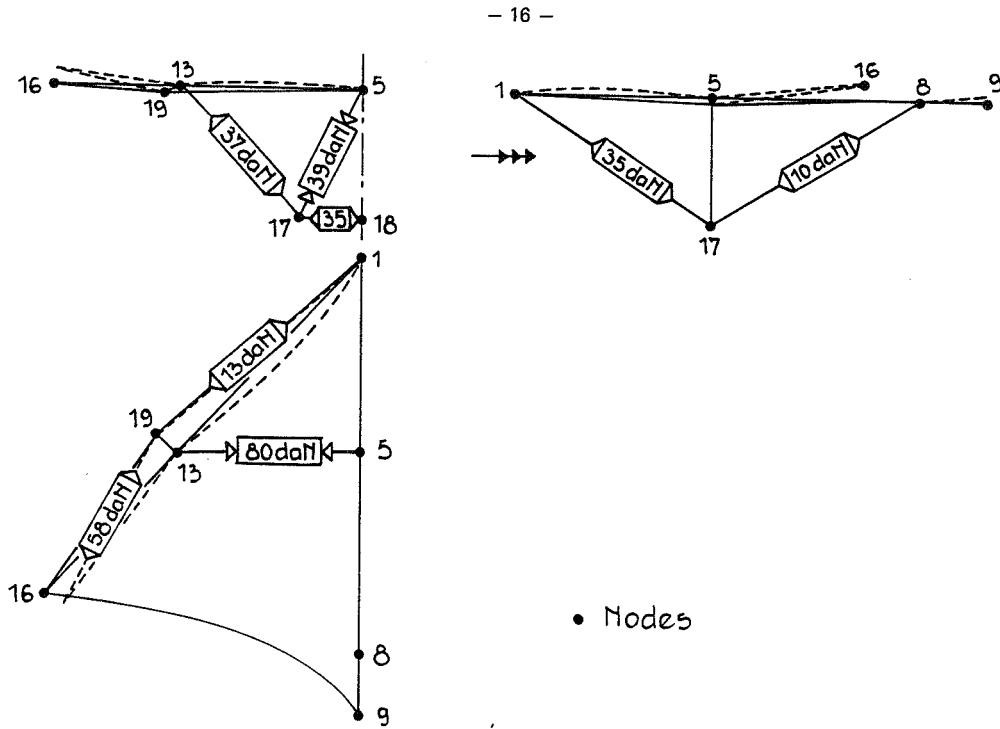


Fig. 24 - Finite elements stresses and displacements as provided by the computer. Swallowtail. Cruise A.O.A.

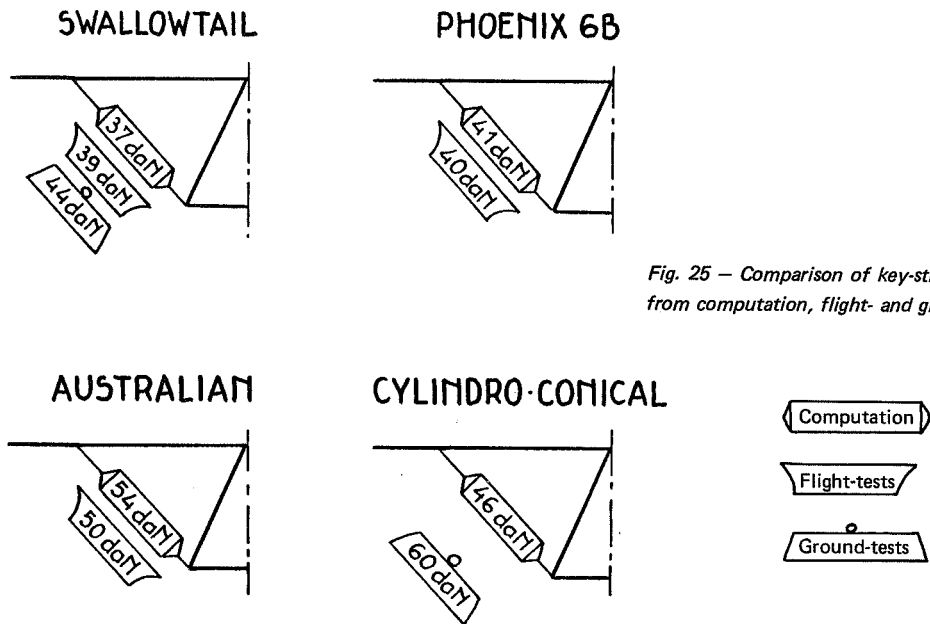


Fig. 25 - Comparison of key-stresses from computation, flight- and ground-tests.

CONCLUSION

The study was most interesting because of its many aspects and the possibility of constant crosschecking between flight and theory. As aircraft, Rogallo wings are really remarkable vehicles. The physical properties of a fabric profile which is self-adapting its own shape to A.O.A. provides a very wide flying envelope, and probably smoother losses of control. But these shape modifications may induce dangerous stability problems, which can be dominated by a good knowledge of aeroelastic effects. Several limits of the flying envelopes were determined, as shown on figures 26 to 31.

But the final aim of the study was a proposal of specifications. Although that question is very difficult to answer [11], it was established that a longitudinal stability criterion should rather refer to "control bar free" curves. But the choice of a minimum required value for $dF/d\alpha$ would be very inadequate because it would result in the acceptance of a few gliders which, being very stable, have a very poor maneuverability. A recommended solution might be to require neutral stability around cruise conditions (min. sink, and max. L/D) and an increasing positive stability at low A.O.A. At stall conditions, the safety problem does not lie in longitudinal stability which is fundamentally very positive, and the certifier's attention should be withdrawn, if possible.

The general problem of hang-gliders acceptance was broadened to the proposal of using two different tools, one for aerodynamics and one for structure. Considering that those accidents which are the consequences of aerodynamic defects result from abrupt discontinuities (mainly $C_{M\alpha}$ and $C_{M\beta}$), it was proposed to build a test vehicle, temporarily called AUTHOPUL (AUTomobile pour les Tests et l'Homologation des Planeurs Ultra-Légers). This is far less precise than a wind-tunnel but it is in the financial range of the flying community, and would allow the removal of severe instabilities. The second tool is the finite element program for structure calculations, still cross-checked with ground tests.

But consideration of several significant accident reports showed evidence that the most important effort to be made for the safety of lang-gliders lies in the operational field rather than in navigability problems.

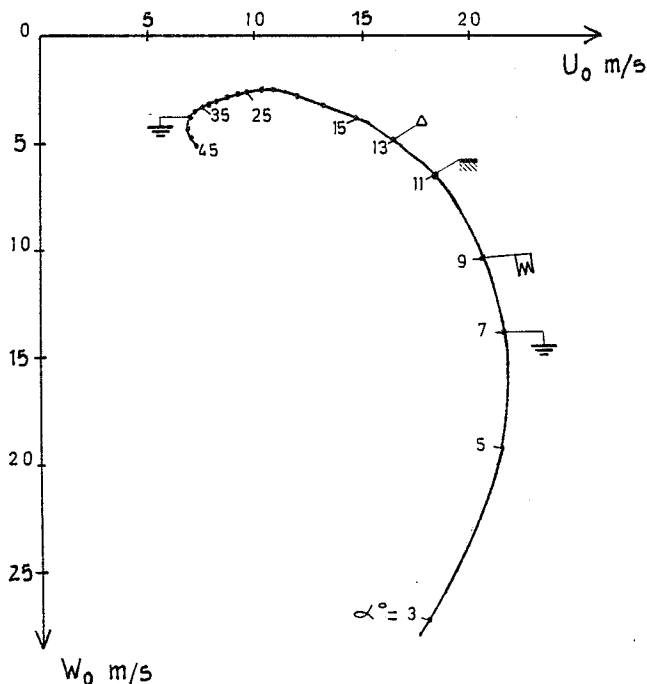


Fig. 26 — Standard.

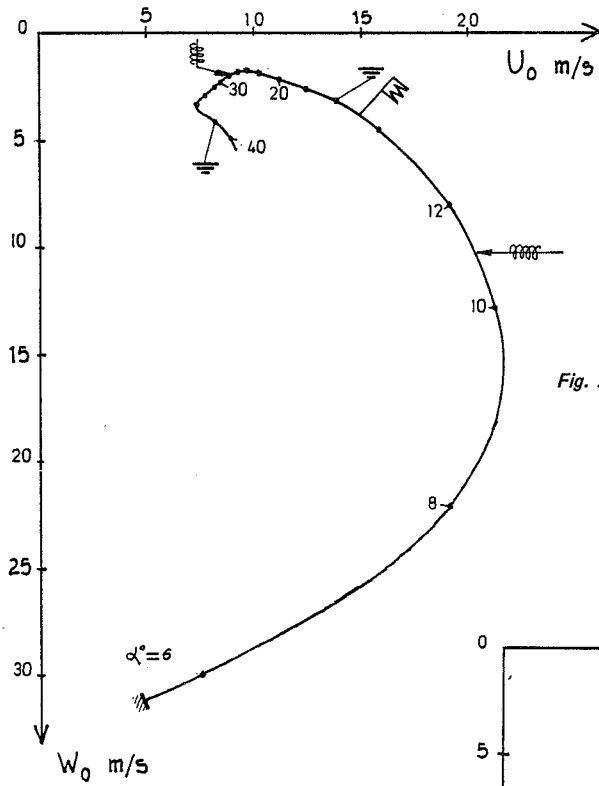


Fig. 27 - Swallowtail.

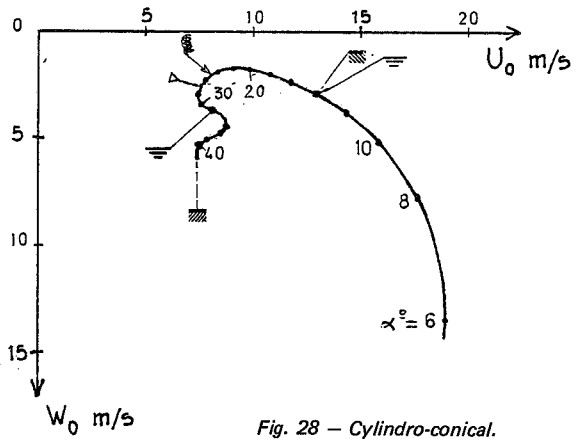


Fig. 28 - Cyllindro-conical.

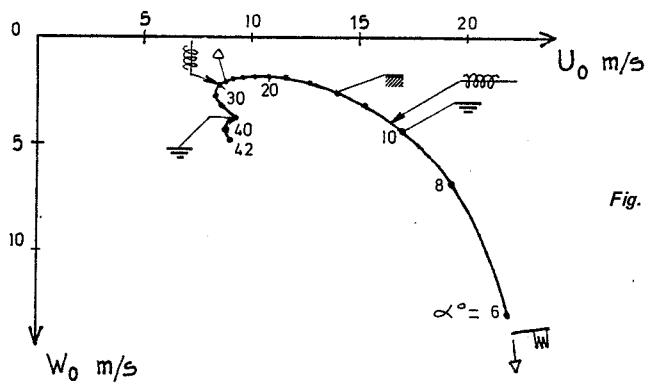


Fig. 29 - Phoenix 6B.

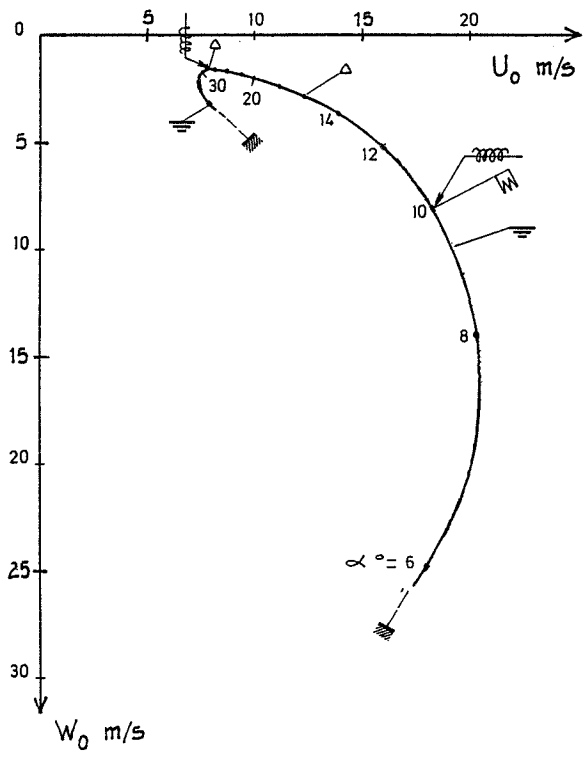


Fig. 30 — Australian shape.

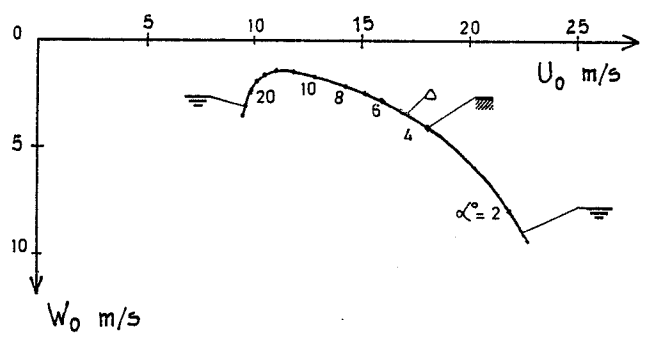


Fig. 31 — Fledgling I.

REFERENCES

- [1] L. MALAVARD et ass. — *Propriétés calculées d' ailes en delta échanuré ou non.* N.T. ONERA No 25 (1955).
- [2] E.C. POLHAMUS — *Experimental and theoretical studies of the effects of camber and twist on the aerodynamical characteristics of parawings having nominal aspect ratio of 3 and 6.* NASA-TN-D-972 (1963).
- [3] R.L. NAESETH and T.G. GAINER — *Low speed investigation of the effects of wing sweep on the aerodynamic characteristics of parawings.* NASA-TN-D-1957 (1963).
- [4] H.R. MENDENHALL, S.B. SPANGLER and J.N. NIELSEN — *Investigation of methods for predicting the aerodynamic characteristics of two lobed parawings.* NASA-CR-1166 (1968).
- [5] N. RIGAMONTI and H. PFLUGSHAUPT — *Untersuchung der stationären Flugzustände von zwei delta. Hängegleitern.* FO-1255.
- [6] Ecole Nationale Supérieure de L'Aéronautique — *Caractéristiques aérodynamiques d'ailes Rogallo.* N.T.1/77.
- [7] C.E. LIBBY and J.L. JOHNSON — *Stalling and tumbling of a radio-controlled parawing airplane model.* NASA-TN-D-2291.
- [8] B. THWAITES — *Aerodynamic theory of sails.* Proc. Roy. Soc. Series A, vol. 261 (1961).
- [9] J.N. NIELSEN — *Theory of flexible aerodynamic surfaces.* Journal of Applied Mechanics, No 63-AMP-29.
- [10] C. LA BURTHE — *Rapport Technique ONERA No 10/5134 S* (1979).
- [11] C. LA BURTHE — *Rapport Technique ONERA No 8/5134 S et 9/5134 S* (1978).

BIBLIOGRAPHY

- P.G. FOURNIER and B.A. BELL — *Low subsonic pressure distribution on three rigid wings simulating paragliders with varied canopy curvature and leading edge sweep.* NASA-TN-D-983.
- S.F. HOERNER — *Résistance à l'avancement dans les fluides.* Gauthier Villars, Paris (1965).
- R.T. JONES — *Properties of low-aspect ratio pointed wings at speeds below and above the speed of sound.* NACA report 835 (1946).
- R. LEGENDRE — *Ecoulement transsonique autour d'ailes à forte flèche.* Publication ONERA No 53 (1952).
- W.H. PHILLIPS — *Analysis and experimental studies of control of hang gliders.* The AIAA/MIT SSA Second International Symposium on the Science and Technology of Low-Speed and Motorless Flight, Cambridge, Mass, 1974.
- F.M. ROGALLO et al. — *Preliminary investigation of a paraglider.* NASA T.N. D443 (1960).

WIND TUNNEL TESTS OF FOUR FLEXIBLE
WING ULTRALIGHT GLIDERS

Robert A. Ormiston
Aeromechanics Laboratory
US Army Research and Technology Laboratories (AVRADCOM)
Moffett Field, Calif. 94035

SUMMARY

The aerodynamic lift, drag, and pitching moment characteristics of four full scale, flexible wing, ultralight gliders were measured in the settling chamber of a low speed wind tunnel. The gliders were tested over a wide range of angle of attack and at two different velocities. Particular attention was devoted to the lift and pitching moment behavior at low and negative angles of attack because of the potential loss of longitudinal stability of flexible wing gliders in this regime. The test results were used to estimate the performance and longitudinal control characteristics of the gliders.

INTRODUCTION

The flexible wing ultralight glider has evolved rapidly within the last several years, and now bears little resemblance to the original parawing configuration developed by NASA. This evolution has been characterized mainly by cut and try flight testing rather than the application of analytical design techniques or conventional wind tunnel testing. While the evolutionary mode of development has yielded relatively advanced configurations, little precise information exists about the aerodynamic characteristics of these gliders. Such information, preferably obtained from careful full scale wind tunnel testing, would be useful for numerous purposes. For example virtually no accurate information on maximum lift coefficients or maximum lift-to-drag ratio exists. Measuring these characteristics would be helpful in guiding future design refinements to enhance performance. Accurate test data on pitching moment characteristics is needed because even the basic static longitudinal stability and control characteristics of flexible wing gliders depend on complex aeroelastic

behavior of the flexible sail and frame. In certain unusual flight conditions, a loss of longitudinal stability may occur, which is believed to have contributed to in-flight structural failures. The identification and solution of such problems is hindered by a lack of accurate aerodynamic pitching moment data for various glider configurations.

The present experiments were undertaken to provide a limited amount of test data on the lift, drag, and pitching moment characteristics of four typical flexible wing ultralight gliders. The tests were carried out using conventional equipment and instrumentation in the settling chamber of a small scale subsonic wind tunnel. Because of certain limitations of the facility and equipment, the range and accuracy of the results are less than might be desirable; nevertheless useful information is provided, and the feasibility of the present techniques was evaluated.

NOTATION

A_p	pilot flat plate drag area, ft^2
b	wing span, ft
\bar{c}	average chord, S/b , ft
C_L	lift coefficient, L/qS
C_D	drag coefficient, D/qS
C_{D_p}	pilot drag coefficient, A_p/S
C_m	pitch moment coefficient, $M/qS\bar{c}$
D	aerodynamic drag, lb
F_c	pilot control force, pull force positive, lb
L	aerodynamic lift, lb
ℓ	distance between pilot tether point and application point of F_c , ft
L/D	lift-to-drag ratio, including pilot drag $C_L/(C_D+C_{D_p})$
M	aerodynamic pitch moment about pilot tether point, positive nose up, ft-lb
q	dynamic pressure, $1/2\rho V^2$, lb/ft^2
R/S	rate of sink, $V \sin(\tan^{-1} D/L)$, ft/min

S	projected wing area, ft ²
V	velocity, ft/sec(or mph)
W _g	glider empty weight, lb
W _p	pilot weight, lb
W/S	wing loading, lb/ft ²
α	angle of attack, measured with respect to keel chord line, degrees
ρ	air density, slugs/ft ³

TEST APPARATUS

The gliders were tested in the 30- X 33-ft settling chamber of a 7- X 10-ft subsonic wind tunnel. Maximum velocity in the settling chamber is approximately 18 mph, but the test velocity was limited to 15.8 mph due to strain gage balance load limits. The gliders were mounted 10 ft above the floor of the settling chamber at the top of the main support strut shown in Figure 1. The gliders were mounted directly to a T-bar adapter frame which clamped to the gliders' triangular control bar. The upper end of the T-bar frame was attached directly to the forward end of a six-component strain gage balance which in turn was mounted on top of the main support strut. Details of the mounting system are shown in Figure 2. With this system, the balance moment center was located very close to the pilot tether point of the glider which was taken to be the aerodynamic force and moment reference center of the glider. The balance mount could be rotated by remote control to vary the glider angle of attack. No provision was made for simulating pilot drag effects. Drag measurements were made of the gliders alone except for the small additional contribution of the T-bar adapter frame drag.

The strain gage balance had a normal force capacity of 1400 lb, an axial force capacity of 280-lb and a rolling moment capacity of 1200-in-lb. Tunnel turbulence and small lateral asymmetries of the gliders produced high rolling moments relative to the balance roll moment capacity and thus limited the maximum test velocities. Because of the low aerodynamic drag at these velocities, and the relatively high balance axial force capacity, the accuracy of the drag measurements was moderately low. The compromise between balance accuracy and capacity resulted from testing very large span models at low velocities using a strain gage balance designed for small, high speed models. The aerodynamic lift and pitch moment were measured with acceptable accuracy.

The four gliders tested were typical of intermediate to moderately high performance flexible wing ultralight gliders. Wing spans ranging from 25 to 30 ft were chosen in order to minimize tunnel wall interference effects as much as possible in the 33-ft wide settling chamber test section. Glider geometric parameters are listed in Table 1 and the wing planforms are illustrated in Figure 3. The Flexi 2 and Cirrus 3 are intermediate performance gliders having moderate billow sails. The Astro and Mirage are moderate to high performance gliders with higher aspect ratio and low to zero billow sails. Both have semi-floating tip ribs that limit the minimum wing tip washout in order to prevent the development of large negative aerodynamic pitching moments at low or negative angles of attack. The Astro was tested both with and without the floating ribs installed to assess their effectiveness. The Mirage was equipped with stiff cambered aluminum airfoil ribs; the other three gliders used flexible plastic or fiberglass battens. Each of the gliders is shown mounted in the wind tunnel settling chamber in Figure 4.

The test procedures were straightforward. After making wind off measurements to obtain model weight tares as a function of angle of attack, the gliders were tested at two different tunnel velocities. The angle of attack was varied while the tunnel velocity was held constant. This produced a variable sail loading which resulted in different wing aeroelastic deformations than would occur in normal flight. This loading effect will be discussed in more detail below. Each glider's test angle of attack range was constrained by balance roll moment limits. At the higher tunnel velocity a smaller range of angle of attack was tested than at the lower velocity.

The data was processed as follows. For each test point, ten sets of balance data were taken and averaged to minimize the effects of tunnel turbulence and scatter in the balance readings. Wind tunnel wall corrections were made to correct the geometric angle of attack for the induced upwash of the tunnel boundaries. At high lift the induced angle was about 2.5° . The model forces were resolved into lift and drag components in the corrected (for induced angle) wind axis system. No other tunnel blockage, buoyancy, or support interference corrections were made. The data was reduced to coefficient form based on the projected wing area (not the flat sail pattern areas) and the wing average chord (wing area divided by wing span). The angle of attack was taken to be the keel angle of attack. The moment center for pitching moments was taken as the pilot tether point. As noted above, the balance accuracy was limited by a combination of low aerodynamic force levels and high balance force capacities. While it is difficult to determine precise accuracies, the following are believed to be reasonable estimates of the accuracy of the data presented below: $C_L = \pm .05$, $C_D = \pm .03$, and $C_m = \pm .02$.

EFFECT OF TEST LIMITATIONS

Before presenting the test results it will be useful to discuss the significance of the two important limitations of the tunnel facility used for the present tests. First, it must be emphasized that the wind tunnel

test results were obtained under conditions different from those experienced by a glider in steady state flight (unaccelerated 1g flight). Aside from measurement errors and wind tunnel wall effects, testing at constant velocity (as in the present tests) generates aeroelastic effects that alter the measured results from results that would be obtained by an exact duplication of actual flight conditions. Keeping the velocity constant as the glider angle of attack is varied changes the total aerodynamic sail loading at each angle of attack. In steady 1g flight the angle of attack and velocity automatically change in such a way that the resultant aerodynamic force remains constant and equal to the total weight of the glider and pilot. Therefore, for a given angle of attack the tunnel test condition and the actual flight condition would not in general produce the same level of aerodynamic load acting on the sail. Since different loads would generate different aeroelastic deflections of the glider sail and frame, the aerodynamic coefficient data, particularly the pitch moment coefficient, would be different for the two conditions. The sail loading effect is also expected to be more pronounced for more flexible structures and higher billow sails.

Of course it would be possible to duplicate the aeroelastic effects of steady flight conditions in the wind tunnel by appropriately varying the tunnel velocity as a function of angle of attack to maintain a constant aerodynamic loading, or vary the angle of attack for a large number of test velocities and crossplot the results for a constant load condition. This procedure was not feasible for the present testing because tunnel and balance limitations did not permit testing at a sufficiently high range of velocities. However the results that are presented for two different test velocities do show the variations that would be anticipated from changes in sail loading.

Because of the relatively small test section size compared to the glider wing spans, the data is significantly influenced by induced flow effects of the tunnel floor and wall boundaries. As noted above, a correction is made for the induced angle of attack which accounts for the first order effects of the tunnel walls on wing angle of attack and the wing induced drag. It does not however, account for the effect of altering the wing span load distribution and the resultant secondary effect on induced drag. For the larger span gliders tested, this wall effect increases the loading at the wing tips and would be expected to slightly reduce the measured drag by reducing the induced drag. This is due to the fact that flexible wing gliders generally exhibit substantial tip washout which degrades the span load distribution by reducing the local section angle of attack at the tips. The effect of wall interference is to make up part of the lift lost to washout. Another effect of increasing the wing tip loading due to wall effects would be to promote tip stalling compared to free air testing. The effective reduction in washout due to wall induced effects at high lift conditions was not excessive however, being on the order of 1° to 2° .

RESULTS

Two sets of results are presented. First the lift, drag, and pitch moment coefficients as a function of angle of attack for two test vel-

ocities are presented for the five different glider configurations tested (Flexi 2, Cirrus 3, Mirage, Astro, and modified Astro without floating tip ribs). The second set of results gives the longitudinal control and performance characteristics derived from the basic wind tunnel test data. For these results, an arbitrary pilot drag increment is added to the drag data of each glider.

Figures 5 through 9 show C_L , C_D , and C_m vs α for all of the glider configurations. The data points are labelled according to the measured test dynamic pressure, $q=0.25, 0.38, \text{ and } 0.64 \text{ lb/ft}^2$. For standard sea level density the corresponding test velocities for these three dynamic pressures are $V=9.9, 12.2, \text{ and } 15.8 \text{ mph}$ respectively. Generally the effects of increasing dynamic pressure are to increase sail loading, increase washout, and thereby reduce the lift coefficient slightly and increase the pitch moment. Figures 10-12 compare the faired lift, drag, and pitching moment curves of the five configurations. This comparison provides the most concise summary of the basic results. Generally the gliders can be divided into two relatively distinct categories, each having certain unique aerodynamic features. First are the low aspect ratio, moderate billow gliders, the Flexi 2 and the Cirrus 3. Second are the higher aspect ratio low billow gliders with the floating tip ribs, the Mirage and Astro.

Consider the lift curves in Figure 10. The low aspect ratio gliders exhibit a distinct zero slope nonlinearity in the region of zero lift due to sail luffing. With the sail loaded, the lift curves are quite linear, and no sign of stall is evident even at high angles of attack and relatively high lift coefficients (maximum angle of attack was limited by balance loads). The high aspect ratio gliders exhibit virtually no luffing behavior in the zero lift region, except for a mild curvature of the lift curves near zero lift. Stall begins at moderate angles of attack and maximum lift coefficients of about 1.4 are exhibited with very gentle stall behavior. The modified Astro develops more lift at low angles of attack than the standard Astro configuration due to reduced tip washout with the floating tips removed. If the wing were more highly loaded at low angles of attack, these differences would be much smaller.

The drag curve comparisons are given in Figure 11 and no major surprises are to be found. As indicated earlier the absolute accuracy of the drag curves is less than desired but the trends appear reasonable. The high aspect ratio configurations exhibit a rather abrupt increase in the slope of the drag curve between 10° to 12° angle of attack. Visual observations of wool tufts attached to the upper wing surface indicated that the drag rise point coincided with the onset of flow separation. The separation began at the wing tips and extended gradually inboard from the tips as the angle of attack increased. The wing root became stalled only at the highest angles of attack tested, approximately 30° to 35° .

The pitching moment curves in Figure 12 are particularly interesting. It is believed that the artificial loading conditions produced during the tunnel testing influenced both the absolute pitch moment levels as well as the slope of the pitch moment curves. Therefore only certain conclusions can be drawn. First consider the low aspect ratio gliders for

which the loading effects are believed most pronounced. In the normal angle of attack range the pitch moments are negative, i.e. there is no zero moment trim point. If results were available at higher velocities and the results were crossplotted for a constant loading conditions, it is believed that these curves would indicate trimmed ($C_L=0$) stable ($dC_m/d\alpha < 0$) behavior at a reasonable angle of attack ($\alpha \sim 15^\circ$). As they stand the results show larger negative values and lower slopes than are consistent with observed control characteristics of these particular gliders. At negative angles of attack, the sails of the low aspect ratio gliders become unloaded, and collapse against the glider crossbar structure radically altering the wing camber and twist. The result is negative washout at the wingtips, and large effective camber near the root of the wing, both of which contribute to yield a large negative pitch moment. The practical significance of these results is that if transient negative angle of attack conditions were encountered in flight, a divergent pitch instability could possibly result.

The high aspect ratio, low billow glider configurations compared in Figure 12 exhibit quite different behavior although the sail loading effects still appear to be significant because of the inconsistency between the measured and observed flight trim characteristics. The most significant departure from the low aspect ratio gliders is that the Astro and Mirage exhibit a positive increment in pitch moment as the sail unloads in the zero lift region. It is interesting that this phenomenon manifests itself in the moment curve but not the lift curve. The increase in moment is believed due to the effective increase in washout (i.e. wing twist) as the inboard portion of the wing unloads and settles onto (trailing edge down) the wing cross spar. While the floating tip ribs of the Astro are effective in maintaining sufficient washout to produce positive pitch moments at low and negative angles of attack, the lower minimum angle of the Mirage floating tip rib was evidently insufficient to produce comparable results. Interestingly, while the modified Astro (tip rib removed) did exhibit much lower pitch moment at negative angles of attack compared to the standard Astro, it also exhibited a positive moment increment at the zero lift point. It was anticipated that this configuration would exhibit the opposite behavior, i.e. a negative pitch moment increment due to loss of washout at negative lift similar to the low aspect ratio gliders. A possible explanation of this behavior is that camber variations of the pre-tensioned, zero-billow sail counteracted the loss of washout at zero lift conditions.

To summarize the pitch moment results, the low billow, tip-rib-supported configurations exhibited more favorable pitch moment characteristics at negative angles of attack than did the lower aspect ratio, larger billow sail configurations.

Finally, the high aspect ratio configurations exhibited stable pitching moment changes at stall, i.e. an increased negative slope of the moment curve. (The low aspect ratio gliders' test angles of attack did not extend into the stall region.) This is somewhat surprising in view of the observed separation at the wing tips and the well known tendency of moderate and high aspect ratio swept wings to exhibit pitchup tendencies

at stall. It is possible that the high twist of the present flexible wing configurations helps to prevent such behavior.

The second set of results in Figures 13-17 was prepared to illustrate the applicability of the wind tunnel test data to performance and longitudinal control predictions and to indicate typical flight characteristics of the glider types tested. For these results, a nominal wing loading based on manufacturer specifications was assigned to each glider and an incremental pilot drag coefficient was also added to the drag coefficient test data. This drag was scaled to pilot size which was related to pilot weight. The pilot weight was determined by the individual glider empty weight and the assigned wing loadings. The pilot drag to weight relationship is given by the following formula

$$C_{D_p} = \frac{A_p}{S} = \frac{2.5}{S} \left(\frac{W_p}{160} \right)^{2/3}$$

This is based on assuming a flat plate drag area of 2.5 ft² for a 160-lb pilot and relating pilot size to weight by a square-cube relation. Table 2 gives the relevant parameters for pilot drag calculations for each glider. The glider airspeed, sink rate, and control forces were calculated for standard sea level conditions $\rho = 2.378 \times 10^{-3}$ slug/ft³ using appropriate relations. The control forces were determined from the following relation

$$F_c = C_m q S \bar{c} / \ell$$

where ℓ was assumed to be 5.0 ft for all the gliders. This relation assumes that the pitch moment coefficient is taken about the pilot tether point and that the pilot control force is applied to the control bar a distance ℓ from the tether point.

As discussed above, the effects of the test loading conditions are not believed very significant for lift and drag coefficient data and thus the L/D and sink rate performance are believed to be reasonably valid in this respect. The low accuracy of the drag coefficient data does limit the absolute accuracy of the performance data; therefore, valid comparisons between the different glider types cannot be made. Again, the variations in L/D and R/S with airspeed are more accurate. Finally because the test loading conditions have a substantial effect on the pitch moment coefficient results, the control force variations with velocity are not fully representative of actual flight conditions.

Figures 13-17 indicate that maximum L/D values occur only for a relatively narrow velocity range; the minimum sink rate is not quite so sensitive to velocity. For the Astro and Mirage, the minimum sink rate condition coincides with the point where wool tuft observations indicated the onset of flow separation. The effects of test velocity are relatively small for L/D and sink rate, but are more substantial for the longitudinal control force. Even though the pitch moment coefficient data was generally negative, the resulting control forces are not excessive. A positive

slope of the control force versus velocity curve indicates a statically stable configuration. Nearly all configurations show a very stable slope near the minimum flight speed. The Astro shows a reasonably well behaved control force variation that is stable at all velocities, trims to zero force (although at a rather unrealistic 53 mph) and exhibits a large increase in stability at stall. Finally, the high lift coefficients yield relatively low minimum velocities.

For comparison purposes, the varied L/D and sink rate curves are given in Figures 18 and 19.

CONCLUDING REMARKS

Testing of full scale flexible wing ultralight gliders in the settling chamber of a subsonic wind tunnel provided useful information about the glider aerodynamic characteristics. The limitation on maximum test velocity prevented full simulation of load conditions corresponding to normal flight. Two low aspect ratio moderate billow gliders exhibited sail luffing effects in the lift curves, increased negative pitching moment at negative angles of attack, and evidence of high maximum lift coefficients. The higher aspect ratio, low billow configuration lift curves showed only minor evidence of zero lift sail luffing; the pitch moment curves showed a positive moment increment as lift decreased below zero. The high aspect ratio configurations showed gradual lift and increasingly stable moment variations at stall although wool tuft flow visualization indicated flow separation commencing at the wing tips. The drag variation with angle of attack increased abruptly with the observed onset of flow separation. The effect of floating tip ribs was to substantially increase the wing pitching moment of the Astro at negative angles of attack. The Mirage floating tip ribs appeared to be less effective, presumably because of a lower minimum washout angle. Except for control force characteristics, performance estimates based on the test data appear consistent with typical operating experience.

TABLE 1 - GLIDER GEOMETRIC PROPERTIES

	Flexi 2	Cirrus 3	Mirage	Astro
Projected wing area, ft ²	192.0	193.1	113.6	144.4
Wing span, ft	29.43	28.14	25.56	28.74
Nose angle, degrees	95	91	112	108
Leading edge sweep, degrees	42.5	44.5	34.0	36.0
Aspect ratio	4.50	4.09	5.77	5.70
Root chord, ft	15.04	12.83	7.58	9.23
Average chord, ft	6.53	6.87	4.44	5.02
Moment center, percent of root chord behind root chord leading edge	49.0	58.1	66.0	62.1
Vertical moment center, distance below bottom of keel tube, ft	0.47	0.58	0.47	0.50
Billow, per side, degrees	2.5	1.25	0.66	0.0
Number of battens or ribs per side	2	6	4	4
Floating tip rib minimum washout (estimated), degrees	----	----	8	16

TABLE 2 - PILOT DRAG DATA

Glider	W_g , lb	W/S lb/ft ²	W_p , lb	C_{D_P}
Flexi 2	41	1.0	151	.0125
Cirrus 3	39	1.05	164	.0131
Mirage	35	1.1	90	.0150
Astro	40	1.2	133	.0153

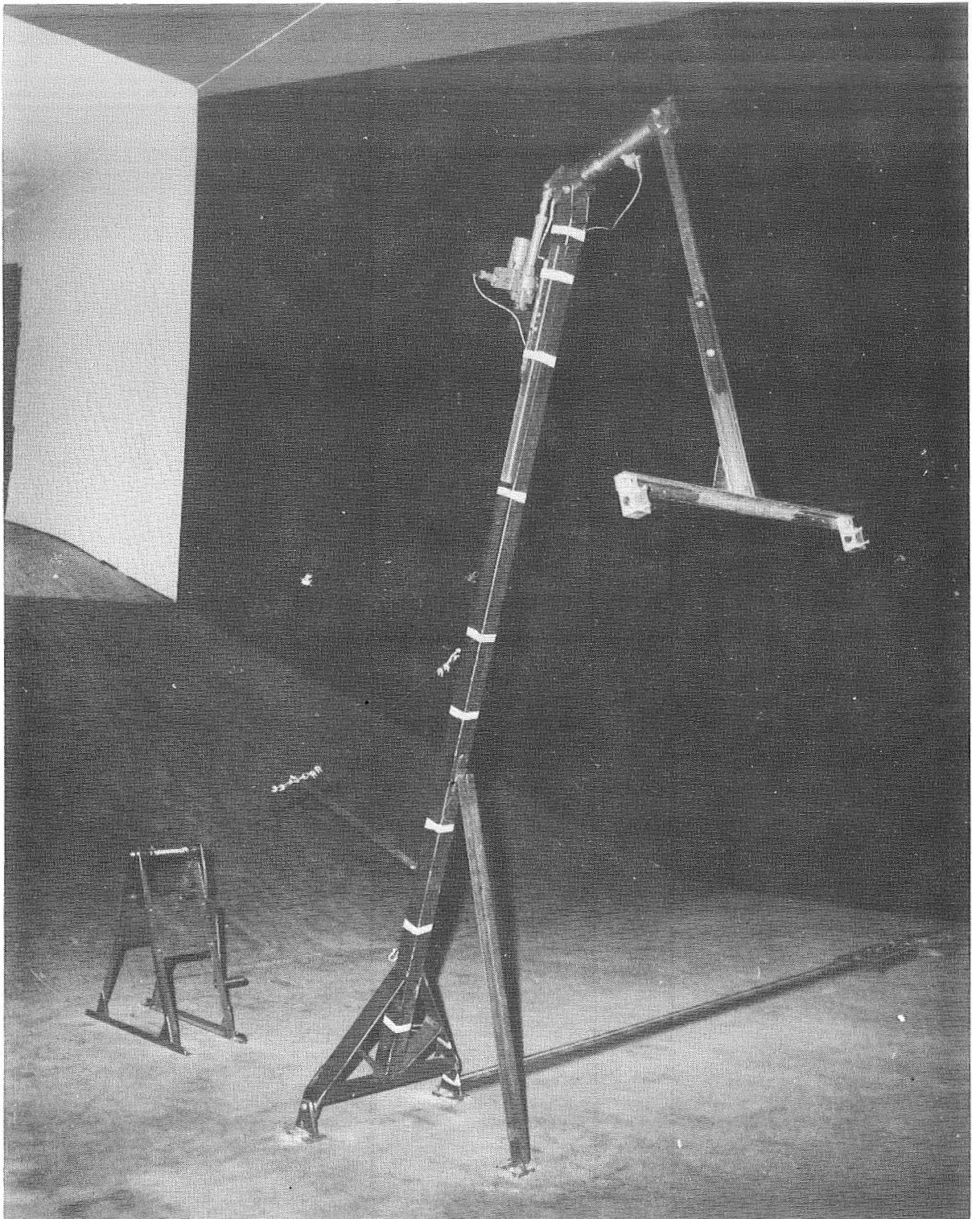


Figure 1 - Main support strut and T-bar adapter frame.

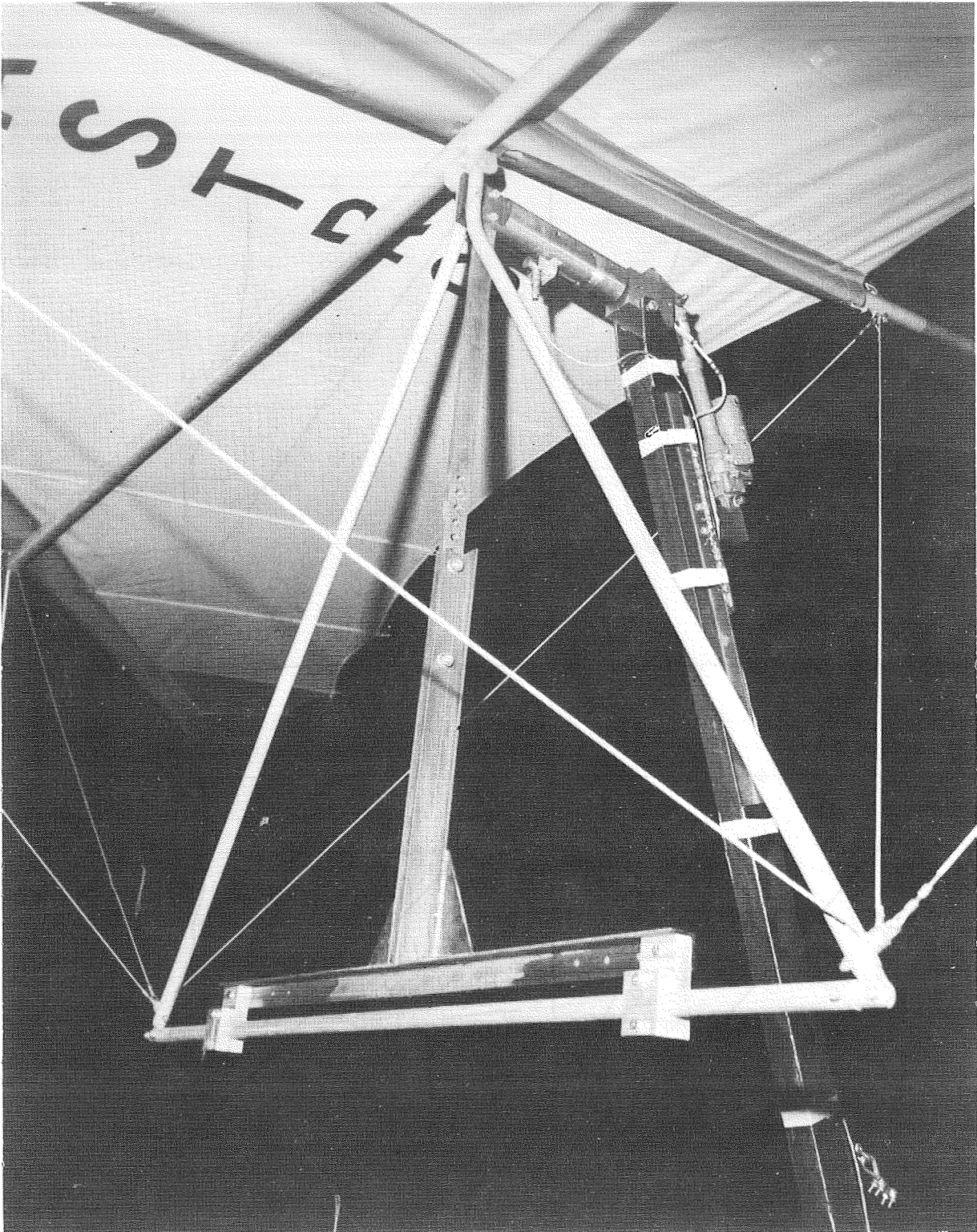


Figure 2 - Details of glider mounting on T-bar adapter frame.

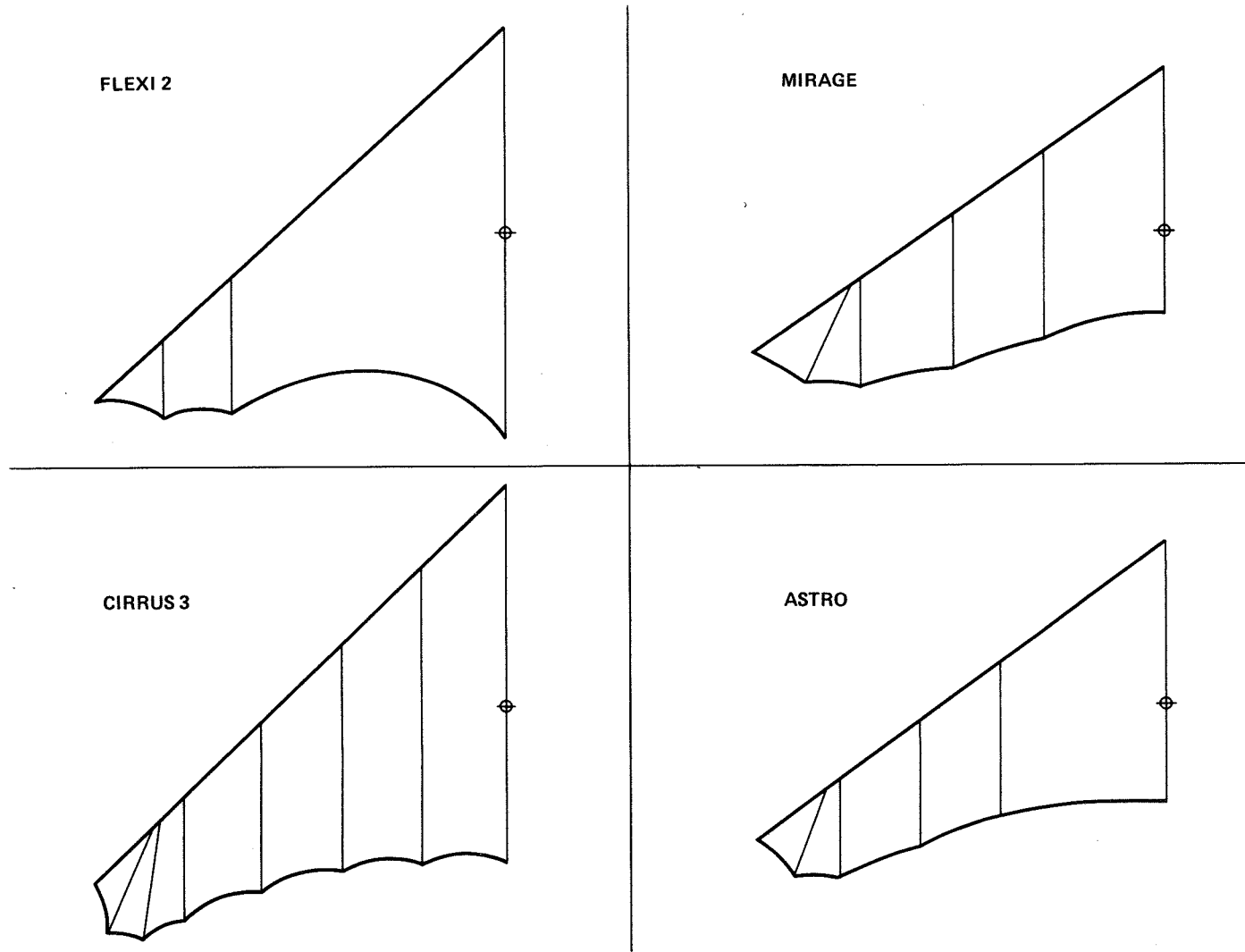


Figure 3 - Glider wing planforms.

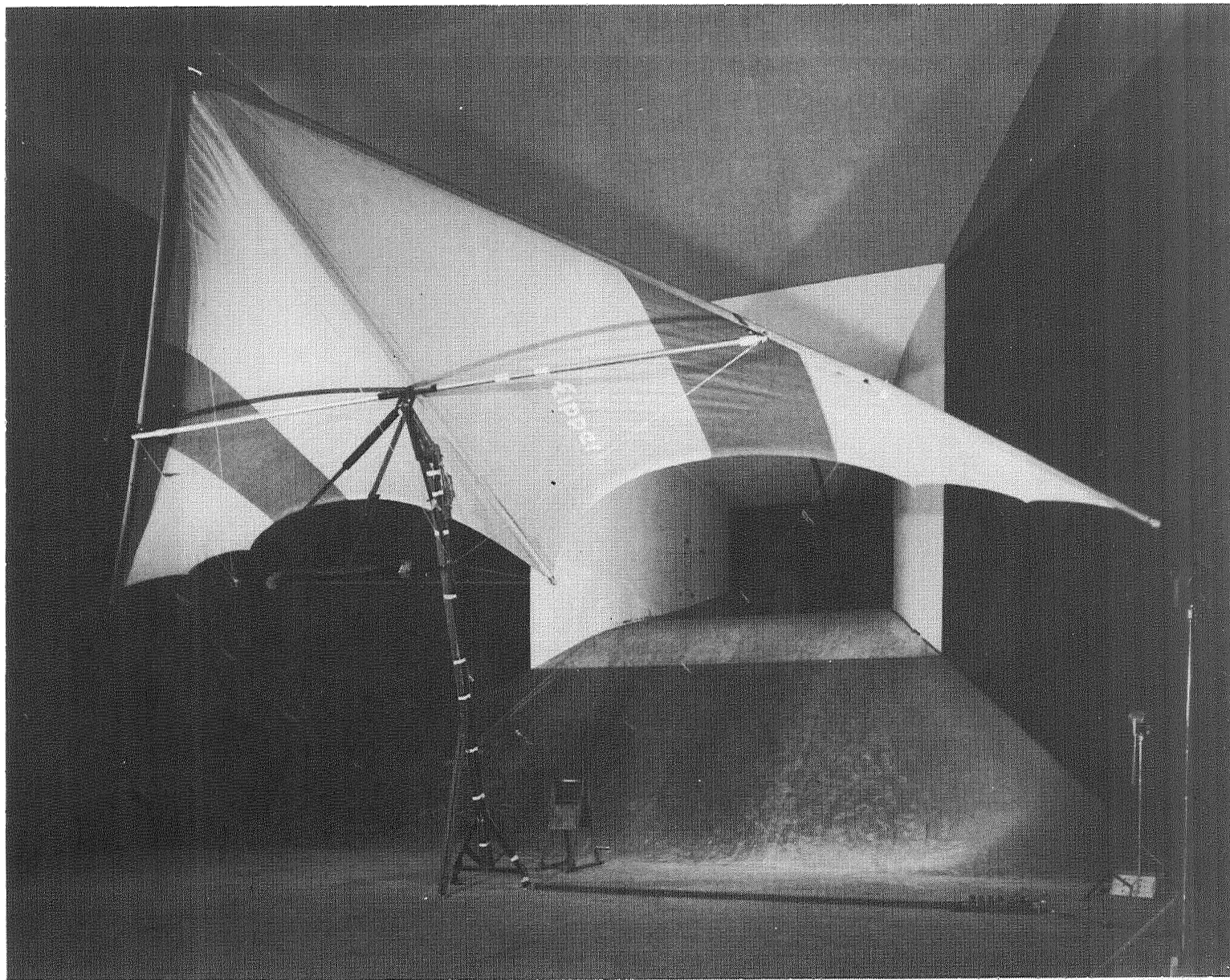


Figure 4a - Flexi 2.

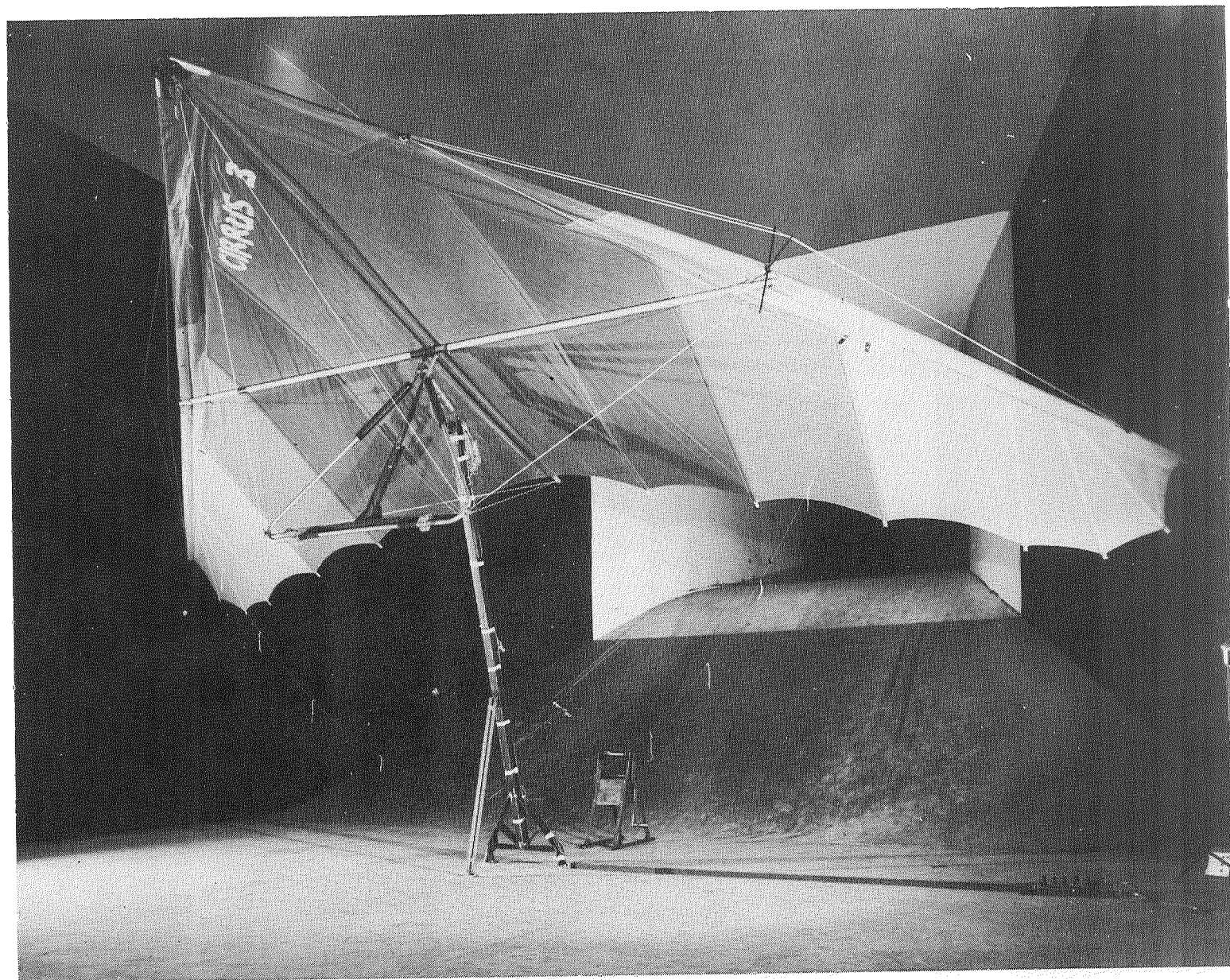


Figure 4b - Cirrus 3.

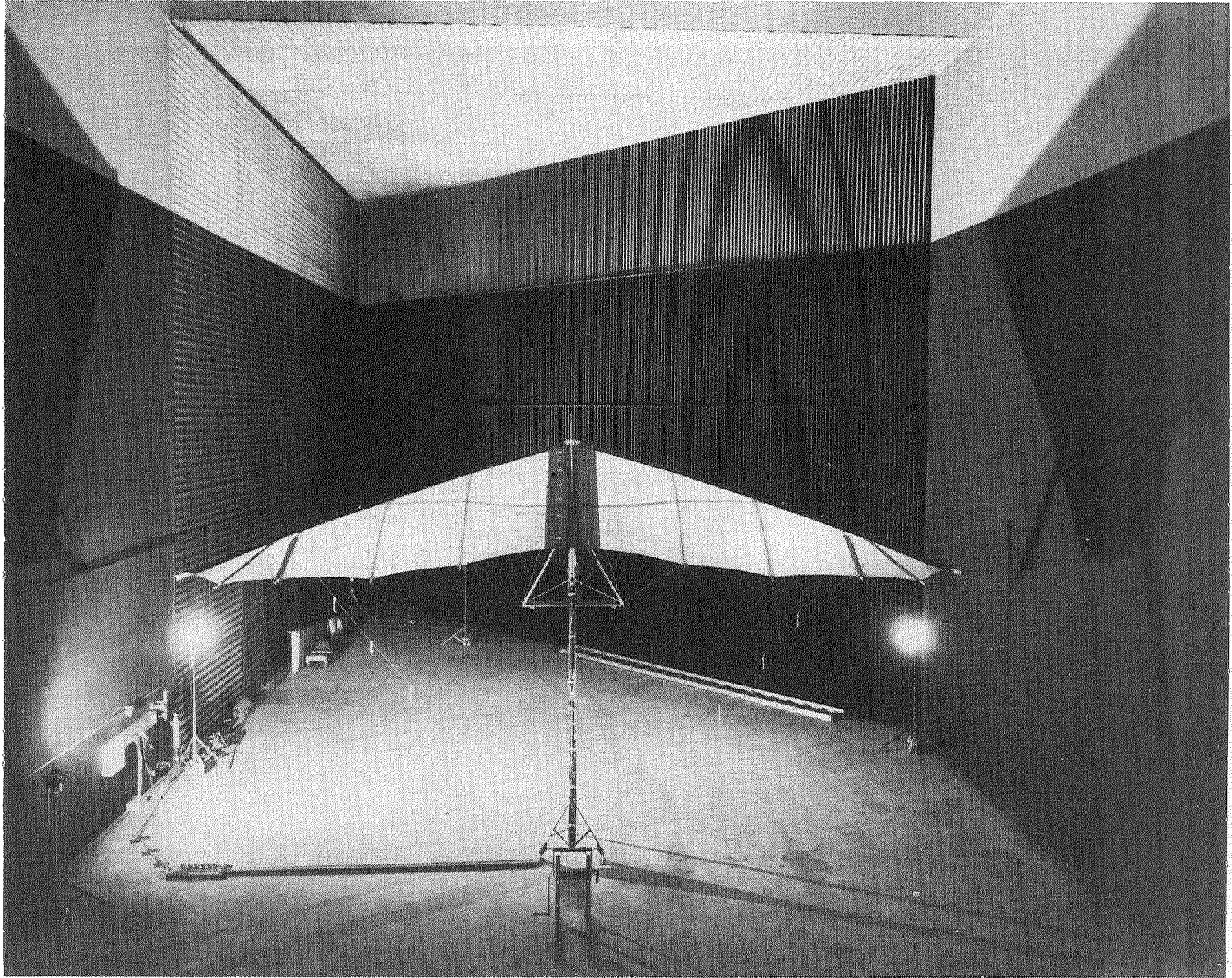


Figure 4c - Mirage.

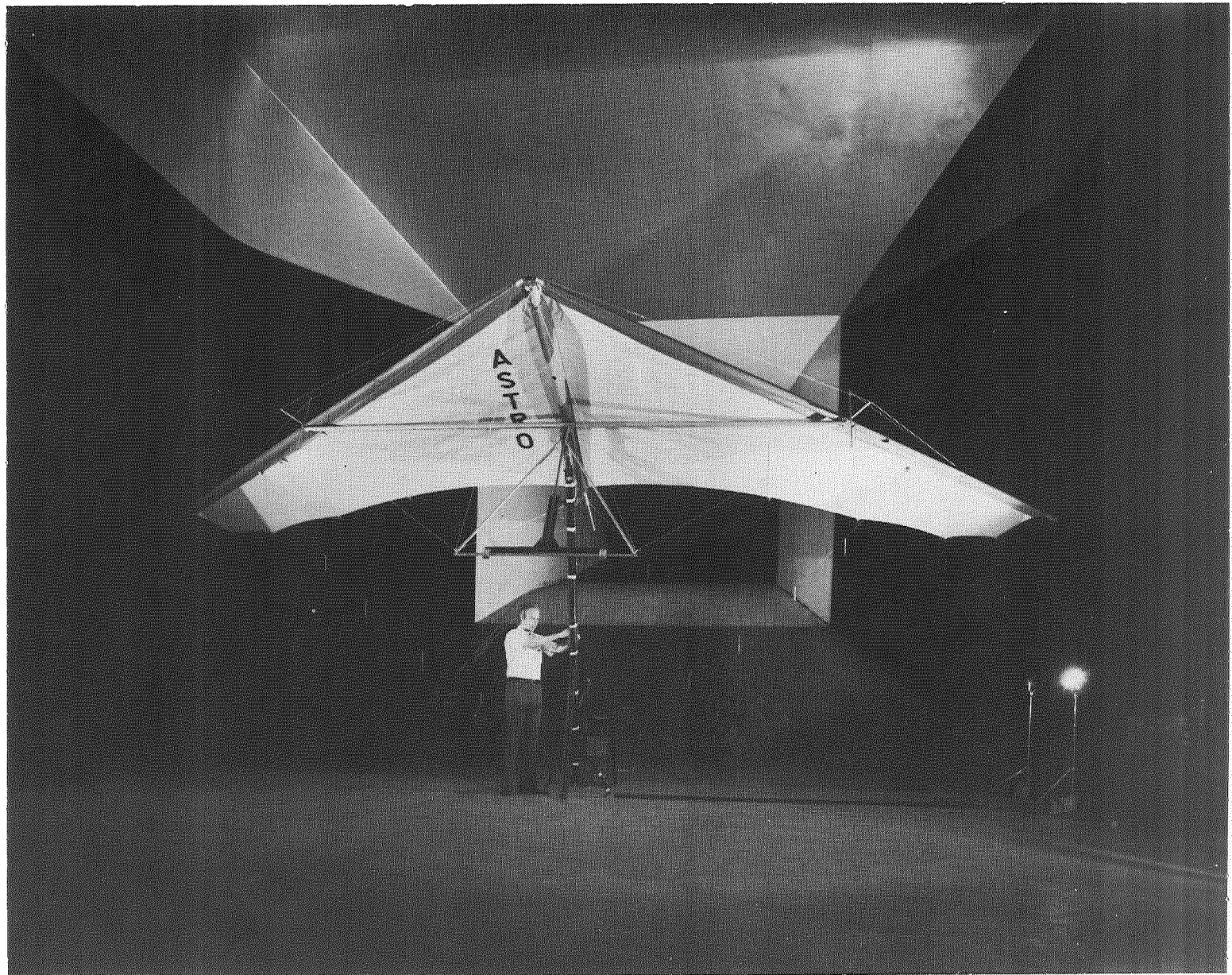


Figure 4d - Astro.

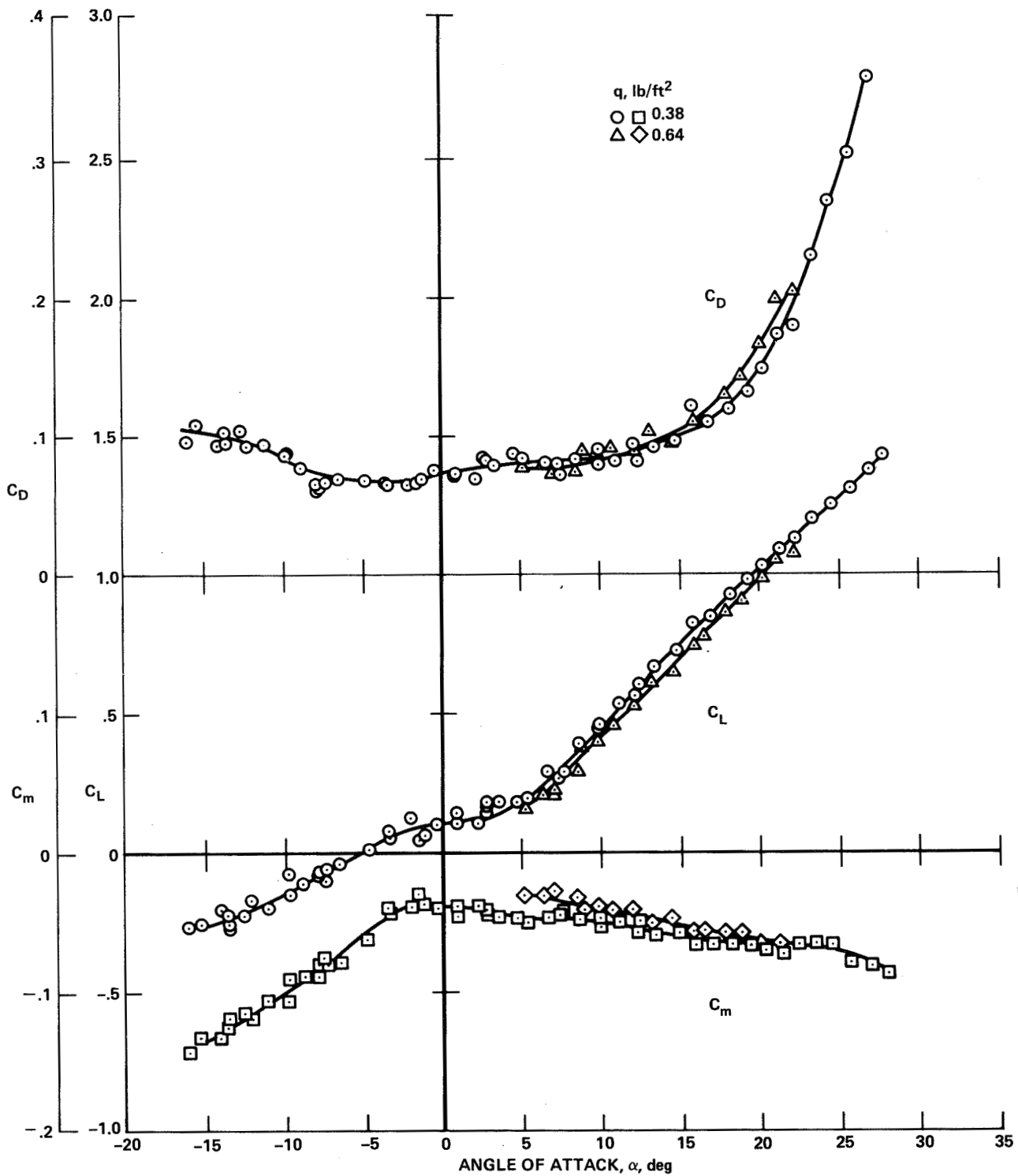


Figure 5 - Flexi 2 lift, drag, and pitch moment coefficient test data.

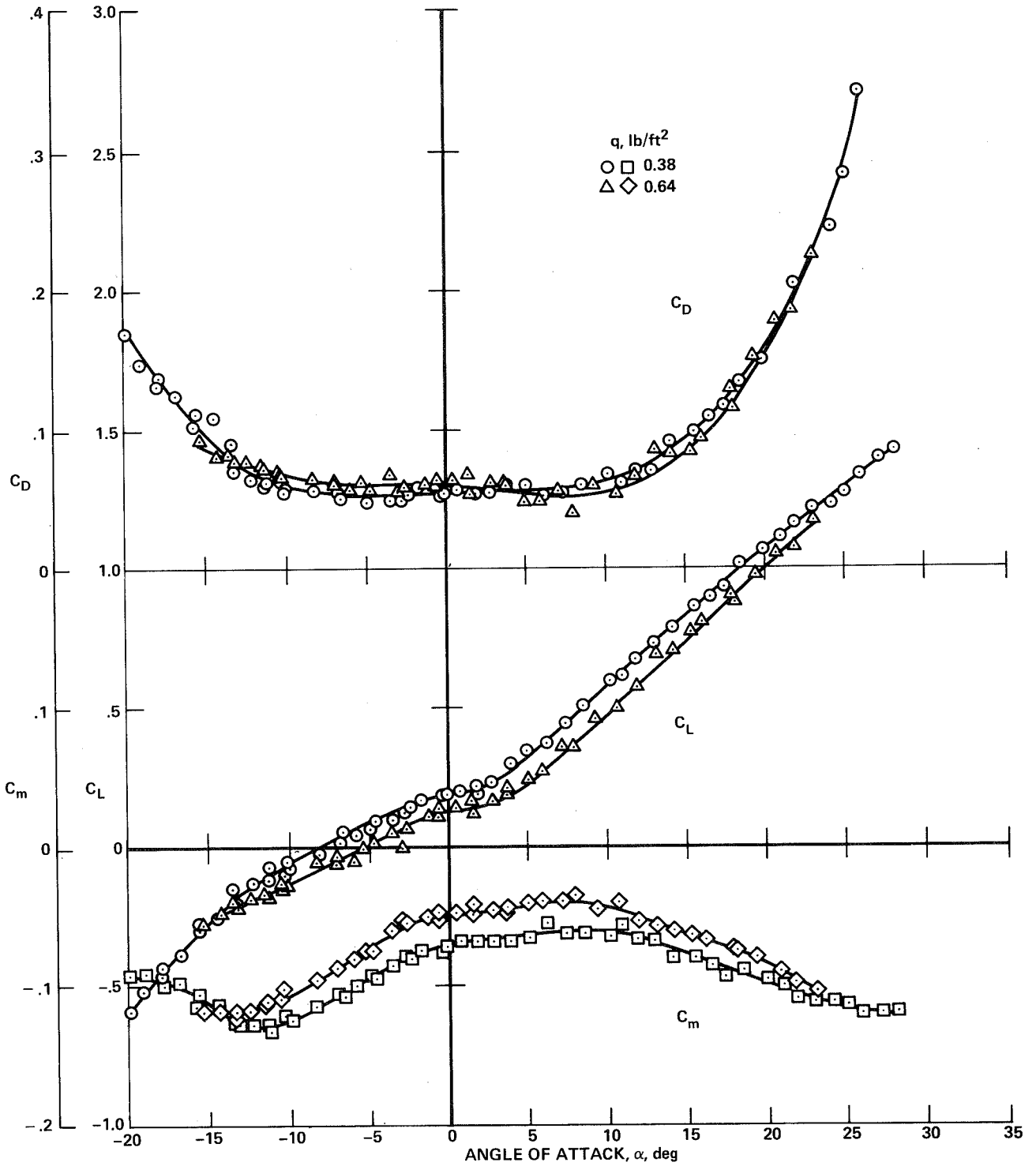


Figure 6 - Cirrus 3 lift, drag, and pitch moment coefficient test data.

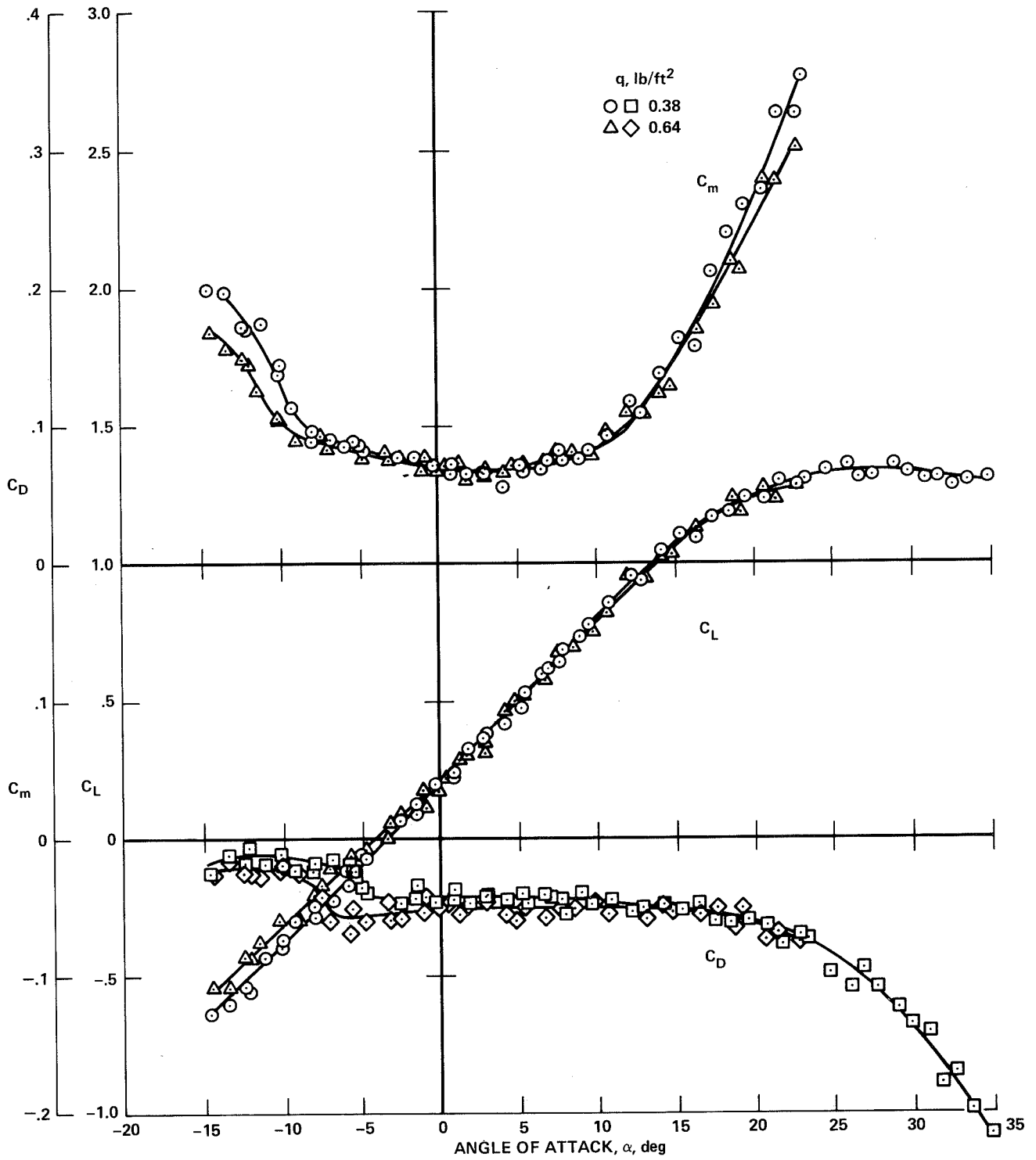


Figure 7 - Mirage lift, drag, and pitch moment coefficient test data.

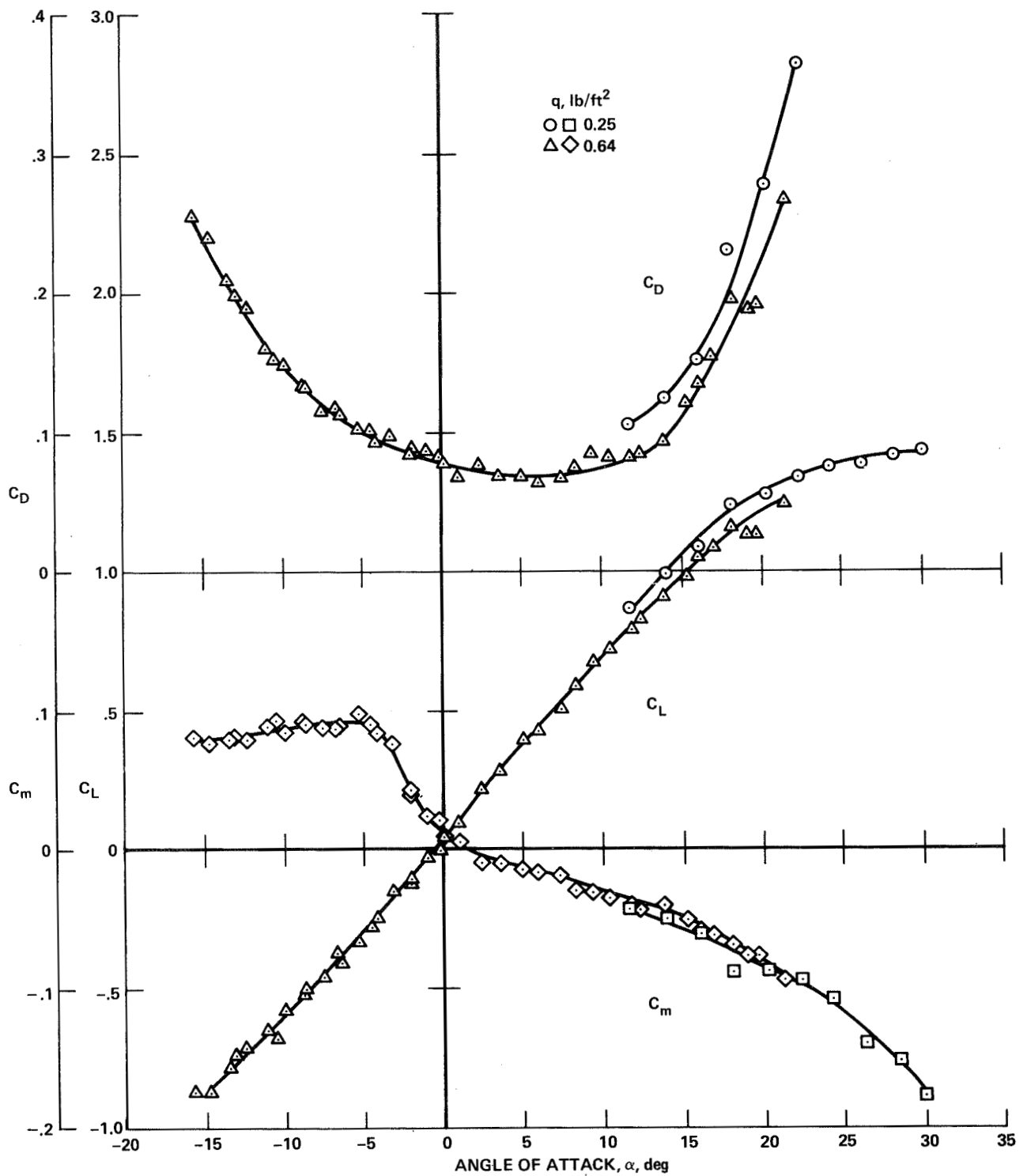


Figure 8 - Astro lift, drag, and pitch moment coefficient test data.

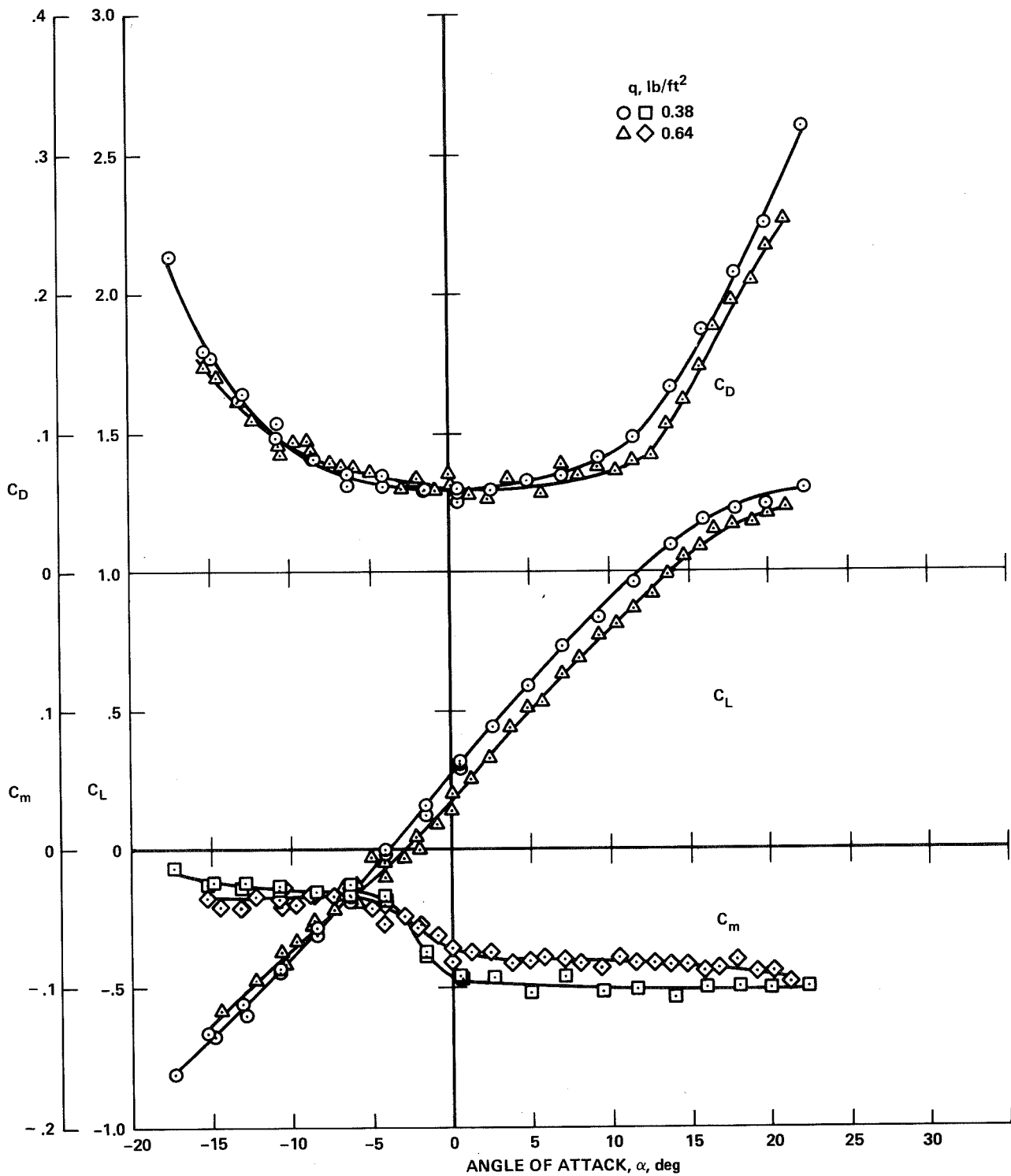


Figure 9 - Modified Astro (floating tip ribs removed) lift, drag, and pitch moment coefficient test data.

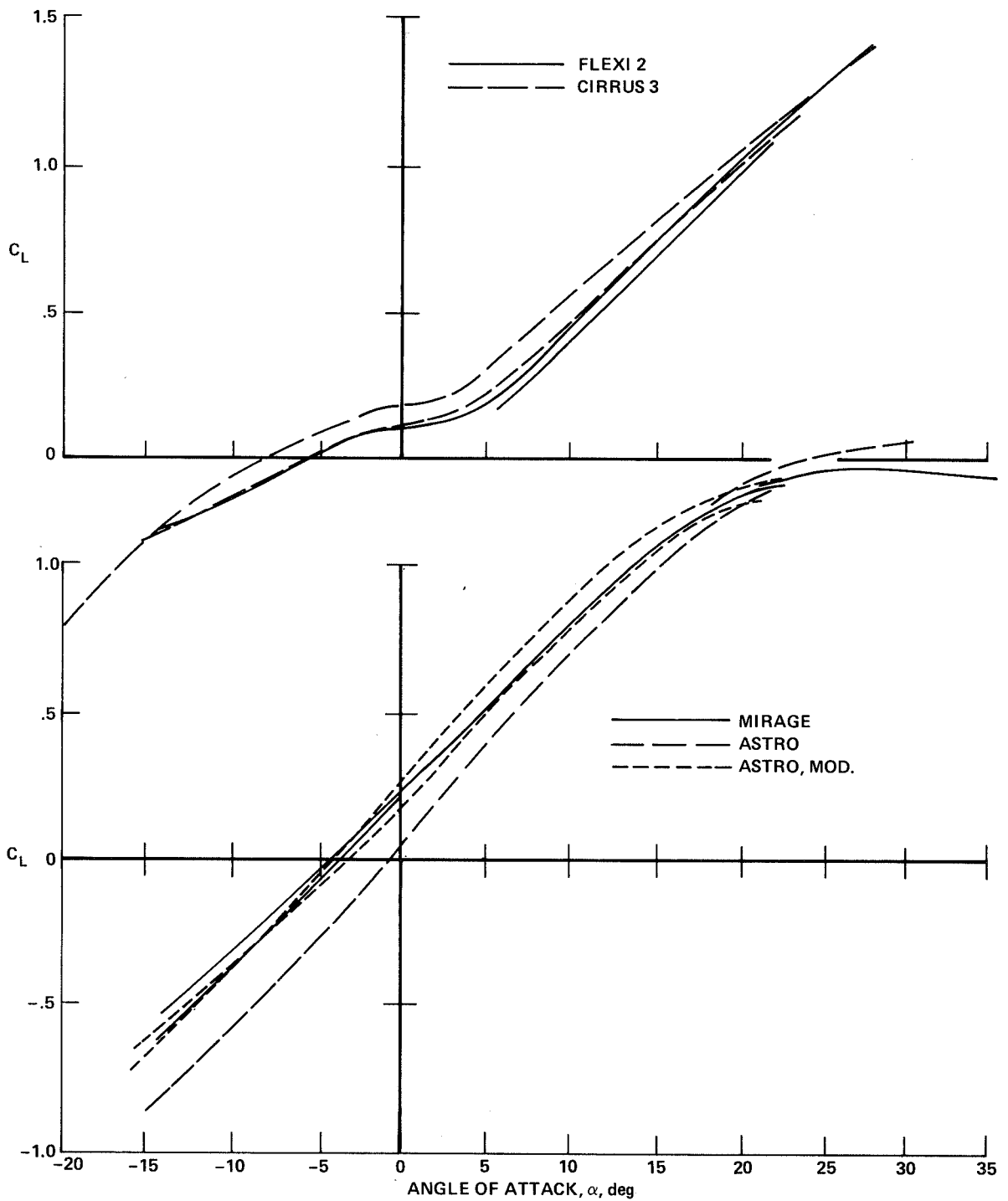


Figure 10 - Comparison of faired lift coefficient curves from Figures 5-9.

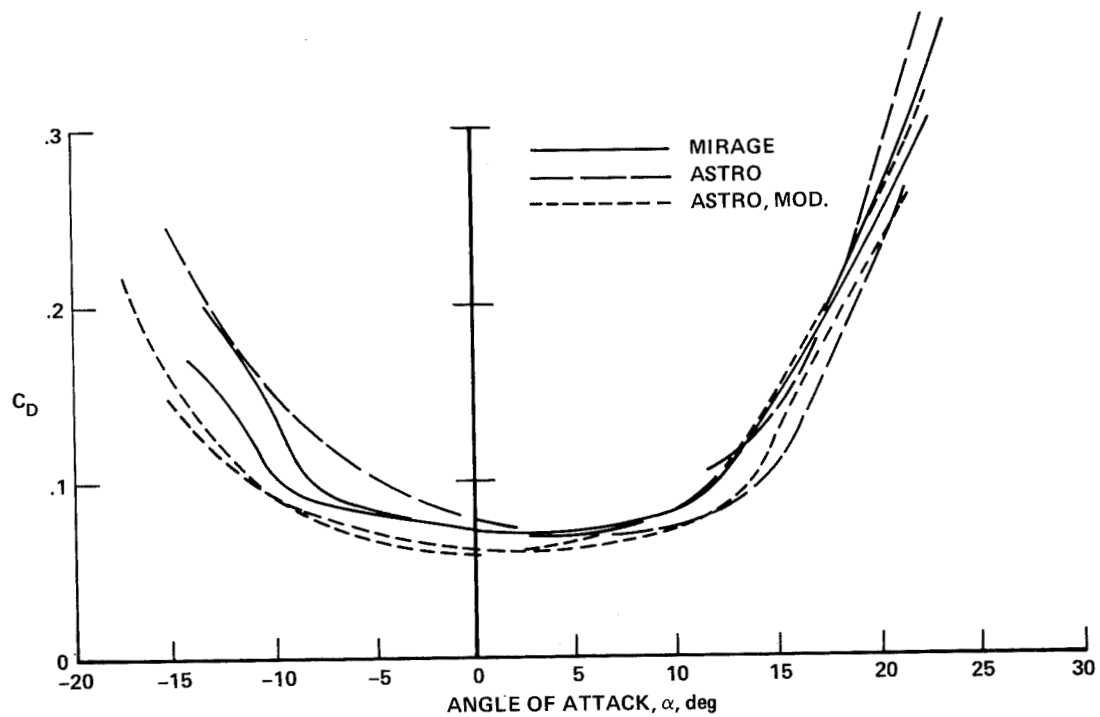
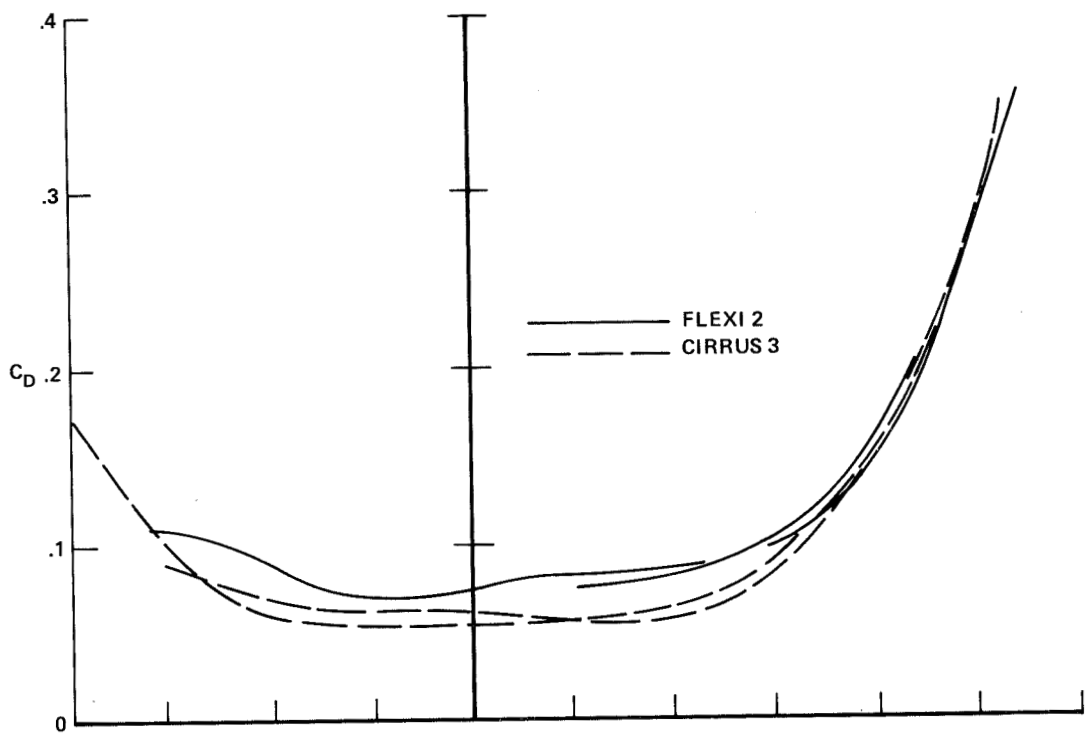


Figure 11 - Comparison of faired drag coefficient curves from Figures 5-9.

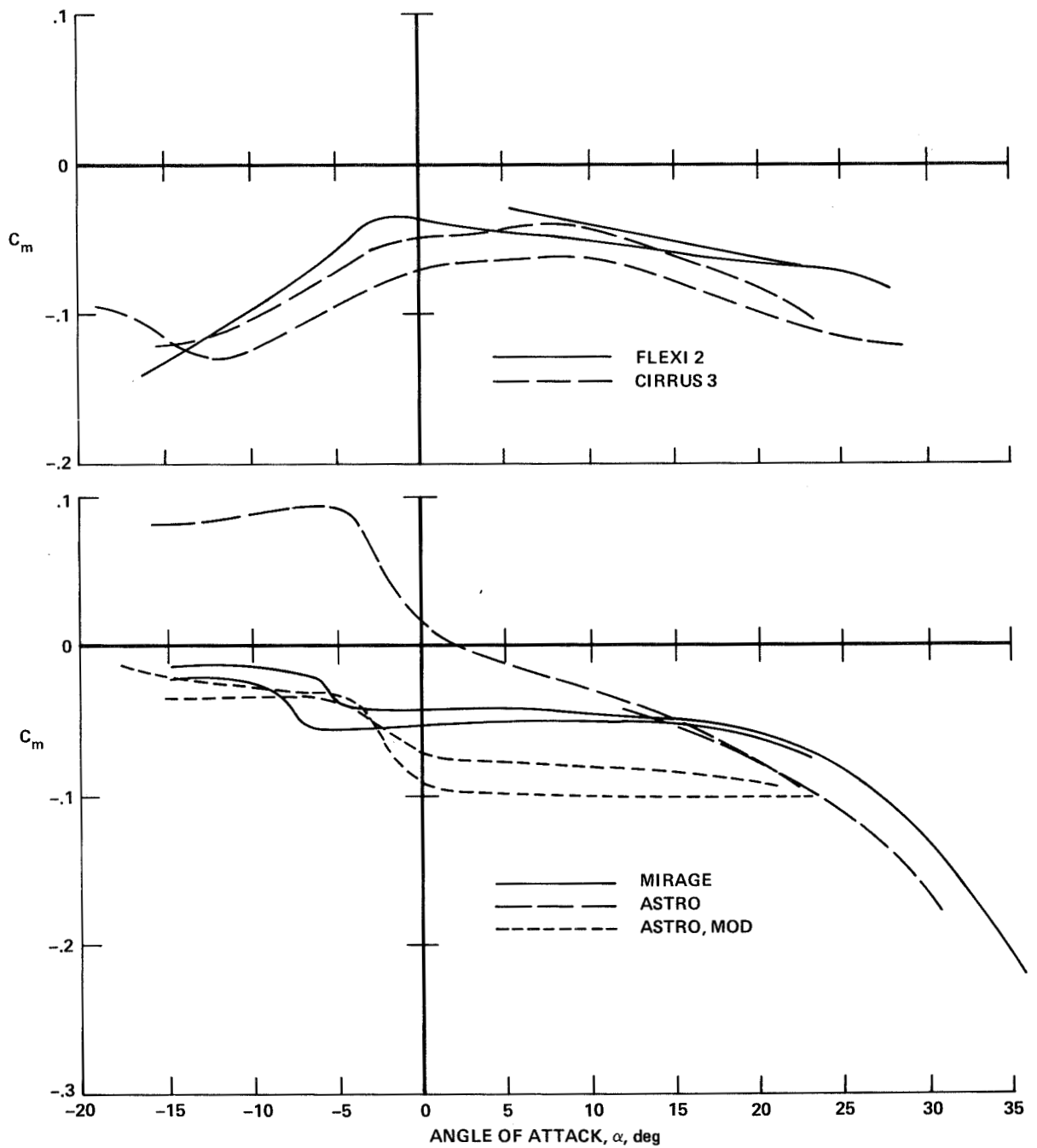


Figure 12 - Comparison of faired pitch moment coefficient curves from Figures 5-9.

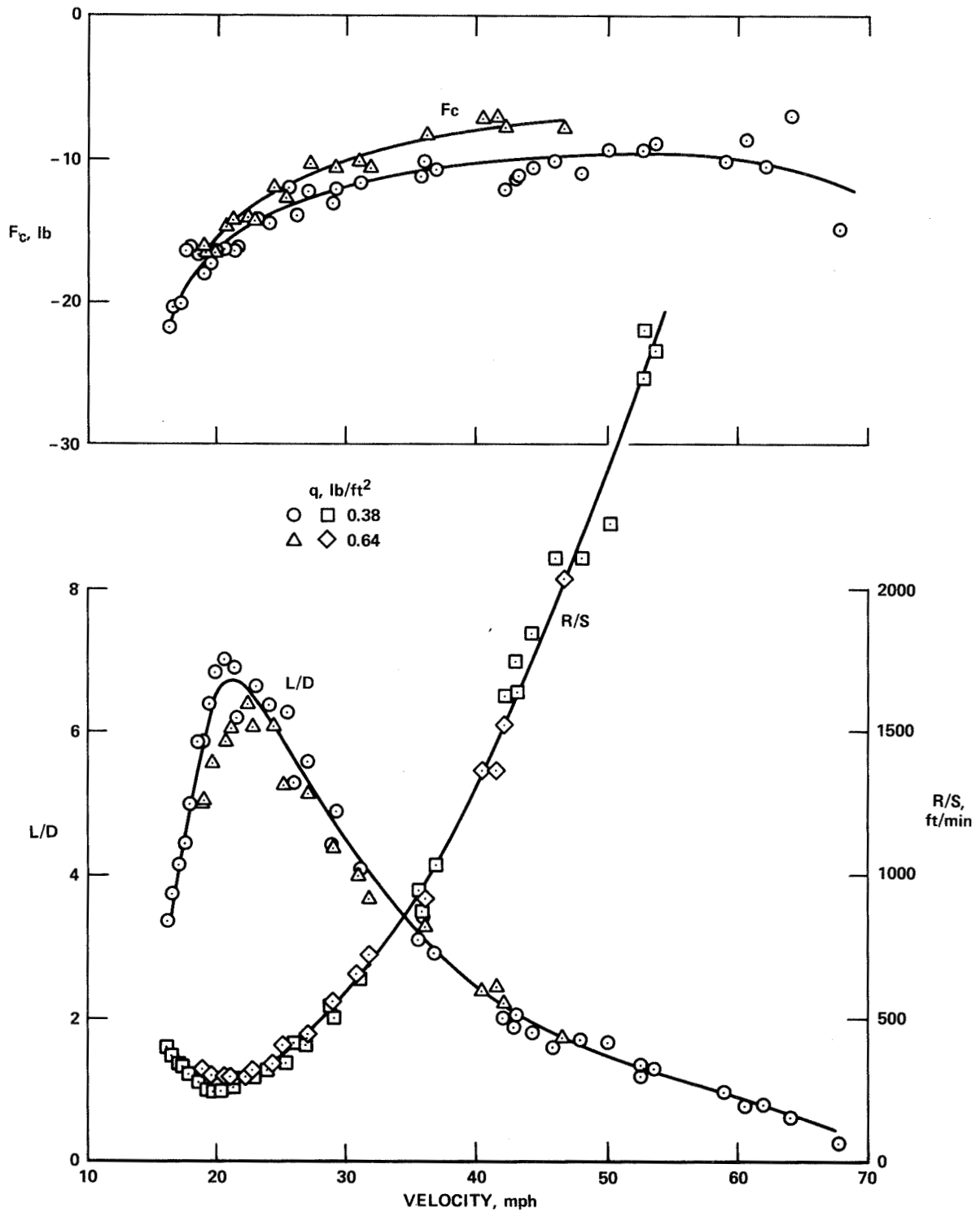


Figure 13 - Flexi 2 control force, L/D, and sink rate versus velocity, pilot drag included.

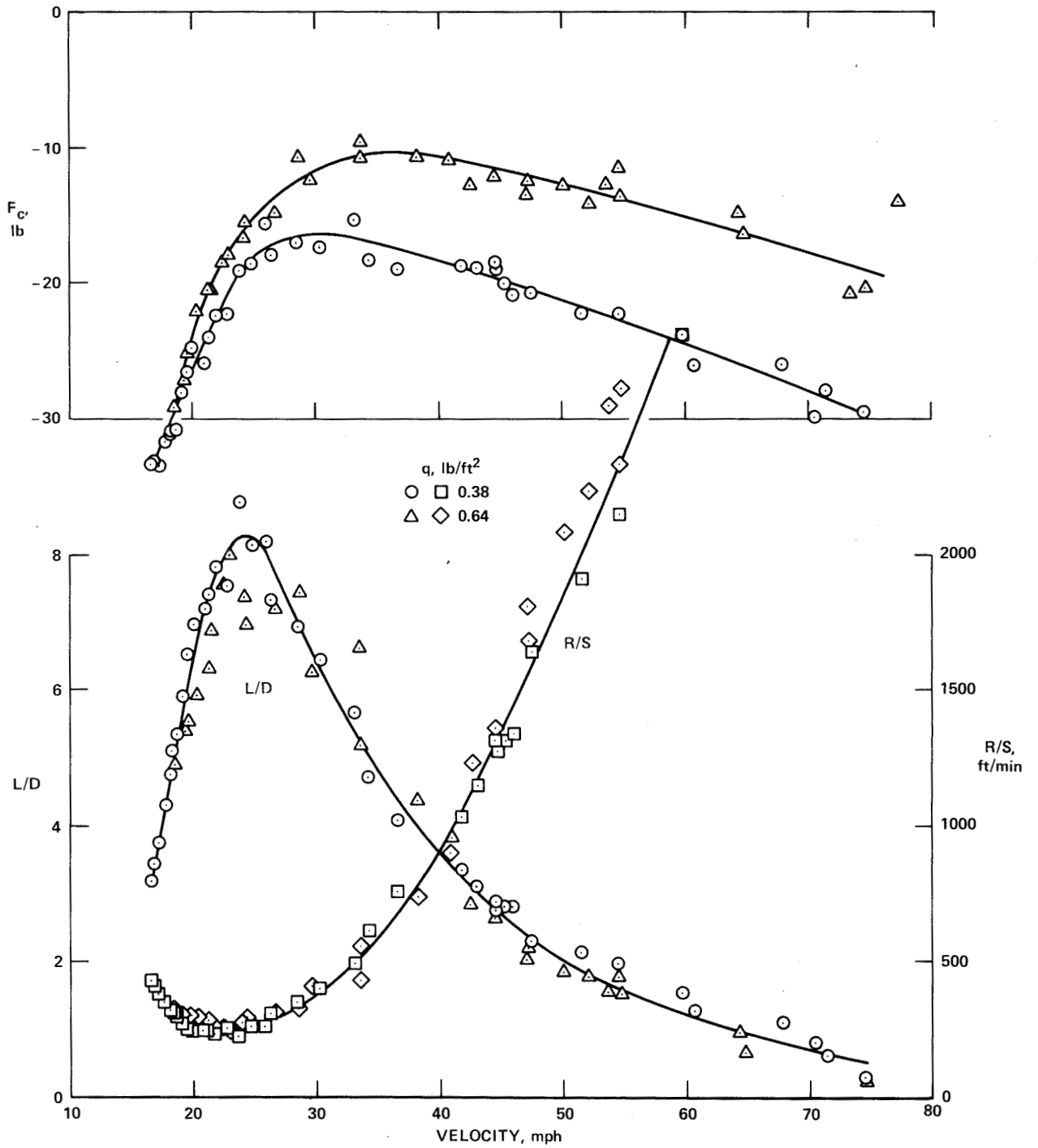


Figure 14 - Cirrus 3 control force, L/D, and sink rate versus velocity, pilot drag included.

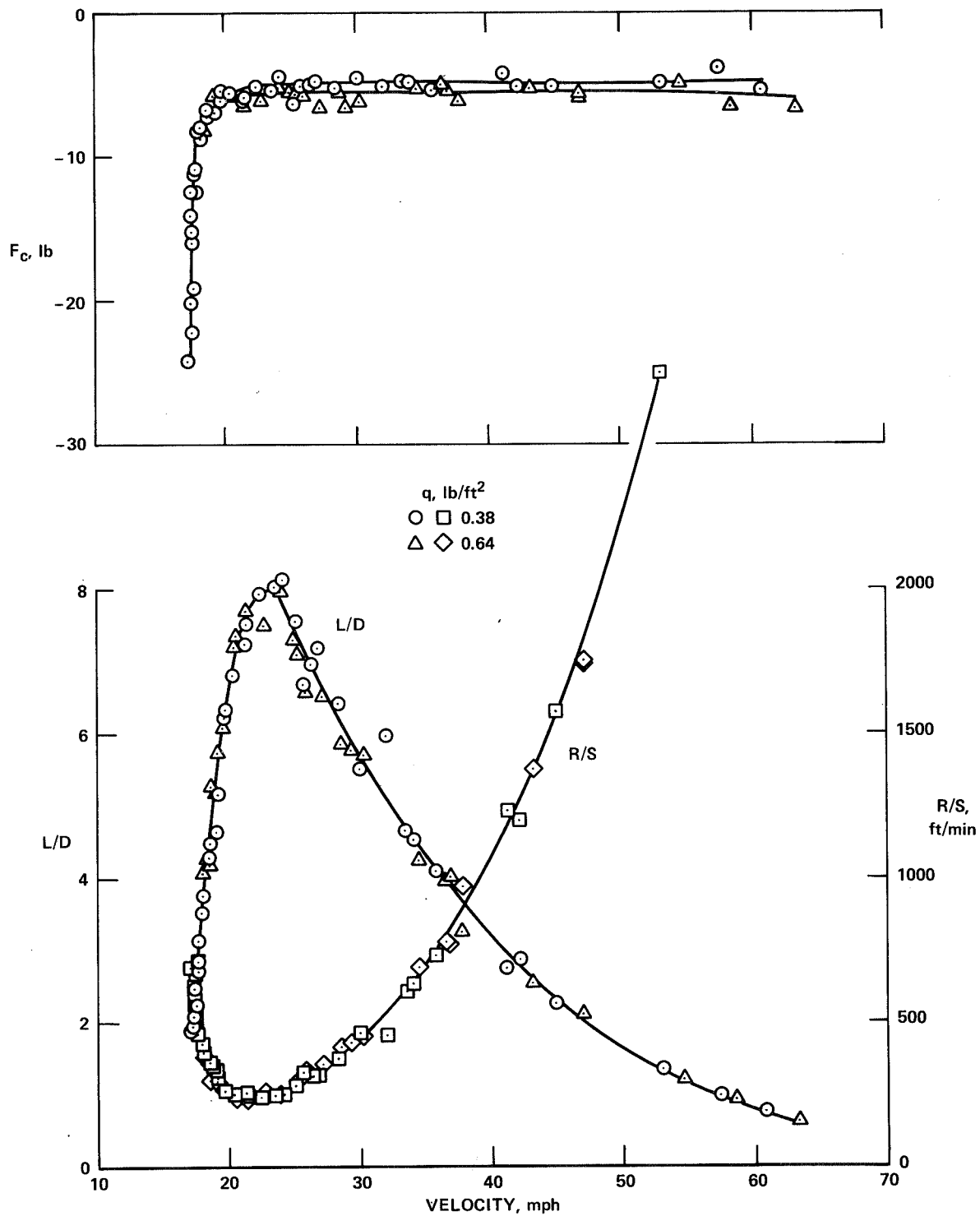


Figure 15 - Mirage control force, L/D, and sink rate versus velocity, pilot drag included.

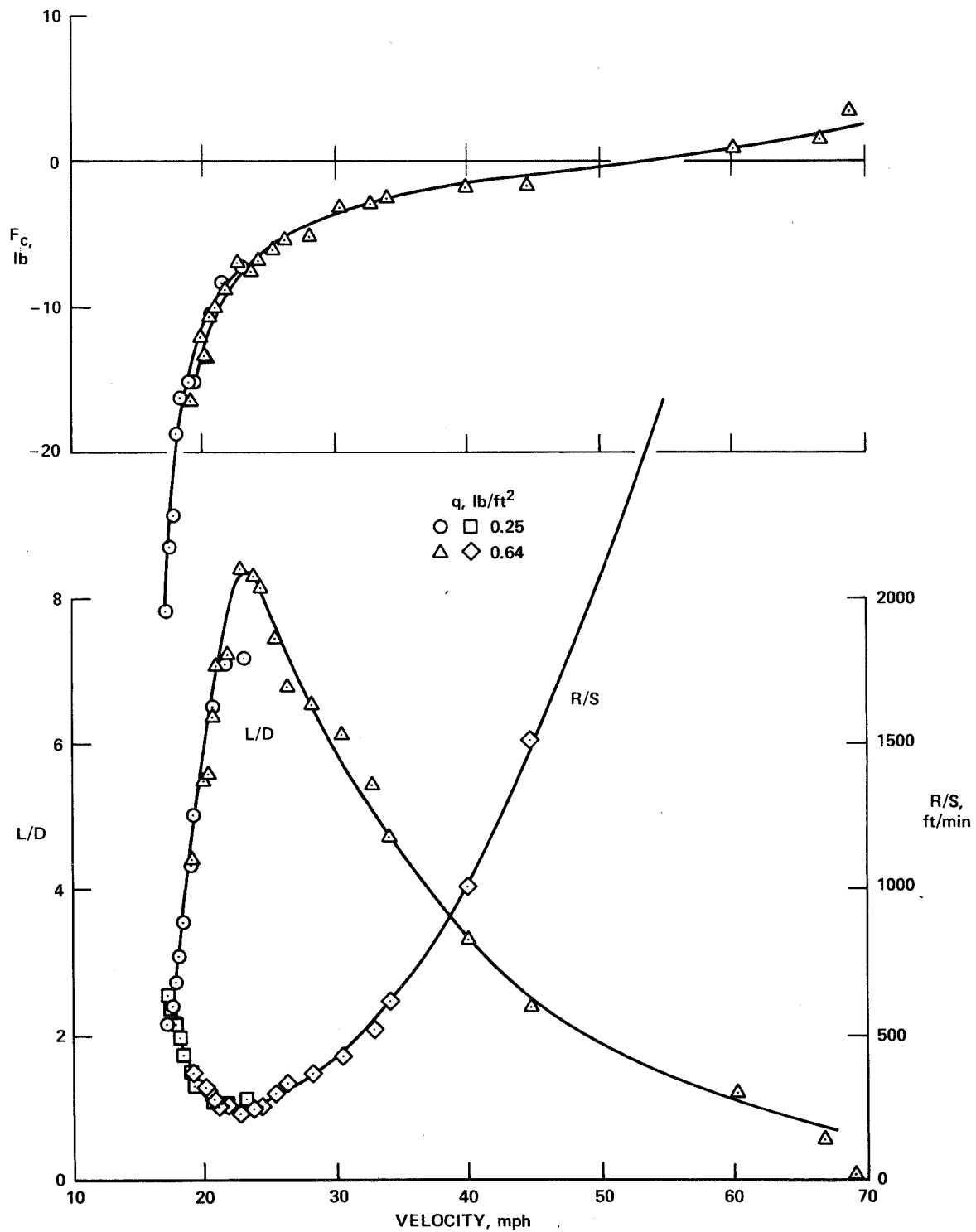


Figure 16 - Astro control force, L/D, and sink rate versus velocity, pilot drag included.

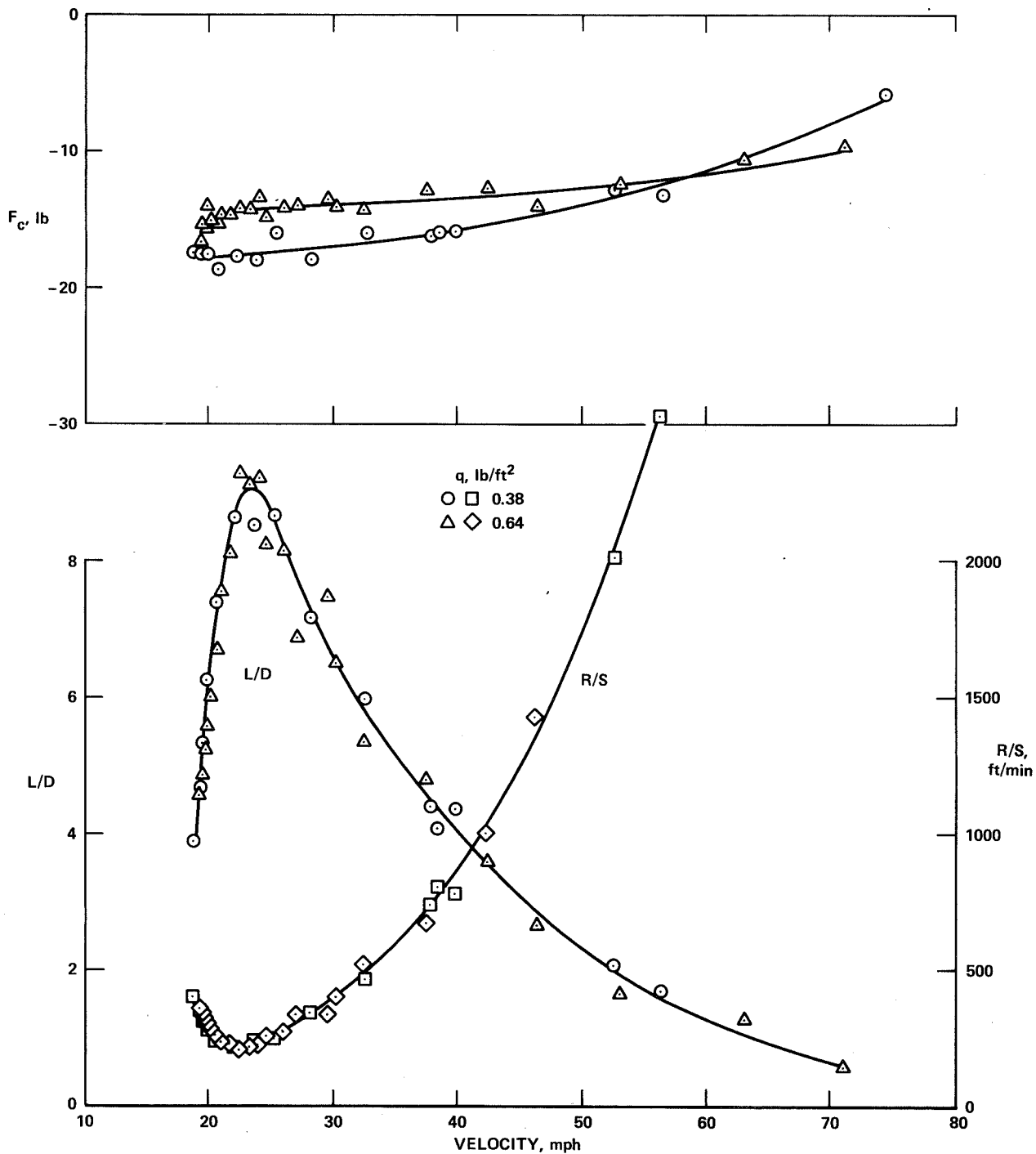


Figure 17 - Modified Astro (floating tip ribs removed) control force, L/D, and sink rate versus velocity, pilot drag included.

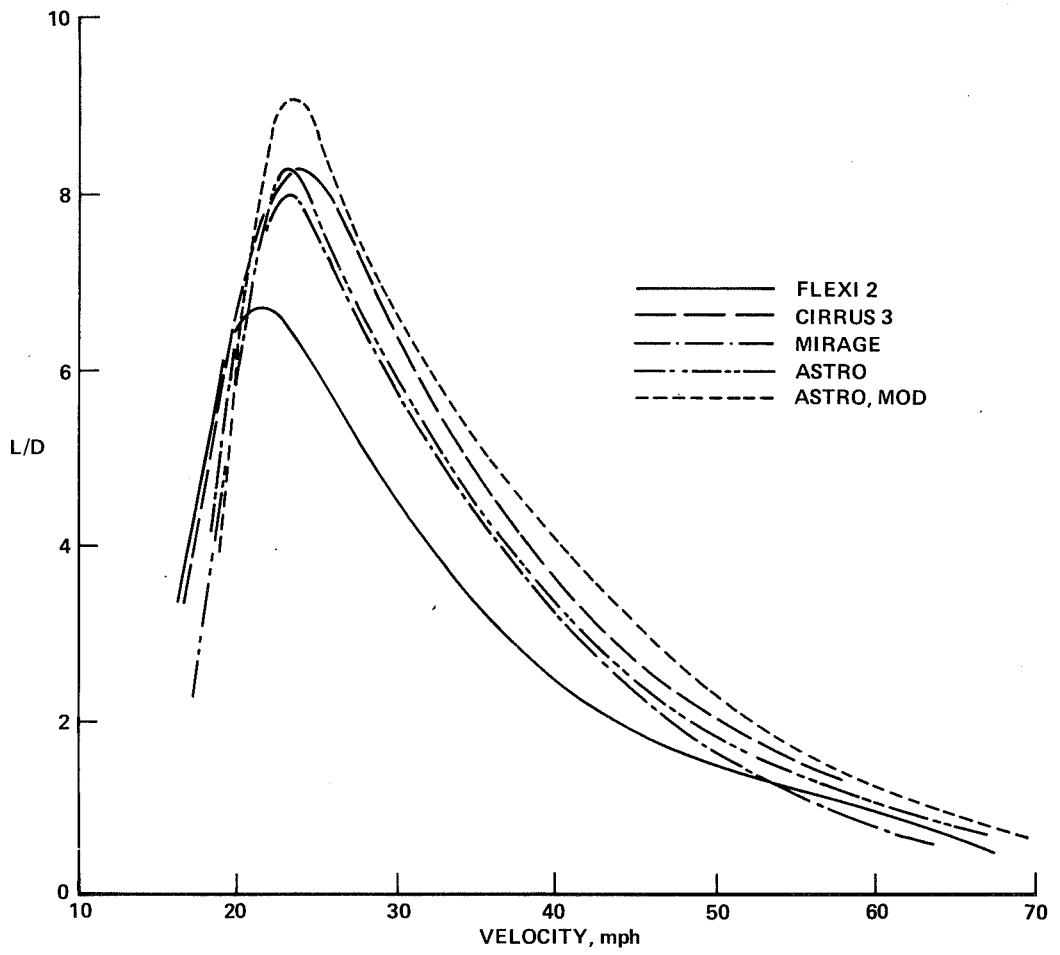


Figure 18 - Comparison of faired L/D versus velocity curves.

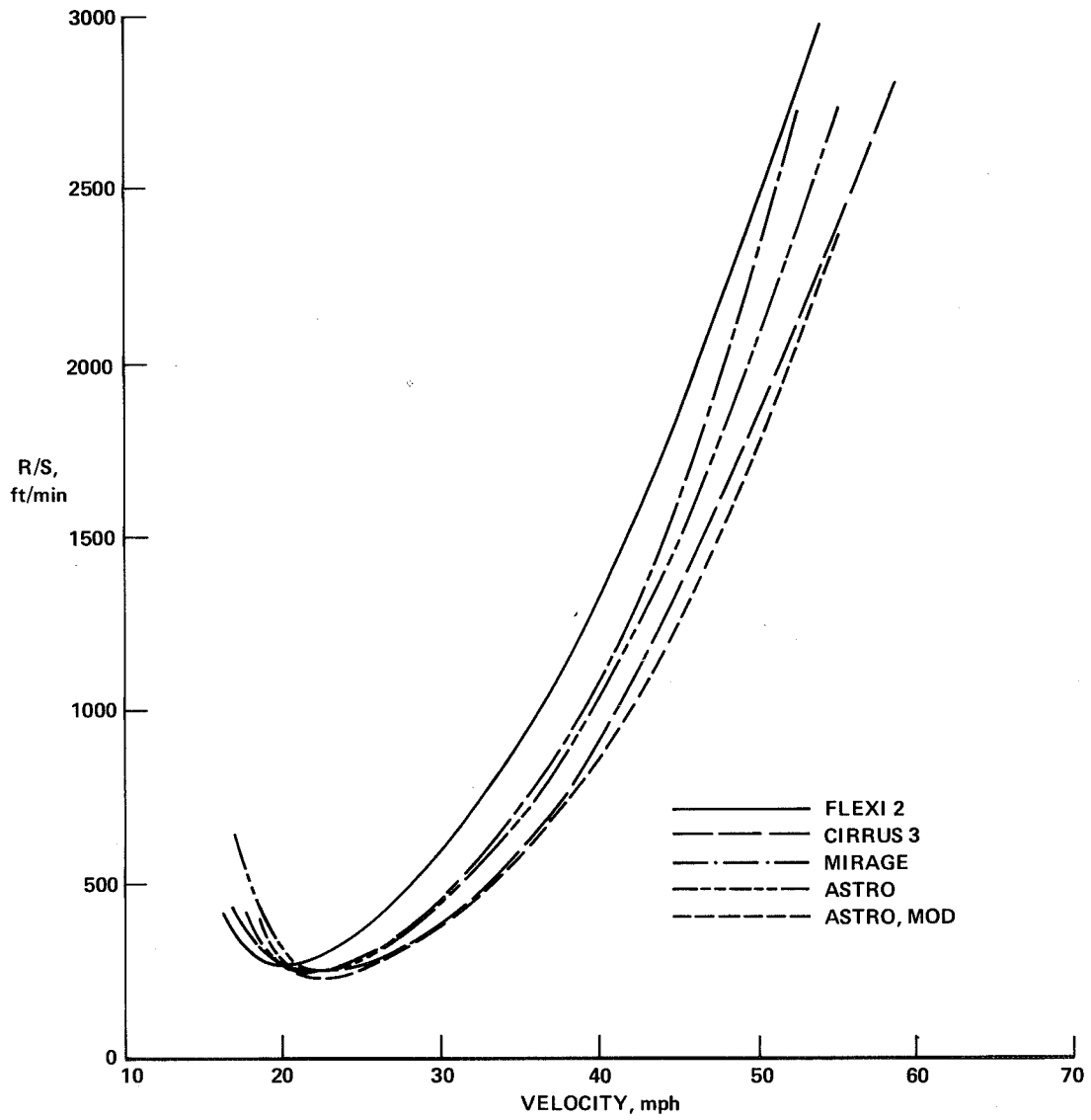


Figure 19 - Comparison of faired sink rate versus airspeed curves.

Page intentionally left blank

CONTEMPORARY SOARING NOMENCLATURE

S. O. Jenko
AMTECH Services*

INTRODUCTION

Considerable technical progress took place during the past two decades in the field of soaring. In contrast, basic terminology in many languages is lagging seriously. English, one of the leading languages, is no exception. Because of this situation, misunderstandings occur which under some circumstances may result in undesirable consequences, hindering further technical developments as well as soaring activities. For years, the author has given considerable thought to this terminology problem. The following definitions were established and compiled by mid-1973, followed by minor additions (1974 and 1977).

PROPOSED DEFINITIONS

GLIDER (with or without auxiliary power): any manned flying device which is not capable of cross-country soaring flight without any power, under "normal" soaring conditions

SAILPLANE (with or without auxiliary power): any manned flying device which is fully capable of cross-country flight without any power, under "normal" soaring conditions

The above differentiation is based on technological progress from the inception of powerless flying. First it was gliding a few feet above the slope of a hill. Then, with substantial design improvements of gliders and discoveries of various atmospheric phenomena, foundations were laid for soaring, that is, flying without any use of power for a substantial length of time, gaining altitude, and flying long distance either in one or separate flights.

The ability to reach these basic objectives of soaring depends on the skill of the pilot and on atmospheric conditions as well as on the performance of the sailplane. Thus the stipulation of "normal" soaring conditions may present a problem. What is a normal soaring day in one area of a country (e.g., Texas) may be a booming day in most other areas. While one could specify a certain range for the upward air velocity component (slope wind, up-drafts due to various other sources), no such attempt is made here. An upward air velocity component of 1 m/sec (approximately 200 fpm) might be considered a lower limit of a "normal" soaring condition.

*Aeromechanical Technology Services.

A much easier approach to establish the imaginary dividing line between a glider and a sailplane would be based on historical developments: for a glider $L/D < 17$; for a sailplane $L/D \geq 17$.

Both criteria (normal soaring condition and L/D specification) appear to be reasonably equivalent.

ULTRALIGHT GLIDER(ULG) (includes hang glider) or SAILPLANE(ULS): a manned flying device as described previously having a wing loading $w \leq 10 \text{ kg/m}^2$ (approximately 2 lb/ft^2)

LIGHT GLIDER(LG) or SAILPLANE(LS): a manned flying device as described previously having a wing loading $w = 10$ to 25 kg/m^2 (approximately 2 to 5.1 lb/ft^2)

GLIDER or SAILPLANE: a manned flying device as described previously having a wing loading $w = 25$ to 40 kg/m^2 (approximately 5.1 to 8 lb/ft^2)

During the development of gliders and sailplanes over several decades the wing loading increased noticeably. What appeared to be a "normal" wing loading some 35 years ago is considered "light" today. In view of the increased interest in hang gliders, human-powered aircraft, and other similar, vastly improved sailplanes under development which due to the energy shortage, may well be the only means of soaring in the future, an attempt is made to define these aircraft. Since the wing loading is one of the factors governing the plane's performance, the above specified ranges are in order.

AUXILIARY POWERED GLIDER(APG) or SAILPLANE(APS); LIGHT AUXILIARY POWERED GLIDER(LAPG) or SAILPLANE(LAPS); ULTRALIGHT AUXILIARY POWERED GLIDER (ULAPG) or SAILPLANE(ULAPS): a manned flying device as described previously having an auxiliary engine to take off and to overfly with power any severe downdraft areas which would otherwise result in a landing; power loading $p \geq 9 \text{ kg/HP}$ (approximately 20 lb/HP)

Since the beginning of soaring, attempts have been made to overcome the two inherent disadvantages of a sailplane: inability to take off with initial climb and to overfly large areas of sink without landing. Various kinds of propulsion were and are being installed as an auxiliary source of power which preferably would not decrease the sailplane's performance during the soaring phase of flight.

The above definition should cover any auxiliary power installation regardless of whether the available power is sufficient for takeoff and initial climb or sustention of level flight only.

The expression "self-launching sailplane" (SLS) for an auxiliary powered sailplane (APS) should not be used because it suggests an ultralight (hang) glider or sailplane which can be launched by the pilot's feet (i.e., without any mechanical power); it is also not consistent with the decades old concept of an APS, described above.

Another expression, "motorglider", denoting an auxiliary powered sailplane (APS) appears to be inappropriate for several reasons. Most likely it is an old translation of the German word "motorgleiter" by people whose technical and linguistic knowledge was rather poor. It is an accepted view here (USA) that there is a difference between the two words "motor" (electric) and "engine" (combustion). The bridge between the two kinds of energy conversion devices is rocket propulsion: it can be called either a rocket motor or a rocket engine.

Furthermore, it should be noted that even Germans apparently have preferred for some time the term "MOTORSEGLER". Unfortunately there is no comparable, elegant translation available in English.

POWERED GLIDER(PG) or SAILPLANE(PS): a glider or a sailplane converted into a powered aircraft; the engine is essential for flying operation

On occasion a glider or a sailplane is converted into a powered aircraft by installing an engine which produces a substantially higher power than required for flying an auxiliary powered glider or sailplane. Thus soaring flight becomes an exception in the usual flight operation of a powered glider or sailplane.

One, but not the only such example, is the Schweizer SGS 2-32 sailplane which has been used in various development, research, and promotional projects. In some extreme cases the power installation and other modifications made were of such extent that the identity of the original sailplane almost vanished.

HUMAN POWERED AIRCRAFT(HPA): a manned flying device powered only by human efforts

This definition covers any heavier than air, manned flying device, which by its nature is an ultralight sailplane of high performance.

CONCLUDING REMARKS

One would expect that in view of substantial technological developments resulting in outstanding performance of today's sailplanes appropriate terminology would be widely in use. Apparently this is not the case.

This paper presents proposed nomenclature as a beginning effort to improve the present unsatisfactory condition. It should also serve as a guide for comparable improvements in other languages.

Page intentionally left blank

ATTENDEES

BILL ABEYOUNIS
NASA Langley Research Center
Hampton, Va., USA

EDUARD AGUSTO
Associação Brasileira de Vôo a Vela,
S. Paulo, Brazil

STEPHEN L. AICHOLZ
Media, Pa., USA

HOLT ASHLEY
Stanford University
Stanford, Calif., USA

DONALD D. BAALS
The George Washington University
Joint Institute for Advancement
of Flight Sciences,
Hampton, Va., USA

BEN BADENOCH
Danville, Calif., USA

PAUL BAKER
Williamsburg, Va., USA

RICHARD W. BARNWELL
NASA Langley Research Center
Hampton, Va. USA

PATRICK J. BEATTY
Bedfordview, S. Africa

GERD W. BERCHTOLD
Technical University of Munich
Munich, W. Germany

WILLIAM D. BERTELSEN
Bertelsen, Inc.,
Neponset, Ill., USA

WILLIAM R. BERTELSEN
Bertelsen, Inc.,
Neponset, Ill., USA

KEVIN BLACK
Durham College
Ontario, Canada

W. S. BLANCHARD, JR.
NASA Langley Research Center (Ret.)
Hampton, Va., USA

FORREST BLOSSOM
Soaring Society of America, USA

KENN ALLEN BLUMENSTOCK
Columbia Plastics., Inc.,
Columbus, Md., USA

RAY BORST
N. Huntingdon, Pa., USA

CHARLES LINN BOTZKO
Elmore, Ohio, USA

STEVE BOWEN
Bethlehem Steel Corp.
Nashville, Tenn., USA

ELMAR BREITBACH
DFVLR, Gottingen, W. Germany

BRUCE BROSI
Boston, Mass., USA

JOE ALLEN BROWNLEE
Mississippi State University
Mississippi State, Miss., USA

GIFFORD BULL
Mississippi State University
Mississippi State, Miss., USA

JAMES BURLEY
NASA Langley Research Center
Hampton, Va., USA

ROBERT CALLAGHAN
Atherton, Calif., USA

JOHN CAMPBELL
The George Washington University
Joint Institute for Advancement of
Flight Sciences
Hampton, Va., USA

WALTER H. CARNAHAN
Rochester, N.Y., USA

ROBERT A. CHAMPINE
NASA Langley Research Center (Ret.)
Hampton, Va., USA

ROBERT EDWIN CHENEY
Cheney Models
Jackson, N.H., USA

ALEJANDRO CHITTY
North Carolina State University
Raleigh, N.C., USA

DONALD L. CIFFONE,
NASA Ames Research Center
Moffett Field, Calif., USA

LES CLANTON
Santa Monica, Calif., USA

DAVID W. CODER
David W. Taylor Naval Ship Research
and Development Center
Bethesda, Md., USA

KENNETH N. COLE
NASA Langley Research Center
Hampton, Va., USA

WILLIAM B. COMPTON, III
NASA Langley Research Center
Hampton, Va., USA

WILLIAM CONARD
Tidewater Soaring Society, USA

JAMES DAVID CONNERTON
Columbia Plastics, Inc.
Columbia, Md., USA

E. J. CROSS
Mississippi State University
Mississippi State, Miss., USA

K. MICHAEL DAY
American Standard Co.
Dearborn, Mich., USA

DANIEL J. De VRIES
Kentwood, Mich., USA

JOHN DeYOUNG
Kentron International, Inc.
Hampton, Va., USA

MICHEL J. DOUTRELOUX
Planten en Moretus
Antwerp, Belgium

ED DULLAGHAN
Naval Education and Training Center
Norfolk, Va., USA

JOHN V. DUNCAN
Spartansburg, S.C., USA

JEROME DUPREY
Durham College
Ontario, Canada

LEON EDLING
Kent, Conn., USA

KLAUS EIKEMEIER
DFVLR, Braunschweig, W. Germany

FRAUKE ELBER
Tidewater Soaring Society, USA

WOLF ELBER
NASA Langley Research Center
Hampton, Va., USA

DONALD ELLIOTT
Columbus, Ohio, USA

E. ENEVOLDSON
NASA Hugh L. Dryden Flight
Research Center
Edwards, Calif., USA

RICHARD EPPLER
University of Stuttgart
Stuttgart, W. Germany

WILLIAM V. FELLER
NASA Langley Research Center (Ret.)
Hampton, Va., USA

JAMES C. FERRIS
NASA Langley Research Center
Hampton, Va., USA

GEORGE W. FISHER
Charlotte, N.C., USA

HENRY LEE FISHER
Morrisville, N.C., USA

DEBORAH M. FLAD
Toughkenamon, Pa., USA

MARINA FORD
Lookout Mountain, Tenn., USA

ROBERT E. FORD
Birmingham, Ala., USA

WILLIAM F. FOSHAG
Aerophysics Co.
Washington, D.C., USA

JEAN M. FOSTER
NASA Langley Research Center
Hampton, Va., USA

SAMUEL A. FRANCIS
Marion, Mass., USA

ROBERT CLAYTON GAIRNS
Soaring Association of Canada

H. DOUGLAS GARNER
NASA Langley Research Center
Hampton, Va., USA

JOSEPH GERA
NASA Langley Research Center
Hampton, Va., USA

SAM GREENHALGH
Naval Air Development Center
Warminster, Pa., USA

JAMES B. HALLISSY
NASA Langley Research Center
Hampton, Va., USA

PERRY W. HANSON
NASA Langley Research Center
Hampton, Va., USA

THOMAS E. HEAD
Severna Park, Md., USA

RICHARD F. HELLBAUM
NASA Langley Research Center
Hampton, Va., USA

ROBERT DALE HELTON
NASA Langley Research Center
Hampton, Va., USA

HEINRICH G. HELWIG
Rensselaer Polytechnic Institute
Troy, N.Y., USA

JAMES R. HENRY
Soaring Association of Canada

MANFRED H. HILLER
University of Stuttgart
Stuttgart, W. Germany

WILLIAM TODD HODGES
Army Structures Laboratory
NASA Langley Research Center
Hampton, Va., USA

HAYWOOD HOLDER
U.S. Army
Hampton, Va., USA

REGINALD M. HOLLOWAY
NASA Langley Research Center
Hampton, Va., USA

JAMES HOTELLING
Raleigh, N.C., USA

EDWARD BRUCE JACKSON
North Carolina State University
Raleigh, N.C., USA

PETER F. JACOBS
NASA Langley Research Center
Hampton, Va., USA

HARRY A. JAMES
Teledyne Ryan Aeronautical
San Diego, Calif., USA

CHRISTIAN JANSSEN
Corning Glassworks
Corning, N.Y., USA

SAMO ONJEGIN JENKO
AMTECH Services
Mansfield, Ohio, USA

DAVID G. JONES
Aspen, Colo., USA

TOM C. JONES
Timonium, Md., USA

ROCKY H. W. JOWES
Newport News, Va., USA

THOMAS C. KELLY
NASA Langley Research Center
Hampton, Va., USA

WILLIAM L. KING
Sport Flight, Inc.,
Gaithersburg, Md., USA

ROBERT KNAUFF
U.S. Air Force
Hampton, Va., USA

ILAN KROO
Stanford University
Stanford, Calif., USA

ANDREW M. KUBIAK
Westland, Mich., USA

RICHARD KUHN
NASA Langley Research Center (Ret.)
Hampton, Va., USA

CLAUDIUS LaBURTHE
ONERA, Chatillon, France

WAYNE A. LaDENDORF
DEVRY Technical Institute
Chicago, Ill., USA

DOUG LAMONT
Soaring Society of America, USA

ROBERT T. LAMSON
Soaring Society of America, USA

EUGENE E. LARRABEE
Massachusetts Institute of Technology
Cambridge, Mass., USA

DAVID A. LEEDOM
Santa Barbara, Calif., USA

AUSTIN W. LEFTWICH
Richmond, Va., USA

W. LIEBE
Technical University of Berlin
Berlin, W. Germany

FRANCOIS-XAVIER LITT
University of Liège
Liège, Belgium

ROBERT WARREN LONG
Moore Haron, Fla., USA

PAUL B. MacCREADY
Aero Vironment, Inc.
Pasadena, Calif., USA

JOHN MacKAY
McGill University
Quebec, Canada

JOSEF MANDLA
Soaring Association of Canada

HENRY L. MARKISON
Lansing, Mich., USA

DAVID JOHN MARSDEN
University of Alberta
Alberta, Canada

GLEN L. MARTIN
Kentron International, Inc.
Hampton, Va., USA

PETER MASAK
Soaring Association of Canada

MARK D. MAUGHMER
Princeton University
Princeton, N.J., USA

KAY MAYLAND
Technische Hochschule Darmstadt
W. Germany

CATHERINE F. AND JERRY McADEN
Lorton, Va., USA

ALBERT M. McCARTY
Naval Air Development Center
Warminster, Pa., USA

HUGH McCAY
Hampton, Va., USA

ESTER M. AND JACK R. McGONIGLE
McMurry, Pa., USA

JOHN H. McMASTERS
Boeing Commercial Airplane Co.
Seattle, Wash., USA

GREGORY R. MOLENAAR
Hang Gliders International Co.
Bethesda, Md., USA

LAWRENCE C. MONTOYA
NASA Hugh L. Dryden Flight
Research Center
Edwards, Calif., USA

MARTIN MOORE
Apex, N.C., USA

PIERO MORELLI
Politecnico di Torino
Torino, Italy

RUDOLF MUELLER
Soaring Association of Canada

DIETER AND HROSWITH C. MUSER
DFVLR, Stuttgart, W. Germany

HENRY T. NAGAMATSU
Rensselaer Polytechnic Institute
Troy, N.Y., USA

JAMES L. NASH-WEBBER
Massachusetts Institute of Technology
Cambridge, Mass., USA

ORAN W. NICKS
NASA Langley Research Center
Hampton, Va., USA

W. BARRY NIXON
Princeton University
Princeton, N.J., USA

WALDO OEHRMAN
NASA Langley Research Center
Hampton, Va., USA

LACH OHMAN
Bryan, Ohio, USA

ALLEN ORMSBEE
University of Illinois
Urbana, Ill., USA

CARL ARTHUR OSOJNAK
Birmingham, Mich., USA

BERNARD PAIEWONSKY
McClellan, Va., USA

STANLEY PELKOWSKI
Tidewater Soaring Society, USA

JIM ALEX PENLAND
NASA Langley Research Center
Hampton, Va., USA

WERNER PFENNINGER
NASA Langley Research Center
Hampton, Va., USA

JIM PETERS
Baltimore, Md., USA

WILLIAM H. PHILLIPS
NASA Langley Research Center (Ret.)
Hampton, Va., USA

P. KENNETH PIERPONT
NASA Langley Research Center
Hampton, Va., USA

BION LEE PIERSON
Iowa State University
Ames, Iowa, USA

VIC POWELL
National Aeronautic Association
Washington, D.C., USA

DECIO PULLIN
Associação Brasileira de Vôo a Vela
S. Paulo, Brazil

THOMAS H. PURCELL
Flight Dynamics, Inc.,
Raleigh, N.C., USA

BALLARD QUASS
NASA Langley Research Center
Hampton, Va., USA

JAMES C. REDDING
Webster, N.Y., USA

WILMER H. REED, III
NASA Langley Research Center
Hampton, Va., USA

MICHAEL M. REISMAN
Chattanooga, Tenn., USA

RONALD E. RENU
North Carolina State University
Raleigh, N.C., USA

KURT REUPKE
Grumman Aerospace Corp.
Bethpage, N.Y., USA

WILLIAM K. RICKSON
Millbrae, Calif., USA

DONALD R. RILEY
NASA Langley Research Center
Hampton, Va., USA

DAVID ROBSON
Baltimore, Md., USA

FRANCIS M. ROGALLO
Kitty Hawk, N.C., USA

NELSON M. ROGERS
Wright Patterson Air Force Base
Ohio, USA

GIULIO ROMEO
Politecnico di Torino
Torino, Italy

ROBERT A. ROSE
Bihrl Applied Research
Hampton, Va., USA

LAWRENCE C. ROSSI
Salisbury, Md., USA

JOHN F., ROURKE, JR.
NASA Langley Research Center
Hampton, Va., USA

MURRAY I. ROZANSKY
MIRCO, Hopewell, N.J., USA

ROBERT RUELLE
University of Illinois
Urbana, Ill., USA

JOHN M. RUSSELL
Massachusetts Institute of Technology
Cambridge, Mass., USA

GUY J. SANDER
University of Liège
Liège, Belgium

LOYAL WADE SAVARIA
Wonder Valley Soaring School
Fresno, Calif., USA

PATRICIA LYNN SAWYER
Tidewater Soaring Society, USA

FREDERIC H. SCHMID
Metairie, La., USA

HARRIS M. SCHURMEIER
NASA Jet Propulsion Laboratory
Pasadena, Calif., USA

LES E. SCHWEIZER
Schweizer Aircraft Corp.
Elmira, N.Y., USA

GEORGE SEIRMARCO
Tidewater Soaring Society, USA

GASTON R. SERVANT
Hang Gliders International Co.
Bethesda, Md., USA

WILLIAM GRIER SEWALL
NASA Langley Research Center
Hampton, Va., USA

EDGAR D. SEYMOUR
Glider Pilots Ground School
Rochester, N.Y., USA

DANA SEYMOYR
Toronto, Canada

NELSON AND REIDUN SHAPTER
McLean, Va., USA

TIMOTHY M. SHEARS
Grand Rapids, Mich., USA

YOUNG T. SHEN
David W. Taylor Naval Ship
Research and Development Center
Bethesda, Md., USA

S. SIDDIQI
University of Illinois
Urbana, Ill., USA

DAVID J. SIEGFRIED
New Britain, Pa., USA

ROBERT A. SIMONDS
LTV Corp.
Hampton, Va., USA

DAVID J. SLIWA
University of Illinois
Urbana, Ill., USA

KENNETH J. SLIWA
Harris Hill Soaring Corp.
Elmira, N.Y., USA

SHIRLEY A. SLIWA
National Soaring Museum
Elmira, N.Y., USA

STEVEN M. SLIWA
NASA Langley Research Center
Hampton, Va., USA

A. J. SMITH
Soaring Society of America, USA

BERNALD S. SMITH
National Soaring Museum
Elmira, N.Y., and
Soaring Society of America, USA

GRANT M. SMITH
Poplar Lake, Ill., USA

PAUL M. SMITH
LTV Corp.
Hampton, Va., USA

ROBERT E. SMITH
Pascagoula, Miss., USA

STANLEY W. SMITH
Newark, Del., USA

JAROSLAW SOBIESKI
NASA Langley Research Center
Hampton, Va., USA

DAN MICHAEL SOMERS
NASA Langley Research Center
Hampton, Va., USA

CHARLES M. SOUTHALL, III
Poquoson, Va., USA

CHRISTOPHER STARBUCK
Wildwood, Ga., USA

HERBERT A. STOKELY
Virginia Beach, Va., USA

FLOYD J. AND FRANCES SWEET
Soaring Society of America, USA

ADAM SWETNICK
Gaithersburg, Md., USA

KATHLEEN K. TAYLOR
Brookhaven National Laboratory
Upton, N.Y., USA

WALTER TAYLOR
Newport News, Va., USA

M. P. TETER
Corning Glassworks
Corning, N.Y., USA

R. VICTOR TURRIZIAOI
Kentron International Inc.
Hampton, Va., USA

VADYM V. UTGOFF
U.S. Naval Academy
Annapolis, Md., USA

BRIAN UTLEY
Soaring Society of America, USA

OTTO WAGNER
Technical University of Munich
Munich, W. Germany

MICHAEL WATERS
Sport Flight, USA

PETER WAY
Massachusetts Institute of Technology
Cambridge, Mass., USA

QUENTON E. WEAVER
Asheboro, N.C., USA

DAVID V. WEBBER
Chads Ford, Pa., USA

TOM WILLIAMS
North Carolina State University
Raleigh, N.C., USA

JERZY S. WOLF
Aviation Institute
Warsaw, Poland

LARRY EARL WOODS
Hydrospeed
Ontario, Canada

RAY YOUNG
Aero Club Albatross
Somerville, N.J., USA

JAMES W. YOUNGBLOOD
NASA Langley Research Center
Hampton, Va., USA

1. Report No. NASA CP-2085, Part II		2. Government Accession No.		3. Recipient's Catalog No.	
4. Title and Subtitle THE SCIENCE AND TECHNOLOGY OF LOW SPEED AND MOTORLESS FLIGHT				5. Report Date June 1979	
				6. Performing Organization Code	
7. Author(s) Perry W. Hanson, compiler				8. Performing Organization Report No. L-12973	
				10. Work Unit No. 505-02-23-01	
9. Performing Organization Name and Address NASA Langley Research Center Hampton, VA 23665				11. Contract or Grant No.	
				13. Type of Report and Period Covered Conference Publication	
12. Sponsoring Agency Name and Address National Aeronautics and Space Administration Washington, DC 20546				14. Sponsoring Agency Code	
15. Supplementary Notes					
16. Abstract The Third International Symposium on the Science and Technology of Low Speed and Motorless Flight was held at the NASA Langley Research Center, March 29-30, 1979. The NASA Langley Research Center sponsored the symposium in cooperation with the Soaring Society of America (SSA). The symposium provided a forum for the interchange of information on recent progress in the science and technologies associated with low speed and motorless flight. This conference publication includes 28 papers presented at the symposium and 1 additional paper. The papers deal with low speed aerodynamics, new materials applications and structural concepts, advanced flight instrumentation, sailplane optimal flight techniques, motorsoarers, and ultralight sailplanes and hang gliders.					
17. Key Words (Suggested by Author(s)) Low speed aerodynamics Optimum design Low drag airfoils Advanced instrumentation Structural analysis			Composite materials Ultralight sailplanes Hang gliders		
18. Distribution Statement Unclassified - Unlimited Subject Category 01					
19. Security Classif. (of this report) Unclassified		20. Security Classif. (of this page) Unclassified		21. No. of Pages 305	
				22. Price* \$11.75	

* For sale by the National Technical Information Service, Springfield, Virginia 22161

NASA-Langley, 1979